UNIVERSITÉ DE LORRAINE | BIBLIOTHÈQUES UNIVERSITAIRES

AVERTISSEMENT

Ce document est le fruit d'un long travail approuvé par le jury de soutenance et mis à disposition de l'ensemble de la communauté universitaire élargie.

Il est soumis à la propriété intellectuelle de l'auteur. Ceci implique une obligation de citation et de référencement lors de l'utilisation de ce document.

D'autre part, toute contrefaçon, plagiat, reproduction illicite encourt une poursuite pénale.

Contact bibliothèque : ddoc-theses-contact@univ-lorraine.fr
(Cette adresse ne permet pas de contacter les auteurs)

LIENS

Code de la Propriété Intellectuelle. articles L 122. 4
Code de la Propriété Intellectuelle. articles L 335.2- L 335.10
http://www.cfcopies.com/V2/leg/leg_droi.php

Characterization of the poromechanical coupling in soft biological tissues: application to the temporomandibular joint disc

---

PhD Thesis

submitted and defended publicly on November 24th 2025
as a partial requirement to qualify for the degree of:

Doctor in Mechanical Engineering - Material Mechanics

by

Caio DE OLIVEIRA CAFIERO

Composition of the Jury:

Président du jury:	Romain NICOT	Professeur des Universités / Praticien hospitalier - Université de Lille / Centre Hospitalier Universitaire de Lille
Rapporteur:	Pauline ASSEMAT	Chargée de recherche HDR - Institut de mécanique des fluides de Toulouse
Rapporteur:	Simon LE FLOC'H	Professeur des Universités - Université de Montpellier
Examinateur:	Jessica SCHIAVI-TRITZ	Chargée de recherche HDR - Université de Lorraine
Directrice de thèse:	Anne-Sophie BONNET	Professeur des Universités - Université de Lorraine
Co-directeur de thèse:	Adrien BALDIT	Maître de Conférences HDR - Université de Lorraine

---

LEM3 – Biomechanics and Bioengineering of the Musculoskeletal System – UMR CNRS 7239

Acknowledgements

First and foremost, I would like to express my sincere gratitude to my thesis supervisors, Anne-Sophie Bonnet and Adrien Baldit, for their invaluable support and outstanding scientific guidance throughout these years. Beyond their academic excellence, their availability, steady support and human perspective have constantly motivated me and made this period of personal and professional growth lighter and truly enriching.

I would also like to thank Simon Le Floc'H and Pauline Assemat for taking the time to evaluate this work as well as Jessica Schiavi-Tritz and Romain Nicot for their availability and willingness to participate on the jury.

I am also grateful to the other project collaborators, who kindly devoted their time to support this work and broaden my perspective on different dimensions of knowledge. I would like to thank Fanélie Wanert from IHU Strasbourg and La Maison Wagner for providing the samples that were used in this work. I am also grateful to Chrystelle Po and Aurore de Cauwer from the ICube laboratory for their support with MRI imaging and sample harvesting. Thanks to Sebastien Leclerc for the MRI images of the post-experiment samples, Jean-Marc Allain for the OCT images, and Gilles Dusfour for his collaboration in the image correlation analysis. I also thank Lionel Ardrizzini and Paul Vialat for machining the parts for the devices we developed, Mateo Barbosa and Laurent for their support, Théophile Gross and Boris Piotrowski for their help with the computing cluster and Andrea Cappella and Boris Chevrier for training me in SEM usage.

I extend my gratitude to the other members of the biomechanics team, Cynthia Dreistadt and Émilie de Brosses for their support and enriching discussions, both of them contributing to such a pleasant atmosphere in the corridors.

I would like to thank Emilien Schall for his company in our nice shared office throughout this entire PhD period and for his helpful 3D printing tips. Martin Boillat for our wandering discussions, for helping me push Emilien's car and for our shorter but memorable office mate period. Emilie Wiedemann-Fodé for her kindness and for the cheerful visits to our office. Alexis da Rocha for his ongoing stream of insights and partnership at conferences and Marine Bekrar for taking on the challenge of the direct permeation device project (and succeeding). I also thank the other PhD students and researchers at LEM3 : Alex, Achref, Aicha, Laís, Joé, Paul, Aymeric, Daniel, Julien, and many others, for the knowledge-sharing, beers, unforgettable moments in the Vosges and for sharing the same PhD struggles and laughs along the way.

My sincere thanks to Nathalia Soar, whose affection and support made the most difficult days lighter and who has been a source of inspiration to me in both my personal and professional life, complemented by our scientific exchanges and the comfort of feeling at home. I would like to thank Thiago Kirazian for offering me a different outlook on the world and for the countless one-of-a-kind conversations we had, scientific and non-scientific alike. Thank you to Sarah, my long-standing and cherished friend, whose presence and support I have always felt even across the distance. I also thank my dear friends Isadora, Manuela, Baptiste, Helène, Anna, Letícia, Donadio and Braga with whom I could always count during this period and who were always cheering for my success.

Finally, I want to express my heartfelt thanks to my parents, Marcelo and Simone Cafiero, who, even across the long and challenging distance, have remained a constant source of strength and comfort in my life, guiding and inspiring me to be a better person to this day.

I am extremely grateful to all of you. Muito obrigado!

Résumé en français

Caractérisation des couplages poromécaniques dans les tissus biologiques mous : application au disque de l'articulation temporomandibulaire.

Mots clés : couplage poromécanique; tissus biologiques mous; disque de l'articulation temporomandibulaire; expérimentation; simulation.

La structure complexe des tissus biologiques mous, tels que le cartilage, joue un rôle central dans la détermination de leur comportement mécanique. Ces tissus peuvent subir d'importantes déformations, et leurs propriétés mécaniques varient selon la direction en raison de leur microstructure fibreuse anisotrope. Ce sont des matériaux mécaniquement non linéaires, hétérogènes et poreux composés principalement de fluide, qui peut s'écouler et interagir avec la phase solide qui constitue le tissu, affectant ainsi la mécanique observée. La reproduction des conditions physiologiques lors des essais mécaniques exige le contrôle de facteurs tels que l'hydratation et la température pour simuler au mieux l'environnement originale du tissu.

Ce travail porte sur l'étude du disque temporomandibulaire, un composant essentiel de l'articulation temporomandibulaire (ATM) qui relie le crâne à la mandibule et est responsable de plusieurs fonctions essentielles de la vie quotidienne, telles que la mastication et la parole. L'ATM est une articulation synoviale recouverte d'une membrane de tissu conjonctif qui produit et stocke le liquide synovial. Ce liquide lubrifie l'articulation, participe à la nutrition cellulaire et à l'élimination des déchets métaboliques du tissu.

Le disque de l'ATM est un tissu fibrocartilagineux qui répartit les contraintes appliquées lors du chargement de la mandibule et participe au guidage de ses mouvements. Il est situé entre deux structures osseuses : le condyle mandibulaire et la fosse temporale. Pour permettre une ouverture et une fermeture correctes de la mandibule, le disque doit suivre le déplacement du condyle et glisser dans l'espace situé entre la mandibule et l'os temporal, étant constamment soumis à des chargements de traction et de compression.

Diverses pathologies peuvent altérer le bon fonctionnement de l'ATM, provoquant des douleurs aiguës, des difficultés à effectuer des mouvements et de l'inconfort qui impactent profondément la qualité de vie des patients. Les dysfonctionnements articulaires sont souvent associés à des altérations de ce disque, et la compréhension de son comportement mécanique est essentielle pour améliorer les simulations numériques des pathologies, ainsi que pour proposer et valider des solutions prothétiques ou des remplacements discaux. L'ATM étant une articulation synoviale faiblement vascularisée, il est également intéressant de comprendre les phénomènes de diffusion des fluides au sein de ses composants, liés à la nutrition et à la viabilité de ses cellules.

Le comportement du disque de l'ATM a été peu exploré dans la littérature, principalement en ce qui concerne son aspect biphasique et le traitement des troubles de l'ATM sans arthroplastie totale reste un défi. Peu d'études ont exploré l'interaction entre les phases fluide et solide dans le tissu discal, et celles qui l'ont fait proposent différentes approches de caractérisation des matériaux et des valeurs de paramètres distinctes. Les travaux actuels de cette thèse s'appuient sur la théorie poromécanique de la caractérisation des matériaux biphasiques appliquée aux tissus cartilagineux, et étendent ce cadre à l'étude expérimentale et numérique du disque de l'ATM. Cette approche associe la mécanique de la phase solide du tissu, formée par une matrice poreuse principalement composée de collagène, à la phase fluide, représentée par le liquide synovial imprégnant la matrice. Pour réaliser des caractérisations de ce type,

il est nécessaire d'établir une définition de la phase solide, liée à la mécanique du réseau de collagène qui constitue la partie la matrice poreuse du matériau, associée à une définition de perméabilité (k), qui décrit la dynamique des fluides au sein du tissu en utilisant la loi de Darcy.

Cette thèse fait suite à une étude principale de l'équipe BIO2MS du laboratoire LEM3, rapportée dans Tappert (2020), qui a analysé la mécanique des disques temporomandibulaires porcins par une approche monophasique hyperélastique. La base de données utilisée dans les travaux précédents, ainsi qu'une partie du dispositif expérimental et quelques échantillons restants ont été exploités au long de la thèse. Des nouveaux échantillons de disques ATM ont été également collectés spécifiquement à cet effet au cours du développement de la thèse, afin de permettre la réalisation de multiples essais sur chacun d'eux. Les résultats de ce travail visent à enrichir la littérature sur les aspects poromécaniques des disques ATM en proposant des paramètres et en discutant de leur nature multiphasique, anisotrope et hétérogène du matériau.

Au total, quatre têtes de porc ont été prélevées au cours de la thèse, permettant d'obtenir huit disques temporomandibulaires destinés aux campagnes d'essais de l'étude. Dans un premier temps, des essais de compression sphérique ont été réalisés sur des disques d'ATM porcins. L'objectif était de réaliser des essais non destructifs sur plusieurs zones des échantillons, les disques étant comprimés à l'aide de sphères rigides. Ces essais permettent de préserver les contraintes internes du matériau et d'évaluer la relation force/déplacement pour différents rayons d'outils de compression et fréquences de chargement. Le système expérimental vise à reproduire les conditions physiologiques d'hydratation, de température et d'osmolarité des disques.

Les résultats des expériences ont montré que l'augmentation du rayon de la sphère de compression entraînait des forces résultantes plus importantes, comme prévu, en raison de la compression de plus grandes portions du matériau. La réponse viscoélastique du disque a été mise en évidence par la variation de l'amplitude des forces mesurées avec différentes fréquences de chargement, ainsi que par l'hystérésis inter et intracyclique. Les résultats ont corroboré l'applicabilité de la théorie biphasique au comportement des tissus discaux. Des vitesses de compression plus élevées ont généré des forces de réaction plus importantes, associées à l'écoulement du fluide et à sa résistance à la traînée. Les régions latérale, centrale et médiale des disques de l'ATM ont été comparées, mais aucune différence significative de rigidité n'a été observée lorsqu'ils étaient soumis à une compression sphérique.

Une approche de caractérisation hyperélastique monophasique a initialement été présentée, basée sur les travaux de Tappert (2020). Ces travaux proposent des mises à jour du modèle développé lors du travail précédent, permettant de définir des paramètres de caractérisation hyperélastique à partir des valeurs de force et de déplacement observées, identifiant ainsi la contrainte effective équivalente à une contrainte compression uniaxiale sur le matériau. Cette première exploration des résultats repose sur une approche monophasique, dans laquelle les paramètres peuvent servir de valeurs d'entrée pour définir le comportement de la phase solide du matériau dans des modèles plus sophistiqués. Cette méthode présente un fort potentiel d'application en raison de la rareté des approches qui adaptent le modèle de Hertz à la caractérisation de fines couches de matériaux hyperélastiques soumises à une compression sphérique lorsqu'elles sont détachées de la surface.

En parallèle, un modèle d'éléments finis axisymétrique a été créé sur Abaqus, pour représenter la compression d'une sphère sur le disque, cette fois en utilisant l'approche poromécanique. Deux définitions biphasiques pour le matériau constituant le disque ont été adoptées sur la base de modèles disponibles dans la littérature. Le déplacement imposé dans les simulations a reproduit ce qui a été réalisé lors des expériences de compression sphérique et l'erreur entre la force simulée et la force mesurée expérimentalement dans un cycle de chargement a été comparée. Après avoir effectué les simulations, il est devenu évident que les paramètres de la littérature n'étaient pas adéquats pour reproduire les expériences réalisées ici, et un processus d'optimisation a été appliqué pour ajuster leurs valeurs afin d'obtenir une meilleure approxi-

mation des courbes expérimentales.

L'optimisation des simulations éléments finis a fait varier les paramètres du matériau afin de réduire l'erreur quadratique moyenne entre les valeurs de force simulées et expérimentales. Les résultats optimisés consistent en des modules de cisaillement allant de 4.14 kPa (petits rayons) à 1.75 kPa (grands rayons), proches des valeurs de Wu et al. (2015) pour les disques porcins (2.5 à 4.0 kPa). La méthode a également obtenu un module volumique compris entre 4.04 et 2.23 kPa et une perméabilité comprise entre 1.09 et 1.26 $\times 10^{-15} m^4/Ns$, comparables aux données de Kuo et al. (2010) sur des disques humains et Tverje & Nyashin (2010) sur des disques porcins. Cependant, ces résultats ne concordent pas avec ceux d'autres études de la littérature explorant le disque, dans lesquelles la perméabilité a été définie à des ordres de grandeur différents des valeurs obtenues ici, comme $(3.24 \pm 2.29) \times 10^{-17} m^4/Ns$ (Li et al., 2021).

L'un des avantages des essais non destructifs de compression sphérique réside dans la possibilité d'étudier plus en détail les mêmes échantillons par d'autres approches expérimentales. Afin d'accroître la fiabilité de ces résultats, d'autres méthodes de caractérisation ont également été appliquées et leurs résultats comparés à ceux obtenus pour la compression sphérique. Ainsi, des échantillons cylindriques de 10 mm de diamètre ont été découpés dans la zone centrale des disques afin d'être utilisés ultérieurement dans des expériences de compression confinée et de perfusion directe, réalisées sur des dispositifs sur mesure.

Les échantillons cylindriques ont été filmés immédiatement après découpe afin d'être analysés par corrélation d'images, permettant ainsi d'identifier les déformations associées à la libération des contraintes internes du matériau. Cette déformation, anisotrope, a indiqué une plus grande résistance du matériau à l'expansion dans la direction antéropostérieure (le long du réseau de fibres), corroborant l'hypothèse selon laquelle les fibres jouent un rôle majeur dans la résistance à la traction du matériau, conformément à l'orientation du réseau de fibres.

Une fois filmés, les échantillons ont été soumis à des tests de compression confinée. Contrairement à la compression sphérique, qui ne déforme que la partie la plus superficielle des disques, la compression confinée sollicite l'ensemble de la structure des échantillons selon la direction supérieure-inférieure avec un piston poreux. Les échantillons sont comprimés à l'aide d'un piston poreux, confinés latéralement par une chambre et placés sur une base poreuse, ce qui permet l'exsudation du fluide par leurs surfaces supérieure et inférieure. Des essais de fluage ont été réalisés, avec l'application d'une force constante de 4N pendant une période de deux heures.

À partir d'un modèle de la littérature décrivant le déplacement d'une colonne biphasique unidimensionnelle sous charge de fluage, un algorithme d'optimisation a été développé pour définir les paramètres matériaux correspondant à chaque résultat expérimental de compression confinée. Cet algorithme a comparé l'erreur quadratique moyenne entre les déplacements expérimentaux et théoriques, en faisant varier les paramètres définissant la perméabilité et la phase solide afin de minimiser cette erreur. La méthode a permis d'estimer les valeurs moyennes du module de cisaillement de $\mu = 43.88 \pm 10.85$ kPa et du module volumique $\kappa = 61.50 \pm 32.13$ kPa, en supposant un comportement linéarisé pour la phase solide, et $\mu = 22.98 \pm 9.04$ kPa et $\kappa = 74.56 \pm 38.26$ kPa pour l'approche néo-Hookéenne compressible pour la phase solide, ce qui représente une augmentation d'ordre de grandeur par rapport aux résultats trouvés en compression sphérique. Les valeurs de perméabilité pour la compression confinée étaient de l'ordre de $10^{-15} \pm m^4/Ns$, démontrant une équivalence avec ce qui a été mesuré par compression sphérique.

Par la suite, les mêmes échantillons cylindriques ont été utilisés pour des essais de perfusion directe à l'aide d'un dispositif conçu sur mesure. Pendant ces essais, les échantillons étaient à nouveau confinés latéralement, ce qui permettait au fluide de s'écouler à travers les cylindres par leurs faces supérieure et inférieure. Une pression était appliquée à la base de l'échantillon, et le fluide le traversait. La mesure de la différence de pression entre l'entrée et la sortie du

système ainsi que celle du débit du fluide à la sortie a permis d'estimer la perméabilité du tissu. À ce jour, la perfusion directe n'a donné qu'un seul résultat, dont l'ordre n'a pas pu être reproduit pour les autres échantillons.

Classiquement, dans d'autres études de la littérature enlèvent les surfaces inférieure et supérieure des échantillons, afin de réduire leur épaisseur et de faciliter la traversée du fluide pendant l'essai. Cette pratique est également adoptée dans d'autres travaux sur le disque de l'ATM, y compris lors des essais de compression confinée. Cependant, dans le présent travail, cette couche externe n'a pas été retirée, dans le but de mesurer la perméabilité des disques sur l'ensemble de leur épaisseur, dans des conditions aussi proches que possible des conditions physiologiques. Cela dit, cette particularité de l'essai, associée à de possibles endommagements de la structure solide des disques préalablement testés en compression confinée, pourrait également avoir représenté l'une des principales difficultés rencontrées lors de la réalisation de l'expérience présentée ici.

L'analyse des données IRM a été réalisée sur les disques avant et après la campagne d'essais. Le volume des échantillons cylindriques a tendance à diminuer après la campagne d'essais, ce qui peut être lié à des déformations permanentes auxquelles les disques ont été soumis durant les essais, ainsi qu'à la contraction de leur structure lors de la coupe. L'imagerie IRM des échantillons utilisés en compression confinée et en perfusion directe a permis d'observer à nouveau la nature anisotrope de la déformation des échantillons le long de leur épaisseur, ainsi que le rôle des fibres de collagène du matériau dans le maintien de son expansion antéropostérieure.

D'autres échantillons de disques ont été lyophilisés afin d'être observés au moyen d'un microscope électronique à balayage (MEB) à vide dégradé, ce qui a permis la capture d'images sans métallisation préalable des échantillons. Les images obtenues par le MEB ont démontré l'hétérogénéité structurelle du disque. Une couche externe fine, continue et dense recouvrant les surfaces supérieure et inférieure du tissu a été identifiée, suggérant une organisation différenciée par rapport aux régions internes du matériau. Cette couche superficielle, bien que déjà mentionnée dans une étude de la littérature utilisant des images de tomographie par cohérence optique (OCT), était beaucoup plus visible dans les échantillons analysés après lyophilisation, permettant une visualisation directe de sa morphologie et de son épaisseur relative.

Ce résultat renforce l'importance de prendre en compte, dans les futures analyses mécaniques et de modélisation, la nature potentiellement multicouche du disque. L'impact de cette couche superficielle dense sur la mécanique n'a pas encore été testé lors d'analyses poromécaniques et elle pourrait jouer un rôle significatif dans la perméabilité et le comportement mécanique global du tissu. Par conséquent, l'inclusion de ces aspects structurels dans les modèles constitutifs et les interprétations expérimentales peut représenter une avancée importante dans la compréhension du comportement biomécanique du disque de l'articulation temporomandibulaire.

Des essais de traction ont également été réalisés sur des échantillons de disques, traités selon une approche d'ajustement de courbe hyperélastique monophasique. Les résultats ont indiqué des valeurs différentes du module de cisaillement selon les régions du matériau, suggérant une hétérogénéité structurelle et une anisotropie. Les échantillons antérieurs et postérieurs présentaient un module de cisaillement μ de 7.73 ± 6.07 kPa et 14.88 ± 5.52 kPa, tandis que les régions médiales et latérales présentaient un μ égal à 77.57 ± 106.83 kPa et 83.96 ± 105.52 kPa respectivement, ce qui différait du module de cisaillement obtenu par compression dans la direction supérieure-inférieure du matériau par compression sphérique ou confinée.

Les modèles appliqués dans cette étude présentent des limites importantes dont il faut tenir compte lors de l'interprétation des résultats. Parmi celles-ci, l'hypothèse d'une perméabilité constante, isotrope et homogène du matériau se distingue, ce qui simplifie considérablement le comportement réel du tissu. En pratique, la perméabilité est susceptible de varier spatialement en fonction de l'orientation des fibres et du degré de compression appliqué, facteurs qui influen-

cent directement l'écoulement du fluide interstitiel et le couplage poromécanique du matériau.

De plus, les essais de traction ont été analysés selon une approche monophasique, ne considérant que la contribution de la phase solide hyperélastique à la réponse mécanique du tissu. Cette simplification néglige le rôle potentiel de la phase fluide et les phénomènes de dissipation associés au mouvement du fluide à travers la matrice lors de la déformation, ce qui peut entraîner des écarts entre le comportement expérimental et théorique, notamment sous charge dynamique ou sous fortes déformations. Dans les futures simulations numériques biphasiques du comportement en traction, il serait pertinent d'inclure la viscosité intrinsèque à la phase solide dans ce cas, compte tenu de la contribution plus importante du réseau de collagène à la contrainte de traction.

Malgré ces limitations, de telles approximations sont souvent adoptées dans les études préliminaires car elles permettent d'identifier les principaux paramètres mécaniques du tissu et fournissent une base solide pour le développement de modèles plus complexes à l'avenir, capables d'intégrer l'hétérogénéité, l'anisotropie et les effets de couplage fluide-solide de manière plus réaliste.

Les essais de perfusion directe, bien qu'ils n'aient fourni qu'un seul résultat pour l'instant, ont révélé des difficultés potentiellement liées à la forte épaisseur des disques. De futures études pourraient explorer des échantillons microtomisés à différentes profondeurs, permettant ainsi de cartographier la perméabilité sur toute l'épaisseur et de développer des modèles numériques multicouches plus réalistes. Le dispositif de perfusion directe, développé et utilisé pour la première fois dans le cadre de ce projet, a montré un fort potentiel d'application pour de futures études. Il a été testé sur d'autres matériaux, tels que la gelée de Wharton et des éponges domestiques commerciales, et a démontré une bonne capacité à mesurer la perméabilité ainsi qu'à reproduire les effets de la variation de perméabilité en fonction de la déformation imposée.

De plus, l'influence de la fréquence de chargement sur les essais de compression sphérique n'a pas encore été explorée par la simulation, malgré la nature viscoélastique du tissu. L'utilisation d'un logiciel alternatif, tel que FEBio, pourrait permettre des simulations biphasiques avancées avec des lois de perméabilité dépendantes de la déformation, rapprochant ainsi les modèles du comportement physiologique réel.

La base de données de l'equipe BIO2MS a été enrichie de 8 disques supplémentaires présentant divers résultats expérimentaux. Ces disques ont également été soumis à une compression sphérique sous relaxation de contrainte (déplacement constant imposé des sphères), mais et ces résultats n'ont pas été inclus dans la thèse. Il serait intéressant de vérifier les paramètres estimés par optimisation pour le contexte de relaxation de contrainte. Avec davantage d'échantillons de disques, il sera également possible d'explorer plus en détail l'anisotropie des disques grâce à d'autres campagnes d'essais, avec des disques pouvant être dédiés exclusivement à la production d'échantillons différentes orientations du réseau de fibres.

Actuellement, l'équipe BIO2MS dispose d'un modèle éléments finis du disque porcin obtenu par numérisation 3D, dans lequel les paramètres biphasiques obtenus ici peuvent être appliqués à des géométries plus réalistes que le modèle axisymétrique. Ainsi, les essais axisymétriques réalisés dans cette étude pourront être comparés ultérieurement à ceux réalisés sur une géométrie de disque plus représentative. En parallèle, un modèle Abaqus intégrant la structure osseuse de l'ATM, de la mandibule et du crâne, avec une cinématique spécifique au sujet, est également disponible (de Oliveira Cafiero, 2021), et l'intégration des définitions poromécaniques constitue une étape prévue de son développement. L'établissement d'un modèle complet de l'ATM, intégrant un comportement biphasique du disque obtenu à partir d'une vaste campagne d'essais, ouvre de grandes perspectives pour des études futures, permettant l'analyse de contextes pathologiques et de leurs éventuelles solutions.

Contents

List of Symbols xviii

General introduction and motivation 1

1 Introduction to poromechanics and the characterization of soft biological tissues 3
1.1 Mechanical behavior of soft biological tissues . . . 3
1.1.1 Tissue microstructure and its impact on mechanics . . . 3
1.1.2 Theoretical models for soft tissues' characterization . . . 5
1.1.2.1 Hyperelastic models . . . 5
1.1.2.2 Viscoelastic models . . . 7
1.1.2.3 Poromechanical models . . . 8
1.2 Techniques for mechanical testing . . . 10
1.2.1 Confined compression tests . . . 11
1.2.2 Direct permeation . . . 14
1.2.3 Spherical compression tests . . . 15
1.2.4 Tensile tests . . . 18
1.3 Biomechanical study of the temporomandibular joint disc . . . 19
1.3.1 Anatomy of the temporomandibular joint . . . 20
1.3.2 Disc composition and structure . . . 21
1.3.3 Disorders and therapeutic approaches for the temporomandibular joint . 23
1.3.4 Biomechanical analysis of the temporomandibular disc . . . 24
1.3.4.1 Numerical simulations of the joint . . . 24
1.3.4.2 Characterization techniques applied to intact discs . . . 27
1.3.4.3 Tensile tests performed on the disc . . . 30
1.3.4.4 Confined compression tests performed on the disc . . . 31
1.3.4.5 Direct permeation of the temporomandibular disc . . . 32
1.3.4.6 Imaging techniques applied to the disc . . . 32
1.4 Thesis objectives and strategy . . . 33

2 Spherical compression characterization and poromechanical coupling of the temporomandibular joint disc 36
2.1 Experimental testing on temporomandibular discs . . . 36
2.1.1 Sample harvesting . . . 36
2.1.2 Test protocol . . . 39
2.2 Spherical compression experimental results . . . 42
2.3 Monophasic hyperelastic characterization . . . 45
2.3.1 Introduction . . . 45
2.3.2 Materials and Methods . . . 46
2.3.2.1 Finite Element Model . . . 46
2.3.2.2 Contact radius analysis . . . 48
2.3.2.3 Other analysed aspects . . . 48
2.3.2.4 Effective stress and strain . . . 49
2.3.2.5 Model validation with uniaxial compression . . . 50
2.3.3 Results and discussion . . . 50
2.3.3.1 Sample thickness variation . . . 51

2.3.3.2 Stress-strain analysis . . . 53
2.3.4 Application to experimental results . . . 55
2.4 Biphasic axisymmetric Finite Element model . . . 58
2.4.1 Geometry and mesh definitions . . . 58
2.4.2 Boundary conditions and simulation steps . . . 59
2.4.3 Material behavior definitions . . . 60
2.5 Model testing with literature parameters . . . 61
2.6 Towards a biphasic characterization: finite elements spherical compression optimization . . . 67
2.6.1 Inverse method optimization algorithm . . . 67
2.6.2 Optimization results . . . 68
2.6.2.1 Sphere radius influence . . . 68
2.6.2.2 Disc zones difference . . . 70
2.6.2.3 Comparison of operators . . . 72
2.7 Conclusion . . . 73

3 Further exploration of poromechanical aspects and effects of tissue microstructure 75
3.1 Sample preparation . . . 75
3.2 Confined compression tests . . . 76
3.2.1 Experimental testing setup . . . 76
3.2.1.1 Development of confined compression bench . . . 76
3.2.1.2 Test protocol . . . 77
3.2.2 Parameter obtention through finite differences optimization . . . 78
3.2.2.1 Compressive displacement analysis . . . 78
3.2.2.2 Optimization algorithm . . . 82
3.2.3 Results and discussion . . . 84
3.3 Direct assessment of permeability . . . 90
3.3.1 Development of a custom bench for direct permeation tests . . . 90
3.3.2 Device validation . . . 92
3.3.2.1 Sponge samples . . . 93
3.3.2.2 Temporomandibular disc samples . . . 94
3.3.2.3 Wharton's Jelly samples . . . 95
3.4 Microstructure observation . . . 96
3.4.1 Optical coherence tomography . . . 96
3.4.2 Scanning electron microscopy . . . 98
3.4.3 Magnetic resonance imaging . . . 102
3.4.4 Inner stress release . . . 105
3.4.5 MRI of cut specimens . . . 108
3.4.6 MRI volume analysis . . . 109
3.5 Tensile response analysis . . . 112
3.5.1 Experimental tests . . . 112
3.5.2 Tensile results data treatment method . . . 113
3.5.3 Results . . . 114
3.6 Conclusion . . . 117

General conclusion and perspectives 119

A Spherical compression system stiffness compensation 123

B Spherical compression monophasic characterization complementary results 124

C Spherical compression biphasic simulation fluid velocity for blocked superficial flow 128

D Spherical compression biphasic optimization results details 129

E Confined compression results details 130

F MRI images of cut samples 131

Bibliography 132

List of Figures

1.1 Scanning electron microscopy images of fibrocartilage in different scales, showing the collagen structure. a) Rabbit skin's collagen structure, adapted from Yang et al. (2015). b) Rat medial collateral ligament (Franchi et al., 2010). c) Porcine intervertebral disc (Wu et al., 2014). 4

1.2 Experimental results from Tanaka et al. (2003b) showing the effect of cyclic compression by means of a cylindrical tool on fibrocartilaginous tissue samples, illustrating nonlinear viscous effects of the material. 5

1.3 Confined compression test with porous piston and (a) impermeable base and (b) porous free-draining base, adapted from Ateshian (2017). Depending on the adopted configuration and the data processing methods used, symmetry conditions can be applied to ensure equivalence between the two types of setups. 11

1.4 Experimental confined compression setup used to analyse bovine articular cartilage (Zimmerman et al., 2021). 12

1.5 Comparison of the displacement of the superior surface of a column under confined compression, using similar material parameters but different constitutive law definitions (Selvadurai & Suvorov, 2016). A constant stress of -0.3MPa was applied to the top, demonstrating the validation of the displacement calculation method proposed by the authors against a finite element simulation under the same conditions. 13

1.6 Direct permeation device used to determine the hydraulic permeability of human medial collateral ligament specimens under various levels of compressive strain (Weiss & Maakestad, 2006). 14

1.7 Spherical indentation scheme adapted from Tappert (2020). H - initial sample height, R - spherical compression tool radius, d - spherical compression tool displacement, a - contact radius, δ - penetration depth, R_δ - penetration depth measurement distance, u_y^δ - vertical displacement of sample surface, $\vec{g}$ - gravity. . 16

1.8 Spherical compression experiment conducted on temporomandibular joint disc and experimental result with curve-fitting using the Hertz model for material characterization 17

1.9 a) Representative stress-strain curves from biaxial tensile tests conducted on aortic tissue samples. The red curve represents the tensile response of the material when stretched along the circumferential direction of the arteries, whereas the blue curve, which exhibits lower stiffness, corresponds to the longitudinal direction. This highlights the anisotropic behavior of the tissue. The regions labeled as "initial slope" and "stiff slope" indicate the change in material stiffness as the collagen fibers progressively align and stretch (Chow & Zhang, 2011). b) Results from incremental stress-relaxation tests conducted on temporomandibular discs, showing the progressive decrease in measured stress at each compression step (Detamore & Athanasiou, 2003). 18

1.10 a) Tensile test of hydrated Wharton jelly membrane samples highlighting the damage on the structure in the end of the test (Baldit et al., 2022). b) Biaxial tensile test on aortic tissue (Chow & Zhang, 2011). 19

1.11 Temporomandibular joint location, showing disc position and internal joint structures in sagittal and coronal views (Willard et al., 2011). 20

1.12 Temporomandibular joint with the mandible in closed (a) and open (b) positions (Drake et al., 2010). The mandibular movements of protrusion and depression are indicated. . . . 21
1.13 a) TMJ disc, indicating the different tissue zones and anatomical orientation axes (Willard et al., 2011). b) Fiber network orientation in different regions of the disc, as observed via scanning electron microscopy. Fibers tend to align anteroposteriorly in the intermediate zone, while the peripheral structure in the anterior, posterior, lateral, and medial regions forms a ring-like pattern surrounding the center of the disc (Detamore et al., 2005). c) Scanning electron microscopy images of a sagittal section of the temporomandibular disc, illustrating the superior and inferior fiber network arrangement. (Juran et al., 2015). . . . 22
1.14 Figure from Ortún-Terrazas et al. (2021). a) Diagram showing model's mesh, with boundary conditions and muscle elements positioning. b) Boundary conditions applied inside the TMJ, showing elements representing the disc, muscles, articular cartilage and ligaments. . . . 26
1.15 Stress distribution [Pa] in disc in multiple different mandible conditions, with a hyperelastic Mooney-Rivlin definition (Sagl et al., 2019). . . . 27
1.16 a) Experimental apparatus used for the experiment, depicting a human TMJ disc between two indenters and submerged in saline solution controlled at 37°C, b) stress-strain relation of 10 loading cycles in the same sample, showing loading history dependent mechanical response and loss or energy of the material. Modified from Beek et al. (2003). . . . 28
1.17 a) Storage modulus and b) loss modulus variation for multiple dynamic loading frequencies, adapted from Barrientos et al. (2016). This image highlights the viscous aspects of the material. . . . 28
1.18 TMJ disc initial and steady-state modulus in relation to tested zone (Lumpkins & McFetridge, 2009). . . . 29
1.19 Specimen cut from the central zone of a porcine TMJ disc. The figure shows the contours of the space occupied by the sample over time, demonstrating the evolution of its shape from the moment of cutting (Tappert et al., 2022). . . . 30
1.20 a) Schematic illustration of specimen preparation from temporomandibular discs for tensile testing, designed to fit into custom-made grips. The disc on the left is prepared for anteroposterior tensile loading, while the disc on the right is prepared for mediolateral loading. The dashed lines indicate the cutting locations used for specimen preparation (Beatty et al., 2001). b) Sample strip positioned between custom-made clamps (Li et al., 2021). . . . 31
1.21 OCT performed on dehydrated human discs from Mărcăuteanu et al. (2010). Figure (a) shows a superior view of a disc, with the sagittal plane perpendicular to the image and indicated by the black marking painted on the sample. The white arrow in (a) shows the imaged zone in (b), where a sagittal view is represented. In Figure (b), the upper black region corresponds to air, while the tissue structure appears in white. . . . 33

2.1 harvested right TMJ disc sample with surrounding tissues. Sample 230524-Head1-Right. . . . 37
2.2 a) Freshly harvested porcine TMJ disc over a 3D printed condyle; b) Disc and condyle inside the saline solution filled tube to be introduced in the MRI machine. c) Sagittal cut of disc inside MRI. . . . 38
2.3 MRI device at the ICube laboratory used for imaging fresh TMJ disc samples (7 Tesla Bruker Biospec 70/30 USR). . . . 38

2.4 Experimental setup used for spherical compression tests. 39
2.5 Disc positionned over 3D printed condyle just before testing. The disc, glued to the condyle, is partially submerged in fluid and the 3 mm radius compressing sphere is positioned over the sample. 40
2.6 Experiemental protocol developed in Tappert (2020) for spherical compression tests. The preload value is related to sphere radius (table 2.1) and number of cycles depends on loading frequency (0.01 Hz/0.1 Hz/1 Hz). 41
2.7 Spherical compression results for central zone of one disc, showing the variation of sphere radius for a loading frequency of 0.1 Hz. Sample 240311-Head1-Right. 42
2.8 Maximum forces measured for the first loading phase after pre-conditioning cycles. Average forces ± standard deviation (n=8) for different disc zones, loading frequencies and sphere radius. 44
2.9 Spherical compression results for central zone of one disc, with different loading frequencies and sphere radius equal to 1.75 mm. Sample 240311-Head1-Right. . 45
2.10 Geometry, mesh and boundary conditions of the axisymmetric FE model of a disc placed in between a rigid support and a rigid spherical compression tool. The • represents the point of tie-constraint placement between the tip of the compression tool and one node of the mesh. Adapted from Tappert (2020). . . . 47
2.11 Simulated spherical compression FE results. The vertical displacement is shown for samples of $h = 0.5$, $L = 25R$ with different density values (0.01, 1.00 and 10.00 kg/L), in a state of compression representing $d/R = d_{max}/R$. 50
2.12 Comparison of simulations' force displacement results with respect to the Hertz model. Each result correspond to a different thickness ratio that was adopted, and the image highlights the difference in force measurement observed. 51
2.13 Comparison of dimensionless contact radius (a/R) as a function of dimensionless tool displacement (d/R) for samples of different initial thickness. The figure shows how the contact radius evolves as the sphere compresses the samples in controlled displacement, and the continuous lines represent the performed fittings used for matching the measured simulated data. 52
2.14 Fitting of β (a) and m (b) as a function of h. These fittings allow to predict the values of the parameters from equations 2.7 and 2.8, allowing to define the relation between contact radius a/R and imposed displacement d/R based on different sample thickness values. 53
2.15 Effective stress vs corresponding stretches for various values of h in spherical compression. 54
2.16 Calculated values of effective stress vs strain for spherical compression simulations in comparison to theoretical Neo-Hookean uniaxial compression eulerian stress vs strain. The approximation of the values to the equivalent theoretical curve in black indicates the model's ability to, at different thickness ratios, converge to the same stress-strain relationship. 54
2.17 Fitting of equation 2.13 representing the evolution of χ as function of h. Knowing χ allows direct definition of effective strain based on current contact radius (see equation 2.12). 55
2.18 Example of eulerian stress-strain (σ^* - ε^*) curve obtained after application of the spherical compression monophasic data treatment method, with the two-term Ogden model with fitting parameters μ_1, μ_2, α_1, α_2 and associated determination coefficient R^2. Sample 240311-Head2-Right. 57

2.19 Mesh used for simulations, with rigid bodies definitions for support and sphere. Gravity was applied along the vertical axis of the figure (represented by $\vec{g}$) and pore pressure was set to 0 for all edges of the specimen, indicated by the red marking. The imposed displacement was applied to the reference point of the rigid body representing the sphere. 59
2.20 Examples of experimental curves obtained for $f = 0.01$ Hz and different sphere radii. The red dot indicates the instant at which contact was considered established and, from this threshold, the experimental displacement data were considered for introduction into the simulation. Sample 240311-Head2-Right. . . 60
2.21 Simulation results for R = 1.75 mm, highlighting the a) true compressive strain in the Y direction (S22), b) effective stress in the Y direction and c) the pore pressure. 62
2.22 Instantaneous fluid velocity for state of maximum compression in simulation of Figure 2.21. 63
2.23 Simulation in which contact with the sphere was set as impermeable to fluid flow. The graph show the results in force measurement, highlighting low difference in force measurement. 64
2.24 Representative results of experimental force and displacement compared with simulations of the models in table 2.6. The results correspond to the same disc (sample 240311-Head2-Right), subjected to a loading frequency of 0.01 Hz with different sphere radii, being a) R = 0.875 mm, b) R = 1.75 mm and c) R = 3 mm. 65
2.25 Representative results of experimental force and displacement compared with simulations of the models in table 2.6. The results correspond to the same disc (sample 240311-Head2-Right) as Figure 2.24, subjected to a compression where R = 3 mm and higher loading frequencies of a) f = 0.1Hz and b) f = 1 Hz. . . . 66
2.26 Optimization results for different sphere radius on central zone of TMJ sample 240311-Head2-Right. The figure shows the comparison of force-displacement curves on one loading and unloading cycle of spherical compression, comparing the experimentally obtained results to the ones obtained through FE simulations. 69
2.27 Sherical compression optimization results for different disc zones on TMJ sample 240311-Head2-Right with R=3mm and f=0.01Hz. 71
2.28 Optimization results comparison between operators, for a spherical compression test of R=1.750 mm at f = 0.01 Hz. The force and displacement data from experiments from different test campaigns were passed through the same algorithm to obtain poromechanical parameters. 73

3.1 Scheme of disc indicating the central punched zone (red) with rectancular cuts for surrounding specimens in the anterior (A) and posterior (P) zones (blue) and in the medial (M) and lateral (L) zones (green). 75
3.2 TMJ sample and cut specimen from its central zone, immediately after being cut. The disc presents dark markings on its surface that were placed over them with graphite powder for image correlation analysis purposes, to be discussed further. Specimen 230524-Head1-Right, corresponding to the same uncut sample shown in Figure 2.1. 76
3.3 Confined compression device, showing a) porous base and lateral confinement chamber, b) porous piston and c) complete system submerged in saline solution during testing with a TMJ sample. 77

3.4 Uni-dimensional model proposed in Selvadurai & Suvorov (2016). Figure shows the example of a spacial division of the sample in 11 nodes, with a symmetry condition applied at the bottom of the sample (dashed line). Since it is a one-dimensional problem, the column can only be compressed vertically, through the action of the force vector $\vec{F}$. Zero pore pressure, shown in red, is applied at the top of the sample representing free fluid flow at the extremities of the sample. . 79
3.5 Confined compression results for sample 230524-Head1-Left. The force was recorded over time, and the transition to steady force creep load is shown in the zoom in the beginning of the curve. 83
3.6 Experimental displacement for confined compression of a TMJ sample 230524-Head1-Left, showing the identification of the portion of the data to be used in fitting. 84
3.7 Confined compression a) before the beginning of the test, b) immediatly in contact establishment and c) after 2h of creep test. Sample 230524-Head1-Left. . . 85
3.8 Experimental fitting of confined compression results for sample 230524-Head1-Left, with strains calculated based on the displacements of sample's superior surfaces. The parameters obtained for the three model definitions are provided. Strain here was calculated based on initial configuration L/L_0. 86
3.9 Simulated displacement for each of the nodes over the length of the test, for different model definitions for sample 230524-Head1-Left. The measured displacement corresponds to the solution of the partial differential equation governing the column displacement, calculated for the nodes of the symmetric one-dimensional mesh defined to represent the uniaxial compression of the TMJ disc specimen. . 87
3.10 Effective stress evolution over the nodes of a LE solution. Results are based on the calculated displacement, that allowed to calculate the stress acting on the solid phase of the material for the experimental results of Sample 230524-Head1-Left. 88
3.11 Pore pressure evolution over the nodes of a LE solution, calculated once the effective stress was known. Sample 230524-Head1-Left. 89
3.12 a) Design of the direct permeation device and b) manufactured prototype. . . . 91
3.13 a) Thermoregulated chamber in which the device was placed. b) Final direct permeation device. 92
3.14 Direct permeation results on sponge sample for different degrees of compression. 93
3.15 Measured values of permeability for different imposed strains on a sponge sample. 94
3.16 Fluid flow through one TMJ sample with 100 kPa applied. Sample 230524-Head1-Left. 95
3.17 OCT device used on disc. 97
3.18 OCT image of the superior surface from central zone of sample 240311-Head2-Left. 97
3.19 Lyophilizer used for freeze drying the samples. 98
3.20 Top view of the positioning of the freeze-dried discs for SEM imaging, with conductive carbon adhesive tape (in black) and a fixation screw. Positioning for viewing a) sagittal and b) transverse planes (with the upper surface of the disc facing upwards). 98
3.21 SEM image of sagittal view of freeze-dryed disc sample 230524-Head1-Right. . . 99
3.22 SEM image of sagittal view of freeze-dryed disc sample 240311-Head2-Right. The highlighted zones illustrate the exterior layer of different structure from the rest of the sample, that covers the superior and inferior surfaces of the disc. . . . 100
3.23 SEM image of frontal view of freeze-dryed disc sample 240311-Head2-Right. . . . 101
3.24 SEM image of superior view of freeze-dryed disc sample 240311-Head2-Right. a) Intact superior surface, b) disc after the removal of the superior surface. 101

3.25 a) Avance III 600 Wide Bore (Bruker, Germany) MRI device used for visualizing discs. b) Disc sample inside of tube used for introduction into the MRI machine. 103
3.26 MRI image of middle layer of a whole porcine TMJ disc (sample 230524-Head1-Right). Acquisition parameters: Spin Echo (MSME) : FOV 3cm, slice 0.5mm, 512*512 pixels, TE 8.8ms, TR 2000ms, 15 slices, 16 averages. 104
3.27 Diffusion Tensor Image of middle layer of a whole porcine TMJ disc (sample 230524-Head1-Right). The images show the diffisivity in the X, Y and Z directions, with a logarithmic scale on the left on m^2/s. Image specifications: FOV 3 cm, slice 1 mm, 256×256 pixels, TE 20.5 ms, TR 2000 ms, 4 averages, delta 5 ms, DELTA 8.8 ms, B values from 25 to 800. 105
3.28 Cut disc filmed during a period of one hour. Sample 240311-Head2-Left. 106
3.29 Anteroposterior strain measured by DIC method showing initial and final configuration of disc sample 240311-Head2-Right. 107
3.30 Mediolateral strain measured by DIC method showing initial and final configuration of disc sample 240311-Head2-Right. 107
3.31 MRI of three different slices of the same disc (sample 240311-Head2-Right), with a 0.5 mm distance between slices. The orientation of the fiber network in the anteroposterior axis is visible, as is the deformation of the sample in relation to its original 10 mm circular geometry. Acquisition parameters: Spin Echo (MSME) – FOV 3 cm, slice thickness 0.5 mm, matrix 512 × 512 pixels, TE 8.8 ms, TR 2000 ms, 10 slices, 8 averages. 108
3.32 Segmentation workflow for sample 240311-Head1-Left. a) Full intact disc MRI with selected voxels for the segmentation. The red line indicates the 10 mm diameter b) Digitally selected 10 mm diameter undeformed disc, simulating the cut specimen from figure (a). c) Cut disc MRI, with selected voxels for segmentation. d) 3D structure obtained from the segmentation of figure (c). 110
3.33 Ideal cylinder height for undeformed state of the disc (green) and deformed state (blue). The measured values correspond to the mean dimensions estimated from the segmentation of all MRI data, associated to the standard deviation for all six discs that were imaged. 111
3.34 TMJ disc tensile specimen. Sample 240311-Head2-Right. 112
3.35 Experimental tensile results for sample 240311-Head2-Right. a) Measured force over time showing pre-conditionning cycle (in the zoom), two relaxation phases and sample detachment in the loading phase of the third relaxation step, around 2000 s. b) Stress-strain behavior derived from experimental result in figure (a). 114
3.36 Bilinear fit of stress-strain cuve for sample 240311-Head2-right. 115
3.37 Hyperelastic fit of stress-strain curve for sample 240311-Head2-right. 115

B.1 Influence of density variation on contact radius evolution for simulations of $h = 0.5$, $L = 25R$, $\nu = 0.499$ 124
B.2 Influence of sample length variation on contact radius evolution for simulations of $h = 0.5$, $\rho = \rho_0$, $\nu = 0.499$ 124
B.3 Influence of Poisson's ratio variation on contact radius evolution $h = 0.5$, $\rho = \rho_0$, $L = 25R$. 125
B.4 Relationship between d/R and δ/R for measurements of δ/R at distance $R_\delta = 5R$ from the symmetry axis. 125
B.5 a) Comparison of analytical stress vs stretch to the uni-axial cube compression. b) Finite elements results 1/4th of 3D neo-Hookean cube in uniaxial compression with 37.5% imposed strain 126

B.6 Engineering effective stress (σ_{eng}) vs strain (ε_{eng}) for spherical compression simulations in comparison to the neo-Hookean uniaxial compression model. 126
B.7 Lagrangian effective stress (S) vs strain (E) for spherical compression simulations compared to a neo-Hookean uniaxial compression model. 127

C.1 Fluid flow velocity field for biphasic axisymmetric compression referring to section 2.5 with Model 2 parameters from table 2.6, analogous to Figure 2.22 but with the application of the impermeable boundary condition referring to Figure 2.23. 128

F.1 MRI of disc samples (names on images) on the central slice. The deformation pattern was the same in relation to the orientation of the fiber network for all discs. Acquisition parameters: Spin Echo (MSME) – FOV 3 cm, slice thickness 0.5 mm, matrix 512 × 512 pixels, TE 8.8 ms, TR 2000 ms, 10 slices, 8 averages. 131

List of Tables

1.1 Permeability values from different experimental studies, with regional variations. a)Li et al. (2021), b)Wu et al. (2017), c) Kim et al. (2003), d)Tverje & Nyashin (2010), e)Kuo et al. (2010). 34

2.1 Preload forces and maximum displacements for multiple compression tool radii. The calculations to obtain the force values are described in Tappert (2020) in order to guarantee an equivalent stress state with different sphere radii. 41
2.2 Optimization results for parameters β and m. 52
2.3 Optimization results for β and m. 53
2.4 Optimization results of parameter χ 55
2.5 Spherical compression optimization results for monophasic characterization of second order Ogden model. Comparison of results for tests conducted in the central part of porcine TMJ discs. 57
2.6 Summary of model parameters from literature. Model 1 was defined with parameters from Ortún-Terrazas et al. (2020) and Model 2 associates the results from Tappert (2020) and Wu et al. (2017). 61
2.7 Optimized parameters for spherical compression simulations for different values of sphere radius for all zones of the discs. General mean ± standard deviation. . 70
2.8 Optimized parameters for spherical compression simulations for all radii. General mean ± standard deviation. 72
2.9 Optimized parameters for spherical compression simulations showing a comparison of the influence of operator. General mean ± standard deviation. 73

3.1 Material parameters for linearized approach, obtained through confined compression optimization. 89
3.2 Material parameters by model, showing mean results ± standard deviation (n=8). 90
3.3 Length changes in anteroposterior and mediolateral directions for different samples.109
3.4 Mechanical properties of the disc using bilinear and hyperelastic models. 116

D.1 Permeability Data by radius and disc zone. 129
D.2 Shear modulus by radius and disc zone. 129
D.3 Bulk modulus by radius and disc zone. 129

E.1 Confined compression parameter results for multiple behavior laws 130

List of Symbols

Symbol	Description
W	Strain energy density function
$\mathbf{S}$	Second Piola-Kirchhoff stress tensor
$\boldsymbol{\sigma}$	Cauchy stress
$\boldsymbol{\sigma}_e$	Effective stress (poromechanics)
$\boldsymbol{\sigma}^*$	Effective stress (mechanics)
$\mathbf{B}$	Left Cauchy-Green strain tensor
$\mathbf{C}$	Right Cauchy-Green strain tensor
I_1,I_2,I_3	Invariants of strain tensors
μ	Shear modulus
κ	Bulk modulus
λ	Stretch
E	Young modulus
ν	Poisson's ratio
$\mathbf{w}$	Fluid flow relative to solid
$\mathbf{v_s}$	Velocity of the solid phase
p	Pore pressure
k	Hydraulic permeability [$\mathrm{m}^4/(\mathrm{N}\cdot\mathrm{s})$]
$\hat{k}$	Intrinsic permeability [m^2]
η	Fluid dynamic viscosity [Pa·s]

General introduction and motivation

The complex structure of soft biological tissues, such as cartilage, plays a central role in determining their mechanical behavior and must be carefully taken into account in studies. Such tissues can undergo large deformations, with mechanical properties that vary according to the loading direction due to their fibrous microstructure. They are mechanically nonlinear, inhomogeneous and porous materials, composed primarily of fluid, which can flow and interact with their solid structure and affect the observed mechanics. The reproduction of physiological conditions during experiments demands control of factors such as hydration and temperature.

This work focuses on the study of the temporomandibular disc, an essential component of the temporomandibular joint (TMJ) which connects the skull to the mandible and is responsible for a number of essential functions used in daily life, such as chewing and speech. Various pathologies can affect its proper functioning, causing acute pain, difficulty in performing movements, and discomfort that profoundly impact people's quality of life. The TMJ disc is a fibrocartilaginous tissue, which distributes stress and guides the movement of the mandible. Joint dysfunctions are often associated with alterations in this disc, and understanding its mechanical behavior is essential for improving numerical simulations of pathologies as well as for proposing and validating prosthetic solutions or disc replacements. Since the TMJ is a synovial joint with low vascularization, it is also interesting to understand fluid transport phenomena within its components, which relate to the nutrition and viability of its multiple elements.

The behavior of the TMJ disc has been minimally explored in the literature, and the treatment of TMJ disorders without full joint replacement remains a challenge. Few studies have explored the interaction between fluid and solid phases in the disc's tissue, and those that have propose different material characterization approaches and distinct parameters values.

The current work is based on the poromechanical theory of biphasic materials characterization, commonly applied to cartilaginous tissues, and extends this framework to the experimental and numerical investigation of the TMJ disc. This approach couples the mechanics of the solid phase of the tissue, formed by a porous matrix mainly composed of collagen, to the fluid phase, represented by the synovial fluid permeating the matrix. This thesis is divided into three parts.

Chapter 1 discusses the state-of-the-art in the mechanical analysis of soft biological tissues, presenting theoretical models, experimental and data treatment techniques. The TMJ anatomy and dysfunctions will be introduced, with details on the structure and composition of the disc, as well as current analyses exploring the mechanics of this tissue.

Chapter 2 focuses on spherical compression, a nondestructive testing technique applied to porcine TMJ discs in the current work. The experimental protocol is described, followed by the evolution of a monophasic material characterization model based on spherical compression, initiated in a previous work by the team. Experimental results will be compared to finite element simulations that applied biphasic definitions proposed in the literature. An inverse method optimization algorithm will be applied to these simulations allowing to obtain biphasic parameters for characterizing the discs poromechanical response based on experimental data.

Chapter 3 continues the experimental campaign, where confined compression, direct permeation and tensile tests were conducted on the same discs to enable poromechanical characterization. Various imaging techniques were then applied to the discs, seeking to relate the material's microstructure to the observed mechanics.

The results of this work aim to enrich the literature on the poromechanical aspects of TMJ discs by proposing characterization parameters with discussions around the multiphase, anisotropic, and heterogeneous nature of the material.

Chapter 1

Introduction to poromechanics and the characterization of soft biological tissues

1.1 Mechanical behavior of soft biological tissues

The mechanical behavior of soft biological tissues varies according to their nature and the stimuli to which they are subjected in the body. This work focuses on the mechanics of cartilaginous tissues. To understand and model the mechanical phenomena they exhibit, it is advantageous to, at first, examine them at the microstructural scale.

1.1.1 Tissue microstructure and its impact on mechanics

Cartilage is a type of connective tissue with multiple functions, including facilitating smooth gliding movements between bones, contributing to the growth of long bones and providing structural support to other structures. It can be found in three different forms in the human body. Hyaline cartilage is the most abundant one, with high resistance to compression and may be found for example covering bone surfaces in joints (Drake et al., 2010). Elastic cartilage has high flexibility and composes structures such as the external ear and larynx. Fibrocartilage can be found in the skin, intervertebral discs of the spine, in the temporomandibular joint disc and insertions of ligaments and tendons (Benjamin & Evans, 1990; Drake et al., 2010; Yambe et al., 2024).

Cartilaginous tissues are considered porous organic composites consisting primarily of water, that represent around 60-80% of their total weight depending on tissue's nature and individual characteristics (Cederlund & Aspden, 2022). The fluid permeates the pores of a three-dimensional network known as extracellular matrix (ECM). The main components of the ECM are collagen fibers, that constitute 60 to 80% of the tissue's dry weight (Almarza & Athanasiou, 2004) and play an important structural role, being a protein that provides tensile strength, structural integrity and elasticity. There are 28 types of collagen molecules, with type I being the most abundant in fibrocartilages and type II more common in articular cartilage covering the bones (Sharabi, 2022; Benjamin & Evans, 1990). Some examples of the collagen network in fibrocartilages is shown in Figure 1.1.

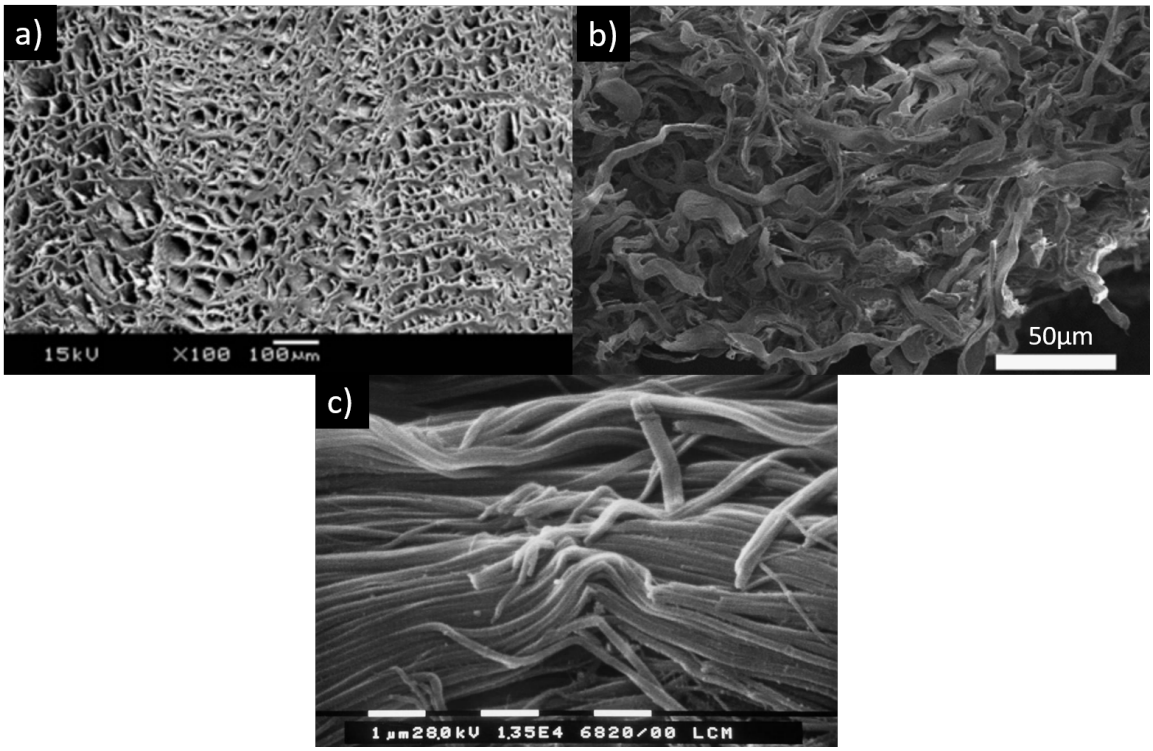

Figure 1.1: Scanning electron microscopy images of fibrocartilage in different scales, showing the collagen structure. a) Rabbit skin's collagen structure, adapted from Yang et al. (2015). b) Rat medial collateral ligament (Franchi et al., 2010). c) Porcine intervertebral disc (Wu et al., 2014).

The ECM also presents other fibrous proteins in its structural composition, such as elastin, responsible for ensuring the elasticity and resilience of tissues (Poole & Mostaço-Guidolin, 2021). The fiber network has a high influence on the mechanical response of tissues to tensile loads. Consequently, a preferential orientation of ECM's fibers leads to direction-dependent variations material's mechanical properties known as anisotropy (Wright et al., 2016; Benjamin & Evans, 1990; Woo et al., 1976).

Tissue hydration is primarily assured by the proteoglycans, attached to the ECM through physical and chemical interactions. Proteoglycans are macromolecules consisting of a protein core linked to negatively charged polysaccharide chains, called glycosaminoglycans (GAGs) (Almarza & Athanasiou, 2004; Detamore et al., 2005). Because of this negative charge, the GAGs interact with positive ions in the fluid and attract them to tissue's pores, keeping it hydrated thanks to the osmotic effect that is generated (Zimmerman et al., 2021).

When subjected to deformations, the interstitial fluid becomes pressurized and may flow, though this process does not occur instantaneously. It is hypothesized that the diffusive drag induced by fluid movement within the tissue, associated with the viscous nature of the solid collagen matrix, gives the tissue time-dependent mechanical response, known as viscoelasticity (Mow et al., 1984). This means that the resistance of the material to compression is related not only to the composition of its solid part, but also to the presence of the water-rich fluid (consequently incompressible) that permeates the pores of the structure. Fluid dynamics, therefore, plays a highly relevant role in the mechanical response of the material to compression (Mow et al., 1984; Tanaka et al., 2003a).

Being a living tissue, cells may be found both in the synovial fluid and in the collagen structure. Some cells are responsible for the production of type I collagen fibers in the case of fibroblasts, and for the production of type II collagen and GAGs, in the case of chondrocytes (Almarza & Athanasiou, 2004). Fluid transport and diffusion within the tissue's structure is

also essential for cell nutrition and metabolic waste management due to the lack of blood vessels in cartilages (Benjamin & Evans, 1990; Drake et al., 2010).

1.1.2 Theoretical models for soft tissues' characterization

Historically, soft biological tissues have had their behavior modeled by different approaches. Assuming a linear stress-strain relation to the material and identifying its Young's modulus can be useful to approximate the magnitude of the efforts during deformation and to characterize specific portions of experimental results, as done in Griffin et al. (2016).

However, such tissues are capable of undergoing large nonlinear deformations, demanding more sophisticated models for a more representative portrayal of their behavior. To illustrate, Figure 1.2 shows an example of a stress vs strain curve measured after cyclic compression of a fibrocartilaginous tissue (Tanaka et al., 2003b).

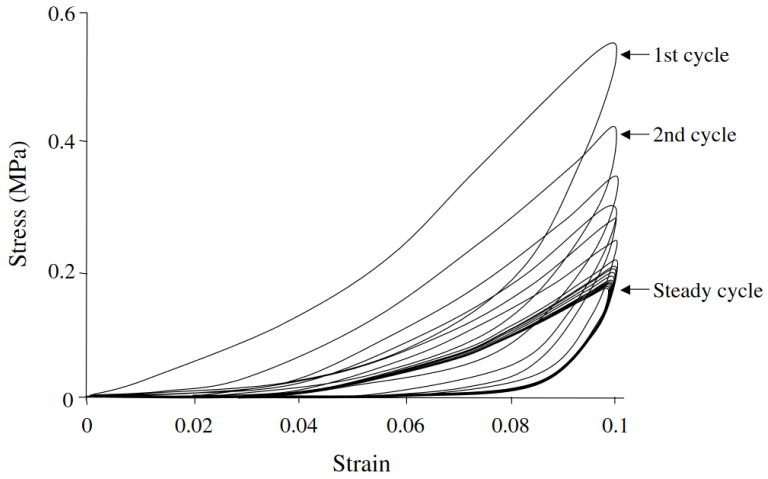

Figure 1.2: Experimental results from Tanaka et al. (2003b) showing the effect of cyclic compression by means of a cylindrical tool on fibrocartilaginous tissue samples, illustrating nonlinear viscous effects of the material.

The imposed loading history affects the mechanical response observed in subsequent cycles, where the magnitude of stresses tends to decrease and stabilize. This temporal variation in behavior, also evidenced by intercyclic hysteresis, is related to the previously mentioned viscous effects. The stress evolution in the material is nonlinear, which requires mechanical models capable of capturing the observed nonlinearity in large strains, such as the hyperelastic framework, which will be discussed below.

1.1.2.1 Hyperelastic models

Originally developed to model rubber (Mooney, 1940; Rivlin & Saunders, 1950), hyperelastic models are capable of representing materials submitted to large nonlinear strains. The stress acting on the system may be defined through the second Piola-Kirchhoff tensor $\mathbf{S}$

$$\mathbf{S} = 2\frac{\partial W}{\partial \mathbf{C}} \tag{1.1}$$

where W is the strain energy density function, which characterizes the constitutive behavior of the material by relating the stored elastic energy to the strain state of the material, which is described by the right Cauchy-Green strain tensor $\mathbf{C}$.

This is a purely Lagrangian approach, allowing to identify stress based on the reference configuration state of the system, which is useful when working with deformable solids (Cowin & Doty, 2007). Depending on the type of stress-strain curve that one wishes to represent, W may be defined in multiple ways, as in the example of the Mooney-Rivlin model

$$W = C_{10}(I_1 - 3) + C_{01}(I_2 - 3) + \frac{1}{D}(J-1)^2 \tag{1.2}$$

where C_{10} and C_{01} are material parameters related to the shear modulus through $\mu = 2(C_{10} + C_{01})$ and D is related to bulk modulus through $\kappa = 2/D$, which may be identified by experimental fitting. For an isotropic approach, where material properties are considered the same in all directions, the strain energy density is a function of the three principal strain invariants of the left or right Cauchy-Green tensors, represented by I_1,I_2 and J in the equations and defined by

$$I_1 = tr(\mathbf{C}) \tag{1.3}$$

$$I_2 = \frac{1}{2}[tr(\mathbf{C})^2 - tr(\mathbf{C}^2)] \tag{1.4}$$

$$I_3 = J^2 = det(\mathbf{C}) \tag{1.5}$$

The right Cauchy-Green tensor $\mathbf{C}$ is defined based on the deformation gradient $\mathbf{F}$ through $\mathbf{C} = \mathbf{F}^T\mathbf{F}$. The operators tr and det are respectivelly the trace and determinant of the tensors.

The solid is considered to be a continuous medium, where the initial coordinates of an arbitrary point in the reference configuration are denoted by $X_i (i = 1, 2, 3)$, while its position after deformation in the current configuration is $x_i (i = 1, 2, 3)$. The deformation gradient tensor $\mathbf{F}$ is

$$\mathbf{F} = \frac{\partial x_i}{\partial X_j} \tag{1.6}$$

and the Jacobian of the transformation is $J = det(\mathbf{F})$. Each association of parameters, with a polynomial or exponential combination of the invariants, defines a strain energy density function (Chagnon et al., 2015), seeking to reproduce what is experimentally observed in the mechanical behavior of a material. The neo-Hookean model, defined by equation 1.7, is a particular case of application of equation 1.2, being simpler since it eliminates the term associated with I_2, and still is capable of reproducing non-linearities of hyperelastic materials.

$$W = C_{10}(I_1 - 3) + \frac{1}{D}(J-1)^2 \tag{1.7}$$

Anisotropy may be introduced into models to represent the privileged orientation of the fiber network within the tissue. Due to the great diversity of tissues and behaviors observed, several approaches to this problem have been adopted (Chagnon et al., 2015). One of the solutions used in Tong & Fung (1976) is to define the strain energy density as a function of components of the Green-Lagrange strain tensor $\mathbf{E} = (\mathbf{C} - \mathbf{I})/2$, where $\mathbf{I}$ is the identity matrix. By attributing different weights to the contribution of each component, anisotropy is taken into account.

Another approach defines W by an isotropic contribution and an anisotropic portion as in the example:

$$W = W^{iso}(I_1, I_2) + \sum_i W^{aniso}(I_1, I_2, I_4^{(i)}, I_5^{(i)}) \tag{1.8}$$

where $I_4^{(i)}$ and $I_5^{(i)}$ are invariants defined through a transformation of the right Cauchy-Green tensor by orientation tensors in direction i of the fiber network. One major difficulty here is to identify and differentiate the individual contributions of the isotropic matrix and the fiber network, which in practice act together as a whole. Those solutions may associate the invariants with polynomial, exponential, power or other types of equations. Besides these, the so-called anisotropic statistical approaches propose a change in scale to represent the apparent characteristics of the material, based on the energy of a single fiber and a choice of fiber distribution function (Chagnon et al., 2015).

Due to their ability to deal with large strains, isotropic and anisotropic hyperelastic constitutive laws are often the model of choice for the treatment of soft biological tissues (Miller, 2005; Lin et al., 2009; Geerligs et al., 2011; Iivarinen et al., 2011; Rashid et al., 2012; Zhang et al., 2014; Chagnon et al., 2015; MacManus et al., 2017; Oddes & Solav, 2023). However, they do not integrate yet the notion of time dependence on the mechanical response, which is necessary to represent tissue's dissipative viscoelastic behavior.

1.1.2.2 Viscoelastic models

The Maxwell and Kelvin-Voigt models are the simplest viscoelastic representations, that relate material behavior with the equivalent of an association of linear springs and dashpots (Aernouts et al., 2012). They present a viscous response, although are limited when wishing to represent stress relaxation effects, which is the progressive diminution of observed stress in a material after imposition of a constant position-controlled strain (Aernouts et al., 2012).

Other models better adapted to represent creep and stress relaxation exist, such as the quasi-linear viscoelasticity (QLV) theory. Initially developed by Fung in 1981 (Fung, 1993; Puso & Weiss, 1998), the QLV assumes that the viscoelastic behavior is composed of a nonlinear elastic response associated to a relaxation function through a convolution product, that may be used to calculate the second Piola-Kirchhoff tensor $\mathbf{S}$

$$\mathbf{S}(t) = \int_0^t G(t-\tau)\frac{d\mathbf{S}_e(\tau)}{d\tau}d\tau \tag{1.9}$$

The convolution is a linear transformation with $G(t-\tau)$ representing a relaxation function that governs the time-dependent behavior, t the current time and τ an integration variable representing past time. $\mathbf{S}_e$ is the elastic response's second Piola-Kirchhoff stress. The convolution integrates the contribution of the product of both functions from all past instants. The difference $(t-\tau)$ indicates the elapsed time and thus allows the material's loading history to impact in the model's response. Choosing distinct relaxation and elastic response functions allows the reproduction of different observed behaviors.

Tissue anisotropy may be introduced in the model's response, for example, by defining a strain energy density function for the elastic response in the form of equation 1.8. Labus et al. (2021) used this approach for their model, applying it to experimental data of biaxial tension over a fibrocartilaginous tissue. They highlighted the importance of exploring multiple loading conditions, so that possible nonlinear behaviors dependent on the strain rate can be observed. In Puso & Weiss (1998), the elastic response was defined through a transversely isotropic Mooney-Rivlin strain energy density function, with the introduction of fiber contribution. Relaxation $G(t-\tau)$ is often expressed as series of exponential functions, as performed in Kazemi & Li (2014), that modeled cartilages and menisci of the knee joint.

Over the years, viscoelastic models have been widely used for the treatment of biological tissues (Puso & Weiss, 1998; Jachowicz et al., 2007; Yuya et al., 2010; Aernouts et al., 2012; Commisso et al., 2014; Kazemi & Li, 2014; Budday et al., 2015; Wu et al., 2015; Wright et al., 2016; Gutman et al., 2018; Labus et al., 2021). Besides the QLV model, there are

other approaches that include the notion of monophasic viscoelasticity. However, these models analyze the material as being composed of a single phase, and even though they mechanically represent what is observed, they do not take into account the interaction of the solid phase of the materials with the high amount of fluid inside of them. Poromechanical models seek to introduce this dynamics into the modeling of the tissues, and will be discussed below.

1.1.2.3 Poromechanical models

Poromechanical models deal with the mechanics of porous materials, in this case completely saturated with fluid. The presence of fluid within the structure requires it to be considered as a mixture composed of multiple phases. Models that integrate these concepts will also be referred to here as biphasic models.

As previously stated, the interstitial fluid's movement affects the dynamics of multiple functional solutes within the tissue. Modeling the interactions between solid and fluid phase enables the understanding of observed mechanics while providing an insight on tissue nutrition, viability and potential degradation (Nickel et al., 2018).

Furthermore, the biphasic model allows to isolate the effective stress, acting exclusively over the solid portion of the material, from the total stress over the structure. The effective stress concept began to be explored in 1871 for treating problems related to porous media in soil mechanics (de Boer & Ehlers, 1990). One major contribution to the subject was published by Biot (1941), where the classical theory of poroelasticity was proposed, with a model that takes into account the three-dimensional elasticity of the solid interacting with fluid displacement for modeling the settlement of soils. Later, the biphasic approach was applied in the study of soft biological tissues through the analysis of articular cartilage experiments (Mow et al., 1980; Lai et al., 1981; Mow et al., 1984).

To present the foundation of the theory's framework, it is necessary to introduce its fundamental relations that derive from mass, momentum and energy balance principles. The biological tissues will be regarded as a mixture of a deformable solid phase representing the ECM (physiologically composed of multiple elements such as collagen, elastin and proteoglycans) and a fluid phase, that completely saturates the pores of the solid matrix. Inertial effects are neglected and both constituents of the mixture are considered intrinsically incompressible, thus having an invariant density (Ateshian, 2017). The saturated mixture condition establishes that all pore volume is occupied by fluid, which leads to

$$\varphi_s + \varphi_l = 1 \tag{1.10}$$

where φ_s is the solid phase's volume fraction, also known as solidity, defined as the ratio of solid volume over the total volume of the mixture. Analogously, φ_f is fluid volume fraction, also referred as porosity of the material and represents the pore volume (equal to fluid volume in the saturated condition) over total volume of the structure. Through the mass conservation principle, the continuity equation for a biphasic medium is

$$\nabla \cdot (\mathbf{v_s} + \mathbf{w}) = 0 \tag{1.11}$$

where $\mathbf{w}$ is the fluid flow relative to the solid and $\mathbf{v_s}$ is the velocity of the solid phase. This relation links the rate of solid volume change (represented by the divergence of $\mathbf{v_s}$) to fluid volumetric flux, establishing the compensatory and interdependent nature of the two quantities. Even being composed by two intrinsically incompressible phases, the resultant mixture may be compressible, since pore volume may vary within the limitations dictated by equation 1.10. Equation 1.11 shows, for example, that a negative solid phase divergence (which results in the reduction of the pore volume) imposes a positive divergence for the fluid flux, indicating its

escape from the zone. Fluid then tends to flow towards regions of lower pore pressure and its flux is described by Darcy's law :

$$\varphi_f(\mathbf{v}_f - \mathbf{v}_s) = \mathbf{w} = -\mathbf{k}\nabla p \tag{1.12}$$

$\mathbf{v}_f$ (in $[m/s]$) is the velocity of the fluid phase. The tensor $\mathbf{k}$ is the hydraulic permeability of the system (measured in $[m^4/Ns]$) and ∇p (in $[Pa/m]$) is the pressure gradient of the fluid. Darcy's law was initially defined empirically in 1856, but it can also be demonstrated by fluid's momentum balance in the biphasic theory (Ateshian, 2017) and is valid for describing steady state single-phase flows in porous media for low Reynolds numbers (Whitaker, 1986). The hydraulic permeability tensor $\mathbf{k}$ is often simplified to a scalar value on the premise of isotropic flow, where $\mathbf{k} = k\mathbf{I}$. It is related to the intrinsic permeability of the material through

$$k = \frac{\widehat{k}}{\eta} \tag{1.13}$$

The intrinsic permeability $\widehat{k}$ (in $[m^2]$) is independent of the nature of the fluid, which influences equation 1.13 through its dynamic viscosity η (in $[Pa.s]$). It is important to note the difference between permeability and porosity and how those two parameters are connected. Permeability indicates the ease with which a fluid can pass through a solid medium, depending on the degree of interconnectivity between the pores and the tortuosity of the path taken inside it (Carman, 1937; Holmes & Mow, 1990). One could then assume that perturbations on the porous structure due to deformation may affect the porosity and, consequently, the permeability. In Lai et al. (1981), the relationship between the intrinsic permeability of the material and strain is explored for uniaxial compression of articular cartilage for small strains

$$\hat{k} = \hat{k}_0 \exp\left(M\frac{du}{dz}\right) \tag{1.14}$$

where $\hat{k}_0$ represents material's initial permeability, M a material fitting constant and du/dz is the dilatation imposed to the tissue during deformation. Other formulations for the same notion are addressed in other works, such as in Argoubi & Shirazi-Adl (1996)

$$k = k_0\left[\frac{e(1+e_0)}{e_0(1+e)}\right]^2 \exp\left[M\left(\frac{1+e}{1+e_0} - 1\right)\right] \tag{1.15}$$

where the void ratio e is related to the porosity φ_f through,

$$e = \frac{\varphi_f}{1-\varphi_f} \tag{1.16}$$

and e_0 is the initial void ratio, which changes during deformation due to variations on pore volume. Material's constitutive relations are obtained through mixture's momentum balance. Since inertial effects are neglected, it is possible to state that

$$\nabla \cdot \boldsymbol{\sigma} = \mathbf{0} \tag{1.17}$$

where $\boldsymbol{\sigma}$ represents mixture's total Cauchy stress, described by

$$\boldsymbol{\sigma} = -p\mathbf{I} + \boldsymbol{\sigma}_e \tag{1.18}$$

The total stress $\boldsymbol{\sigma}$ acting over the structure depends on the effective stress $\boldsymbol{\sigma}_e$ over the solid phase and the isotropic stress of the interstitial fluid, also called pore pressure p. The effective stress $\boldsymbol{\sigma}_e$ is then defined as

$$\boldsymbol{\sigma}_e = \frac{1}{J}\frac{\partial \Psi}{\partial \mathbf{F}}\mathbf{F}^T \tag{1.19}$$

where Ψ is the mixture's Helmholtz free energy, representing the inner energy that performs work isothermally. The specific strain energy density function may be written as $W = \rho_0^s \Psi$, where ρ_0^s is the solid phase's initial and constant density (Holmes & Mow, 1990; Wriggers, 2008). The definition of Ψ establishes the behavior of the solid porous skeleton, as introduced in the previous sections describing monophasic models. Defining the constitutive relations for $\mathbf{k}$ and Ψ allows modeling the mixture's mechanical response.

Initially, Mow et al. (1980) assumed a formulation for infinitesimal strains and linear elastic behavior for the solid, which was nevertheless capable of representing creep and stress relaxation effects in the material as a whole due to the diffusive drag of the fluid. One of the parameters commonly employed in the literature to characterize the material, along with permeability, is the aggregate modulus H_A (Mow et al., 1980; Ateshian et al., 1997; Kim et al., 2003; Kuo et al., 2010; Gervaso et al., 2014). When dealing with an uniaxial compression context with a biphasic material, the imposition of a constant compressive strain ε_0 results in a stress relaxation effect. The measured stress decays exponentially from its maximum value over time until it reaches an equilibrium stress σ_∞ (Mow et al., 1984). The aggregate modulus H_A fits into this relationship through

$$\sigma_\infty = \varepsilon_0 H_A \tag{1.20}$$

being then a parameter related to material's stiffness at equilibrium (Mow et al., 1984; Oatis, 2009). It relates to other constants through

$$H_A = \lambda_s + 2\mu_s = \frac{E_s(1-\nu_s)}{(1+\nu_s)(1-2\nu_s)} \tag{1.21}$$

where λ_s and μ_s are the Lamé coefficients, E_s is Young's modulus an ν_s Poisson's ratio, all of them corresponding to the solid phase. Multiple models derived from the biphasic poroelasticity of Mow et al. (1980), with other definitions of intrinsically hyperelastic solid phases (Selvadurai & Suvorov, 2016), viscoelastic solid phases (Mak et al., 1987; DiSilvestro et al., 2001; Baykal et al., 2013) and fiber-reinforced viscoelastic solid phase incorporating fiber reorientation (Seifzadeh et al., 2011), for example. Also, the so-called triphasic model adds one more phase to the mixture, including charged ions that interact with fluid allowing the observation of osmotic effects (Zimmerman et al., 2021).

The described concepts are widely used for the treatment of various types of soft biological tissues (Lai et al., 1981; Argoubi & Shirazi-Adl, 1996; Heneghan & Riches, 2008; Gervaso et al., 2014; Wei et al., 2014; Li et al., 2021; Ortún-Terrazas et al., 2021; Shi & Myers, 2023). Adaptations to the described formulations are used for material characterization and depend on the specific testing context and on the employed boundary conditions.

1.2 Techniques for mechanical testing

This section aims to introduce techniques currently used to characterize soft biological tissues. Initially, two classic test methods for obtaining biphasic properties of materials will be presented: confined compression and direct permeation. Then, spherical compression, an example of non-destructive testing, will be described followed by tensile tests, which is useful in the current context for observing anisotropic characteristics of tissues. The experimental approaches as well as the result processing methods will be discussed.

1.2.1 Confined compression tests

Confined compression is a classic characterization method for hydrated porous materials, that was used in the first validations of the biphasic model for articular cartilage (Mow et al., 1980; Ateshian et al., 1997). A cylindrical sample is placed inside an impermeable rigid chamber that confines it radially (see Figure 1.3), thus maintaining a constant sample cross section throughout the entire test and reducing the problem to a one-dimensional analysis. The tissue is then compressed by a porous piston that allows free fluid flow through it. Depending on the adopted configuration, the inferior support of the sample can also be permeable, as shown in Figure 1.3.

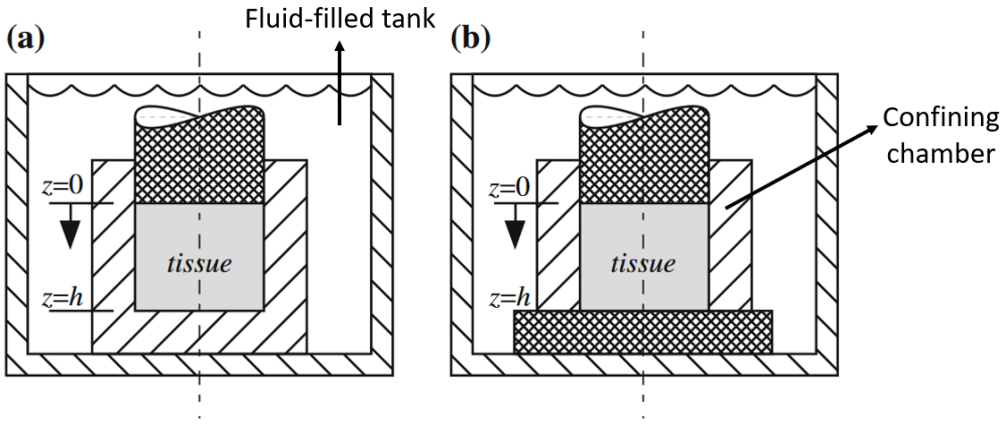

Figure 1.3: Confined compression test with porous piston and (a) impermeable base and (b) porous free-draining base, adapted from Ateshian (2017). Depending on the adopted configuration and the data processing methods used, symmetry conditions can be applied to ensure equivalence between the two types of setups.

These are setups that are not available for purchase on the market and must be custom made for specific projects. They are usually only represented by means of diagrams indicating their operating principle in the literature. The production methods and structural details, such as the nature of the porous pistons for example, are not shown in detail. An example of an experimental setup is illustrated in Figure 1.4.

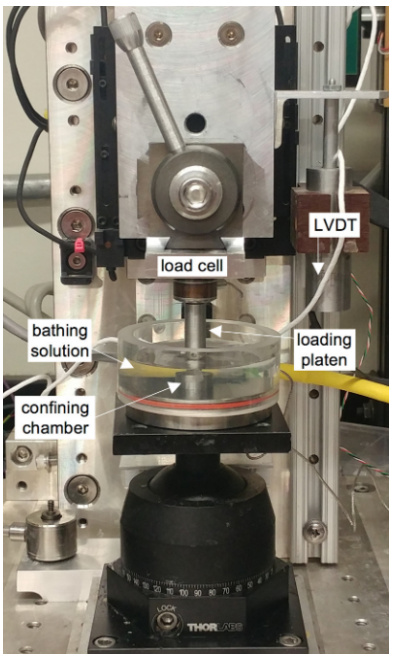

Figure 1.4: Experimental confined compression setup used to analyse bovine articular cartilage (Zimmerman et al., 2021).

The entire system remains submerged in fluid while piston's force and displacement are recorded throughout the test. Stress-relaxation tests consist of prescribing a constant compressive displacement to the piston, followed by a phase where its position is kept constant. When performing experiments with soft biological tissues, a decay of the resulting force over time is observed, due to fluid redistribution processes in the material (Mow et al., 1984).

An analogous process occurs in the creep test, where a constant compressive force is instantaneously applied over the sample. In this case the piston is force-controlled and the temporal evolution of the displacement $u(X,t)$ is observed. To identify material parameters from both output data, the formulations of the biphasic theory are adapted according to test boundary conditions. In this one-dimensional configuration, the equations governing the deformation of the material can be expressed as

$$\frac{\partial \sigma^e}{\partial \lambda}\frac{\partial^2 u(X,t)}{\partial X^2} = \frac{\lambda}{k}\frac{\partial u(X,t)}{\partial t} \tag{1.22}$$

where $u(X,t)$ is the vertical deformation and λ is the stretch defined as $\lambda = 1 + \partial u(X,t)/\partial X$. To define the effective stress in the one-dimensional case, the relation 1.23 was used in Ateshian et al. (1997)

$$\sigma^e = \frac{1}{2}H_{A0}\left(\frac{\lambda^2-1}{\lambda^{2\beta+1}}\right)e^{\beta(\lambda^2-1)} \tag{1.23}$$

where β corresponds to a dimensionless parameter of the material. Once the stress and strain are known, it is possible to define the pore pressure of the fluid. For creep tests for example, the pressure can be defined through

$$\frac{p(h,t)}{H_A} = \frac{\sigma_0}{H_A}\cdot\frac{2}{\pi}\sum_{n=1}^{\infty}\frac{(-1)^n}{n-\frac{1}{2}}\exp\left[-\left(n-\tfrac{1}{2}\right)^2\pi^2\frac{t}{\tau}\right] \tag{1.24}$$

where h is the height of the sample and $\tau = h^2/H_A k$. There are other definitions used for the effective stress, such as in Selvadurai & Suvorov (2016) which proposes a hyperelastic solid phase, with

$$\sigma_e = \frac{4}{3}\left(C_{10} + 2C_{20}\left[\left(\left(1+\left(\frac{\partial u}{\partial X}\right)^{4/3}\right) \quad +2\left(1+\frac{\partial u}{\partial X}\right)\right) - 3\right]\right) \times \left(\left(1+\left(\frac{\partial u}{\partial X}\right)^{1/3}\right) - \left(1+\left(\frac{\partial u}{\partial X}\right)^{-5/3}\right)\right) + \frac{2}{D_1}\frac{\partial u}{\partial X} + \frac{4}{D_2}\left(\frac{\partial u}{\partial X}\right)^3 \tag{1.25}$$

where C_{10}, C_{20}, D_1 and D_2 are material constants that define the second order reduced polynomial strain energy density function.

Different combinations of these parameters can lead to distinct material behavior laws. The result from Selvadurai & Suvorov (2016) in Figure 1.5 illustrates the displacement response of the same material modeled under three constitutive law definitions.

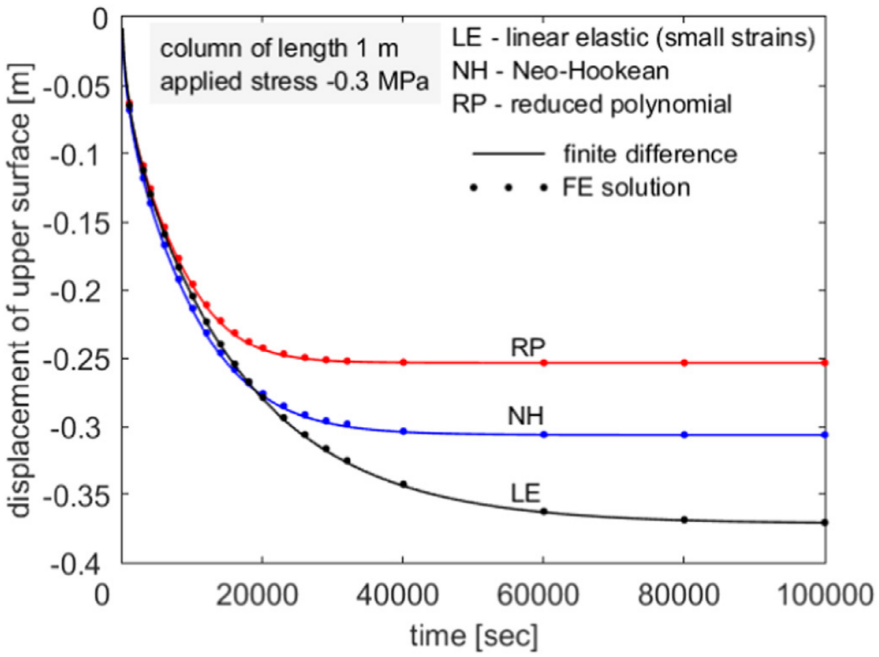

Figure 1.5: Comparison of the displacement of the superior surface of a column under confined compression, using similar material parameters but different constitutive law definitions (Selvadurai & Suvorov, 2016). A constant stress of -0.3MPa was applied to the top, demonstrating the validation of the displacement calculation method proposed by the authors against a finite element simulation under the same conditions.

Starting from the experimental context of an unknown material where a stress-strain curve in creep or stress-relaxation confined compression is available, characterization is performed through optimization techniques. Arbitrary initial values are assigned for the parameters and the stress-strain curve generated by this specific preliminary definition, for example through equation 1.22, is compared with the experimental results. The curve-fitting processe iteratively varies the material parameters' values in loops that seek to minimize the error between what is simulated and what is measured, allowing to estimate parameters within a certain error margin.

Another option is to apply dynamic sinusoidal loads, controlling the piston by force or displacement. This technique can be used in conjunction with other tests, providing complementary insights into the material's viscoelastic behavior. In Ateshian et al. (1997), bovine cartilage was tested for confined compression in stress-relaxation, creep and dynamic loading

conditions. A curve-fitting of the solution of the nonlinear differential equation 1.22 was performed to verify if the proposed framework is capable of reproducing experimentally observed curves specifically on cartilage and identify the material parameters that best approximated the simulated results.

Confined compression is adopted for the characterization of multiple types of soft biological tissues of biphasic nature such as articular cartilage (Ateshian et al., 1997; Cutcliffe & DeFrate, 2020; Zimmerman et al., 2022), knee meniscus (Danso et al., 2018; Morejon et al., 2021), tendons (Solis-Cordova et al., 2023), brain tissue (Haslach et al., 2014), spinal cord grey and white matter (Yu et al., 2020), wharton's jelly (Gervaso et al., 2007) and temporomandibular joint discs (Kuo et al., 2010; Wu et al., 2017).

The relationship between strain and permeability (equations 1.14 and 1.15) is often neglected in the data treatment of confined compression tests. The direct permeation technique, in turn, gets around this problem by allowing the characterization of permeability at constant imposed strain during the experiment period, and will be described below.

1.2.2 Direct permeation

Direct permeation tests aim to assess the permeability of the material by imposing a flow through it. Typically, a cylindrical tissue sample is positioned inside a chamber that confines it laterally and allows fluid flow in only one direction, passing through the material. The sample can be positioned between free-draining porous filters as shown in Figure 1.6.

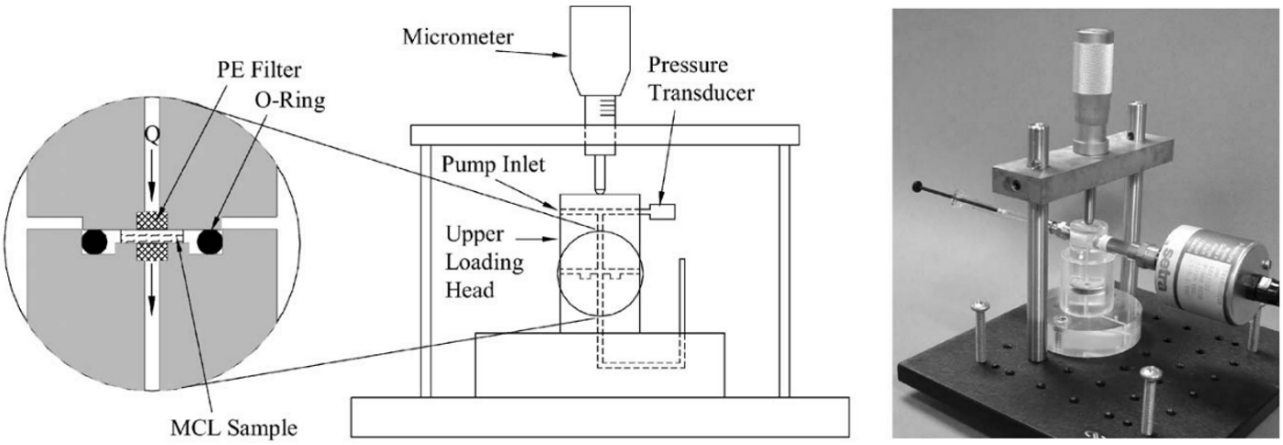

Figure 1.6: Direct permeation device used to determine the hydraulic permeability of human medial collateral ligament specimens under various levels of compressive strain (Weiss & Maakestad, 2006).

The device in Figure 1.6 was used to measure the permeability of the human medial collateral ligament, in which a syringe pump was used to impose a constant flow rate. The same principle was implemented in Kleinhans & Jackson (2018) and Heneghan & Riches (2008) in the measurement of the permeability of pig cartilage meniscus and bovine intervertebral discs respectively, where the measurement of the permeability of the material was made by imposing a known flow rate and waiting for the pressure difference between inlet and outlet to stabilize. The application of Darcy's law (equation 1.12) to the one-dimensional permeation of a sample of thickness h and cross-section A, allows to define the hydraulic permeability (k) in the flow direction (Holmes, 1985; Kleinhans & Jackson, 2018)

$$k = \frac{Qh}{A\Delta p} \tag{1.26}$$

where Q is the unidimensional volumetric flow rate, and Δp is the pressure variation between the inlet and outlet of the tissue. In this case, steady-state flow is assumed and the pressure gradient is uniform with a linear variation throughout the material's thickness h. By imposing a known flow rate and with sample geometry measurements, it is possible to calculate k by measuring the pressure difference between the inlet and outlet.

Similarly, it is possible to determine permeability by imposing a known pressure and measuring the flow rate, as performed in Proctor et al. (1989), which applied the measured values directly to equation 1.26. Ateshian (2017) analyzes the effects of adopting a prescribed pressure for the test and concludes that the flow stabilizes to a steady-state more quickly in pressure-controlled cases than in flow-rate controlled ones, being then a better choice for conducting such experiments.

One of the main difficulties in performing direct permeation tests is ensuring that the fluid does not leak around the edges of the sample (Ateshian, 2017). In order to assure a tight fit in the chamber, a slight clamping strain may be applied to the material, so that its lateral expansion covers possible gaps. Another alternative is to change the composition of the solution to ensure that the osmotic effect swells the sample and guarantees better tightness (Ateshian, 2017).

Depending on the configuration of the device, it is possible to perform the test at different degrees of compression of the tissue specimen, allowing verification of strain dependent permeability relationships such as the equations 1.14 and 1.15, as performed by Kleinhans & Jackson (2018) in the study of the knee meniscus. In these examples of direct permeation, unidirectional flow through the tissue structure is considered.

The mechanical tests described up to now are classical techniques for the poromechanical characterization of tissues. One of their disadvantages is the sample preparation process, in which specimens need to be cut in the form of the chambers if they are not already cylindrical. Measuring permeability in other directions requires adapted experimental techniques, as in Accadbled et al. (2008), where the permeability of intervertebral discs was measured through radial compression tests. Sperical compression tests, which will be described now, propose a less destructive approach for samples.

1.2.3 Spherical compression tests

Spherical compression is based on the compression of the material by means of a rigid sphere. Characterization may be performed through theoretical models that relate the measured force and displacement to material properties. Although commonly referred to as indentation, which is often associated with plastic strain, these tests will be called spherical compression here in this work.

Tests of this type allow the analysis of different regions of the material while maintaining the integrity of the tested sample, which does not need to be destroyed for preparation or for performing the test (Lee et al., 2016). This avoids affecting the natural flow of fluid within the tissue and does not affect potential the internal stresses inside of the material, which are inherent to biological tissues and can be affected if the sample is cut Tappert et al. (2022).

Due to the geometry of the sphere, a non-uniaxial stress state develops inside the material during compression, requiring models such as that of Hertz (1882), which treats the mechanics of contact for compression of an infinite and linear elastic halfspace by means of the equation

$$F_{Hertz} = \frac{4}{3} E \frac{R^{0.5} \delta^{1.5}}{(1 - \nu^2)} \tag{1.27}$$

where F_{Hertz} is the force, E is Young's modulus, ν poisson's ratio and δ the penetration depth, depicted in Figure 1.7.

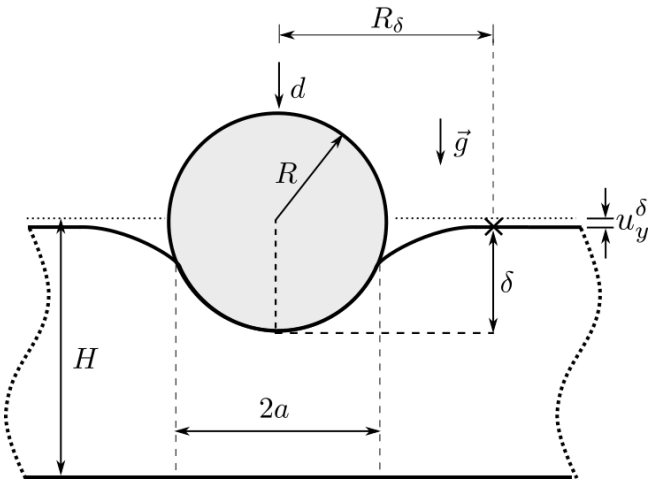

Figure 1.7: Spherical indentation scheme adapted from Tappert (2020). H - initial sample height, R - spherical compression tool radius, d - spherical compression tool displacement, a - contact radius, δ - penetration depth, R_δ - penetration depth measurement distance, u_y^δ - vertical displacement of sample surface, $\vec{g}$ - gravity.

Other models have been proposed subsequently, seeking to consider hyperelastic material behavior (Lin et al., 2009; Zhang et al., 2014; MacManus et al., 2017; Guo et al., 2020b; Du et al., 2023; Oddes & Solav, 2023). To exemplify, Lin et al. (2009) relates the contact radius between sphere and sample (a) to the penetration depth (δ), shown in equation 1.28

$$a = R^{x-\delta y}\delta^z \tag{1.28}$$

where x, y and z are fitting parameters. In their approach, they relate the force and displacement of the spherical compression to effetive stress and strain values equivalent to a hyperelastic uniaxial compression.

To perform the experiments, one possibility is to use atomic force microscopes (AFM) (Xu et al., 2016). Although originally intended to obtain data of sample surface topography, AFM devices are equipped of indenter spheres and a system capable of measuring its force and displacement, allowing them to be used for material characterization in studies such as McCreery et al. (2023). The diameter of collagen fibers is approximately $18 \pm 9\mu m$ (mean $\pm$ STD) (Detamore et al., 2005) and compressing them through spheres of this same scale, as in Yuya et al. (2010) with $R = 50\mu m$, arises questions about whether the analysis is done on a very local scale of the material.

To overcome such limitations, studies such as Tappert et al. (2020) and de Oliveira Cafiero et al. (2025b) perform compression using larger-scale spheres relative to the thickness of the material (with R up to $3mm$ in Tappert et al. (2020)), allowing compression to influence a more extensive portion of the tissue.

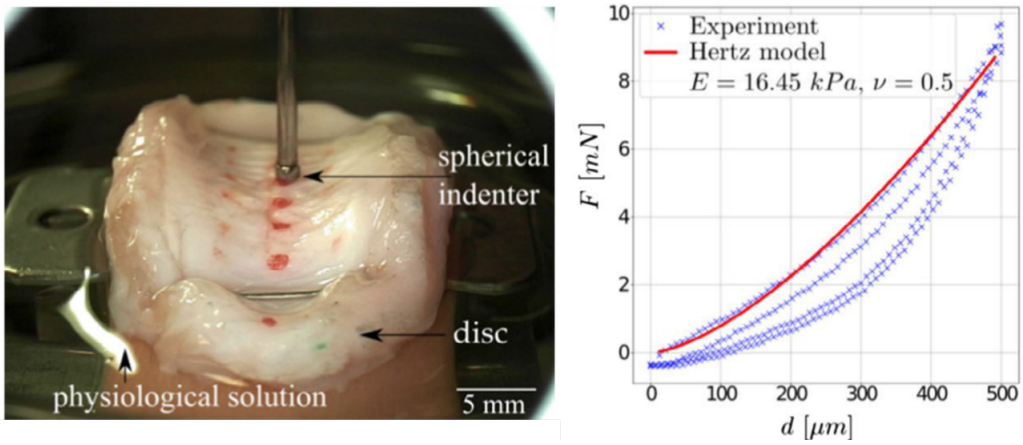

Figure 1.8: Spherical compression experiment conducted on temporomandibular joint disc and experimental result with curve-fitting using the Hertz model for material characterization (Tappert et al., 2017).

The use of larger radius/thickness ratios strays from Hertz model's intended framework, which is corroborated by Wu et al. (2016) that mentions its invalidity when dealing with samples of small thickness, a relevant problem when dealing with thin materials such as the skin (Geerligs et al., 2011; Nachman & Franklin, 2016).

In recent studies that sought to adapt the Hertz model, hyperelastic definitions were applied considering the sphere to be small in comparison to the thickness of the sample. (Merson et al., 2023; McCreery et al., 2023)

A major challenge of spherical compression is contact detection. Due to the geometry of the compression process (see figure 1.7) and experimental conditions (e.g. the sample is submerged in fluid and light refraction distorts its visualization), it is difficult to identify the beginning of contact between the sphere and the sample visually. The force values measured in these low-stiffness tissues can be relatively small, as in Tappert et al. (2020) which obtained maximum forces of 0.016 N, which requires the use of load cells with adequate sensitivity. One possibility to overcome this problem is to apply a threshold criteria for defining the minimum force to be considered as contact with the sample. Besides that, Dai et al. (2019) uses transparent compression spheres to conduct in vivo human skin characterization and, through a camera inside of the compression tool, identifies the evolution of the contact radius with the sample by image correlation.

Some models seek to incorporate poroelasticity into spherical compression. Still dealing with samples completely adhered to the base, Kalyanam et al. (2021) models hydrogels through rheometric tests to obtain shear stress values and estimate material parameters, which are later introduced into a poromechanic FE analysis. The simulation results can then be compared with the experimentally obtained values and optimized to ensure a good fit. A biphasic model proposed in Wang et al. (2020) integrates principles of the Biot model with the Hertz contact model, proposing an analytical formula for force measured in stress-relaxation tests for biological tissues under spherical compression :

$$F(t) = F_{Hertz}\left(\frac{1}{1 - Aexp(-\frac{t}{\tau_p})}\right) \tag{1.29}$$

where A is a parameter dependent on the imposed strain rate, t is experimental time and τ_p is a parameter related to the contact radius (a) and fluid diffusivity inside the structure.

The method proposed in their article was used in the treatment of results from spherical compression tests in porcine liver, spleen, kidney and human liver, reporting success in reproducing small scale relaxation curves.

Those are useful methods to characterize tissue behavior when submitted to compressive loadings. Although, due to the described nature of such materials, the mechanical response to tensile forces may differ due to collagen network solicitation. Tensile tests are used for characterizing the tissues in this sense, enabling also the exploration of potential anisotropic effects.

1.2.4 Tensile tests

Tensile testing is one of the most common mechanical characterization methods used in a variety of materials, including soft biological tissues (Scholze et al., 2018). It involves gripping the sample and pulling it apart until a certain degree of deformation or rupture, with sample fixation method depending on the type of specimen. The measured force and displacement are recorded, which allows to estimate stress and strain based on measures of sample cross-section (Navindaran et al., 2023). The stress-strain curves, exemplified in Figure 1.9a, can then be obtained and the direct extraction of properties (e.g., Young's modulus, yield strength, ultimate tensile strength) is conducted identifying key points on the curve or through other curve-fitting procedures, based on constitutive relations specific to the problem.

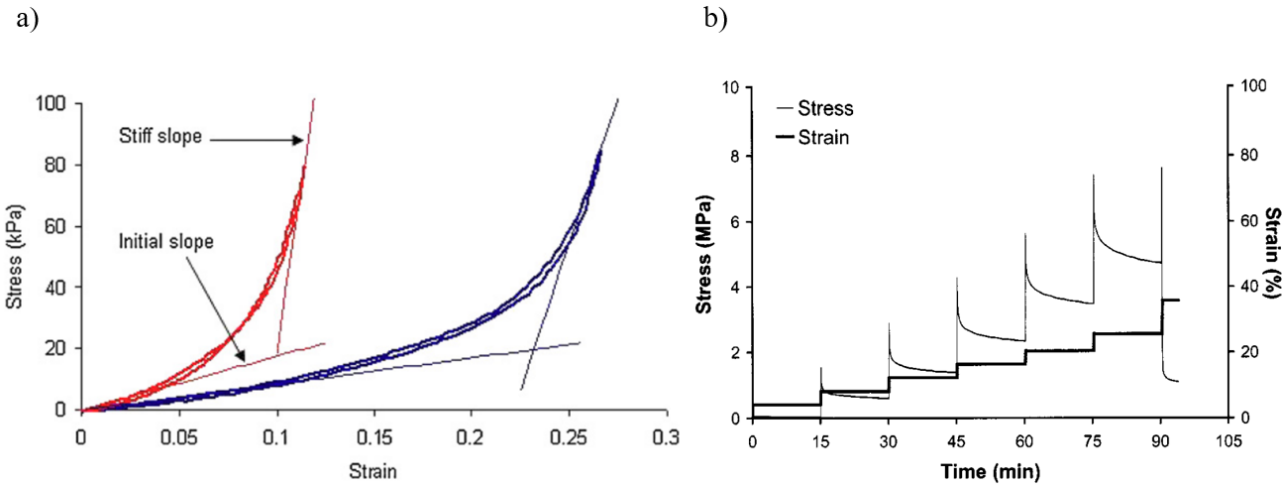

Figure 1.9: a) Representative stress-strain curves from biaxial tensile tests conducted on aortic tissue samples. The red curve represents the tensile response of the material when stretched along the circumferential direction of the arteries, whereas the blue curve, which exhibits lower stiffness, corresponds to the longitudinal direction. This highlights the anisotropic behavior of the tissue. The regions labeled as "initial slope" and "stiff slope" indicate the change in material stiffness as the collagen fibers progressively align and stretch (Chow & Zhang, 2011). b) Results from incremental stress-relaxation tests conducted on temporomandibular discs, showing the progressive decrease in measured stress at each compression step (Detamore & Athanasiou, 2003).

Biaxial analyses on soft biological tissues composed of fibrous structures, such as performed in Chow & Zhang (2011), enable the characterization of anisotropic properties of tissues, since tissue's fibers are stressed in multiple directions and distinct direction-dependent mechanical responses can be identified. The fibers are primarily responsible for the tissue's response to tension, and both their orientation and level of stress are reflected in the stress-strain relationship. At the beginning of the tension process, the fibers of the tissue are not necessarily completely stretched and they gradually align with the direction of loading as they are stressed (Fung, 1993). Consequently, lower material stiffness is observed at the beginning of the test, which

tends to increase as the fibers align, generating the so-called toe region in the stress-strain curve, exemplified in Figure 1.9a.

As a consequence of these dynamics, the tissue's response to tension may be different as to compression (Ateshian, 2017). Even so, the nonlinear and viscous aspect of such materials is still observable in the context of tension, as in the example in Figure 1.9b. Detamore & Athanasiou (2003) were able to observe stress-relaxation effects in temporomandibular joint disc samples when they were subjected to tension. It was hypothesized in a study of the behavior of pig tendons that the main contribution to the viscosity observed in contexts such as this is the progressive reorganization of the tensile collagen network during loading (Solis-Cordova et al., 2023).

Scholze et al. (2020) used 3D printed clamps to hold skin and ligament specimens in tensile testing, highlighting the problem of sample slipping at certain levels of imposed stress. Samples with a high degree of hydration may be prone to slipping and the increase in clamping force is potentially harmful to its structure, motivating solutions such as those of Baldit et al. (2022), which performs tests on thin Wharton jelly membranes and fixing the samples with glue (Figure 1.10a). Chow & Zhang (2011) executed biaxial tensile tests on aortic tissue samples, in this case fixing them in four directions by means of sutures (Figure 1.10b).

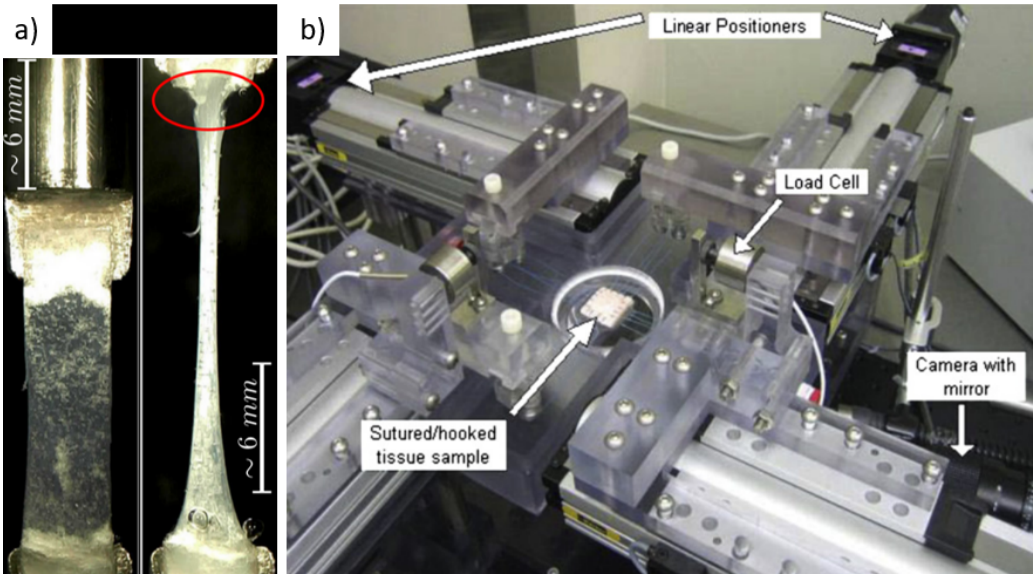

Figure 1.10: a) Tensile test of hydrated Wharton jelly membrane samples highlighting the damage on the structure in the end of the test (Baldit et al., 2022). b) Biaxial tensile test on aortic tissue (Chow & Zhang, 2011).

1.3 Biomechanical study of the temporomandibular joint disc

This thesis focuses on a specific biological tissue: the temporomandibular joint disc. The objective is to characterize its poromechanical behavior to reply to the current need for predictive methods of its mechanical response for various medical applications. Understanding the mechanics of this tissue has the potential to aid in the understanding of pathological phenomena that affect the proper functioning of the joint, to propose substitutes for the disc's material, and to Connelserve as a basis for numerical studies of the joint, which can be used in the investigation of dysfunctions and the proposal of new prosthetic solutions.

1.3.1 Anatomy of the temporomandibular joint

The movements performed by the human mandible can involve a total of six degrees of freedom, with translations and rotations performed in any direction during daily activities (Drake et al., 2010). Under maximum voluntary contraction, the human bite is capable of producing forces greater than 400 N in the posterior dentition of adults (Edmonds & Glowacka, 2020). The combination of complex movement freedom and high mechanical demand requires the presence of a joint that is functional in the long term, composed of tissues that resist the repetitive stress and mechanical loadings experienced over the span of an individual's life.

The human body features two temporomandibular joints (TMJ) which are responsible for ensuring such functioning, systematically combining translations and rotations to perform everyday tasks such as speaking, chewing and other essential activities.

The TMJ allows relative movement between the mandible and the temporal bone thanks to muscle contractions. It is located between the Glenoid fossa (or Mandibular fossa) of the temporal bone and the upper part of the mandible bone, where the condyle (or condylar process) is situated. The bone surfaces in this area are covered by fibrocartilaginous layers (condylar and fossa cartilage) which help to distribute stress and also reduce friction. Figure 1.11 shows the location of the joint and some of its internal structures.

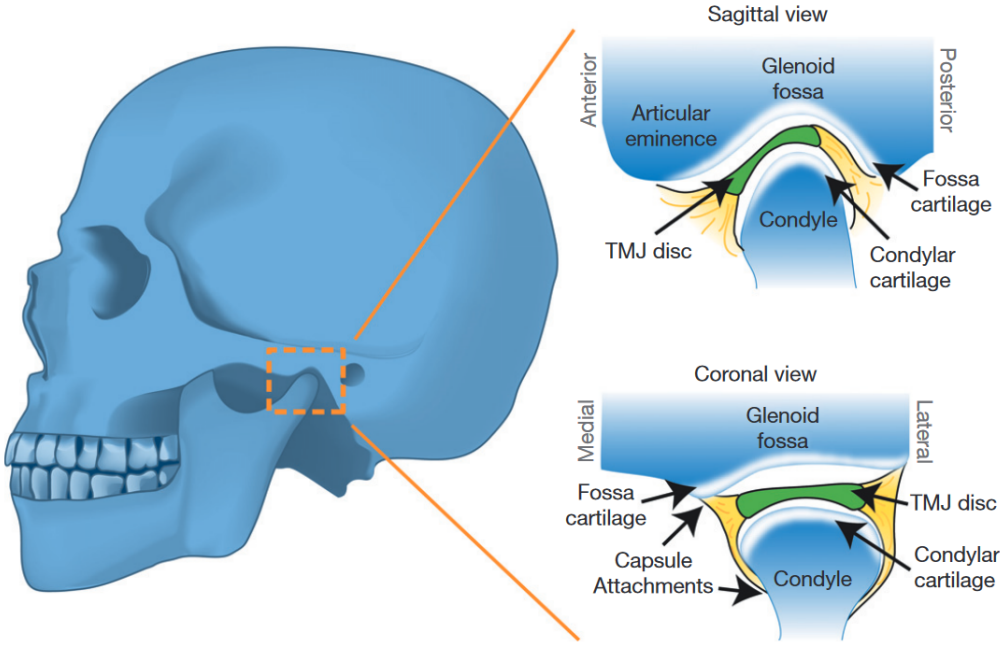

Figure 1.11: Temporomandibular joint location, showing disc position and internal joint structures in sagittal and coronal views (Willard et al., 2011).

It is a synovial joint covered by a connective tissue membrane that produces and stores synovial fluid, illustrated in Figure 1.12. This fluid ensures reduced friction and is crucial for the longevity and nutrition of the involved tissues (Trindade et al., 2021).

Between the two bony structures of the condyle and mandibular fossa lies a fibrocartilaginous disc, that divides the joint into two regions. Its upper portion is responsible for protrusion and retrusion translations (forward and backward movements in the sagittal plane), while the lower part of the joint is responsible for the rotation component of movements, ensuring its depression and elevation (Drake et al., 2010).

For the mandible to open and close properly, the disc needs to follow the displacement of the condyle and slide within the space between the mandible and temporal bone towards

the articular tubercle (Figure 1.12). The main role of the disc is to absorb shocks in the region, deforming itself and improving contact between the cartilage covered bony surfaces to ensure a smooth mandibular movement. This enables force distribution and spreading of the synovial fluid within the joint capsule (Kang et al., 2006). The disc's displacement during mandibular movement is depicted in Figure 1.12b. The disc is held in position in all directions, as illustrated by the yellow elements in Figure 1.11, and the tissue positioned in its posterior portion (represented in yellow in the sagittal view of Figure 1.11) are the so-called retrodiscal tissues.

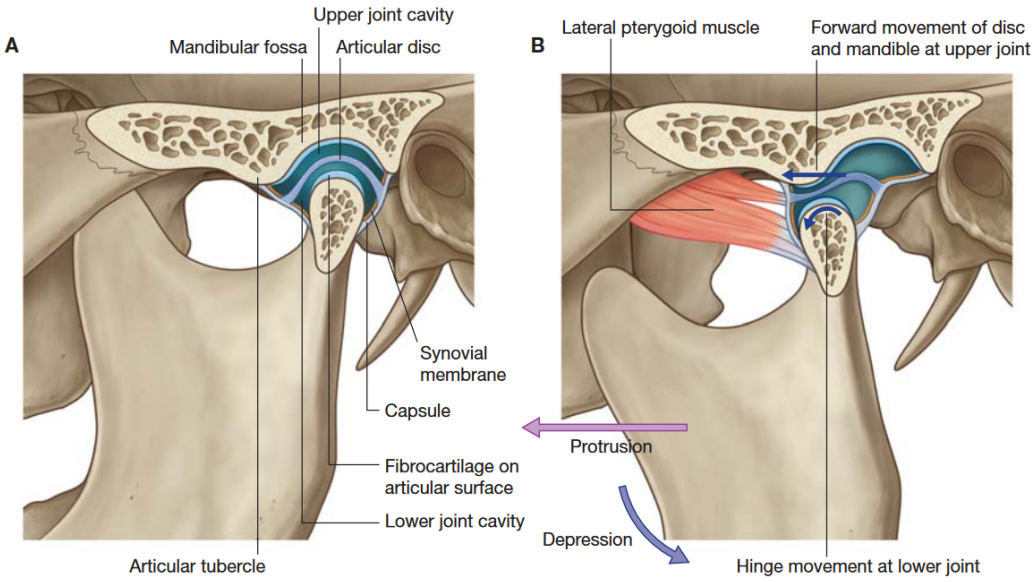

Figure 1.12: Temporomandibular joint with the mandible in closed (a) and open (b) positions (Drake et al., 2010). The mandibular movements of protrusion and depression are indicated.

The disc's tissue is constantly subjected to compressive, tensile and shearing forces in multiple orientations during the functioning of the joint (Kang et al., 2006). One of the main drivers in its movement is the lateral pterygoid muscle (1.12b), attached to the temporomandibular capsule and consequently to the disc, in its anterior portion. When contracting, this muscle pulls the disc forward, being one of the main actors in mandibular protrusion (Drake et al., 2010).

1.3.2 Disc composition and structure

The human articular disc has a biconcave shape, with smaller thickness in its central portion (1 to 4 mm) in relation to its more peripheral zones. The disc has a roughly oval shape (Alomar et al., 2007), with around 19 mm in its mediolateral dimension, while its anteroposterior portion is 13 mm (Detamore & Athanasiou, 2003; Willard et al., 2011). The tissue is composed primarily of water, representing 66 to 80% of its total weight, depending on the age of the individual (Detamore & Athanasiou, 2003). The articular disc presents variability among different animal species. Bermejo et al. (1993), Herring et al. (2002) and Kalpakci et al. (2011) conclude that pig discs resemble human ones in terms of dimensions, compressive properties, collagen and GAG content. Due to their similarity and applicability to human contexts, porcine TMJ discs have historically been adopted as an object of study in several works (Wu et al., 2015; Cisewski et al., 2015; Kuo et al., 2010; Shi et al., 2013; Benavides et al., 2009; Almarza et al., 2006; Beatty et al., 2001; Kuo et al., 2011b,a; Ortún-Terrazas et al., 2020; Wu et al., 2019). Porcine

discs have a slightly larger geometry than humans, with approximately 21 to 25 mm in the mediolateral direction in the case of 8-month miniature pigs (Herring et al., 2002).

To help reference the different zones of the disc, its structure is divided into medial, central, and lateral portions in the mediolateral direction. In the anteroposterior direction, it is divided into anterior, intermediate and posterior portions. Vertically, the disc is divided into superior and inferior zones, as illustrated in Figure 1.13a. The disc's ECM is almost exclusively type I fibrillar collagen, representing 70 to 80% of its dry weight composition (Detamore & Athanasiou, 2003; Fazaeli et al., 2019). The collagen fibers are predominantly positioned anteroposteriorly in its central, medial and lateral zones (Wright et al., 2016). In its anterior and posterior zones, the disc presents fibers distributed in the mediolateral direction, generating a ring-shaped aspect around its central zone, as indicated in the Figure 1.13b. It is speculated that the annular shape assumed by the peripheral zone of the disc is related to its ability to maintain its shape under compressive and tensile stresses Detamore & Athanasiou (2003).

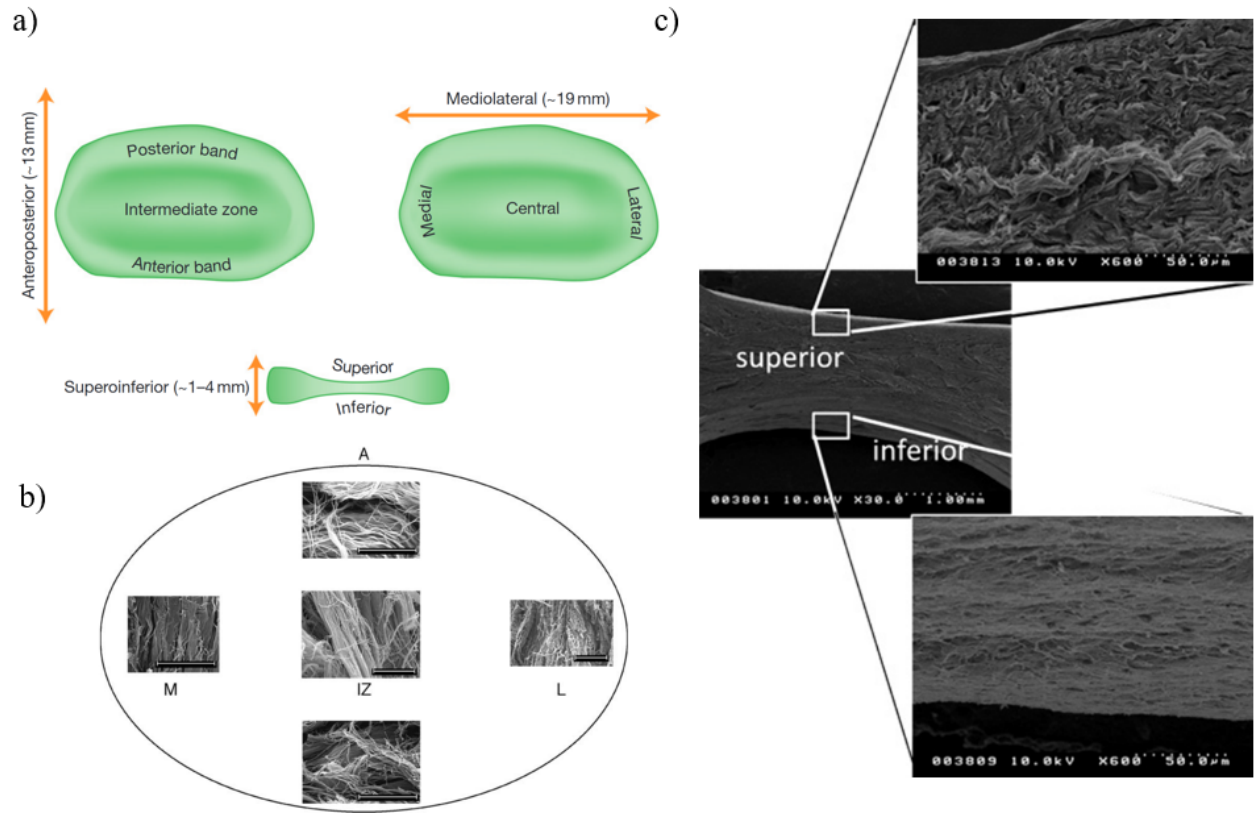

Figure 1.13: a) TMJ disc, indicating the different tissue zones and anatomical orientation axes (Willard et al., 2011). b) Fiber network orientation in different regions of the disc, as observed via scanning electron microscopy. Fibers tend to align anteroposteriorly in the intermediate zone, while the peripheral structure in the anterior, posterior, lateral, and medial regions forms a ring-like pattern surrounding the center of the disc (Detamore et al., 2005). c) Scanning electron microscopy images of a sagittal section of the temporomandibular disc, illustrating the superior and inferior fiber network arrangement. (Juran et al., 2015).

Detamore et al. (2005) performs a immunohistochemical analysis of porcine discs and claims to observe no significant differences in the ECM composition between the upper and lower zones. When it comes to ECM structure organization, scanning electron microscopy (SEM) images performed by Juran et al. (2015) indicate the existence of multiple layers in the upper portion of the disc, while the lower structure has a more homogeneous distribution of fibers, as shown in Figure 1.13c.

The disc is also composed of elastin fibers, representing approximately 1 to 3% of its total weight (Fazaeli et al., 2019). GAGs make up around 5% of its dry weight, with the main types being chondroitin-4-sulfate and chondroitin-6-sulfate. This is a relatively low content compared to hyaline cartilage, which presents 25 to 30% GAG content (Detamore et al., 2005). The distribution of GAGs is not homogeneous in the disc. In the anteroposterior direction, a smaller quantity is reported in the posterior band in relation to the anterior and intermediate ones. In the mediolateral direction, greater quantities were observed in the medial portion, while the lateral and central portions presented similar and lower values. No difference in the presence of GAGs was observed between the superior and inferior portions of porcine discs (Almarza et al., 2006). Due to its relationship with the compressive properties of the disc, this is an indication of the heterogeneity of the disc mechanics (Tanaka et al., 2003a).

The articular disc is poorly vascularized (Trindade et al., 2021; Cisewski et al., 2015) and the transport of nutrients inside it are made thanks to synovial fluid contact with cells. Cells make up approximately 10% of the dry weight of the disc, divided into approximately 70% fibroblasts and 30% fibrochondrocytes. The relationship between nutrient distribution and rate of their consumption by the cells generates a concentration gradient within the material, which is related to the vulnerability of the tissue to degenerative pathologies. Compressive deformations in the disc hinder solute transport in the joint (Wright et al., 2013), indicating its sensitivity to problems such as bruxism and prolonged jaw clenching.

1.3.3 Disorders and therapeutic approaches for the temporomandibular joint

The temporomandibular joint can be affected by temporomandibular disorders (TMDs). One difficulty in understanding epidemiological studies associated with TMJ is the lack of a standardized research method. Studies often do not differentiate between painful and non-painful symptoms, and group all possible dysfunctions into pathological or non-pathological cases, without systematically differentiating the nature of the problems. The meta-analysis conducted by Zieliński et al. (2024) is the most recent, and analyzed a total of 6,984 studies, with 74 deemed pertinent after the systematic review screening process. Only two were conducted in African populations and one in Australia, highlighting a gap in epidemiological knowledge regarding the African and Oceanian populations. After analyzing relevant works on TMDs, the general conclusion in Zieliński et al. (2024) is that the disorders affect on average 34% of the world population. Their occurrences have a higher prevalence in women, with the highest female-to-male ratio of 1.56 in South America and the lowest of 1.09 in Europe. Wright et al. (2016) indicates that female discs tend to relax less and be more rigid than male articular discs. Hormonal differences between individuals are suggested as the cause of this disparity, however there is still no general consensus in literature and further research is needed on the subject (Zieliński et al., 2024).

The TMDs result in symptoms such as muscle pain in the joint region, limitation of mandibular movements, prolonged or momentary jaw locks and deviation of the mandible during movements (Willard et al., 2011). TMDs are the most common cause of pain in the orofacial region and chronic cases are the main reason that lead patients to seek treatment (List & Jensen, 2017).

Several pathological processes can originate from the TMDs. Wear and perforations in the disc are not healed naturally by the body and require surgical intervention to be repaired (Willard et al., 2011). Disc thinning is a factor that can trigger multiple complications and early treatment is ideal to prevent further degeneration and alleviate the symptoms (Vapniarsky et al., 2018). Furthermore, changes in synovial fluid lubrication and overused muscles can cause disc displacement, which in the long term alters the joint's stress patterns and increases tissue degradation, resulting in loss of mobility (Willard et al., 2011). The protrusion of the mandible

(forward projection), imposes the greatest mechanical stress on the disc (Schmolke & Hugger, 1999) and the persistence of excessive efforts on the joint, in cases of bruxism for example, can lead to the emergence of degenerative diseases such as osteoarthritis.

Treatments for dysfunctions may be non-invasive for less severe cases, with the prescription of anti-inflammatories and muscle relaxants. Currently, the most commonly used solutions for treating dysfunctions are physiotherapeutic exercises (González-Sánchez et al., 2023). Such alternatives, although effective in controlling symptoms, are not capable of regenerating damaged tissues such as the disc. Intermediate cases may require direct injections of medication into the joint in the so-called arthrocentesis, where the injected fluid reduces inflammation (Trindade et al., 2021). These procedures can restore joint functionality and prevent worsening of degenerative problems in simpler cases, but more severe scenarios demand enhanced invasive approaches. Problems related to disc misalignment, for example, can be resolved through repositioning surgeries, known as discoplexy (Trindade et al., 2021).

Discectomy, where the disc is completely removed from the joint, results in remodeling of the condyle surface (Vapniarsky et al., 2018). Historically, several disc substitutes have been tested. The use of medical-grade silicone implants was first proposed in 1968 (Trindade et al., 2021) and an evaluative study by Eriksson & Westesson (1992) reported such solution to neither improve clinical outcomes nor prevent the degeneration of bone structures. Proplast-Teflon implants also presented high failure rates and require regular post-surgical monitoring (Henry & Wolford, 1993).

There is still ongoing research for suitable disc substitutes. Current tissue engineering techniques seek biocompatible materials that meet the disc's original mechanical properties and possess long-term stability under high cyclic loads (Acri et al., 2019; Singh et al., 2022; Jiang et al., 2023). Such solutions may use scaffolds that serve as a base for the new tissue developent, being produced using naturally derived collagen, hydrogel or 3D printed synthetic materials for example. Even though they may provide immediate relief for patients and seem to be a promising tool for treatment of dysfunctions, none of the current solutions have yet proved to be a satisfactory replacement for the original tissue and to meet the required mechanical demands (Acri et al., 2019; Trindade et al., 2021; Singh et al., 2022; Jiang et al., 2023).

For cases in which disc substitution alone is not sufficient, complete TMJ replacement prosthesis try to reproduce structures such as the condyle and temporal fossa. The systematic review by Johnson et al. (2017) reports the low number of long-term analyses of the application of TMJ prostheses, also indicating a lack of articles published by surgeons on the subject. Often the manufacturers themselves conduct the research, raising questions about the impartiality of studies (Johnson et al., 2017). Rodrigues et al. (2018) highlights the scarcity of studies on mechanical validation and immunological response of TMJ prosthesis in comparison with other orthopedic joint replacements, performing a bibliographic review that focus on the biomechanical aspect of prosthesis validations. Validations are typically performed using the finite element method (FEM), emphasizing the importance of understanding the mechanical properties of the tissues that compose the joint.

1.3.4 Biomechanical analysis of the temporomandibular disc

1.3.4.1 Numerical simulations of the joint

The mechanical characterization of the temporomandibular disc helps to guide tissue engineering studies, allowing the acquisition of parameters for validation of substitutes. The physical difficulty of positioning sensors and accessing information from inside the joint in vivo, associated with the complexity of obtaining ethical approval for human trials, encourages the emergence of alternative methods of mechanical analysis. An in vitro study by Throckmorton

& Dechow (1994) estimated muscular efforts in the mandible and analyzed the forces at the condyle level during compression of human mandibles, observing forces of up to 210 N. In silico FE analyses allow to estimate the impact of mandibular loading on the disc's tissue, with reported stress values ranging from 0.9 to 14.8MPa under functional loading conditions (Hirose et al., 2006; Mori et al., 2010; Savoldelli et al., 2012; Creuillot et al., 2016), which are results that depend highly on the material definition adopted in each of the models.

Early studies adopted simulations considering TMJ structures as rigid bodies, allowing the estimation of reactions in the joint based on measurements of muscle contraction (Throckmorton & Throckmorton, 1985). Sagl et al. (2019) used a combination of a muscle-driven rigid body model for mandibular movement with a FE modeling of the disc material, with the aim of observing stress patterns on the disc during dynamic activities.

To implement patient-specific FE models, the shape of the biological structures can be acquired through Computed Tomography (CT) or Magnetic Resonance Imaging (MRI) methods, which after a segmentation process are introduced as geometry in the model (Shu et al., 2020). Numerical analyses of this type can serve multiple purposes, as in the example of prosthesis validations in Chen et al. (2018) and Vignesh et al. (2020). The prosthesis geometry is incorporated in the model in interaction with the segmented bones and mechanical solicitations are simulated to verify prosthesis' adequacy.

In the literature, various approaches exist for modeling disc behavior, such as the FE model developed by Tanaka et al. (2001) to study the effect of discrepancies in skeletal geometry and tooth positioning on stress patterns in the human TMJ. To this end, they adopted a definition for the disc with two Young's moduli, where $E = 44.1MPa$ was adopted for a stress range lower than $1.5MPa$ and $E = 92.4MPa$ for higher stresses acting over the disc, based on parameters of tensile tests carried out on dog discs on previous experiments by Tanne et al. (1991).

Aoun et al. (2014) analyzed the effects of mantained jaw clenching on TMJ stress, which then needed a model capable of representing creep and stress-relaxation effects. They adopted a definition that couples hyperelasticity and viscoelasticity in FE, based on experimental data from Beek et al. (2003). The strain energy density function adopted for description of the hyperelastic behavior was the Marlow model, which doesn't requires material parameters and is calibrated directly by the experimental results. However, the available experimental data allowed Aoun et al. (2014) to define only the deviatoric portion of the material's behavior, needing to estimate its volumetric behavior with a Poisson's ratio of $\nu = 0.4$. The original work that performed the experiments (Beek et al., 2003), points to the relevance of a biphasic poromechanical approach to describe the disc, due to its high interstitial fluid content and observed behavior in tests.

A FE model that takes into account deformable joint components, patient-specific geometry and dynamics, muscle element modeling and a biphasic disc definition was developed in Ortún-Terrazas et al. (2021), and their model is illustrated in Figure 1.14.

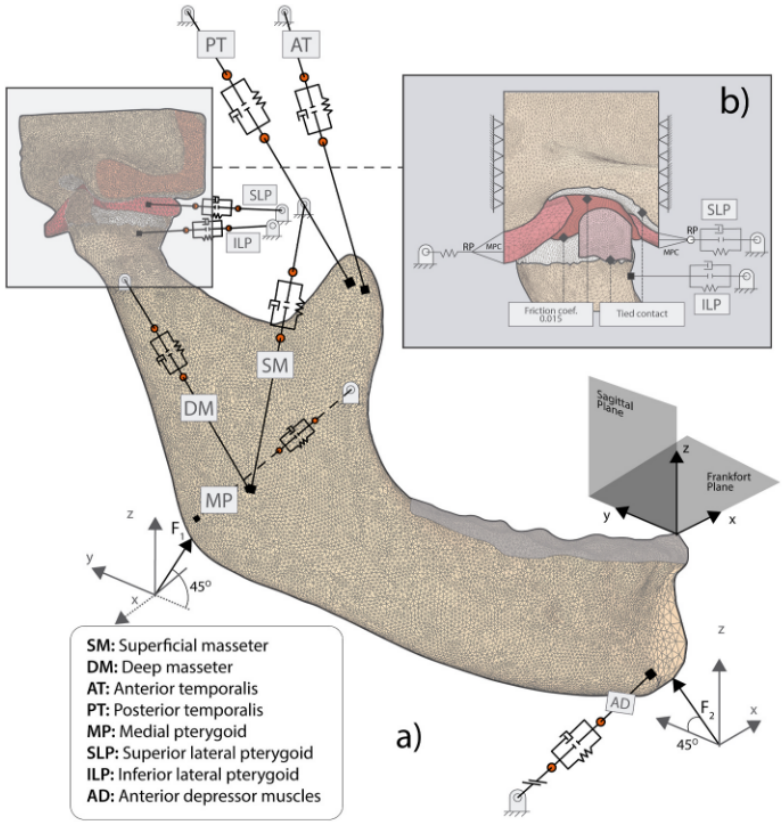

Figure 1.14: Figure from Ortún-Terrazas et al. (2021). a) Diagram showing model's mesh, with boundary conditions and muscle elements positioning. b) Boundary conditions applied inside the TMJ, showing elements representing the disc, muscles, articular cartilage and ligaments.

Ortún-Terrazas et al. (2021) developed FE models of the TMJ based on geometries obtained by MRI and CT data from six patients, to compare the joint dynamics using two different disc definitions. The first was hyperelastic and isotropic, while the second assumed a poromechanical definition with a hyperelastic fiber-reinforced solid phase. The adopted disc parameters came from a previous study (Ortún-Terrazas et al., 2020) that defined the material behavior through numerical FE optimizations based on tensile (Wright et al., 2016) and compression (Beek et al., 2001) experiments. Ortún-Terrazas et al. (2020) observed more realistic dynamics when adopting the poroelastic approach, with better correlation with experimental data when defining the material's solid phase as a hyperfoam (hyperelastic behavior law used for defining elastomeric foams) with a biphasic strain-dependent permeability definition when the material was submitted to compression. A different mechanical response was defined for the tensile response of the same material definition, in which they adopted a fiber-reinforced Holzapfel strain energy function. They adopted an initial mean intrinsic permeability of around $6.88 \times 10^{-15} m^2$ (representing hydraulic permeability of around $9.96 \times 10^{-12} m^4/Ns$ when considering the dynamic viscosity of water at 37°C). In their model, permeability was not constant and decreased with compressive strain through equation 1.15, with a mean value for the adimensionnal fitting parameter M equal to 45.7.

Wu et al. (2019) developed a FE analysis of the TMJ to observe the effects of prolonged jaw clenching on the viability of TMJ cells based on measurements of solute diffusivity by osmotic effects. Cylindrical samples of porcine discs were prepared from circular cuts made in the specimens by means of corneal trepines. They removed the upper and lower faces of the cylinders with a microtome, in order to eliminate the biconcavity of the sample. They positioned the samples in a chamber allowing the measurement of solute diffusivity of glucose and lactate, which play a role in cellular metabolism, and observed an inversely proportional

relationship between the compressive strain imposed and the diffusivity in the material. They applied the parameters to a FE model simulating the whole disc in compression and were able to conclude about the increased vulnerability of the disc to pathologies when in prolonged compression.

This phenomenon is also evident in studies that analyze the electrical conductivity of the disc, also related to the ion diffusivity inside the tissue (Kuo et al., 2011b). The conductivity of the material in this case is proportional to the volume fraction of water inside it and, through conductivity measurements, Kuo et al. (2011b) and Wright et al. (2013) were able to observe the decrease in ion diffusivity in the disc as a function of the strain imposed on porcine and human discs, respectively.

The definition of disc behavior directly influences the state of stress distribution in the TMJ and its dynamics, which are commonly the focus of mechanical studies of the joint. Figure 1.15 shows an analysis of disc stress distribution in different conditions in the work of Sagl et al. (2019), with a hyperelastic material definition based on experiments from Beek et al. (2001).

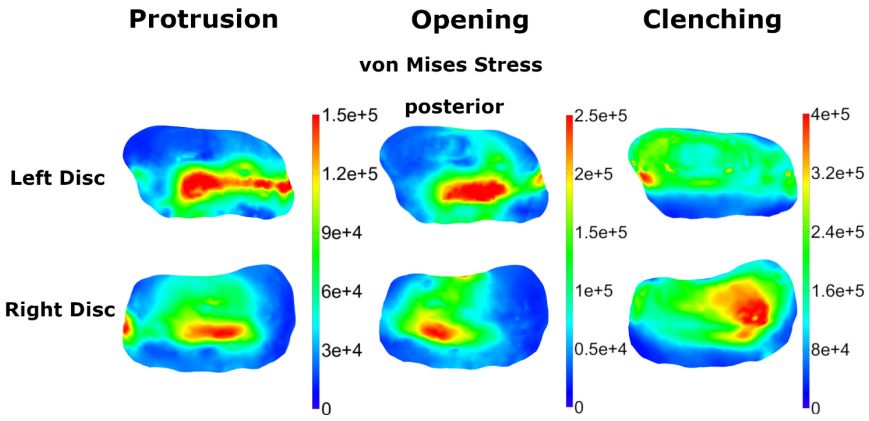

Figure 1.15: Stress distribution [Pa] in disc in multiple different mandible conditions, with a hyperelastic Mooney-Rivlin definition (Sagl et al., 2019).

The adopted models and chosen parameters, originating from experimental investigations, are essential for the simulation to be as reliable as possible. The existing definitions and characterization methods applied to the TMJ disc will be discussed below.

1.3.4.2 Characterization techniques applied to intact discs

En effet, comme mentionné ci-dessus, ces travaux retirent souvent les surfaces supérieure et inférieure des échantillons afin de faciliter la traversée du fluide pendant les essais.En effet, comme mentionné ci-dessus, ces travaux retirent souvent les surfaces supérieure et inférieure des échantillons afin de faciliter la traversée du fluide pendant les essais. In order to perform ex vivo tests, testing conditions seek to approximate the physiological context of the sample, for example keeping them hydrated and submitted to controlled temperatures around 37°C (Detamore & Athanasiou, 2003). In order to avoid possible osmotic effects that affect fluid movement into or out of the material, saline solutions or phosphate buffered saline solutions may be used to assure tissue hydration for instance (Detamore & Athanasiou, 2003).

Beek et al. (2001) performed cyclic compression tests on seven human temporomandibular discs using a universal testing machine. The discs were glued between two indenters and were tested in the anterior, intermediate and posterior zones. The experimental results allowed the observation of hysteresis loops in the stress-strain curves, indicating energy dissipation. Figure 1.16 illustrates the used device and shows one of the obtained results.

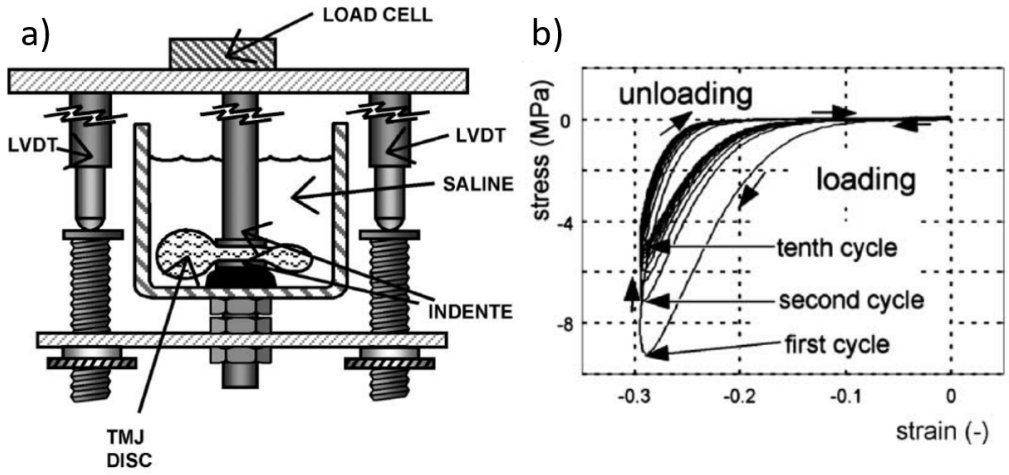

Figure 1.16: a) Experimental apparatus used for the experiment, depicting a human TMJ disc between two indenters and submerged in saline solution controlled at 37°C, b) stress-strain relation of 10 loading cycles in the same sample, showing loading history dependent mechanical response and loss or energy of the material. Modified from Beek et al. (2003).

Figure 1.16b shows that material behavior tends to stabilize after a few loading cycles. Due to this phenomenon, it is common practice to perform preconditioning cycles before starting the tests (Wright et al., 2016; Calvo-Gallego et al., 2017). This allows to observe the behavior from the moment the material's response has stabilized, approaching testing conditions to the physiological context of permanent behavior, with a more repeatable mechanical response.

In Barrientos et al. (2016), intact porcine discs were tested by being compressed between structures representing the condyle and the temporal fossa, obtained from the reconstruction of CT images of the donor pig. In a viscoelastic approach, they performed dynamic stress relaxation tests to observe the compressive storage modulus E' (linked to the elastic component of the material), the compressive loss modulus E'' (viscous component of the behavior) and the loss tangent $tan\ \delta$ (ratio between the two other measured quantities). An increase in the compressive properties of the disc was observed at higher loading frequencies, highlighting its viscous behavior, as Figure 1.17 shows.

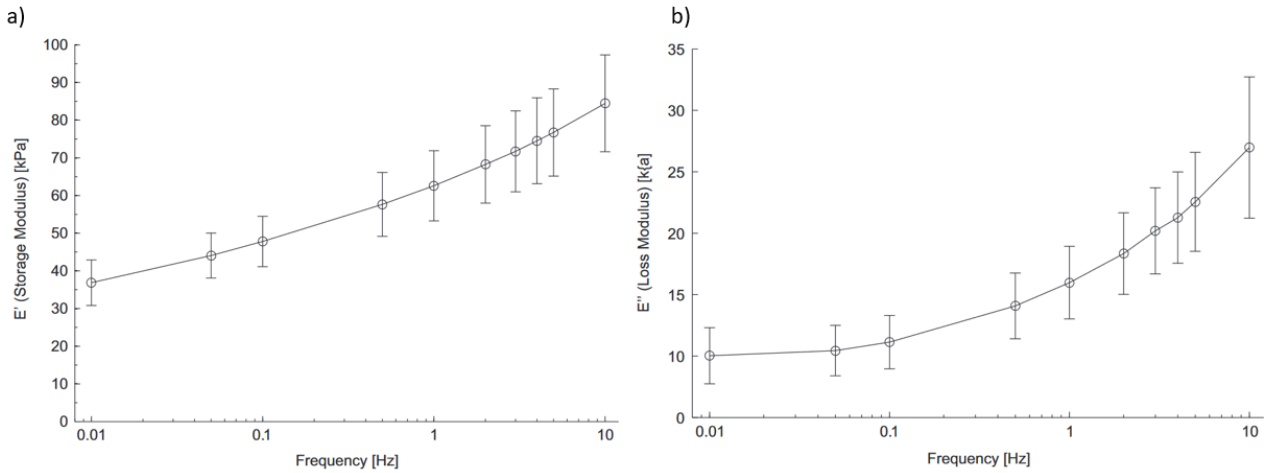

Figure 1.17: a) Storage modulus and b) loss modulus variation for multiple dynamic loading frequencies, adapted from Barrientos et al. (2016). This image highlights the viscous aspects of the material.

Tests conducted on smaller portions of the disc enable the exploration of variations between

different zones of the material (Lumpkins & McFetridge, 2009; Fazaeli et al., 2016; Tappert et al., 2017). Lumpkins & McFetridge (2009) analyzed multiple zones of porcine discs in cyclic compression between two plates and measured the initial compressive modulus E_{int} (obtained by not yet stabilized the stress-strain relationship immediately at the beginning of the test) and the steady-state compressive modulus E_{SS} (obtained by the slope of the stress-strain curve when the tissue reached the steady-state). The stiffness values were found between 0.5 and 2.5 MPa and the initial modulus E_{int} was higher than E_{SS} in three different zones of the disc (medial, central and lateral). The highest value of E_{int} was measured in the lateral zone and the lowest E_{int} and E_{SS} were found in the central zone, as shown in Figure 1.18.

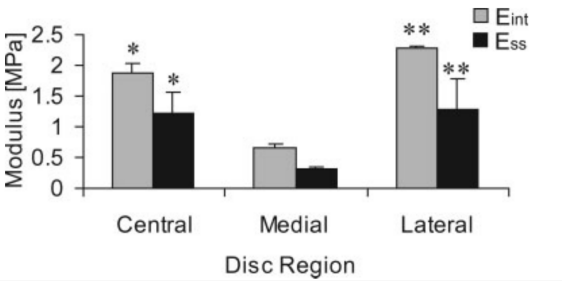

Figure 1.18: TMJ disc initial and steady-state modulus in relation to tested zone (Lumpkins & McFetridge, 2009).

In contrast to these results, Fazaeli et al. (2016) tested porcine discs in compression with a cylindrical indenter and observed the lowest E_{int} values in the lateral zone, in the order of 0.05 MPa. They observed the highest E_{int} in the posterior zone approximately 0.13 MPa and, for all zones, none of the E_{int} values exceeded 0.2 MPa. On the other hand, Beek et al. (2001) performed the indentation of human discs and observed the behavior of the anterior, intermediate and posterior zones. Their experiments indicated a higher stiffness for the intermediate zone and a lower stiffness for the posterior zone.

Studies such as these demonstrate the heterogeneity, the influence of the imposed strain rate to the results and the variability of results between studies. Spherical compression tests on porcine discs performed in Tappert et al. (2020) explored the influence of compressing sphere radius variation. Greater stiffness was observed for tests conducted using larger spheres and the experimental results suggested a different mechanical behavior depending on the penetration depth in the material, as the targeted zone compressed by the sphere varies with the radius of the compressor used.

In Kim et al. (2003), a flat and porous indenter was used on porcine discs, where creep tests of indentation were performed and the linear biphasic theory was applied to obtain parameters through the model proposed in (Mow et al., 1989). In this case, the highest stiffness values were observed in the medial part of the disc, where $H_A = 28.9 \pm 12.3$ kPa and the lowest in the lateral portion $H_A = 16.3 \pm 2.1$ kPa. An average permeability of $24.1 \times 10^{-15} m^4/Ns$ was obtained.

Tappert et al. (2022) analyzed the effects of cutting a cylindrical sample from the center of the TMJ disc. After removal, the cylinder and disc were filmed for approximately one hour and a digital image correlation (DIC) algorithm established the stress-free strains (also known as eigenstrains) of the different zones of the specimen. They were able to observe the temporal deformation of the disc after cutting, attributed to the release of internal stresses that were acting on the disc and shown in Figure 1.19.

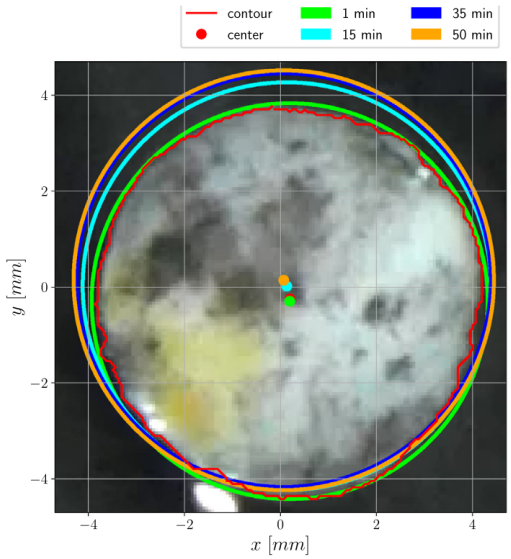

Figure 1.19: Specimen cut from the central zone of a porcine TMJ disc. The figure shows the contours of the space occupied by the sample over time, demonstrating the evolution of its shape from the moment of cutting (Tappert et al., 2022).

It was concluded that a radial pre-tensioning exists in the central zone of the disc, likely serving to compensate for the daily loads to which the tissue is subjected. This highlights the influence of the sample preparation process on the observed behavior. Although this is an often unavoidable effect, depending on the type of test, it should be considered when interpreting experimental results.

1.3.4.3 Tensile tests performed on the disc

Tensile tests on the disc allow access to its anisotropic tensile properties by preparing samples with different collagen network orientations. When it comes to human samples, tensile stress-relaxation tests were performed in Wright et al. (2016). The human samples consisted of strips of material cut in multiple directions on the disc, held between two clamps. In their study, they obtained a Young's modulus of 9 MPa in the central mediolateral direction and 16 MPa in the central anteroposterior direction, calculated as a slope of 40-100% of the stress-strain curve during the loading phase of the applied strain increments.

Beatty et al. (2001) tested the central intermediate zone of porcine discs under tensile impulse loading in the mediolateral and anteroposterior directions, with sample geometry shown in figure 1.20a. They observed a stiffness 10 to 15 times greater for the anteroposterior region than for the mediolateral region of the discs, obtaining an apparent stiffness of 3.2 MPa in the mediolateral direction and 76.4 MPa in the anteroposterior direction for a displacement rate of 500 mm/min. In contrast, tests also performed on porcine discs by Matuska et al. (2016) reported a stiffness of 140 MPa in the anteroposterior direction.

Li et al. (2021) proposed a biphasic transverse isotropic model for the treatment of tensile test results on porcine TMJ discs. They considered, for a sample cut in the anteroposterior direction and pulled between customized clamps (Figure 1.20b), a material model with one set of Young's moduli and Poisson's ratios for the axial plane (in the direction of the fibers, physiologically oriented in the anteroposterior plane) and another set of parameters for the transverse planes. Porosity was included by atributing a constant permeability in the transverse plane. In this case, the permeability indicates the behavior of the fluid when the fibers are pulled by the clamps, squeezing them and expelling the fluid in the direction of the transverse plane to the sample.

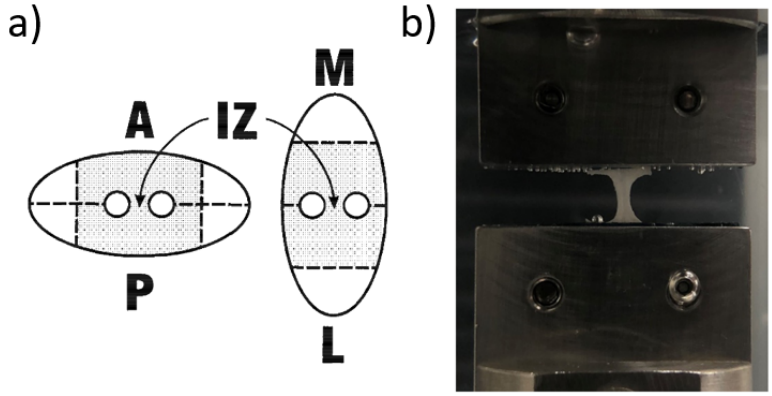

Figure 1.20: a) Schematic illustration of specimen preparation from temporomandibular discs for tensile testing, designed to fit into custom-made grips. The disc on the left is prepared for anteroposterior tensile loading, while the disc on the right is prepared for mediolateral loading. The dashed lines indicate the cutting locations used for specimen preparation (Beatty et al., 2001). b) Sample strip positioned between custom-made clamps (Li et al., 2021).

Through stress-relaxation tests, they performed the curve-fitting and reported good representation of the model only for low tensile strains of around 0-4%. They defined for this range of loading a transverse stiffness of 7.2MPa, axial stiffness of 13.5MPa and a permeability of $32.4 \times 10^{-18}\ m^4/Ns$ in the transverse direction. However, the model wasn't able to reproduce higher strain curves and the study concluded that the viscoelastic behavior attributed to fluid movement had a small contribution when compared to the viscoelasticity of the solid matrix, demanding then another definition of solid phase.

Multiple theoretical models were used to represent the viscoelastic properties of TMJ discs in tension, including a nonlinear viscoelastic model constructed with a four-mode Maxwell model and second-order Mooney-Rivlin models as elastic elements, as described in (Koolstra & Tanaka, 2009). A Prony series model in Gutman et al. (2018), which analyzed the influence of fiber alignment on the material's viscoelastic properties, found that the degree of alignment of the collagen fibers influences the distribution of GAGs in the structure and, consequently, the material's response to compression.

1.3.4.4 Confined compression tests performed on the disc

Confined compression, although widely used in biomechanical contexts for biphasic treatment of materials, has not been widely explored for the temporomandibular disc. Kuo et al. (2010) performed confined compression tests on 12 human TMJ discs of average age of 78 years old, with samples of approximately 5 mm in diameter and 1.4 mm in thickness, that were cut from the anterior, posterior, lateral, medial and central intermediate zones of discs. The inferior and superior superficial layers of the samples were completely cut with a sledge microtome, aiming to prepare specimens as cylindrical as possible. The tests consisted of compressing the discs in stress relaxation, and then performing a 2h creep test, followed by a cyclic sinusoidal dynamic test.

By curve-fitting of the creep test results to the biphasic theory of Mow et al. (1980), they reported aggregate moduli values for different zones of the disc with magnitudes ranging from 18.61 ± 3.02 kPa (in the anterior zone) to 74.93 ± 10.99 kPa (in the intermediate zone). The extreme permeability values reported were $(3.74 \pm 0.78) \times 10^{-15}\ m^4/Ns$ (in the intermediate zone) and $(8.07 \pm 1.55) \times 10^{-15}\ m^4/Ns$ (in the posterior zone).

Porcine discs were tested in confined compression by Wu et al. (2017). A similar procedure was used to remove 5 cylindrical samples from the discs, with a diameter of 5 mm and a

thickness of 1 mm. Sample's superior and inferior surfaces were also cur by means of a cryogenic microtome. The parameters were obtained by optimizing a FE model, allowing the identification of average values of aggregate modulus of 77 ± 40 kPa and permeability of $(8.8 \pm 3.8) \times 10^{-16}\ m^4/Ns$. In comparison to the results of Kuo et al. (2010), Wu et al. (2017) claims to observe more homogeneous compressibility moduli for the different zones of the material, attributing this difference to the young age of the pigs compared to the more advanced age of the human discs used for the other study.

1.3.4.5 Direct permeation of the temporomandibular disc

Tverje & Nyashin (2010) appears to be the only study to perform direct permeation tests on a TMJ disc. They studied the permeability of a porcine disc by preparing a cylindrical sample of 15mm diameter that had its upper and lower faces cut with a cryogenic microtome, obtaining a thickness of 0.5 mm.

They applied pressure to the system through a 1 m column of fluid for a period of six hours. Using the equation 1.26, they were able to calculate the hydraulic permeability of $5.86 \times 10^{-15}\ m^4/Ns$. Subsequent histological analyses reported the absence of destructive changes in the material after their testing procedure.

To understand and analyse the results provided for the material properties thanks to the various experiments, it is useful to understand the structure's properties is to investigate methods of observing it. The following section describes some of the imaging techniques used on TMJ discs.

1.3.4.6 Imaging techniques applied to the disc

Magnetic resonance imaging (MRI) is often performed over the entire TMJ in vivo to analyze different imaging protocols and equipment (Stehling et al., 2007; Whyte et al., 2021; Kopp et al., 2024), and to develop models to improve diagnoses (Li et al., 2024). Such images are capable of well representing the positioning of the disc within the joint, but do not provide details on tissue microstructure due to resolution limitations.

A specific TMJ disc analysis was performed in Benavides et al. (2009). They performed diffusion tensor imaging (DTI) on porcine TMJ discs. DTI is a modality of MRI capable of measuring water molecule diffusion inside of a tissue, through the assessment of their random translational motion (Brownian motion). By imposing magnetic field gradient pulses in multiple directions, it is possible to observe displacement distribution of water molecules inside each image voxel and calculate a diffusivity tensor capable of representing diffusion anisotropy within the tissue (Le Bihan et al., 2001).

Tissue diffusion anistotropy was measured for 10 porcine discs, indicating greater anisotropy and diffusivity values in posterior and anterior bands of the disc in comparison to its intermediate portion. The reported diffusivity values ranged from $0.96 \times 10^{-3} mm^2/s$ to $1.42 \times 10^{-3} mm^2/s$.

Scanning elecron miscroscopy (SEM) is an imaging method used for various purposes, consisting in bombarding a sample with an electron beam, generated and accelerated through objective lens towards the sample by an electron gun system. The high-energy electrons interact with the specimen and produce signals, such as secondary electrons, that depend on the surface topography and composition. The emitted electrons are captured by detectors and the processed results produce the images (Kaburagi & Hishiyama, 2016).

SEM images are capable of providing information about material surface topography, in the present context allowing the observation of the microstructure of the collagen network of the disc. Studies such as Beatty et al. (2001) and (Kang et al., 2006) used this method to identify damage to the collagen structure of the material after its submission to stresses. Other

articles analyze the orientation of the collagen fibers along the structure (Minarelli, 1997; Shi et al., 2013; Detamore et al., 2005) or explore the multilayer aspects of the material Juran et al. (2015). These studies allow the observation of the orientation and structure of the fiber network, described in previous sections.

The classical SEM method requires that the observed material be conductive, ensuring proper alignment of the electron beam that generates the image. When working with soft biological tissues, it is common practice to coat the material with a conductive metallic layer. In the case of disc studies, all specimens were coated with a thin layer of gold or gold-palladium alloy to facilitate image acquisition (Beatty et al., 2001; Kang et al., 2006; Minarelli, 1997; Shi et al., 2013; Detamore et al., 2005)

Another technique also employed on the TMJ disc was Optical Coherence Tomography (OCT). It is a non-invasive imaging technique that consists on emitting infrared light that penetrates the surface of the observed sample and is reflected. The intensity of the reflected light and the delay in its arrival at a sensor allow the production of a two-dimensional image across the thickness of the analyzed material (Psomadakis et al., 2021; Huang et al., 1991). This technique is widely used in ophthalmology in both clinical and research settings, allowing in vivo analysis of the cornea (Psomadakis et al., 2021). It is also applied to other biological tissues such as skin and nails, allowing the visualization of layers within the material (Psomadakis et al., 2021). In Mărcăuteanu et al. (2010), dried human discs were imaged through OCT, and the result is shown in Figure 1.21.

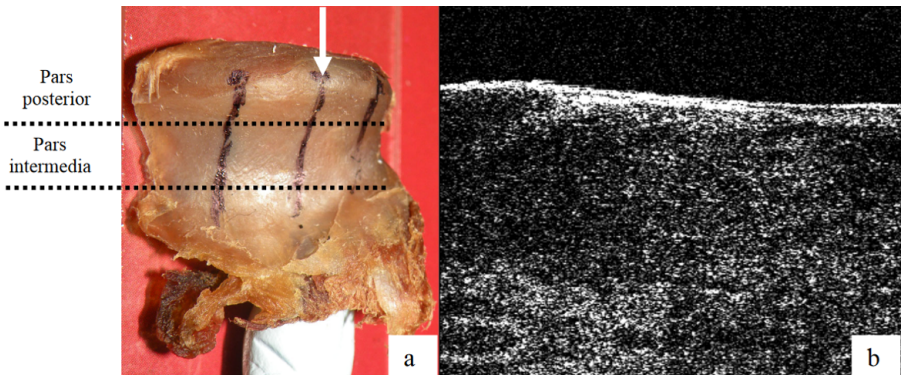

Figure 1.21: OCT performed on dehydrated human discs from Mărcăuteanu et al. (2010). Figure (a) shows a superior view of a disc, with the sagittal plane perpendicular to the image and indicated by the black marking painted on the sample. The white arrow in (a) shows the imaged zone in (b), where a sagittal view is represented. In Figure (b), the upper black region corresponds to air, while the tissue structure appears in white.

Figure 1.21b shows evidence of a thin outer layer (in white) covering the outermost portion of the disc, which may be a good indication of material inhomogeneity that has not yet been addressed in poromechanical studies.

1.4 Thesis objectives and strategy

Throughout this chapter, the main elements that constitute cartilages and how their structure interacts with the interstitial fluid were described. The nature of these interactions provides soft biological materials of this type the capacity to undergo large deformations, exhibiting a nonlinear, viscous, anisotropic, heterogeneous and multiphasic mechanical response. Some theoretical and experimental approaches for characterizing these behaviors were described, introducing some of the tools that will be used in this work for studying the poromechanics of the temporomandibular joint disc.

The high incidence of TMJ dysfunctions and the difficulty in finding suitable substitutes for the disc draws attention to the scarcity of studies that explore the properties of the TMJ disc with agreed-upon or consistent findings. Studies such as Wright et al. (2013) and Wu et al. (2019) highlight the interest in modeling tissue mechanics in interaction with diffusive properties of solutes inside the disc, due to their relation to tissue viability. A diversity of constitutive laws attributed to the material was observed, with some of them being poromechanic and taking into account fluid interaction with the solid structure of the tissue.

Chapter 1 showed the diversity of stiffness parameters attributed to studies of the disc, ranging from 0.05 MPa (Fazaeli et al., 2019) to 44.1 MPa (Tanaka et al., 2001) in compression and values ranging from 13.5 MPa (Matuska et al., 2016) to 140 MPa (Li et al., 2021) in anteroposterior tension. Permeability in turn had average values reported ranging from $9.96 \times 10^{-12} m^4/Ns$ (Ortún-Terrazas et al., 2021) to $2.41 \times 10^{-14} m^4/Ns$ (Kim et al., 2003), with other studies reporting it to be $3.24 \times 10^{-17} m^4/Ns$ (Li et al., 2021), $3.74 \times 10^{-15} m^4/Ns$ (Kuo et al., 2010), $8.8 \times 10^{-16} m^4/Ns$ (Wu et al., 2017) and $5.86 \times 10^{-15} m^4/Ns$ (Tverje & Nyashin, 2010). As a common issue in the biomechanics field, tests were performed in specimens of different origins and conservation history, with distinct testing methods and experimental conditions. This implies the assumption of different boundary conditions and theoretical models adaptations to extract results from experimental data. Table 1.1 groups experimentally measured permeability of different studies in literature, including regional variations over the specimens.

Reference	Type	Average	Permeability k $[m^4/Ns]$				
			Central	Anterior	Posterior	Lateral	Medial
a	pig	$(3.24 \pm 2.29) \times 10^{-17}$	$(32.4 \pm 22.9) \times 10^{-18}$	–	–	–	–
b	pig	$(8.8 \pm 3.7) \times 10^{-16}$	$(8.4 \pm 3.8) \times 10^{-16}$	$(8.7 \pm 3.4) \times 10^{-16}$	$(9.6 \pm 3.8) \times 10^{-16}$	$(6.7 \pm 3.8) \times 10^{-16}$	$(10.5 \pm 3.4) \times 10^{-16}$
c	pig	2.41×10^{-14}	$(2.28 \pm 0.98) \times 10^{-14}$	$(2.67 \pm 0.83) \times 10^{-14}$	$(2.64 \pm 0.63) \times 10^{-14}$	$(2.93 \pm 1.40) \times 10^{-14}$	$(1.54 \pm 0.70) \times 10^{-14}$
d	pig	5.86×10^{-15}	5.86×10^{-15}	–	–	–	–
e	human	5.66×10^{-15}	$(3.67 \pm 0.67) \times 10^{-15}$	$(8.95 \pm 1.17) \times 10^{-15}$	$(8.07 \pm 1.55) \times 10^{-15}$	$(3.74 \pm 0.78) \times 10^{-15}$	$(3.86 \pm 0.70) \times 10^{-15}$

Table 1.1: Permeability values from different experimental studies, with regional variations. a)Li et al. (2021), b)Wu et al. (2017), c) Kim et al. (2003), d)Tverje & Nyashin (2010), e)Kuo et al. (2010).

The aim of this study is to characterize the behavior of the TMJ disc through a poromechanical approach. This thesis follows on from a main study of the BIO2MS team of the LEM3 laboratory, reported in Tappert (2020), which analyzed the mechanics of discs using a monophasic approach. The database used in the previous work, as well as part of the experimental apparatus and some remaining samples, were leveraged and will be described throughout this thesis. New samples of TMJ discs were collected during the thesis development specifically for this purpose, so that multiple tests would be performed in each one of them.

The experimental results will be used as a basis for model calibration and validation. Chapter 2 starts by performing spherical compression experiments on porcine TMJ samples. A monophasic characterization method first developed in Tappert (2020), underwent some evolutions shown here, and was used for the monophasic characterization of the discs tested here. The experimental results were then compared with an axisymmetric FE model that simulated the disc by defining it with biphasic parameters from the literature. Through inverse characterization method based on the optimization of the simulations, optimized parameters that better fitted the experimental curves were estimated.

Chapter 3 describes devices for conducting biphasic characterization tests of confined compression and direct permeation that were developed and manufactured during the course of this thesis. The experiments and data processing algorithms will be described, allowing to obtain preliminary permeability and solid phase parameter values. During the preparation of the cylindrical samples for the confined compression test, the samples were cut and their deformation

immediately after this process was filmed, allowing the application of an image correlation analysis procedure. MRI images of all samples were captured before the test campaign and after the preparation and cutting of the samples, fostering discussions about the internal stresses acting on the material. Optical correlation tomography (OCT) and SEM images were performed to observe the ECM structure. Finally, tensile tests were also conducted and the obtained results will be presented.

The general conclusions will be provided at the end, addressing the observations regarding the disc's structure and mechanics, the contributions of this work to advancing the understanding of disc poromechanics, and the future perspectives of the project.

Chapter 2

Spherical compression characterization and poromechanical coupling of the temporomandibular joint disc

2.1 Experimental testing on temporomandibular discs

Initially, spherical compression tests were conducted on porcine TMJ discs. The objective was to perform non-destructive tests in multiple zones of the samples, allowing the preservation of internal stresses in the material and accessing the compression force/displacement relationship for different compressor tool radii and loading frequencies.

Tappert (2020) performed spherical compression tests on TMJ discs, which were imaged using optical 3D scans for dimensional measurements and disc curvature estimation. The curvature analysis confirmed that the selected radii of the compression spheres (0.875 mm, 1.75 mm, and 3 mm) would not reach the edges of the samples. The same compression sphere diameters used in the work of Tappert (2020) were used in the current thesis to characterize other TMJ discs, in order o enrich the BIO2MS team's database and current literature.

2.1.1 Sample harvesting

A total of four pig heads were collected during the course of the thesis, from which eight temporomandibular discs were obtained for use in the study's testing campaigns.

The first head was supplied by a local slaughterhouse (la Maison Vagner, Marange Zondrange, France), from a hybrid large white - landrace pietran breed. Because of the slaughterhouse's protocols, information on the exact age, sex and weight of the pig could not have been be provided accurately.

The other three heads were obtained in collaboration with the IHU Strasbourg (University Hospital Institute – Institute of Image-Guided Surgery) and with the ICube laboratory, both located in Strasbourg, France. The heads were collected at the IHU after the pigs had been slaughtered, having previously been used in other studies that did not involve the TMJ. The specimens were obtained from healthy animals with body weight of around 44 kg and an age of 6 months at the time of harvesting.

For each head, scissors, a knife and a scalpel were used for dissection. Initially, the masseter and pterygoid muscles were cut, freeing the movement of the mandible and allowing it to open. Tendons, ligaments and other structures that held the mandible were cut and allowed it to be separated from the skull. The discs were identified after the mandible was separated, remaining attached either to the glenoid fossa or the condylar process, and were then carefully dissected and removed. The objective was to preserve the anatomical structures surrounding the disc, including the retrodiscal tissue and pterygoid muscle, allowing the sample to be manipulated without direct contact with the disc itself. Mantaining the surrounding tissues also facilitates the distinction of the anatomical regions on the tissue.

An example of disc is shown in Figure 2.1.

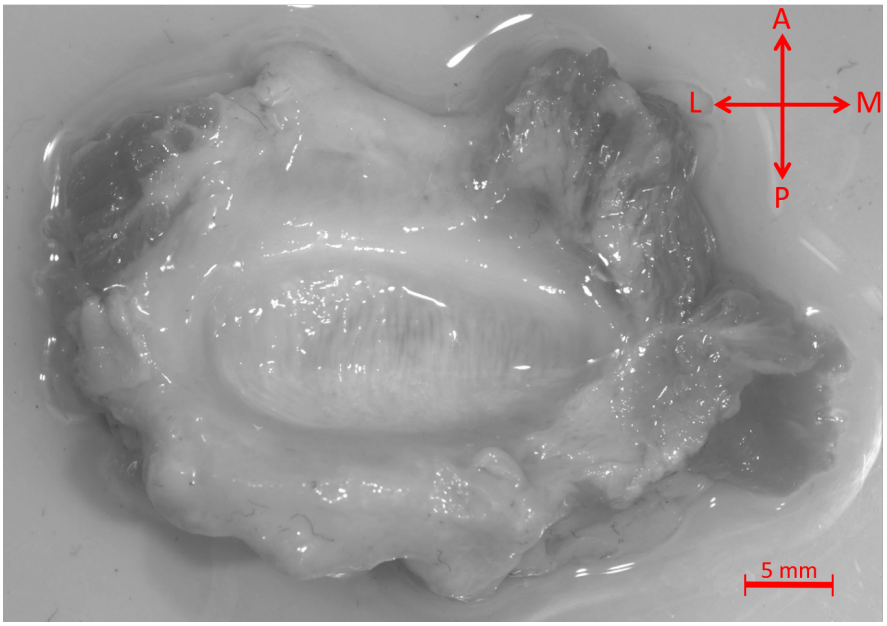

Figure 2.1: harvested right TMJ disc sample with surrounding tissues. Sample 230524-Head1-Right.

The Figure 2.1 shows the lower face of one of the discs, which is physiologically in contact with the condyle. The central part of the sample, oval in shape, is where the disc itself is located. The surrounding tissues were kept in the sample, allowing the specimen to be manipulated without direct contact with the disc.

The anterior portion of the sample (A) corresponds to the insertion portion with the lateral pterygoid muscle. In its posterior portion (P), in the lowest part of the figure, is located part of the retrodiscal tissue that was sectioned. The fibrous structure of the material can be seen with the naked eye to tend to orient itself along the anteroposterior axis, which aligns with the direction of muscle traction.

Each sample will be named by taking into account the harvesting date, to which pig head it corresponds to and the anatomical side in the form YYMMDD-HeadX-Side.

The samples were stored in airtight containers submerged in saline solution (9g NaCl/L) and then kept in a refrigerator at 4°C. For the six discs collected at the ICube laboratory, MRI was performed the following day of disc harvesting, with the help of Dr. Chrystelle Po and Dr. Aurore de Cauwer. To do so, the discs were positioned inside a container compatible with MRI device chamber dimensions, shown in Figure 2.2.

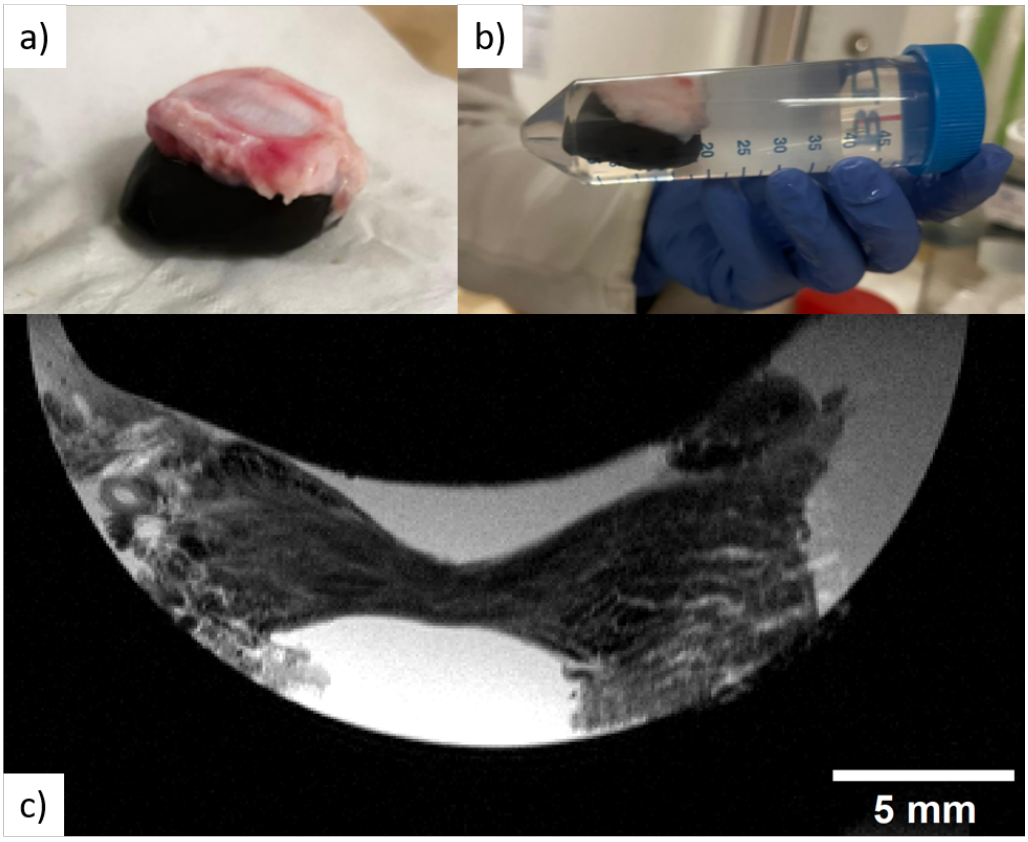

Figure 2.2: a) Freshly harvested porcine TMJ disc over a 3D printed condyle; b) Disc and condyle inside the saline solution filled tube to be introduced in the MRI machine. c) Sagittal cut of disc inside MRI.

An example of result is shown in Figure 2.2c. MRI acquisitions were performed using a 7.05 T Bruker BioSpin system (Biospec model) shown in Figure 2.3, with a T2-weighted TurboRARE sequence (TR = 3000 ms, TE = 14.1 ms, slice thickness = 0.5 mm, spacing between slices = 0.5 mm, 4 averages).



Figure 2.3: MRI device at the ICube laboratory used for imaging fresh TMJ disc samples (7 Tesla Bruker Biospec 70/30 USR).

The discs were then transported to Metz, France and frozen at -20°C. For thawing, the

containers were kept in a refrigerator at 4°C overnight before testing.

2.1.2 Test protocol

The spherical compression tests were conducted by seeking to reproduce physiological conditions of sample hydration, temperature and osmolarity of the surrounding fluid. The complete setup used for the test is shown in Figure 2.4.

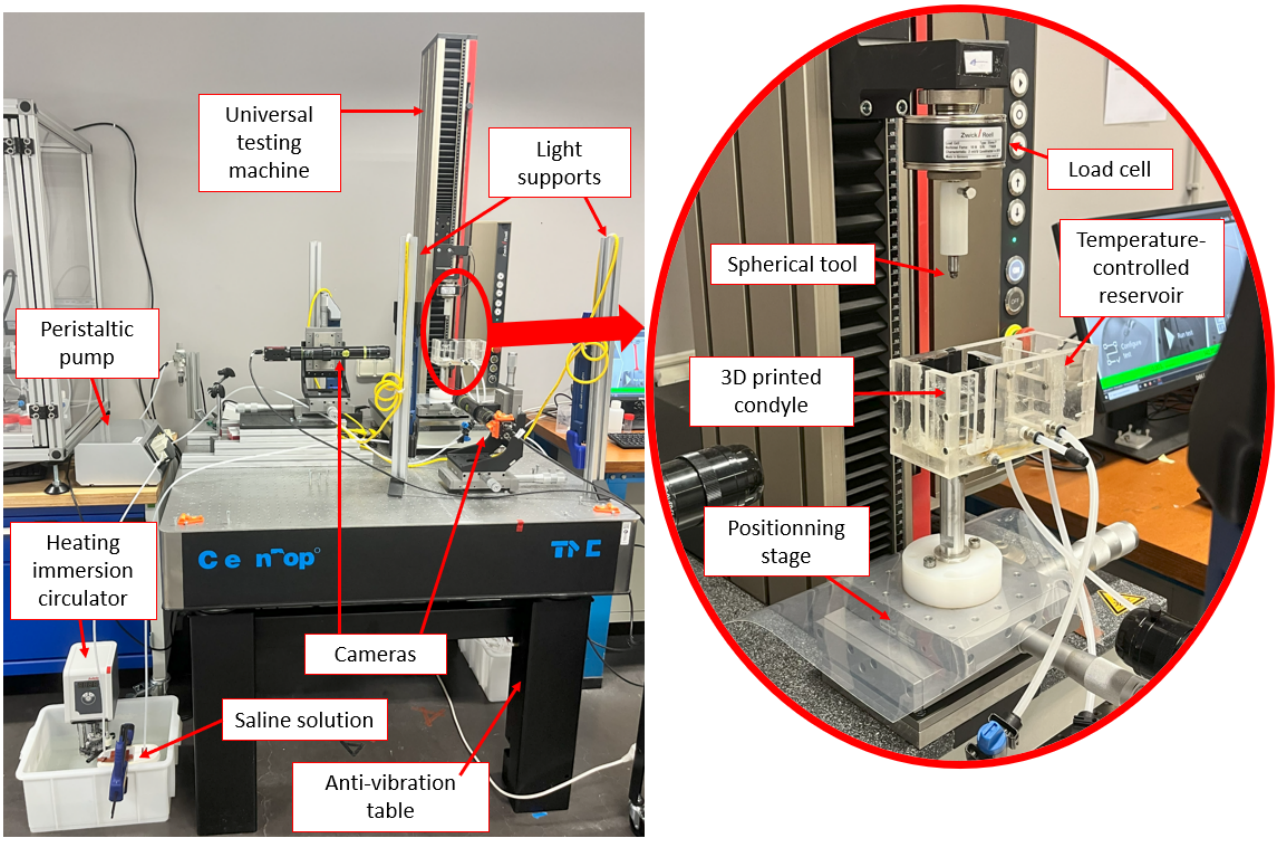

Figure 2.4: Experimental setup used for spherical compression tests.

The samples were placed inside a chamber filled with saline solution (9g NaCl/L). The fluid was heated inside another external reservoir by means of a heating immersion circulator and kept in circulation through a peristaltic pump. In this setup, the fluid inside the chamber was constantly renewed through inlet and outlet tubing, while the temperature was actively regulated to maintain stable physiological conditions close to 37°C. The fluid height inside the chamber was adjusted to keep the discs partially submerged, constantly hydrated but with their upper surface free so that the compressing spheres were not submerged in the process.

A universal testing machine (Zwicki, Zwick Roell, Ulm, Germany) was used in conjunction with a 10N loadcell (Xforce P, accuracy class 1 above 0.04 N and 0.5 above 0.2 N). The steel spheres were attached to the loadcell and positioned over the sample.

The disc was positioned over a 3D printed condyle, with geometry obtained from 3D scans of porcine condyles in Tappert (2020). The scanned condyle does not correspond exactly to the same pig as the tested samples, however it allowed obtaining a geometry close to the physiological shape, with a curvature that allowed the accommodation of the discs. The peripheral tissue zone around the disc was carefully glued to the condyles using cyanoacrylate. The system composed of sample holder and hydration chamber was positioned over a micrometric XY positioning stage, which allowed the adjustment of the position of the whole system under the testing machine.

The entire system described above was kept on an anti-vibration table equipped with Gimbal Piston Air Isolators, reducing the influence of external mechanical disturbances on the load cell reading.

The loading protocol was previously designed in the work of Tappert (2020) and used for the hyperelastic characterization of porcine discs. This experimental protocol was idealized to allow exploring various aspects of the material, such as hyperelastic and viscous effects in spherical compression. In order to enrich the team's database, the same protocols were applied in the samples of the present work. The isolation table, the XY positioning stage, the lighting and camera system are new additions to the setup compared to its last use in the work of Tappert (2020).

Before the tests began, the heating immersion circulator was activated and the fluid was put into circulation. The temperature that reached the sample reservoir was measured using a thermometer and, after a period of around one hour, the desired 37°C was reached and kept stable. The disc, glued to the condyle support, was then inserted into the system and the spherical tool was positioned over the zone to be tested. Figure 2.5 shows a disc positionned on the testing setup.

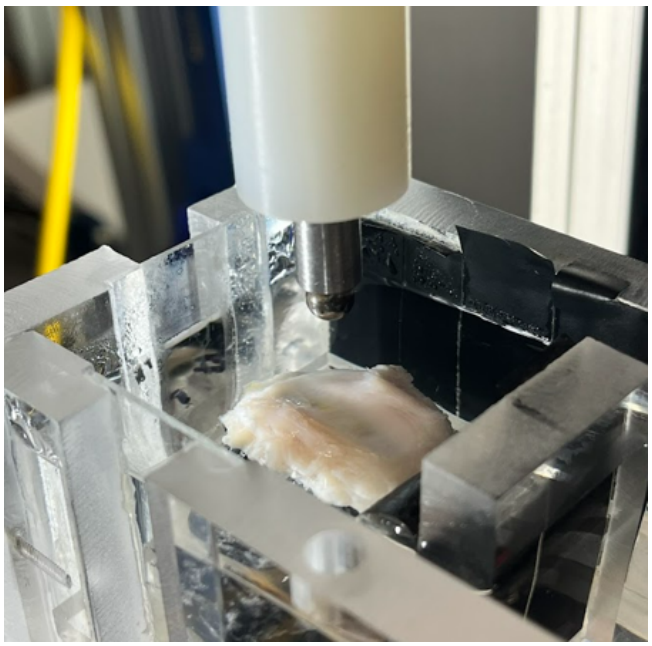

Figure 2.5: Disc positionned over 3D printed condyle just before testing. The disc, glued to the condyle, is partially submerged in fluid and the 3 mm radius compressing sphere is positioned over the sample.

The loading frequencies established for the tests were 0.01 Hz, 0.1 Hz and 1.0 Hz. The lowest frequency aims to represent quasi-static loading conditions, such as clenching contexts. The other higher frequencies were established in order to remain consistent with the human chewing frequency, physiologically between 0.1 and 2.0 Hz (Druzinsky, 1993). Due to the limitations of universal machine used in the tests, the actual frequencies applied during the tests were approximately 0.01 Hz, 0.095 Hz, and 0.625 Hz. A discussion about the analysis of the viable frequency possibilities for the compression device may be found in Tappert (2020).

The protocol consists of a preconditioning phase, followed by a cyclic test and a final relaxation phase. The number of cycles for each of the frequencies was chosen in order to keep a similar load application time span between all tests and is shown in Figure 2.6.

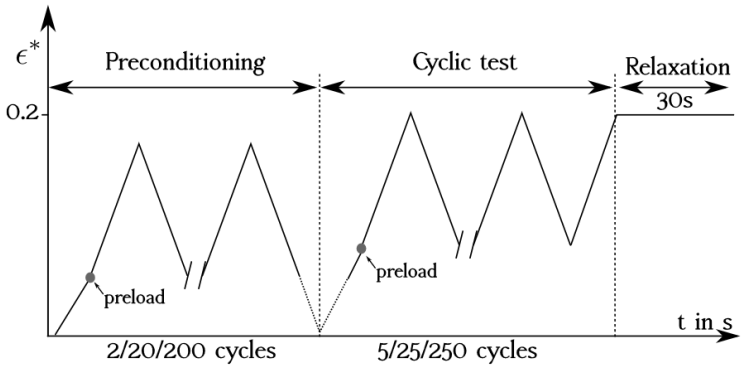

Figure 2.6: Experiemental protocol developed in Tappert (2020) for spherical compression tests. The preload value is related to sphere radius (table 2.1) and number of cycles depends on loading frequency (0.01 Hz/0.1 Hz/1 Hz).

Steel spheres with radii of 3mm, 1.75mm and 0.875mm were used. A same measured force can represent different stresses on the material depending on the radius of the sphere. In order to impose equivalent prestresses at the beginning of each test, it was necessary to define the preload value to be applied to each of the spheres. The same can be said for the imposed displacement, which was defined to correspond to around 20% of strain on the specimens. The theory to support such assumptions and the calculations to define the imposed force and displacement are described in Tappert (2020), and the results are shown in table 2.1.

Tool radius R [mm]	Preload force [N]	Maximum displacement [mm]
0.875	0.0136	0.1115
1.750	0.0544	0.2071
3.000	0.1600	0.2890

Table 2.1: Preload forces and maximum displacements for multiple compression tool radii. The calculations to obtain the force values are described in Tappert (2020) in order to guarantee an equivalent stress state with different sphere radii.

Having defined the preload force and maximum displacement for each of the tests, the protocol shown in Figure 2.6 was developed. The preconditioning phase consisted of low-speed compression until the preload force was reached. Once reached, preconditioning cycles were performed at a given frequency, with displacement and number of repetitions consistent with table 2.1. The sphere then went back to the initial starting position and begins the cyclic phase, where the preload is reached in low speed to ensure a consistent initial stress between tests. The cyclic phase of the test begins and is followed by 30 second relaxation period at the end.

All system components are subject to deformation when compressed, even when they are more rigid than the samples. A deformation correction procedure based on the stiffness of the other components was performed, and is shown in Appendix A.

For each of the discs, three zones were tested: lateral, intermediate and medial. A waiting period of at least 40 minutes was respected between tests on a same zone, allowing the tissue to relax and return to its original configuration before being loaded again. With the three loading frequency settings, three spheres and three test zones, a total of 27 spherical compression tests were performed on each of the samples. For each disc, two days of testing were required and the samples were kept refrigerated at 4°C overnight in saline solution glued to the support in order to preserve their positioning between tests.

The advantage of conducting the tests using the same protocol as Tappert (2020) is to enrich the team's database, which previously contained results for six pig discs. This will also allow

the current samples, which are fresher than the older ones used in the previous work, to be used in subsequent characterization tests, allowing multiple tests to be performed on the same sample.

2.2 Spherical compression experimental results

Once the described experimental procedures were performed, force and displacement data for all eight discs were obtained, with a total of 216 spherical compression experiments performed. Figure 2.7 shows the experimental results for the central zone of a representative result, at a frequency of 0.1Hz, showing the effect of varying the sphere radius on the mechanical response.

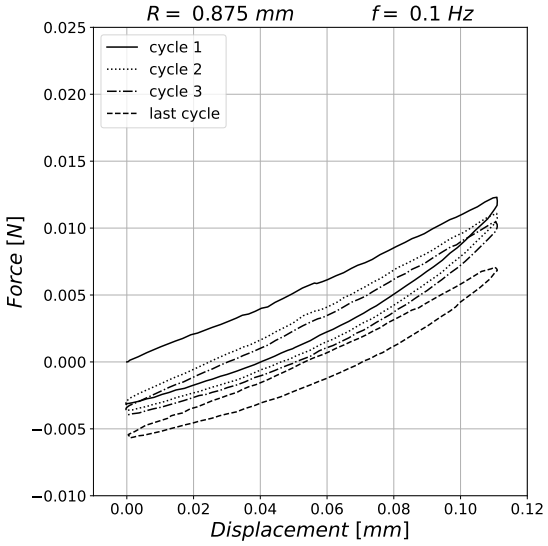

(a)

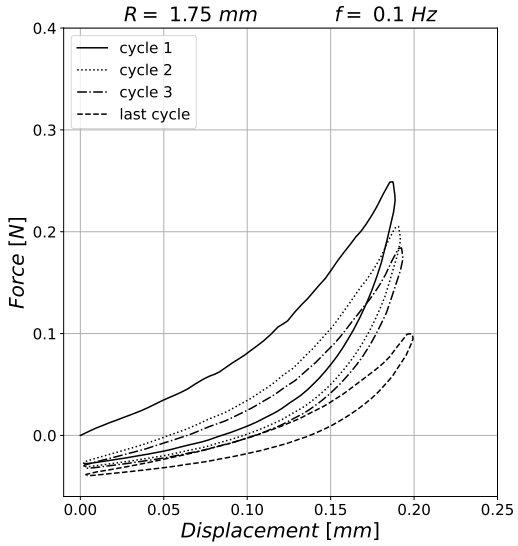

(b)

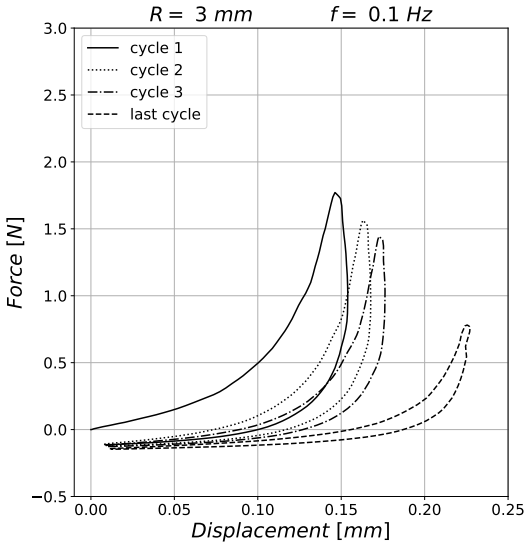

(c)

Figure 2.7: Spherical compression results for central zone of one disc, showing the variation of sphere radius for a loading frequency of 0.1 Hz. Sample 240311-Head1-Right.

The graphs in Figure 2.7 were developed to allow the analysis of the mechanical response

to the different cycles applied. Because of this, Figure 2.7 is limited to showing what occurs in the cyclic phase of the protocol described in Figure 2.6. The beginning of the curves was defined from the moment in which the preload force corresponding to each radius (see table 2.1) was reached.

Since the imposed displacement has a linear evolution at all times during the test, the profile of the curves indicates the nonlinearity of the material. The concavity of the curves, being directed upwards, indicates a tendency for the material to become more rigid as the sphere compressed it.

In each cycle, between the loading and unloading phases, there is a decay in the observed forces. This hysteresis highlights the viscous nature of the material, which causes its mechanical response to depend on the applied load history. One of the possible explanations for this is fluid movement. Once compressed, part of the fluid is expelled from the region, causing its stiffness to be lower during the phase in which the sphere returns to its initial position. This statement is corroborated by the biphasic theory (see discussion around equation 1.11), given the nature of this material.

However, it is appropriate to be cautious when postulating such hypotheses, as viscosity is not an exclusive characteristic of biphasic materials. This behavior is also observed in monophasic materials, for instance rubber, in which the molecular interactions of the structure also generate viscous effects (Kumar & Lopez-Pamies, 2016). This questions fall into a major point of discussion in the poromechanics field, given the difficulty of experimentally dissociating the viscous contribution of the multiple system components when working with biological tissues. An interesting future possibility is to apply these characterization methods to tissues from which water has been removed, for example through freeze-drying, and analyze the observed mechanics. This has not yet been performed on TMJ disc tissues, and it is not guaranteed that the freeze-drying process can truly assure the observation of the intrinsic properties of the solid phase, since this context is not physiological for the original material and the drying process might damage the solid phase affecting its behavior.

The first cycle is the one in which the greatest hysteresis was observed. It is also the cycle that presents the greatest maximum force, which decreases as more cycles are performed. At the end of each of the compression cycles, the maximum measured force decreases, induced by such viscous effects. Since the graph was constructed in order to start once the preload force of the first cycle was reached, the subsequent cycles start with negative force values because of the imposed shift of the curve, thus representing the decay of the efforts involved in each repeated cycle (and not necessarily meaning that the sample is submitted to traction). This is consistent with previous works from Tappert (2020) and expected when working with soft biological tissues.

Figure 2.8 shows the maximum forces for the first loading cycle for all tests performed.

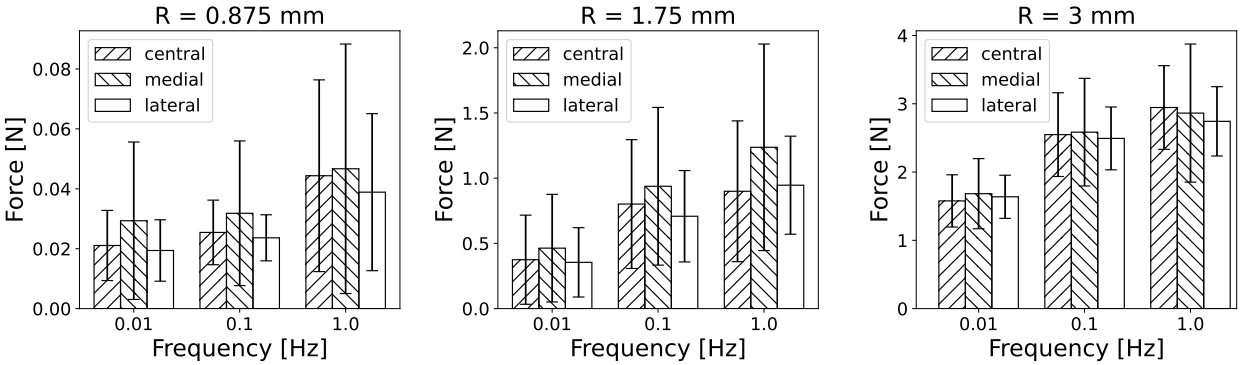

Figure 2.8: Maximum forces measured for the first loading phase after pre-conditioning cycles. Average forces ± standard deviation (n=8) for different disc zones, loading frequencies and sphere radius.

The order of magnitude of the forces measured for different sphere radii is consistent with that reported in Tappert (2020). As also shown there, it is not possible to establish a clear trend of variation among the distinct disc zones, as standard deviations are high. This agrees with the findings of Kuo et al. (2010), who did not detect regional differences in GAG composition, which are linked to fluid retention in each zone and, consequently, to its resistance to compression. Nevertheless, as noted by Tappert (2020), the spheres with radii R = 0.875 mm and R = 1.75 mm exhibited slightly higher force values in the medial zone. Similarly, Fazaeli et al. (2016) reported a higher compressibility modulus for this medial region, in line with this trend, although for the sphere with R = 3 mm the difference relative to other zones was less pronounced. In fact, the experiments performed with R = 3 mm showed proportionally smaller standard deviations, which can be explained by the larger contact area of this sphere that compresses a broader volume of material and is thus less sensitive to regional variations in behavior. Actually, averaging mechanical responses over a wider region, while also compressing deeper tissue zones led to less variation on the mechanical response (see Table 2.1).

The increase in the radius of the spheres (Figure 2.9) is directly proportional to the measured forces. Larger spheres compress a broader and deeper portion of the material, representing greater resistance. Multiple tests in which the spheres vary in size, act on a more or less local scale, allowing different zones of the specimen to be stressed (Tappert, 2020).

Let us now observe representative results for the effect of frequency variation for a sphere of the same radius acting on the central zone of a same sample, in Figure 2.9.

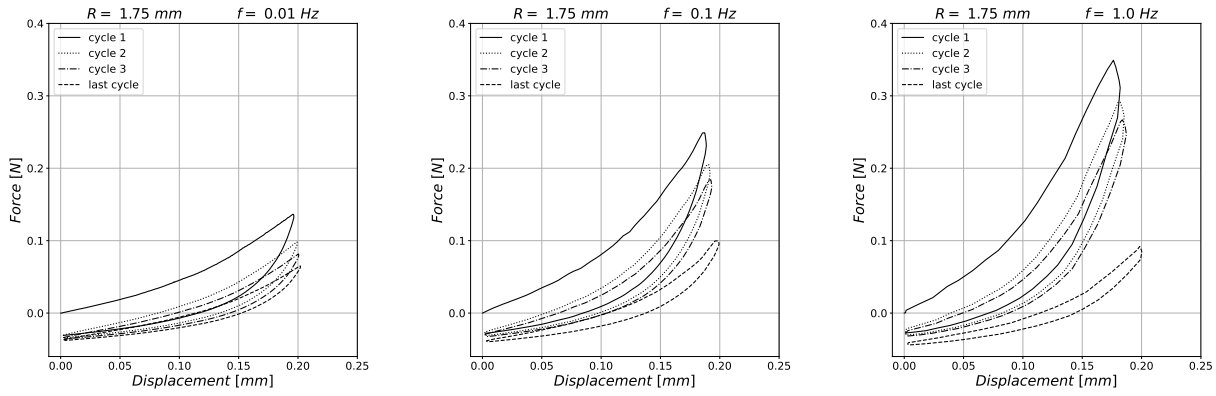

(a) (b) (c)

Figure 2.9: Spherical compression results for central zone of one disc, with different loading frequencies and sphere radius equal to 1.75 mm. Sample 240311-Head1-Right.

Figures 2.9 and 2.8 highlight the influence of compression velocity. As the frequency of cycles increases, the involved forces also increase. A higher compression speed requires the fluid to move more quickly out of the tested zone. Since this displacement is not instantaneous, the increased frequency means that the fluid does not have as much time to move and dissipate, resulting in greater pressure in the material's pores and a mechanical response with greater stiffness.

Regardless of the frequency, the last cycles tend to approach a force of around 0.1 N in Figure 2.9. Since the radius of the sphere is the same, the same volume of tissue is compressed at the end of the cycles. Assuming a decrease in the volumetric fraction of fluid in the region towards the end of the test, the solid phase of the material has a greater contribution to its stiffness.

2.3 Monophasic hyperelastic characterization

2.3.1 Introduction

Part of my doctoral research focused on further developing a method for the hyperelastic monophasic characterization of biological tissues based on spherical compression, initially developed in the work of Tappert (2020). The principle of the method will be described here, followed by some recent developments I worked on, that are part of a yet unpublished article.

The compression of a material by a sphere generates a state of nonlinear stress and strain due to the geometry of the compressing sphere. As the sphere penetrates the sample, the contact radius (a in Figure 1.7) evolves nonlinearly in relation to the imposed displacement (d in Figure 1.7). In contexts like this, it is necessary to adopt models that translate the measured force and displacement into stress and strain.

The Hertz model (see equation 1.27) relates the force measured at indentation to the parameters of a linearly elastic material (Young's modulus E and Poisson's ratio ν) with the sphere penetration depth δ, assumed equivalent to the displacement imposed by the machine ($d = \delta$). The compressed sample is assumed to have linearly elastic behavior and infinite thickness. The contact radius is estimated from the equation 1.28 proposed in Lin et al. (2009) and the effective stress σ^* and strain ε^*, that is, equivalent to an uniaxial compression context, may be approximated by equations 2.1 and 2.2.

$$\sigma^* = \frac{F(t)}{\pi a^2} \tag{2.1}$$

$$\varepsilon^* = 0.2\frac{a}{R} \tag{2.2}$$

Once the effective stress σ^* and strain ε^* are known, it is possible to perform a hyperelastic fitting and estimate the material parameters by choosing a strain energy density function that best describes material behavior (see section 1.1.2.1). The term effective here refers to the equivalent monophasic stress introduced in this section (σ^*) and should not be confused with the equivalent stress denoted in the poromechanics framework (σ_e).

Some studies in the literature address the spherical compression of hyperelastic materials, but consider that the compressed sample is either infinite or very large in size relative to the compressing sphere (Guo et al., 2020a; Du et al., 2023; McCreery et al., 2023; Moghaddam et al., 2020). This is disadvantageous when dealing with the compression of samples that are thin, such as skin or the TMJ disc, which do not satisfy the infinite halfspace condition and can also detach from the base during the compression process, increasing the problem's complexity.

Given the lack of models capable of representing the nonlinearity of thin unbound layers subjected to large deformations in spherical compression, the model proposed here relied on numerical experimentation to define stress-strain relationships for samples of different thicknesses. Obtaining these two quantities allows the characterization of materials as if they had been subjected to uniaxial compression, without interference of the experimental disadvantages of these types of tests for soft biological tissues (such as sample cutting, for example). The model will ultimately be applied to experiments performed on TMJ discs, to be compared with the results of the application of its first version in Tappert (2020). Such a characterization is useful for a first approach to the monophasic definition of the material, to be used for later as input for more sophisticated inverse approaches, such as FE analysis.

2.3.2 Materials and Methods

2.3.2.1 Finite Element Model

It was necessary to establish a relationship between the contact radius a and the displacement d through FE analyses for samples of different thicknesses. Thus, equation 2.1 would allow the calculation of stress based on output data from simulations and, in the future, experiments. An axisymmetric 2D finite element model was developed in the commercial software Abaqus® 2022, and is illustrated in Figure 2.10

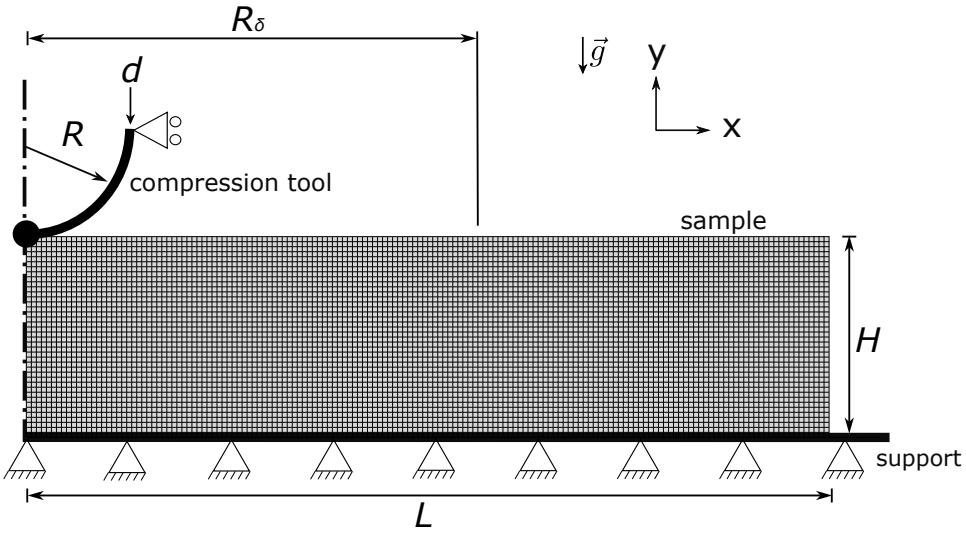

Figure 2.10: Geometry, mesh and boundary conditions of the axisymmetric FE model of a disc placed in between a rigid support and a rigid spherical compression tool. The • represents the point of tie-constraint placement between the tip of the compression tool and one node of the mesh. Adapted from Tappert (2020).

The compression tool and support were considered rigid due to their high properties compared to the tested material, with frictionless interactions due to the high water volume. A sample length of $L = 25R$ was chosen, the sphere radius $R = 1mm$ and multiple thicknesses H were adopted so that the dimensionless thickness ratios $h = H/R$ were defined in the multiple models as $h = 0.5$, 0.75, 1.0, 1.5, 2.0, 5.0, 10.0 and 20.0.

I conducted a mesh study, which was finer when compared to the previous model to allow a more refined and consistent measurement of the contact radius a throughout the simulation. The model was meshed with CAX4RH linear quadrilateral elements (4-node bilinear axisymmetric quadrilateral, hybrid, constant pressure, reduced integration, hourglass control), the number of which varied according to the sample thickness, ranging from 125,000 for $h = 0.5$ to 5,000,000 for $h = 20$, with an element size of $0.01R$.

To define the material, a nonlinear neo-Hookean behavior based on the strain energy density function 2.3 was adopted.

$$W = \frac{\mu}{2}(I_1 - 3) + \frac{\kappa}{2}(J - 1)^2 \tag{2.3}$$

where the two material constants are the shear (μ) and bulk (κ) moduli, defined by the equation 2.4.

$$\mu = \frac{E}{2(1+\nu)} \qquad \text{and} \qquad K = \frac{E}{3(1-2\nu)} \tag{2.4}$$

The choice of initial parameters here was based on that adopted in Tappert (2020), where a Young's modulus $E = 1$ MPa was arbitrarily chosen, considering that the range of Young's modulus for biological tissues varies between kPa and MPa. The relationship between contact radius a and sphere displacement d is independent of the Young's modulus, which only dictates the measured reaction force but does not impact the shape assumed by the sample when compressed, which is related to the geometry of the sphere (Wu et al., 2016). Due to the high hydration rate, the Poisson's ratio was set to $\nu = 0.499$, resulting in $\mu = 0.334\,\text{MPa}$ and $\kappa = 166.667\,\text{MPa}$. The high water content in the material led to adopt a density equal to water's: $\rho_0 = 1 \times 10^3\,\text{kg/m}^3$, as collagen's density is close to $1.3 \times 10^3\,\text{kg/m}^3$ (Kanungo & Gibson, 2009).

The simulation was performed in two consecutive steps, considering the large strains domain. In the first step, gravity was applied, allowing the entire structure to compress under its own weight. The compression tool was connected to the sample by a tie constraint in the initial step (black dot in Figure 2.10), which ensured that it followed the initial displacement of the structure. In the second step, the compression tool's displacement was controlled up to $d_{max}/R = 0.375$, corresponding to 75% of the thinner sample's thickness. The applied boundary conditions are illustrated in Figure 2.10.

2.3.2.2 Contact radius analysis

To identify the stress based on the output of the simulations and experiments, it was necessary to define the relationship between the imposed displacement d and the contact radius a. The contact pressure field output (CPRESS in Abaqus) was used to detect the contact between sphere and sample in the simulations, and contact was considered established when a pressure of 0.01 MPa was reached (1% of the material's Young's modulus). To calculate the contact radius, the contact pressure of a node with coordinate x_1, where the pressure exceeds the contact threshold, and the node with coordinate x_2, adjacent to it and not yet in contact with the sphere, were measured for each increment. The contact radius a was calculated using the equation 2.5.

$$a = \frac{(0.01 - p_1)(x_2 - x_1)}{p_2 - p_1} + x_1 \tag{2.5}$$

where p_1 and p_2 are contact pressures in the nodes of coordinate x_1 and x_2. Tappert (2020) observed from these measurements that the dimensionless contact radius a/R can be defined as

$$\frac{a}{R} = \beta \left(\frac{d}{R}\right)^m \tag{2.6}$$

where β and m are fitting parameters. For each of the different thickness simulations, the values of β and m are different, and were in turn defined as

$$\beta = c_0 + c_1 \times h + c_2 \times (h + c_3)^{c_4} \tag{2.7}$$

$$m = k_0 + k_1 \times h + k_2 \times (h + k_3)^{k_4} \tag{2.8}$$

where c_0, c_1, c_2, c_3,c_4, k_0, k_1, k_2, k_3 and k_4 are fitting parameters. Once known, it is possible to predict β and m for different sample thickness ratios, and consequently define the relationship between contact radius and imposed displacement based exclusively on sample thickness and simulation/experiments outputs.

2.3.2.3 Other analysed aspects

The penetration depth δ (see Figure 1.7) is classically used in spherical compression models as a metric to be related to the contact radius, as in equation 1.28 for example (Lin et al., 2009). It is possible to imagine that, experimentally, measuring the distance between the surface of the sample and the tip of the compression sphere in biological tissue is not straightforward. To use δ, it is necessary to understand how it relates to the displacement imposed by the machine or to the simulated sphere (d/R). Tappert (2020) highlighted that the spherical compression of thin layers of materials, when unbound from the lower support, detach from the base during compression, implying that $d/R \neq \delta/R$ and that δ/R assumes a different value if measured from

different distances from the axis of symmetry. This distance is referred in Figure 1.7 as R_δ, and δ/R is measured from the distance from the tip of the sphere to the surface of the sample u_y^δ. In my work, I analyzed the relationship between the classically used δ/R with the imposed displacement d/R and the contact radius a/R, verifying the range of equivalence between the two metrics and discussing the real usefulness of using δ/R in the analyses.

The sensitivity study of the model was also extended to other aspects of its definition. Simulations with densities ρ = 0.01, 0.5, 1, 2, and 10 times water's density (ρ) were also performed. The effect of sample length (L/R) variation was also studied, with simulations in which $L = 3R$, $4R$, $5R$, $10R$, $15R$, $20R$ and $25R$, as well as the effect of different Poisson's ratios where $\nu = 0.1$, 0.2, 0.3, 0.4 and 0.499 were applied.

2.3.2.4 Effective stress and strain

Both the experiments and the simulation have the force F and displacement d as direct outputs. Using the equation 2.5, it is possible to define the contact radius and, consequently, the effective stress value σ^* through the equation 2.1. Considering the context in which an experimenter wishes to characterize a material with unknown properties, it is not yet possible to directly define the strain value associated with the calculated effective stress σ^*.

The effective stress σ^* is a definition of stress based on the current state of the system for each variable value of the contact radius a/R, therefore equivalent to the Eulerian definition of Cauchy stress σ_{cauchy}, in this case also defined by the equation 2.9.

$$\sigma_{cauchy} = \mu\left(\lambda^2 - \frac{1}{\lambda}\right) \tag{2.9}$$

which is the analytical one-dimensional compression equation for a neo-Hookean incompressible, where λ is the stretch in the loading direction.

To define strain, Lin et al. (2009) adopt the expression 2.2, which is valid only for the small strains regime where $a/R < 0.16$ (Mesarovic & Fleck, 1999; Herbert et al., 2001). Based on this relation, Tappert (2020) proposed the expression for effective strain as

$$\varepsilon^* = \chi' \frac{a}{R} \tag{2.10}$$

where χ' is a fitting parameter. The definition of strain ε^* must have a value of χ' in order to approximate the Eulerian definition of strain, which in the case of large strains may be defined by the Euler-Almansi strain e

$$e = \frac{1}{2}\left(\frac{\lambda^2 - 1}{\lambda^2}\right) \tag{2.11}$$

However, in the current work we observed that the definition of strain through the equation 2.10 is not able to provide a consistent fit for all the different approaches to defining stress and strain (Eulerian, Lagrangian and mixed). To overcome this problem, we propose an extension of the equation 2.2

$$\varepsilon^* = 0.2\frac{a}{R} + \chi\left(\frac{a}{R}\right)^2 \tag{2.12}$$

where χ is a fitting parameter and the equation 2.2 becomes a particular case of this relation for small values of a/R, remaining coherent with the contexts of its classical application for small strains.

Knowing the force F and displacement d, it is now possible to find a/R (through equation 2.6). The effective stress σ^* can then be defined through 2.1 and is assumed to be equivalent

to the uniaxial compression stress defined by the equation 2.9, that is, $\sigma^* = \sigma_{cauchy}$. Through the equation 2.9, the theoretical stretch values λ are calculated for the corresponding stress and the uniaxial strain associated with these stretches is defined by the Euler-Almansi strain through equation 2.11. Finally, a fitting was performed to approximate the equation 2.12 to the equation 2.11, defining a value for χ for a given thickness. Thus, it is possible to know σ^* and ε^* directly through the measurements of F and d/R.

Simulations with multiple thickness ratios were performed, allowing the prediction of the effective strain thanks to the expression.

$$\chi(h) = s_0 + \frac{1}{(h + s_1)^{s_2}} \tag{2.13}$$

where s_0, s_1 and s_2 are fitting parameters. The effective stress and strain can be switched to Lagrangian and mixed configurations by assuming incompressibility ($J = 1$) since the stretches are known, or using the FE method to analyse the evolution of J as function of λ.

The curve-fittings of the equations 2.6,2.7, 2.8 and 2.13 were done using The Constrained Optimization by Linear Approximation (COBYLA) method from Scipy Python, minimizing the least square error between an objective function and the simulated results.

2.3.2.5 Model validation with uniaxial compression

To validate the procedure, the effective stress and strain results were compared to the uniaxial compression of a cube with the same material definition in Abaqus. A 3D deformable part with 1 mm edge length was defined with 2200 C3D8RH elements. Only a quarter of the cube was considered in the analysis due to its symmetry, and it was subjected to compression between two 3D discrete rigid plates composed of R3D4 elements.

The application of the single-phase characterization procedure described above should yield the same stress σ^* and strain ε^* curves as the uniaxial compression of the cube in FE. Thus, it can be concluded that performing spherical compression allows obtaining results equivalent to the uniaxial compression of the same material, validating the method.

2.3.3 Results and discussion

The results show the compression effect on samples, that detach from the inferior base as the sphere is displaced, exemplified in Figure 2.11 for multiple sample densities.

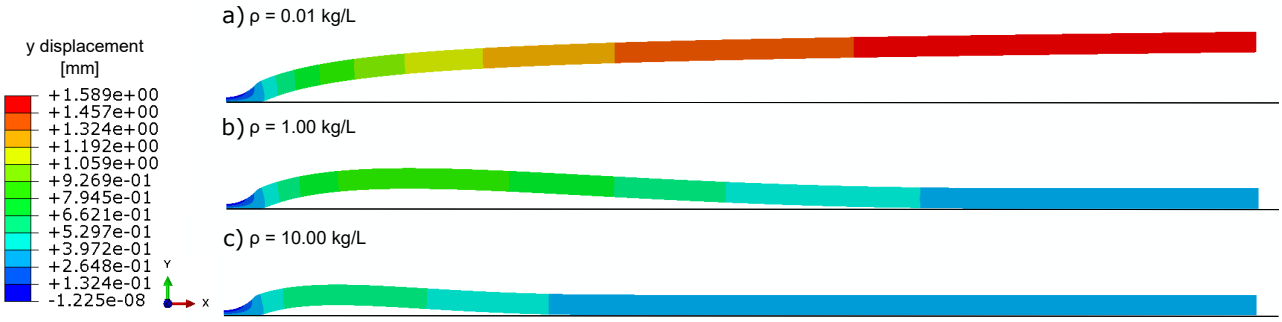

Figure 2.11: Simulated spherical compression FE results. The vertical displacement is shown for samples of $h = 0.5$, $L = 25R$ with different density values (0.01, 1.00 and 10.00 kg/L), in a state of compression representing $d/R = d_{max}/R$.

Figure 2.11 shows the influence of sample density ρ on the analysis. The detachment pattern was different when adopting different densities, indicating that distinct values for δ could be

attributed for a same distance of measurement R_δ (See Figure 1.7). Even with this effect, the evolution of the contact radius a/R was the same as a function of the imposed displacement d/R, and this relationship is illustrated in the Appendix B in Figure B.1. A similar effect was observed when varying the sample length L/R, shown in Appendix B in Figure B.2. Poisson's ratio ν generated a slight variation in the measurement of a/R (see Appendix B, Figure B.3), which nevertheless remained in a close range (a/R between 0.719 and 0.741 at d_{max}/R). The quasi-incompressible case was considered as an initial approach to be taken here and used for the other simulations.

This enables to conclude that equation 2.6 is sufficient to describe the evolution of the contact radius from the direct measurement of d/R, which is a controlled and efficient metric from both an experimental and numerical point of view. This allows us to get rid of the classically used δ, which is difficult to measure experimentally and loses its equivalence with d for thin samples where $h \leq 1.5$ for $d/R > 0.2$, a phenomenon illustrated in Appendix B, Figure B.4.

2.3.3.1 Sample thickness variation

The simulations were also performed varying the sample thickness ratios and maintaining reference values where $\rho = \rho_0$, $\nu = 0.499$ and $L = 25R$. Figure 2.12 shows the comparison of the observed forces with the Hertz model.

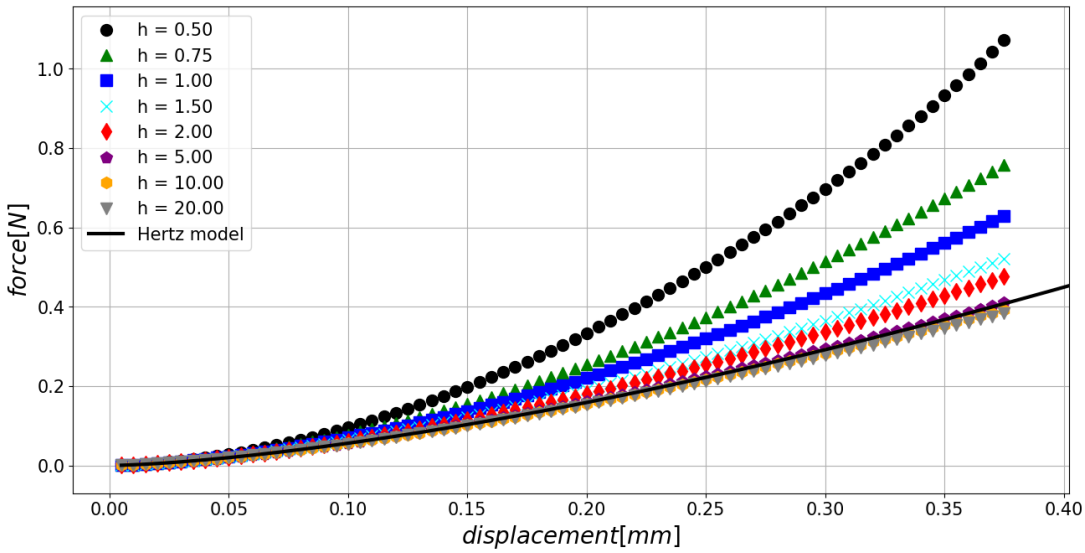

Figure 2.12: Comparison of simulations' force displacement results with respect to the Hertz model. Each result correspond to a different thickness ratio that was adopted, and the image highlights the difference in force measurement observed.

Indeed, the Hertz model is better suited to describe the behavior of thicker material layers and is still a good approximation for, in this case, thickness ratios of $h \geq 5.0$. In the small displacement regime, the force measures are close to each other, but begin to diverge beyond $d = 0.05$ mm, especially for samples in which $h \leq 5.0$. Thickness variation also has a significant effect on the evolution of the contact radius a/R, shown in Figure 2.13.

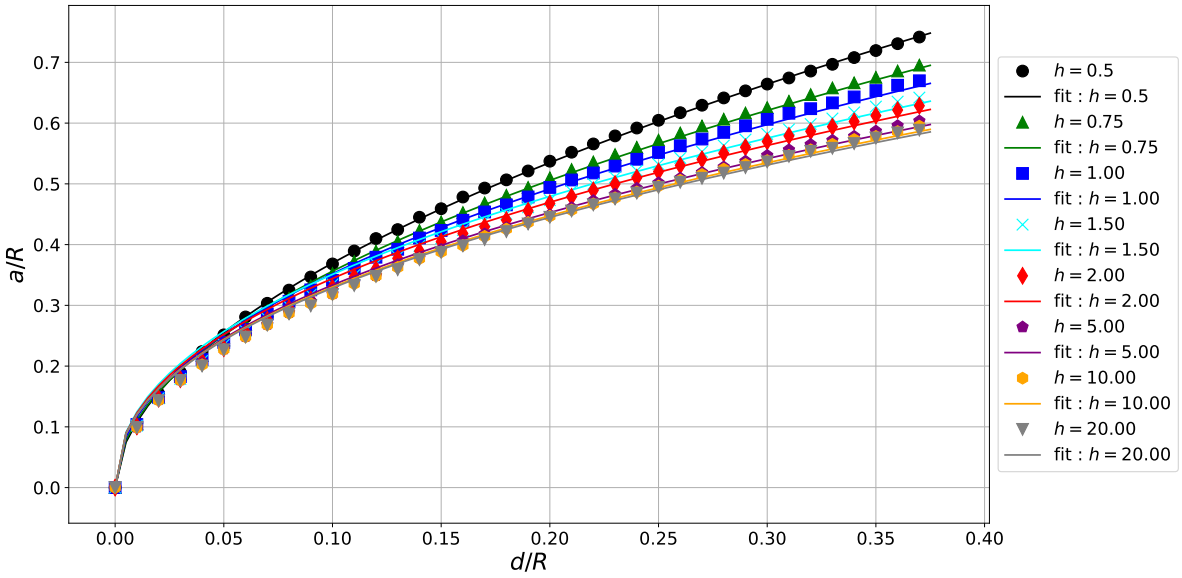

Figure 2.13: Comparison of dimensionless contact radius (a/R) as a function of dimensionless tool displacement (d/R) for samples of different initial thickness. The figure shows how the contact radius evolves as the sphere compresses the samples in controlled displacement, and the continuous lines represent the performed fittings used for matching the measured simulated data.

Figure 2.13 shows the evolution of the contact radius and the fitting that was performed to obtain the parameters β and m of equation 2.6. The obtained values are in table 2.2.

h	0.50	0.75	1.00	1.50	2.00	5.00	10.00	20.00
β	1.263	1.142	1.067	0.989	0.966	0.922	0.907	0.899
m	0.534	0.506	0.481	0.450	0.448	0.442	0.439	0.437
R^2	0.999	0.999	0.999	0.997	0.997	0.997	0.998	0.998

Table 2.2: Optimization results for parameters β and m.

Table 2.2 proposes parameters to be introduced into equation 2.6. To extend its usefulness to other thicknesses, the fittings of the equations 2.7 and 2.8 were also conducted, generating Figure 2.14.

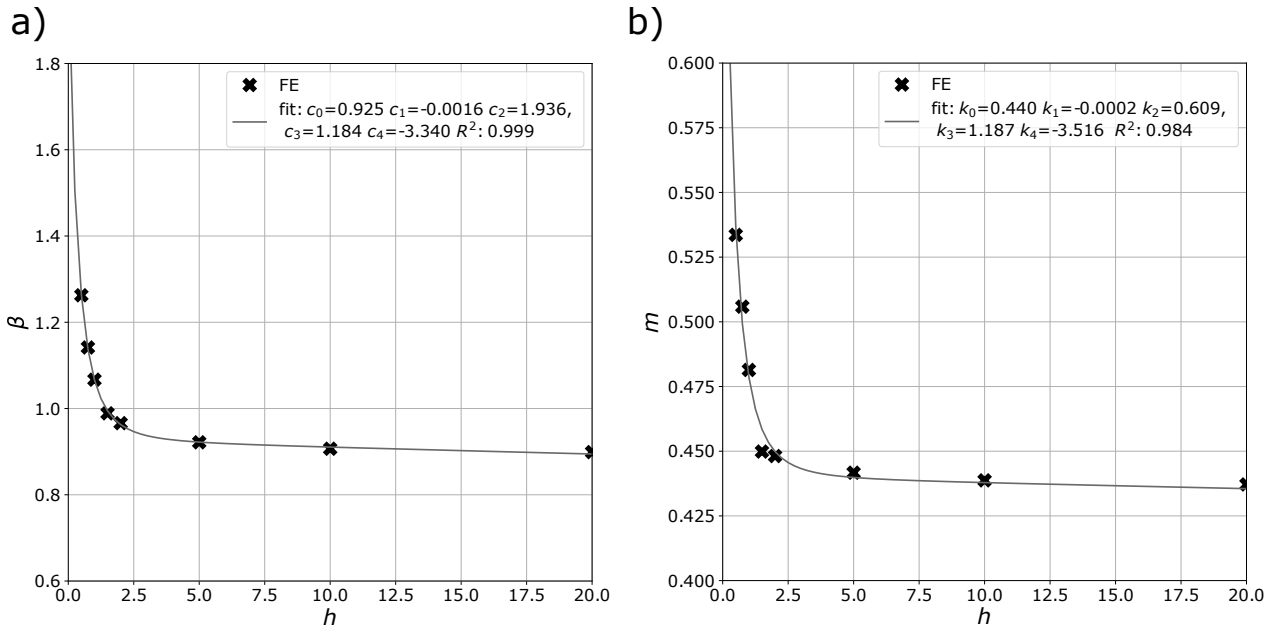

Figure 2.14: Fitting of β (a) and m (b) as a function of h. These fittings allow to predict the values of the parameters from equations 2.7 and 2.8, allowing to define the relation between contact radius a/R and imposed displacement d/R based on different sample thickness values.

The two quantities presented asymptotic behavior for very thin thicknesses, and tended to stabilize as thickness increased. The performed fitting allowed obtaining the parameters c_i and k_i ($i \in [0, 4]$), shown in Table 2.3.

β	c_0	c_1	c_2	c_3	c_4	R^2
	0.925	-0.0016	1.936	1.184	-3.340	0.999
m	k_0	k_1	k_2	k_3	k_4	R^2
	0.440	-0.0002	0.609	1.187	-3.516	0.984

Table 2.3: Optimization results for β and m.

2.3.3.2 Stress-strain analysis

Once the relationship between a/R and d/R is known, it is possible to calculate the stress σ^* using the equation 2.1. The next goal will be to define the effective stain ε^* using the equation 2.11, requiring the definition of values for χ.

The validation process using the cube in uniaxial compression was performed, and the analytical response of the material defined by equation 2.11 was compared with the stress-strain response of the cube. The comparison between the stress results and the stress observed in the validation cube is illustrated in Appendix B, Figure B.5.

Through the analytical solution of compression, each value of σ^* was associated with a stretch λ, and the comparison of the simulations with the theoretical curve is shown in Figure 2.15.

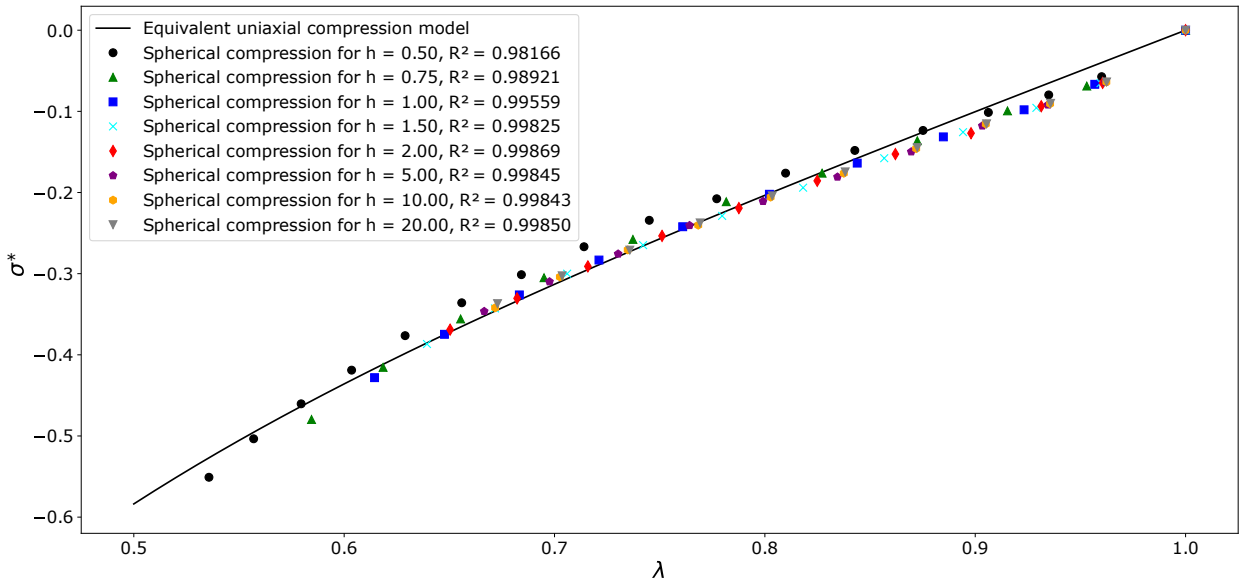

Figure 2.15: Effective stress vs corresponding stretches for various values of h in spherical compression.

The simulated stress values σ^* tend to approximate the continuous curve equivalent to uniaxial compression. This means that, even with different force and contact radius measurements (Figures 2.12 and 2.13), it is possible to find stress values that approximate the theoretical curve satisfactorily ($R^2 > 0.98$), regardless of the simulated sample thickness.

Using the equation 2.11, the stress-stretch curves were then converted to Eulerian stress-strain curves, and the results are shown in Figure 2.16.

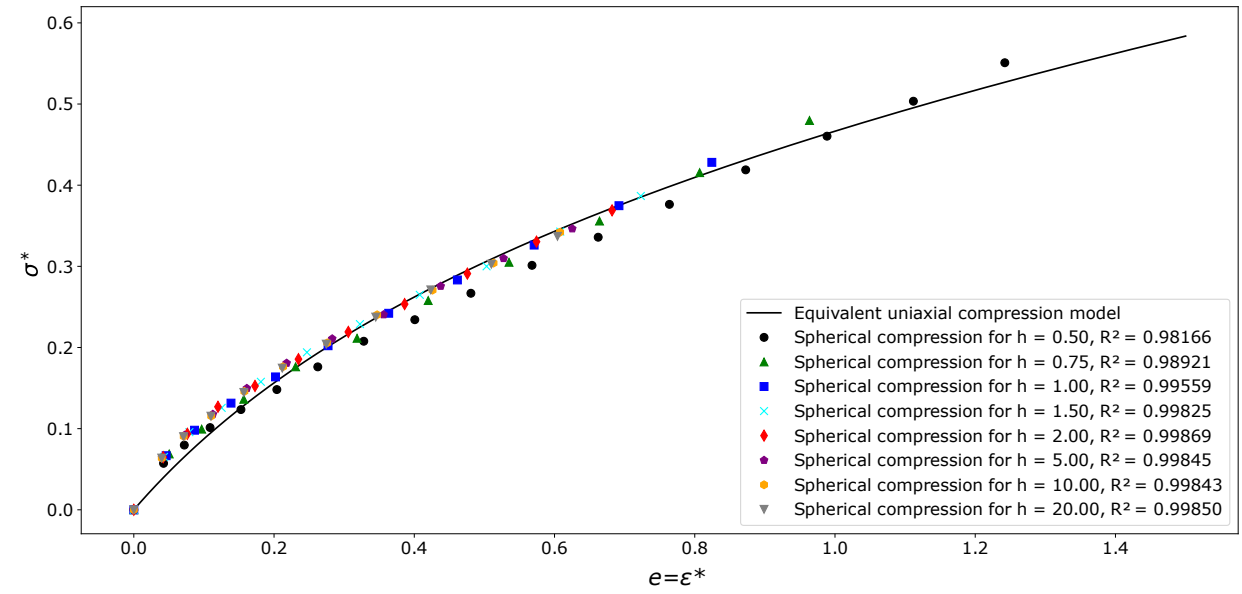

Figure 2.16: Calculated values of effective stress vs strain for spherical compression simulations in comparison to theoretical Neo-Hookean uniaxial compression eulerian stress vs strain. The approximation of the values to the equivalent theoretical curve in black indicates the model's ability to, at different thickness ratios, converge to the same stress-strain relationship.

In order to properly fit the strain ε^*, it was necessary to define different χ values for each simulated thickness, represented in the table 2.4.

h	0.5	0.75	1.0	1.5	2.0	5.0	10	20
χ	0.489	0.461	0.447	0.433	0.428	0.424	0.424	0.424
R^2	0.999	0.999	0.999	0.999	0.999	0.999	0.999	0.998

Table 2.4: Optimization results of parameter χ

Finally, equation 2.13 was used to fit the results shown in table 2.4, allowing to predict the values of χ, shown in Figure 2.17.

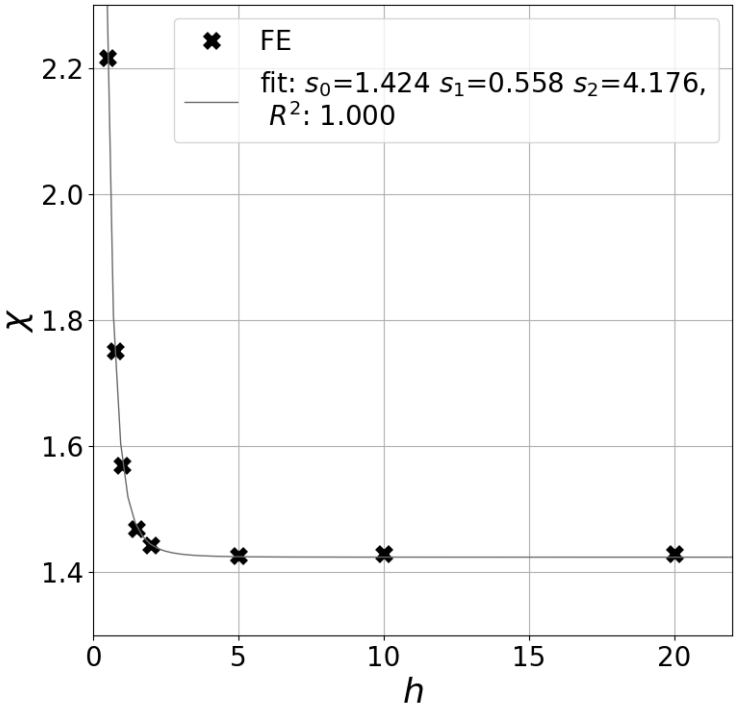

Figure 2.17: Fitting of equation 2.13 representing the evolution of χ as function of h. Knowing χ allows direct definition of effective strain based on current contact radius (see equation 2.12).

Asymptotic behavior was observed for both high and low values of h. By assuming quasi-incompressibility in uniaxial compression, it was also possible to plot the results as a function of engineering stress σ_{eng} and strain ε_{eng}, as well as effective stress-strain curves in the reference configuration, shown in Appendix B, in Figures B.6 and B.7. The same fitting parameter χ was able to satisfactorily reproduce the curves in all these formulations.

2.3.4 Application to experimental results

The stress-strain curves, once obtained, can be used to characterize the material using hyperelastic fittings that consider the uniaxial compression context. Tappert (2020) characterized the curves obtained using the Neo-Hookean (equation 1.7), Mooney-Rivlin (equation 1.2), and Ogden laws of behavior of order one and two, which can be defined by equation 2.14.

$$W = \sum_{i=1}^{N} \frac{2\mu_i}{\alpha_i^2}(\bar{\lambda}_1^{\alpha_i} + \bar{\lambda}_2^{\alpha_i} + \bar{\lambda}_3^{\alpha_i} - 3) + \sum_{i=1}^{N} \frac{1}{D_1}(J-1)^{2i} \tag{2.14}$$

where $\bar{\lambda} = J^{-\frac{1}{3}}\lambda$ and the initial shear (μ) and bulk moduli (κ) are

$$\mu = \sum_{i=1}^{N} \mu_i \qquad \text{and} \qquad \kappa = \frac{1}{D_1} \tag{2.15}$$

The second-order Ogden model best fitted the experimental results from Tappert (2020). This first approach assumed the material's incompressibility, assuming $D_1 = 0$ and reducing the number of parameters to be optimized.

The experimental data to be treated corresponds to the first compression phase of the sphere immediately after the preconditioning phase, ensuring behavior stability. To define the portion of the curve to be observed, it was necessary to identify the beginning of contact between the sample and the sphere.

The definition of the preload force used in the protocol by Tappert (2020) in table 2.1 was made in a way to define a common starting point for the tests, where the stress applied at the beginning would be equivalent regardless of the sphere radii. This does not mean necessarily that contact had not been established between the sample and the sphere before reaching this threshold force. The first compression cycle necessarily included a portion of the curve where contact had not yet been achieved. A contact criterion needed to be defined in order to fix with precision and consistency from which instant the experimental data would need to be observed.

The contact criterion was chosen based on a minimum force of 0.1% of the maximum value detectable by the load cell for the tests with the largest sphere radius, that is, equivalent to 0.01N. For the tests with spheres of smaller radius, a value that generated the same stress was calculated, following the same logic as the work of Tappert (2020). The application of this criterion proved to be repeatable among all 216 tests. It is therefore a promising guideline for identifying the portion of the curve where the force values tended to increase due to contact.

Using the described method, the experimental force F and displacement d curves were converted into effective stress σ^* and strain ε^*, and an example of fitting result for a curve where R=1.75 mm is shown in Figure 2.18.

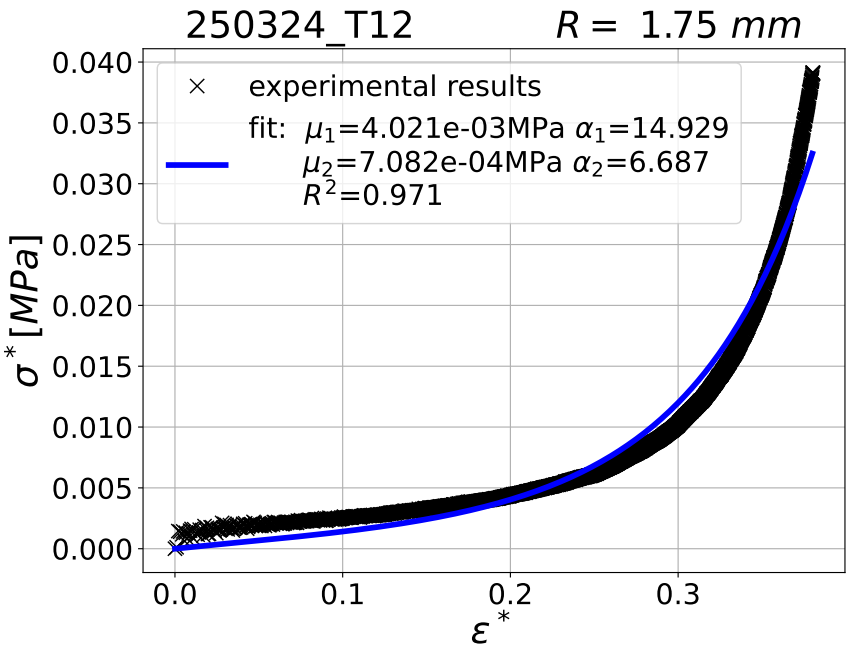

Figure 2.18: Example of eulerian stress-strain (σ^* - ε^*) curve obtained after application of the spherical compression monophasic data treatment method, with the two-term Ogden model with fitting parameters μ_1, μ_2, α_1, α_2 and associated determination coefficient R^2. Sample 240311-Head2-Right.

The fittings satisfactorily reproduced the nonlinearity of the experimental curves. The procedure was applied to the tests conducted in the central zone of the discs, allowing comparison with the results obtained by Tappert (2020) in table 2.5.

	R [mm]	μ_1 [kPa]	α_1	μ_2 [kPa]	α_2	R^2	global μ [kPa]
Tappert (2020)	0.875	9.79	6.21	6.09×10^{-2}	16	-	9.85
	1.75	8.58	4.44	2.89×10^{-2}	58.9	-	8.61
	3	6.56	6.55	3.24×10^{-2}	84.9	-	6.59
Current work	0.875	5.62 ± 5.91	5.90 ± 3.22	0.72 ± 0.02	5.61 ± 1.32	0.92	6.34
	1.75	3.04 ± 3.71	15.39 ± 11.86	0.61 ± 0.63	6.36 ± 6.08	0.89	3.65
	3	3.65 ± 2.08	28.37 ± 9.02	0.68 ± 0.18	6.18 ± 0.57	0.91	4.34

Table 2.5: Spherical compression optimization results for monophasic characterization of second order Ogden model. Comparison of results for tests conducted in the central part of porcine TMJ discs.

The results presented in table 2.5 correspond to the application of the fitting method of the equation 2.10 to the experiments of Tappert (2020), while the current results use the definition of strain ε^* described by equation 2.12.

In both cases, the contribution of the first-order shear modulus terms is more relevant than that of the second-order terms for the composition of the system's energy ($\mu_1 > \mu_2$). The new method resulted in larger values of μ_2, which was potentially compensated by the larger numerical values of α_2 and lower μ_2 in the Tappert (2020) model. Due to the changes applied to the model, it was not expected to obtain the same values for the parameters as in the previous study. Nevertheless, the order of magnitude of the global shear modulus μ remained in the range of kPa.

The objective of this section was to present the evolution of the hyperelastic model I worked on, in parallel with other analyses of the TMJ disc, which will be part of a future article publication. Although capable of reproducing a portion of the experimental curve, this method cannot address the viscous effects experimentally observed with TMJ discs (Figure 2.7). The method is also limited to characterizing the deviatoric behavior of the material, disregarding its compressibility, in this current version. The main advantage by applying it is to obtain initial material parameters non-destructively, thanks to the nature of spherical compression tests. These initial parameters can be used as input values for more in-depth analysis, as in the example of biphasic characterization in FE that will be described below.

2.4 Biphasic axisymmetric Finite Element model

This section will explore the same experimental results that were presented in section 2.2, this time using a poromechanical approach. The objective is to deepen the analysis conducted in the previous section, including the biphasic concepts introduced in section 1.1.2 through an application associating the FE method and optimization.

2.4.1 Geometry and mesh definitions

A 2D axisymmetric finite element model was created in the commercial software Abaqus® 2022 using the implicit Standard solver. A coupled pore fluid diffusion and stress analysis was established, allowing the representation of a porous medium, in this case considered completely saturated. The mesh is attached to the solid phase of the material, with which the fluid interacts and flows according to Darcy's law.

The axisymmetric biological sample was designed with dimensions of 8 mm in length (radial direction) and 2.75 mm in thickness (axial direction), based on thickness measurements of 9 porcine discs by means of the magnetic resonance imaging performed in Tappert (2020).

The final biased mesh uses for the simulations is shown in Figure 2.19. A previous mesh convergence study analyzed the definitions with elements side dimensions ranging from 0.0125 mm to 0.05 mm, from 0.025 mm to 0.1 mm, from 0.05 mm to 0.2 mm and from 0.1 mm to 0.4 mm. It was observed that the force measurements as a function of displacement were equivalent for all definitions and the 0.05 mm to 0.2 mm mesh, illustrated in the figure, was chosen for future simulations.

The disc model was simulated with a total of 900 linear quadrilateral elements of type CAX4PH, which allows bilinear interpolation of both node displacement and pore pressure. The chosen elements allow Abaqus to treat large strains, enabling the definition of hyperelastic behavior laws for the solid phase and representing viscous creep and stress-relaxation effects due to material's biphasic nature.

Considering the greater stiffness of the compression sphere and support in comparison with the analysed biological tissue, a rigid body definition was assumed for both components. Since they are simple geometries (a straight line for the support and a circle arc for the sphere), the rigid bodies were defined as axisymmetric analytical rigid and were therefore not meshed. The support was defined with a length of 10 mm to accommodate the sample satisfactorily. The radius of the semisphere had three definitions: 0.875 mm, 1.75 mm and 3 mm, to be simulated according to the spheres used experimentally for compression. The defined geometries and mesh are illustrated in Figure 2.19.

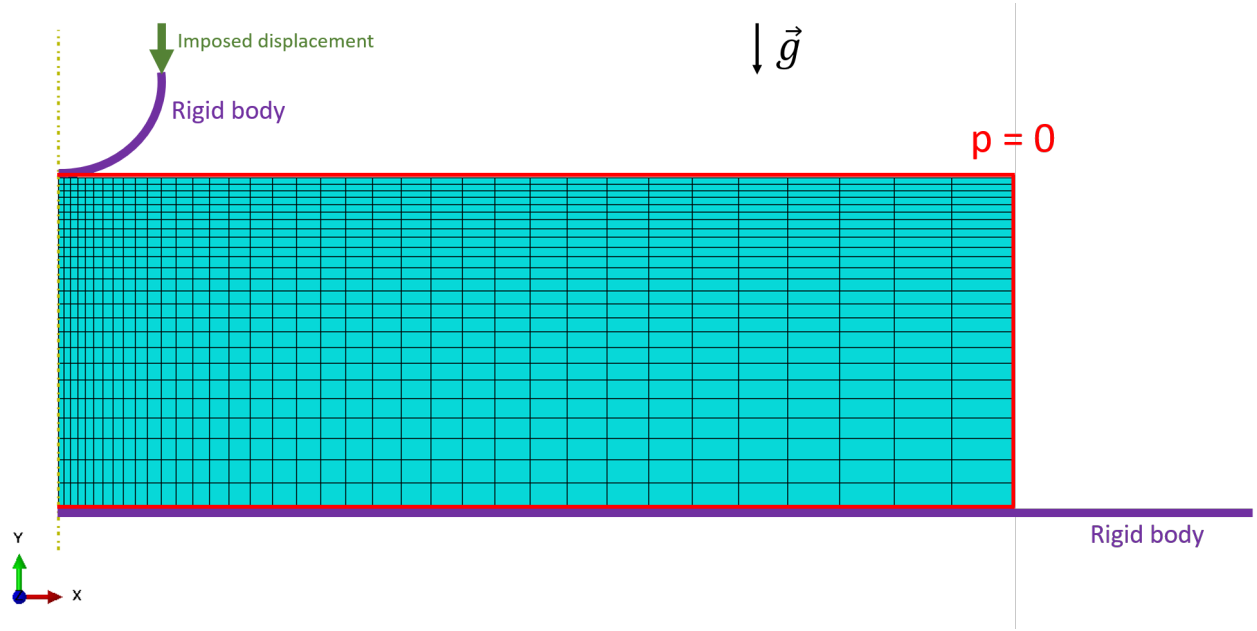

Figure 2.19: Mesh used for simulations, with rigid bodies definitions for support and sphere. Gravity was applied along the vertical axis of the figure (represented by $\vec{g}$) and pore pressure was set to 0 for all edges of the specimen, indicated by the red marking. The imposed displacement was applied to the reference point of the rigid body representing the sphere.

2.4.2 Boundary conditions and simulation steps

The simulation was performed considering a transient flow regime, with the Soils procedure type in Abaqus. A gravity load was imposed on the entire system in an initial step (step 1) The displacement of the rigid semicircle was imposed in a subsequent compression step (step 2) and an unloading step (step 3). Exploring a full loading/unloading cycle like this ensures the observation of material nonlinearity and of the hysteresis in the force-displacement curve. In this case, the hysteresis is purely associated with the fluid movement within the structure, as viscoelasticity of the solid matrix was not introduced in the model.

The simulation time period and the imposed displacements in steps 2 and 3 were chosen to reproduce the experimental protocol of each of the tests, ensuring both strain and strain rate equivalence between simulations and experiments. The portion of the experimental curve corresponding to the first cycle immediately following the preconditioning phase was selected for analysis, in order to capture a more stabilized material response and yet keep compression information from before the preload phase (see Figure 2.5) . To identify the beginning of the curve to be treated, the same procedure described in section 2.3.4 was applied. Figure 2.20 shows an example of a first-cycle result for three tests.

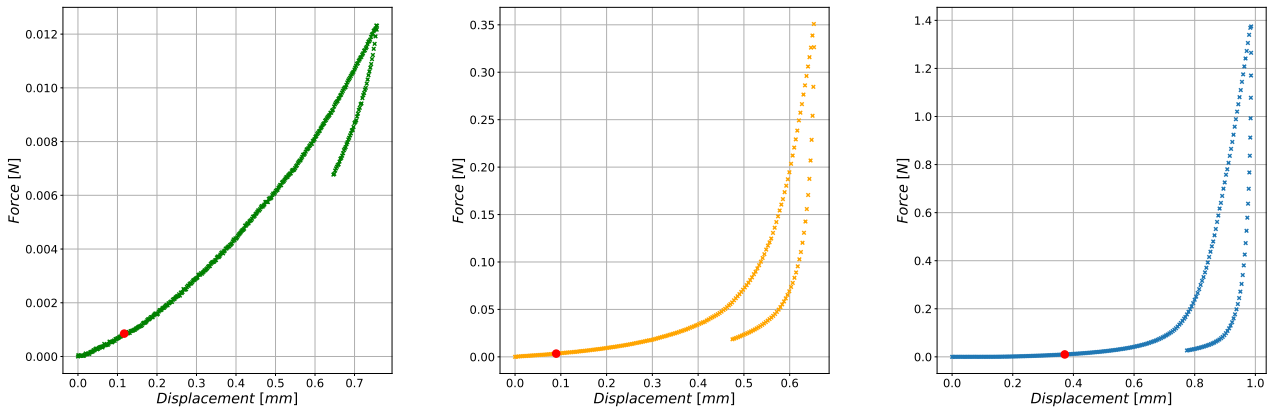

(a) R = 0.875 mm. (b) R = 1.750 mm. (c) R = 3.000 mm.

Figure 2.20: Examples of experimental curves obtained for $f = 0.01$ Hz and different sphere radii. The red dot indicates the instant at which contact was considered established and, from this threshold, the experimental displacement data were considered for introduction into the simulation. Sample 240311-Head2-Right.

Figure 2.20 shows the contact identification according to the criterion previously defined for different examples of compressive sphere radius and with f=0.01Hz.. Due to the smaller force values observed, contacts with sphere radius R=0.875 mm were more difficult to identify, with the force curve showing variations even before the contact point (in red). This raises concerns about the difficulty of performing tests with smaller spheres.

Due to the particularity of each curve, each simulation had different displacement and compression time data. The definition of the boundary conditions for each model was automated by means of Python scripts that read the experimental results and treated them accordingly. The scripts then interacted with the Abaqus interface, assigned the conditions by modifying a base CAE file containing the other model definitions and launched the simulations automatically.

Due to the high water content, a frictionless surface to surface contact was established between sample and surrounding rigid bodies (see Figure 2.19). Experimentally, the lateral and upper faces of the sample were free. The lower surface was in contact with the support, but glued only at the far end and it was considered that the fluid could easily escape through it as well. The top, bottom and side faces of the simulation allow free fluid inflow and outflow by imposing a zero pore pressure on the external surfaces, shown in Figure 2.19 by the red line surrounding the model.

2.4.3 Material behavior definitions

The initial void ratio was set to 4 (see equation 1.16), based on a porosity definition of 80% from Ortún-Terrazas et al. (2020). Permeability was assumed to be independent of the void ratio, and hyperelastic constitutive models from two studies in the literature were selected for the simulations. Based on Ortún-Terrazas et al. (2020), which will also be called Model 1 here, a first-order hyperfoam strain energy density function was assigned, in the form

$$W = \frac{2\mu}{\alpha^2}\left[\hat{\lambda}_1^{\alpha} + \hat{\lambda}_2^{\alpha} + \hat{\lambda}_3^{\alpha} - 3 + \frac{1}{\beta}(J^{-\alpha\beta} - 1)\right] \tag{2.16}$$

where the stretch is represented by $\hat{\lambda}$ and $\hat{\lambda} = \lambda$ in this isothermal case. For a first-order definition of W, μ is the shear modulus and α and β are material parameters, with β related to the Poisson's ratio ν through $\beta = \nu/(1-2\nu)$. The bulk modulus κ is obtained through equation 2.17.

$$\kappa = 2\mu\left(\frac{1}{3} + \beta\right) \tag{2.17}$$

The hyperfoam energy function is capable of reproducing highly compressible materials (Storåkers, 1986). Furthermore, Ortún-Terrazas et al. (2020) reports better representation of their experimental results when adopting this definition in their poromechanical simulation. Based on the average values of Ortún-Terrazas et al. (2020), a sample with a density close to that of water was defined with $\rho = 1000kg/m^3$, with material parameters shown in table 2.6.

In the absence of another complete model proposing hyperelastic porous definition parameters for porcine discs in the literature, definitions from two different works were associated to create another model. Tappert (2020) performed the monophasic characterization of porcine discs through curve-fitting of spherical compression experiments, previously described in section 2.3. The results of the application of this method were chosen initially to define the deviatoric components of equation 2.14, adopting a first-order formulation with parameters $\rho = 1000kg/m^3$, $\mu = 9.79 \times 10^{-}3$ MPa and $\alpha = 6.21$. Even though I obtained monophasic parameters based on the approach from section 2.3, the results from this particular characterization could not be used since the biphasic FE models were created before the model updates from section 2.3. The first-order formulation was chosen due to the low contribution of the other parameters to the material energy. To define solid phase volumetric behavior and biphasic properties, poisson's ratio and average hydraulic permeability proposed in (Wu et al., 2017) were used, with $\nu = 0.125$ ($D_1 = 204.29$ 1/MPa) and $k = 8.8 \times 10^{-16} m^4/Ns$, and the model associating the results from Tappert (2020) and Wu et al. (2017) will be called Model 2. The parameters for both material definitions are presented in table 2.6

Model	μ [MPa]	κ [MPa]	ν	α	k (m^4/Ns)
Model 1	2.16	2.52	0.167	75.00	9.96×10^{-12}
Model 2	9.79×10^{-3}	9.79×10^{-3}	0.125	6.21	8.80×10^{-16}

Table 2.6: Summary of model parameters from literature. Model 1 was defined with parameters from Ortún-Terrazas et al. (2020) and Model 2 associates the results from Tappert (2020) and Wu et al. (2017).

The agreement between the models and experimental data was evaluated by the root mean square error (RMSE) between the respective data sets. Since displacements were applied identically in both simulations and experiments, the RMSE was calculated based on the resulting reaction forces

$$\text{RMSE} = \sqrt{\frac{1}{n}\sum_{i=1}^{n}\left(F_i^{\text{exp}} - F_i^{\text{sim}}\right)^2} \tag{2.18}$$

where F_i^{exp} and F_i^{sim} correspond to the experimental and simulated reaction forces for all n points.

2.5 Model testing with literature parameters

An example of result is shown in Figure 2.21 for a sphere of radius 1.75 mm with the application of Model 2 parameters (see table 2.6) for the largest displacement value imposed in the simulation.

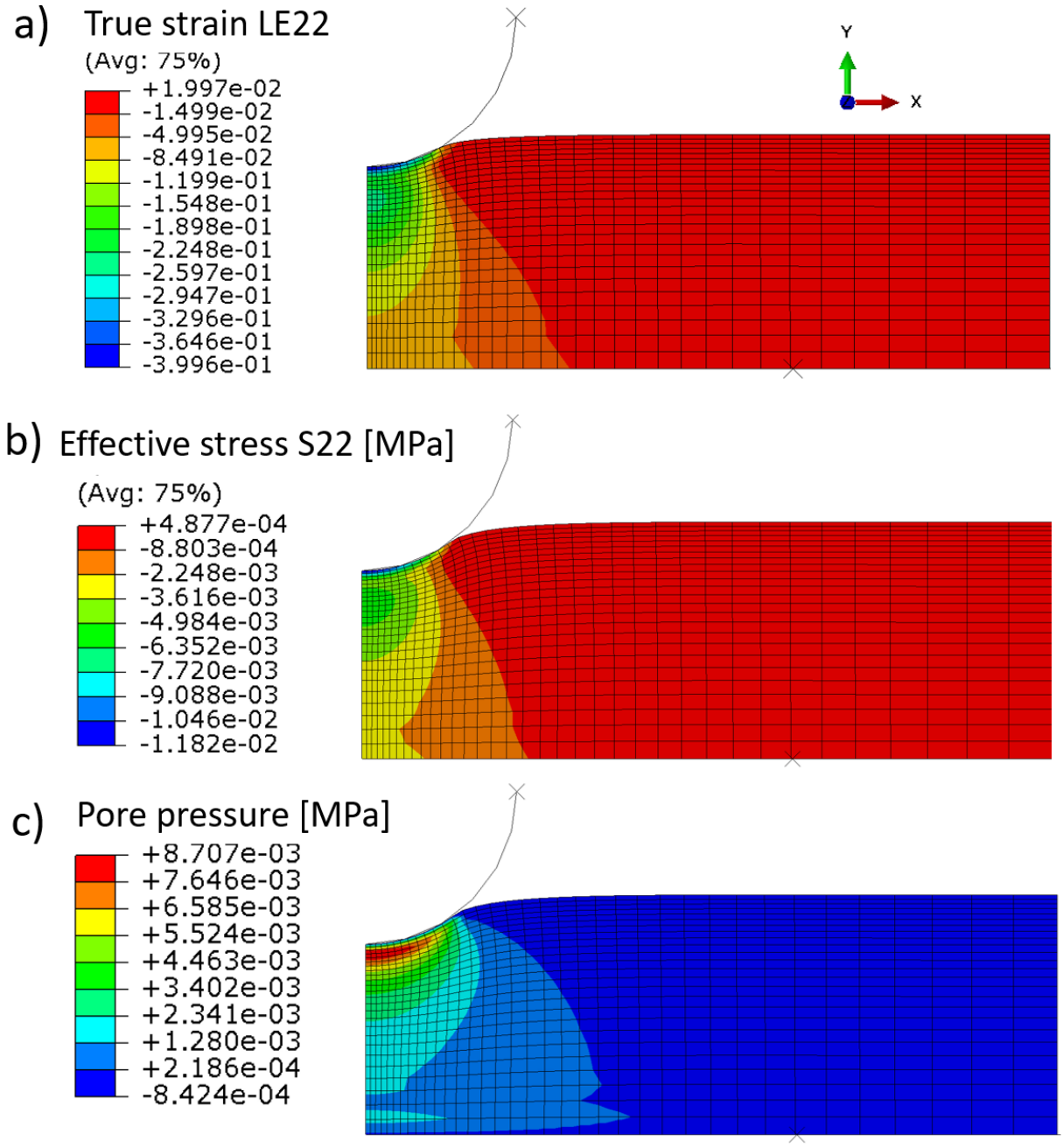

Figure 2.21: Simulation results for R = 1.75 mm, highlighting the a) true compressive strain in the Y direction (S22), b) effective stress in the Y direction and c) the pore pressure.

Figure 2.21a shows the true strain observed in the Y direction, with the highest compressive values identified in the zone closest to the sphere, reaching approximately 0.4. A similar trend is shown for the effective stress component in the Y direction (Figure 2.21b). The highest effective stress values were concentrated directly under the sphere and the nonlinear distribution of the stress developed at this moment in the simulation is shown.

Thanks to the biphasic definition, it was possible to observe the pore pressure independently of the effective stress, in Figure 2.21c. It is interesting to note that the highest fluid pressure values do not correspond exactly to the highest stress points in the solid phase, and that the measurement of the two quantities is independent and respects the 1.18 relationship.

Another interesting field output to observe is the fluid flow velocity. Figure 2.22 shows an example of an observed velocity field.

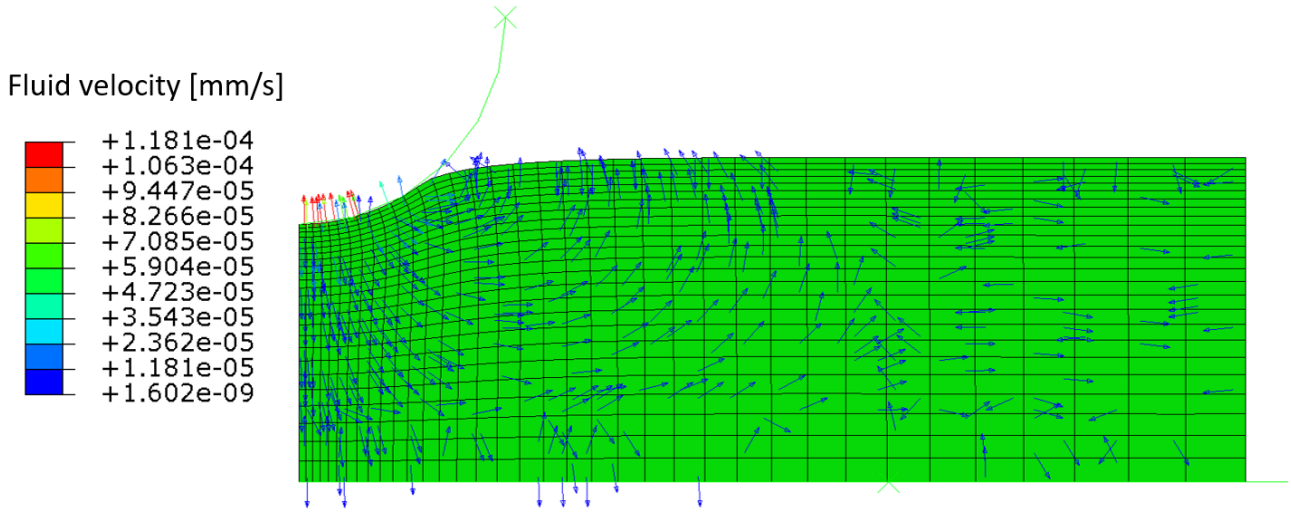

Figure 2.22: Instantaneous fluid velocity for state of maximum compression in simulation of Figure 2.21.

The tendency of the fluid is to escape through the surfaces where the pore pressure was applied as zero, moving away from the compressive sphere and seeking zones of lower pressure (see Figure 2.21c). The highest velocity values, however, are found in this case in the zone directly below the compressive sphere, since it is adjacent to the highest of pore pressure zone (justified by Darcy's equation 1.12).

This raises a relevant question about what happens experimentally. The evolution of the sphere's contact radius occurs according to its penetration into the material. A plausible point of view is that as the sphere penetrates, the pores of the surface in contact progressively become blocked. At the same time, the surface of the sphere and the disc present imperfections that can allow a certain flow, which would cause the appearance of a layer of fluid at the interface of this contact. Due to experimental difficulties, it is difficult to measure the amount of fluid that leaves this contact zone.

Due to software limitations, the pore pressure boundary condition was set to zero around the entire sample, allowing free fluid flow. This approach was necessary because it was not possible to define an evolving fluid boundary at the sample edges. In order to verify the effect of this on the simulations, the most extreme case, in which the zone adjacent to the sphere is impermeable, was simulated, and the result is shown in Figure 2.23.

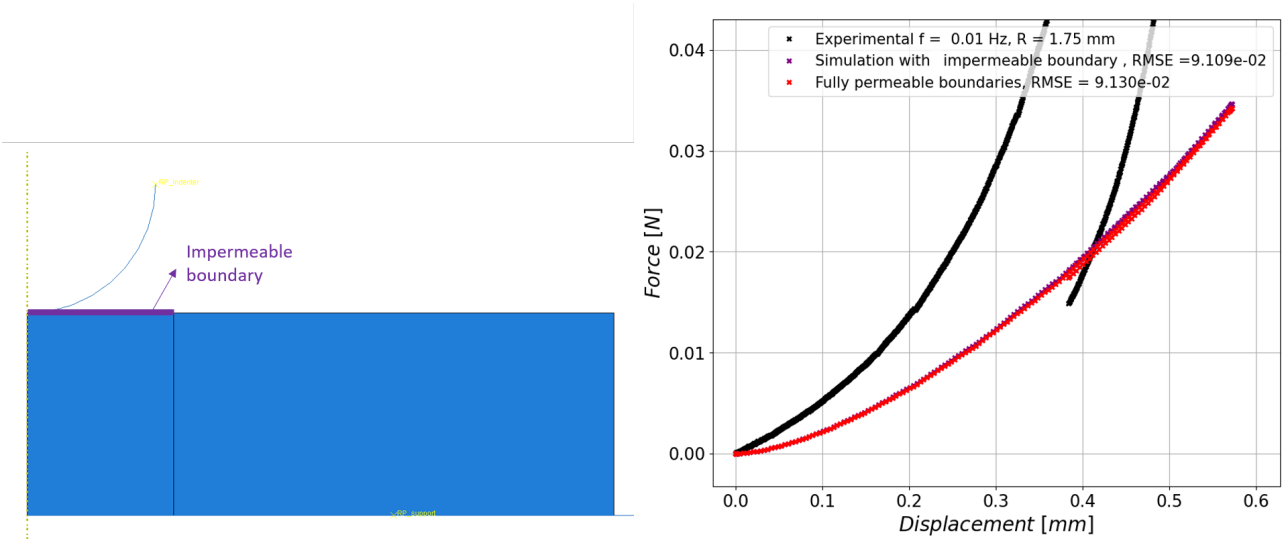

Figure 2.23: Simulation in which contact with the sphere was set as impermeable to fluid flow. The graph show the results in force measurement, highlighting low difference in force measurement.

Little force difference was measured between the two distinct definitions of the pore pressure boundary condition, indicating that this effect had little significance in the results in this case. The figure showing the velocity field of this impermeable boundary simulation was added to Appendix C, in Figure C.1.

Figure 2.24 shows a representative result for the application of literature data for the two models in table 2.6 with the adoption of different compression radii. These are results for the application of stresses on the central zone of a same disc.

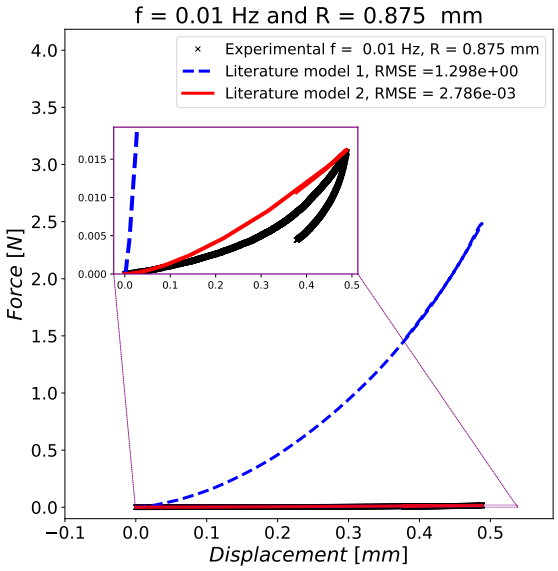

(a)

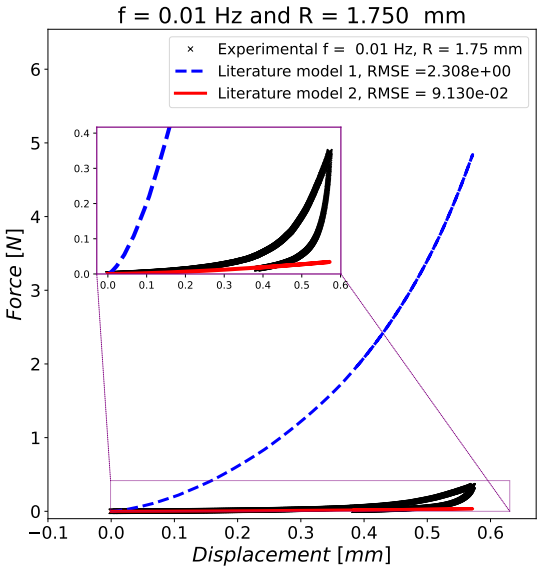

(b)

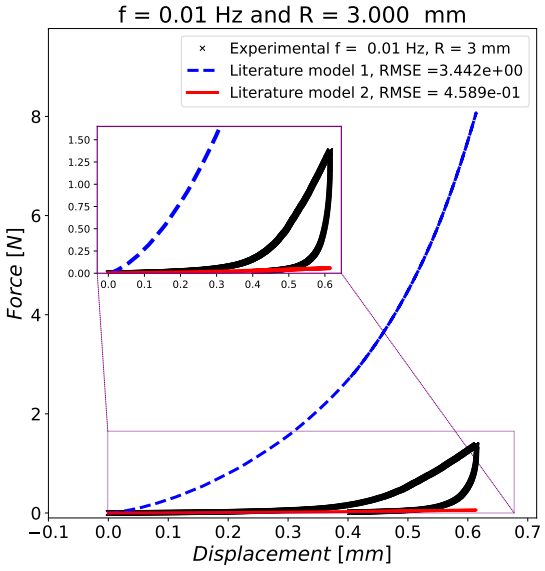

(c)

Figure 2.24: Representative results of experimental force and displacement compared with simulations of the models in table 2.6. The results correspond to the same disc (sample 240311-Head2-Right), subjected to a loading frequency of 0.01 Hz with different sphere radii, being a) R = 0.875 mm, b) R = 1.75 mm and c) R = 3 mm.

The displacement used in the simulations (red and blue curves) reproduced the imposed experimental displacement identically. However, the effect of viscosity was not very marked and the curves presented similar simulated forces between their respective loading and unloading phases. Since the FE model was built with a hyperelastic solid phase without intrinsic viscosity, the hysteresis in the curve was highly linked to the permeability value of the models in the literature. Low permeability prevents the fluid from moving easily, causing the volume fraction ratio of the phases between the different stages of the simulation to be similar and, consequently, little hysteresis to be observed. On the other hand, a too high permeability allows fluid to flow out of the compressed zone more easily. At the same time, it returns more quickly once the loading has been removed, difficulting also the observation of hysteresis. Such an analysis, however, should not be restricted to this aspect alone. A model with very rigid or incompressible

solid phase parameters influences the variation in the fluid volume fraction, which may also have an impact in its viscous effects due to the coupling of equations 1.18 and 1.19. The apparent stiffness of the material proposed by Ortún-Terrazas et al. (2020) was much higher than expected, with force values that were far from the experimental ones, as visible in all subfigures from Figure 2.24. This behavior was systematically observed throughout all the other simulations.

On the other hand, the parameters of the second model, from Tappert (2020) and Wu et al. (2017), were closer to the experimental ones (lower RMSE), but were not able to reproduce them satisfactorily, as shown in the figures. The maximum force value obtained by the smaller sphere was close to experimental results in Figure 2.24a. For larger sphere radii, in all models, the curves presented a maximum force lower than the experimental one.

The variation of the sphere radius in the models generated the expected effect of increasing the maximum force, as observed experimentally. However, the combination of material parameters adopted was not able to reproduce the desired effects of the material. Let us now observe, for the sphere with the largest radius, what happened in the simulations of variation in loading speed, illustrated for higher frequencies in Figure 2.25.

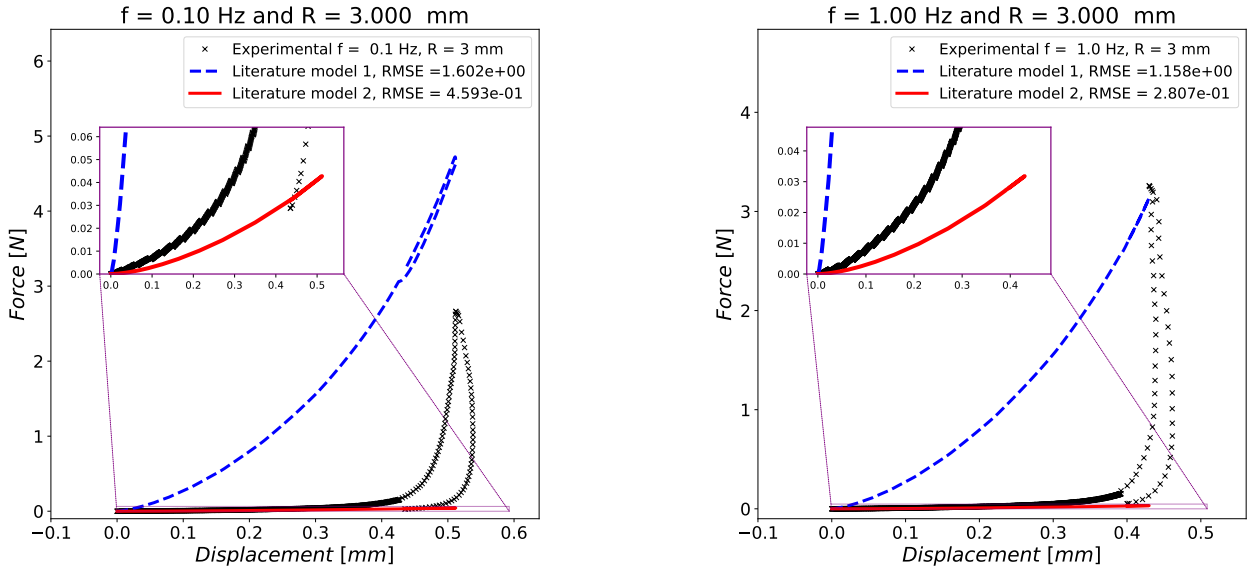

(a) (b)

Figure 2.25: Representative results of experimental force and displacement compared with simulations of the models in table 2.6. The results correspond to the same disc (sample 240311-Head2-Right) as Figure 2.24, subjected to a compression where R = 3 mm and higher loading frequencies of a) f = 0.1Hz and b) f = 1 Hz.

Unlike the experimental results, where the increase in frequency caused an increase in the measured force, the simulations in this case showed the opposite effect. The dependence of the strain rate is strictly linked to the multiphase viscous effects of the material. Considering the discussion above, where the viscous effects could not be reproduced by the simulation in a satisfactory way (curves with very little hysteresis), it can be concluded that the curves with the parameters from the literature were unable to reproduce this behavior.

Another possible reason for this inconsistency was the difficulty of Abaqus/Standard in dealing with the high loading speeds imposed. All low-frequency simulations (f=0.01Hz) were reproducible in the Abaqus simulations. However, as the frequencies increased, convergence problems appeared in the phase of abrupt speed variation after reaching the preload force of the simulations. This problem will be discussed further in the next section, but it is indicative

of the difficulty in interpreting results from higher loading frequencies.

For higher frequency simulations, in the case of Figure 2.25b the simulation using the Ortún-Terrazas et al. (2020) model reached values close to maximum experimental force. However, it presented a much more linear aspect and lacked the viscous effects observed experimentally. The parameters that associate results from Tappert (2020) and Wu et al. (2017) still resulted in a much less rigid behavior observed.

There are multiple simplifications of the model that may account for such dissimilarity. Nevertheless, the application of the parameters from the literature did not come close to the experimental ones in none of the simulated cases satisfactorily. An adjustment of parameters could potentially provide better results and the following sections will present the treatment of the experimental results of the present work in search for a better adapted poromechanical characterization.

2.6 Towards a biphasic characterization: finite elements spherical compression optimization

Section 2.5 addressed the application of literature models in axisymmetric FE spherical compression simulations. The simulated results were unable to satisfactorily reproduce the experimental results, either in terms of expected force magnitude or hysteresis of the force curves.

Then the question arises as to whether there is a set of material parameters that, applied to the described FE model, would result in a better fit of the experimental curves.

The development of a poromechanical characterization method using spherical compression results would be advantageous due to its non-destructive nature to biological tissues. The analytical poromechanical model described by Wang et al. (2020), using the equation 1.29, has been reported to be useful in representing small deformations in stress relaxation curves. However, the team's database produced in Tappert (2020), as well as the experiments performed in this current thesis, includes cyclic experiments in which the displacement varied, allowing us to observe the dynamics of the applied cycles.

To leverage the results currently produced, a procedure for obtaining coupled poromechanical parameters was developed and will be described below.

2.6.1 Inverse method optimization algorithm

The Constrained Optimization by Linear Approximation (COBYLA) algorithm, implemented in the Scipy Python library, had been used for the parameter optimization process of the model described in section 2.4. This method compares the experimental force curve to the simulated force in the FE model in Abaqus and uses the root mean square error (equation 3.17) as a fitting quality metric. This same logic will be applied here, reducing the error between experimental and simulated forces by testing different material definitions.

The algorithm implemented in Python iteratively adjusts the simulation material parameters for the hyperfoam definition (equation 2.16). This definition was judged in Ortún-Terrazas et al. (2020) as a suitable solid phase definition with good response for representing poromechanical phenomena in Abaqus, due to its ability to handle highly compressible materials.

The Python algorithm launches the simulations in Abaqus, compares the RMSE values, and, using the COBYLA method, adjusts the parameters k, μ, α, and ν to reduce the RMSE measured in each optimization. Constraints were imposed on the parameters to keep them within a range of physically possible values, and the optimizations were launched on a remote computing cluster (Cassiopée HPC Platform), lasting approximately 30 hours for each analysed experimental result.

2.6.2 Optimization results

The optimizations were calculated and converged for 61 experimental results of spherical compression that I performed to date: 18 results for R=0.875 mm, 22 for R=1.750 mm, and 21 for R=3.000 mm. In addition to these results, I also applied the optimization procedure to 18 experiments for R=1.750 mm performed during the work Tappert (2020) using the same protocol, in order to enlarge the database and also provide some information regarding the operator's influence.

Simulations at low loading frequencies (0.01 Hz) converged much more easily than those at higher frequencies (0.10 Hz and 1.00 Hz). Some high frequency simulations ran well and showed some results (as shown in Figure 2.25), however, when varying the material definition during optimization, a combination of parameters that presented divergence problems was often tested by the algorithm and prevented progress.

I found that the multiple divergence problems were not limited to the misdefinition of a single parameter, but rather their combination in the constitutive law, which prevented Abaqus from performing the calculations. A pattern in material definition that caused the failure has not been identified to date. One possible cause is Abaqus's difficulty handling high velocities, since poromechanical coupling is only possible in the Standard solver.

Different model variables can still be tested and modified to verify the problem, but the hypothesis that the convergence difficulty is associated with the solver's inability to handle the inertial effects of high frequencies remains the strongest. The problem can still be explored, however this section will be limited to discussing the results for the simulations that presented good fits, at low loading frequencies of 0.01 Hz.

2.6.2.1 Sphere radius influence

Figure 2.26 presents the optimization results for simulations of the same disc for different compression radii.

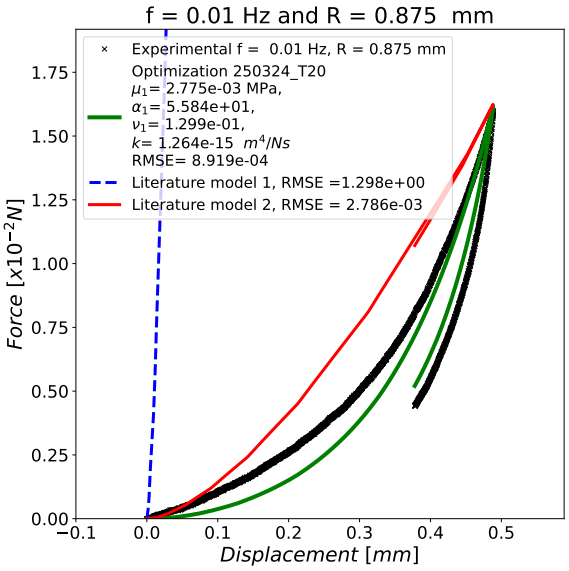

(a) R = 0.875 mm.

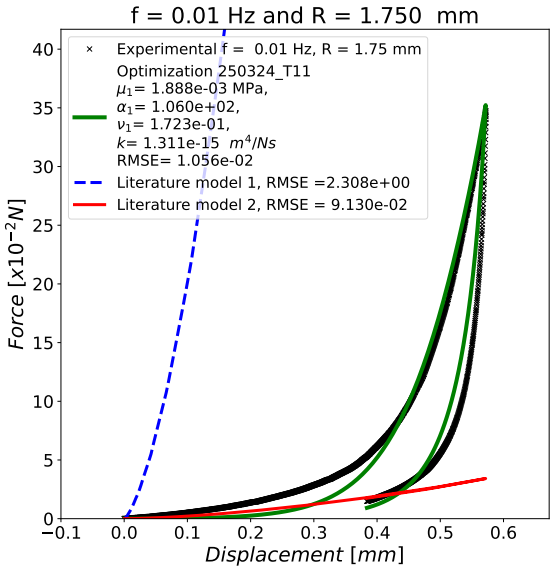

(b)R = 1.750 mm.

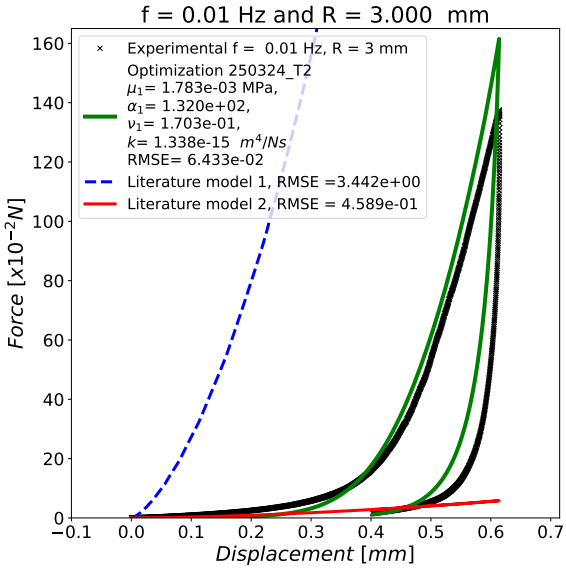

(c)R = 3.000 mm.

Figure 2.26: Optimization results for different sphere radius on central zone of TMJ sample 240311-Head2-Right. The figure shows the comparison of force-displacement curves on one loading and unloading cycle of spherical compression, comparing the experimentally obtained results to the ones obtained through FE simulations.

Figure 2.26 shows the results of the optimizations applied to three experimental results. Adjusting the permeability parameter was essential for good reproduction of viscous effects in the results. Even with variability between experimental samples, it was possible to reproduce the behavior of the discs in FE so that the general appearance of the curves was well represented, with an average value of RMSE $= 3.51 \times 10^{-2}$.

Some discrepancies can be observed, for example, at the beginning of compression up to 0.3 mm of displacement in Figures 2.26a and b, where the simulated sample begins to exhibit greater stiffness and better correlation beyond this point of sphere penetration. For Figure 2.26c, the maximum force was estimated to be higher (1.6 N versus the experimental 1.4 N).

Table 2.7 lists the overall average for the optimization results across the 61 performed simulations.

R [mm]	μ [kPa]	κ [kPa]	ν	α	$k \times 10^{-15}$ $[m^4/Ns]$
0.875	4.14 ± 2.43	4.04 ± 2.57	0.118 ± 0.041	58.59 ± 29.47	1.26 ± 0.22
1.750	1.55 ± 0.54	1.67 ± 0.66	0.145 ± 0.031	76.55 ± 37.58	1.18 ± 2.60
3.000	1.75 ± 0.67	2.23 ± 1.65	0.189 ± 0.039	111.83 ± 43.14	1.09 ± 3.51

Table 2.7: Optimized parameters for spherical compression simulations for different values of sphere radius for all zones of the discs. General mean ± standard deviation.

The smaller spheres imposed lower forces and displacements on the disc structure, having a more local influence and compressing smaller tissue volume during the tests. Therefore, it makes sense that the obtained parameters have different values, given that the tested zone is different for each sphere used. It is also important to emphasize that permeability is considered isotropic. In spherical compression, the fluid presents a multidirectional displacement field (see Figure 2.22), and the estimated permeability in this section consists of an equivalent and isotropic homogenized value.

The smaller sphere (R=0.875 mm) resulted in higher shear modulus μ and bulk modulus κ, indicating greater stiffness and lower isotropic compressibility. For the larger spheres of R = 1.750 mm and R = 3.000 mm, these values are lower and closer to each other, suggesting a reduction in stiffness and an increase in compressibility. It can therefore be said that the lowest isotropic compressibility was found through the R = 0.875 mm tests.

At the same time, the Poisson's ratio ν presents the lowest value for the smallest sphere radius, indicating that the relative compressibility between axes is greater for R = 0.875 mm, in a material that contracts less laterally when compressed axially. This highlights an important point about the fact that Poisson's ratio is not a property that alone defines the absolute compressibility of the material in large strains. In any case, the magnitude of the solid phase properties of the material indicate that it is capable of being subjected to compressions that will allow the observation of poroelastic viscous phenomena.

The value of α is related to the nonlinearity of the curves, and proved to increase with the radius of the sphere, reflecting what can be suggested by Figure 2.7 where the experimental results that adopted smaller radii tend to evolve with less abrupt rates of variation. The permeability k presented values in the order of magnitude of some propositions in the literature (Tverje & Nyashin (2010) and Kuo et al. (2010) in table 1.1) and became smaller for the larger sphere radii. The k values remained within the same order of magnitude of $10^{-15} m^4/Ns$ and were the parameters that, for the adopted solid phase definition, could most satisfactorily reproduce the system's energy loss using the adopted metrics.

The results presented in this section group the experimental results obtained for the different spheres used, considering the TMJ discs as homogeneous and showing the average value of the parameters found. The following section will discuss the observed difference between the disc zones.

2.6.2.2 Disc zones difference

Figure 2.26 shows the results for the same disc sample, being tested in the medial, central and lateral zones by a sphere of R=3.000 mm.

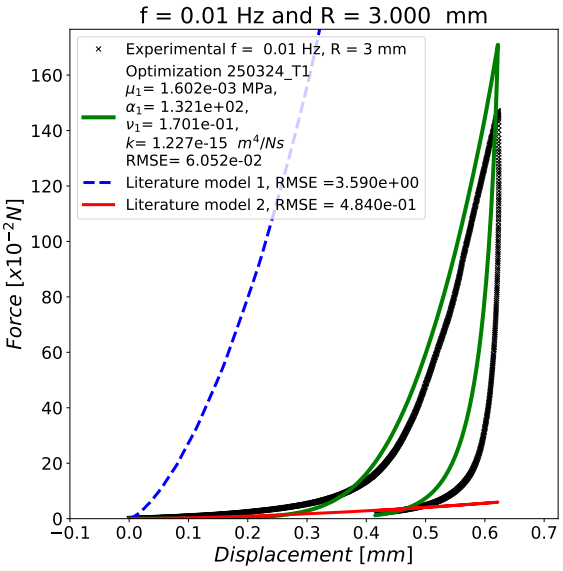

(a) Medial

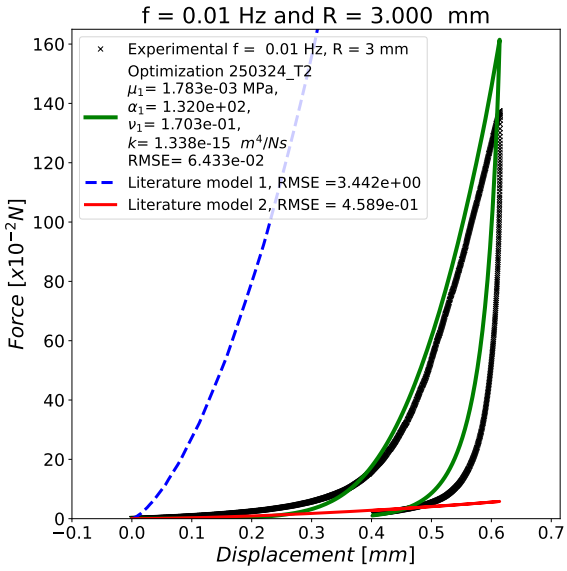

(b) Central

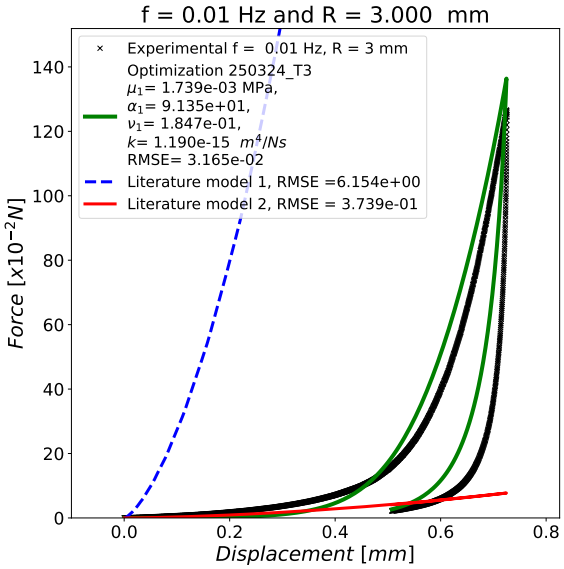

(c) Lateral

Figure 2.27: Sherical compression optimization results for different disc zones on TMJ sample 240311-Head2-Right with R=3mm and f=0.01Hz.

The three curves shown in Figure 2.27 present the same general behavior, with the same effects described previously. The difference in maximum force between experiments and model is also present here, where in the medial zone, for example, there is a difference between the experimental maximum force of 1.47 N and the simulated 1.70 N.

The optimization process calculated the RMSE so that all points on the curve had the same weight. That is, the reproduction of a specific aspect of the curve was not prioritized. Depending on the objective, it would be possible to set constraints so that the simulated maximum force value would be the same as the experimental one, for example. This would penalize the quality of the fitting at other points on the curve, and it was chosen to maintain the general reproduction of the curve for a more comprehensive representation of the material's behavior.

While Figure 2.27 presents the results for a single disc sample, Table 2.8 groups the average results obtained for each of the disc zones.

Zone	μ [kPa]	κ [kPa]	ν	α	$k \times 10^{-15}$ $[m^4/Ns]$
Medial	2.21 ± 1.69	2.50 ± 2.15	0.158 ± 0.037	87.38 ± 42.21	1.14 ± 0.27
Central	2.79 ± 2.44	3.14 ± 2.58	0.158 ± 0.053	77.95 ± 43.39	1.17 ± 0.65
Lateral	2.11 ± 0.90	2.25 ± 0.81	0.143 ± 0.051	85.80 ± 43.03	1.19 ± 0.25

Table 2.8: Optimized parameters for spherical compression simulations for all radii. General mean ± standard deviation.

In this case, all observed parameters remained close to each other and within the same order of magnitude. Maximum shear and bulk moduli values were found in the central zone and minimum values in the lateral zone. The lateral zone also presented the highest permeability, while the medial zone presented the lowest. Given the standard deviations, differences between locations were not significant.

The variation in the tested zone of the discs showed less variability between results than the variation in the sphere radius shown previously in table 2.8. This demonstrates some consistency between the different disc zones tested here and highlights the influence of varying test conditions (such as changing the sphere radius) on the parameters obtained.

Wu et al. (2017) analyzed the different zones of porcine discs and observed values on the order of 10^{-16} m^4/Ns for permeability (see table 1.1), with the medial portion being the most permeable and the lateral portion the least permeable. Even so, the boundary conditions applied in the other characterizations differ from the present study, in the case of Wu et al. (2017) being through confined compression. The same team (Wu et al., 2015) conducted shear tests on similar samples in a rotational shear chamber. They observed small variability in the shear modulus between different zones of the disc, with values ranging between 2.5 kPa and 4.0 kPa and consistent with the values described here (Wu et al., 2015).

By comparing the results with the input values of the optimizations in the literature (see table 2.6), it can be said that the solid phase definition values proposed in the work by Tappert et al. (2020) are in the same order of magnitude as those proposed here, with the exception of the parameter α and the permeability k, which had not been previously fitted.

Appendix D shows detailed results for the optimized parameters based on disc zone and sphere radius, through tables D.1,D.2 and D.3, allowing the individual assessment of each parameter's effect on the material properties.

2.6.2.3 Comparison of operators

The characterization performed in Tappert et al. (2020) used the same experimental procedure. To verify the operator's influence on the execution of the experiments and verify the repeatability of the analysis, the optimization process was also implemented on previous experimental results from six porcine discs tested in Tappert et al. (2020), representing 18 experiments with R = 1.750 mm.

Figure 2.28 shows two representative results for spherical compression on two discs from different studies.

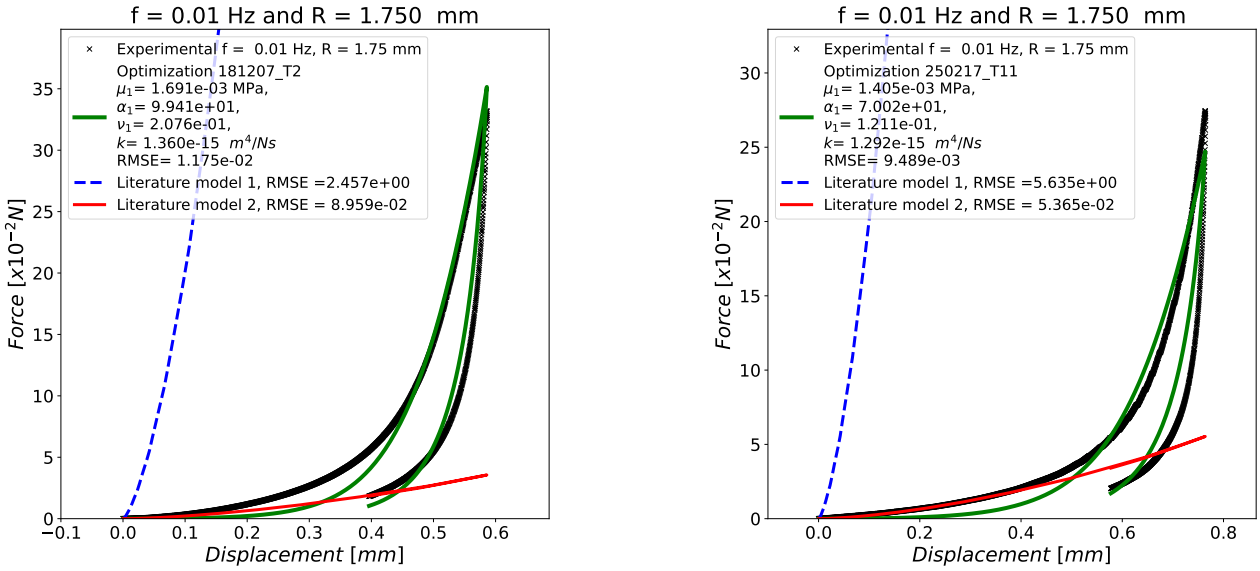

(a) Tappert (2020). (b) Present work.

Figure 2.28: Optimization results comparison between operators, for a spherical compression test of R=1.750 mm at f = 0.01 Hz. The force and displacement data from experiments from different test campaigns were passed through the same algorithm to obtain poromechanical parameters.

The experimental results obtained in the two test campaigns present similar curves. After optimization, the parameters in the table 2.9 were obtained.

Source	μ [kPa]	κ [kPa]	ν	α	$k \times 10^{-15}$ $[m^4/Ns]$
Tappert (2020)	1.97 ± 0.65	1.94 ± 0.57	0.120 ± 0.056	67.66 ± 24.31	1.25 ± 0.19
Present work	1.55 ± 0.54	1.67 ± 0.65	0.145 ± 0.031	76.55 ± 37.58	1.18 ± 0.26

Table 2.9: Optimized parameters for spherical compression simulations showing a comparison of the influence of operator. General mean ± standard deviation.

The experimental data obtained in the previous work could be treated in the same way here, yielding similar values for the material definition parameters. The remaining experimental results will be further processed using the optimization algorithm, allowing full use of the BIO2MS team's entire database for spherical compression results. Besides, it also points out a reasonable interindividual variability which is a strength of the experimental bench and the identification procedure.

2.7 Conclusion

This chapter presents the spherical compression experiments performed on porcine TMJ discs and the corresponding data processing. The testing methodology and the resulting force-displacement curves were discussed, where an increase in maximum force was observed for larger sphere radii and higher loading frequencies, while stiffness variations across disc zones were not significant.

The hyperelastic monophasic characterization approach, based on the work of Tappert (2020), was also introduced. The present work extends this framework by proposing model

updates, integrating these contributions into the discussion and applying the method to the experimental results obtained here.

In a biphasic approach, the force and displacement experimental results of the tests were compared with the simulated FE models, that sought to reproduce experimentally observed mechanics by applying material definitions proposed in the literature. It became evident that the literature parameters were not suitable for reproducing the experiments performed here, and an optimization process was applied to adjust their values for a better fit of the experimental curves. The optimized results consist of shear modulus ranging from 4.14 kPa (small radii) to 1.75 kPa (larger radii), close to the values of Wu et al. (2015) in porcine discs (2.5 to 4.0 kPa). The method also obtained a bulk modulus between 4.04 and 2.23 kPa and a permeability between 1.09 and 1.26 $\times 10^{-15} m^4/Ns$, comparable to data from Kuo et al. (2010) in human discs and Tverje & Nyashin (2010) in pigs (Table 1.1). Still, these results are not aligned with others studies in litereature also shown in table 1.1, in which permeability was defined on different orders of magnitude than the values obtained here.

The obtained results correspond to a solution found by the optimization algorithm and do not necessarily represent the only combination of parameters that approximates well the experimental curves. This is inevitable, since only one force-displacement relationship is used to calculate four optimization coefficients. To increase the reliability of these results, other characterization methods were also applied to be compared with the results obtained here, and will be described in the following chapter.

Chapter 3

Further exploration of poromechanical aspects and effects of tissue microstructure

One of the advantages of conducting non-destructive spherical compression tests is the ability to further explore the samples using other approaches. This chapter will present the follow-up to the spherical compression experiments, where I performed confined compression and direct permeation tests. Imaging techniques such as OCT, MRI, SEM, and DIC were also applied to the samples, seeking to deepen the analysis by relating the observed microstructure to the mechanics presented by the disc tissue.

3.1 Sample preparation

After performing the spherical compression tests in Chapter 2, the samples were stored again in a refrigerator at 4°C, allowing their recovery overnight. The following day, the sectioning scheme shown in Figure 3.1 was performed on all discs, with the aim of removing samples for future mechanical testing.

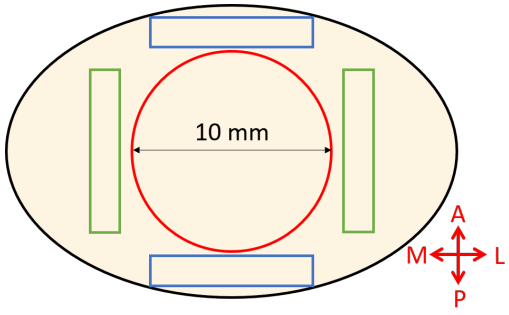

Figure 3.1: Scheme of disc indicating the central punched zone (red) with rectancular cuts for surrounding specimens in the anterior (A) and posterior (P) zones (blue) and in the medial (M) and lateral (L) zones (green).

Specimens in the medial, lateral, anterior and posterior portions (green and blue in Figure 3.1), were collected by means of a scalpel for tensile testing and SEM visualization, and will be discussed later.

Circular specimens from the central area of the disc (red in Figure 3.1) were cut with a 10 mm diameter circular punch. Both biopsy and leather punches (originally designed for cutting leather) were tested for preparing the discs. The advantage of using leather punches is that they maintained their sharpness for a longer time and could be re-sharpened if necessary, ensuring good cutting quality across all samples. The optimal solution associated the leather punch mounted on a vertical press to cut the samples. A cut sample is shown in Figure 3.2.

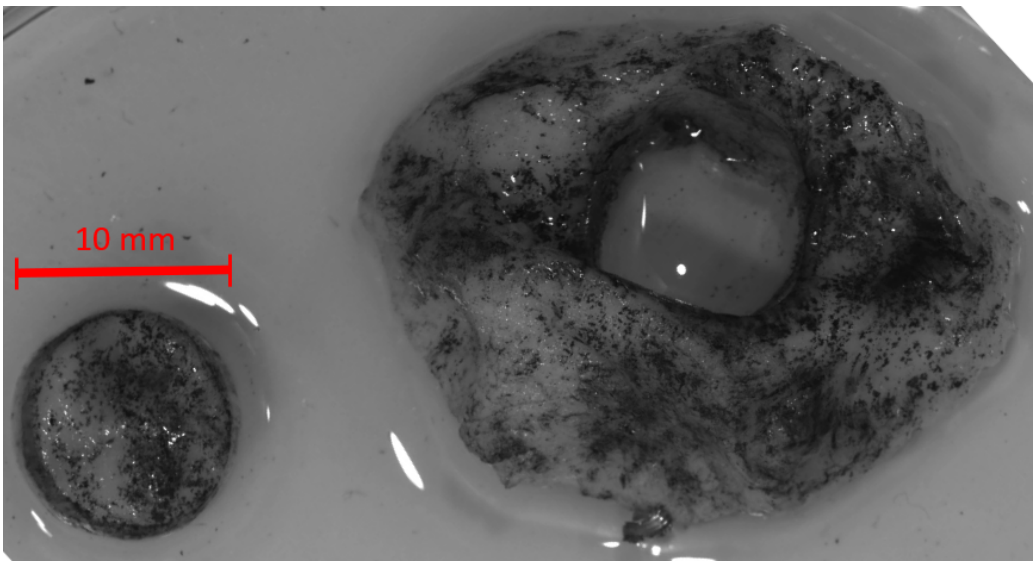

Figure 3.2: TMJ sample and cut specimen from its central zone, immediately after being cut. The disc presents dark markings on its surface that were placed over them with graphite powder for image correlation analysis purposes, to be discussed further. Specimen 230524-Head1-Right, corresponding to the same uncut sample shown in Figure 2.1.

The circular specimens were initially used in confined compression tests, which will be presented below.

3.2 Confined compression tests

3.2.1 Experimental testing setup

3.2.1.1 Development of confined compression bench

In order to perform the biphasic characterization of the TMJ discs, I developed an experimental bench and programs for the treatment of force-displacement data from confined compression tests.

The system used for spherical compression, consisting of the universal testing machine, the anti-vibration table, the hydration tank and the positioning stage were also used in the confined compression tests. Therefore, samples could be kept under the same physiological conditions of hydration, temperature and osmolarity during testing.

A system analogous to that illustrated in Figure 1.3b was developed to be compatible with the existing testing setup shown in Figure 2.4. The system consists of porous support and piston made of sintered stainless steel, commonly used in the chemical, food and pharmaceutical industries as a filter for gases and liquids, among other applications. According to the supplier, the porous steel has a permeability of the order of $1 \times 10^{-8}\ m^4/Ns$, approximately six orders of magnitude greater than the permeability of porcine TMJ discs tested in confined compression in Kuo et al. (2010). Despite being highly permeable, the filters have a rigid and flat enough surface to compress the material in a visually uniform manner. They were judged to be adequate in terms of permeability so as not to impede the flow leaving the sample, and the two porous structures are shown in Figure 3.3a and 3.3b. The superior part of the compressing piston in Figure 3.3b is made of Polyoxymethylene (POM), also known as acetal, polyacetal, and polyformaldehyde, which is used in precision parts thar require high stiffness and good dimensional stability, with low conductivity enabling the system to be isolated electrically. The porous base is placed over an acrylic support.

The lateral confinement chamber (Figure 3.3a) was machined from transparent acrylic, allowing specimen observation during compression to identify air bubbles, assess contact with the sample and facilitate possible test recording. The confining chamber has a height of 10mm and its internal diameter was designed for samples with a 10 mm diameter. The test setup with a TMJ sample inside is illustrated in Figure 3.3c.

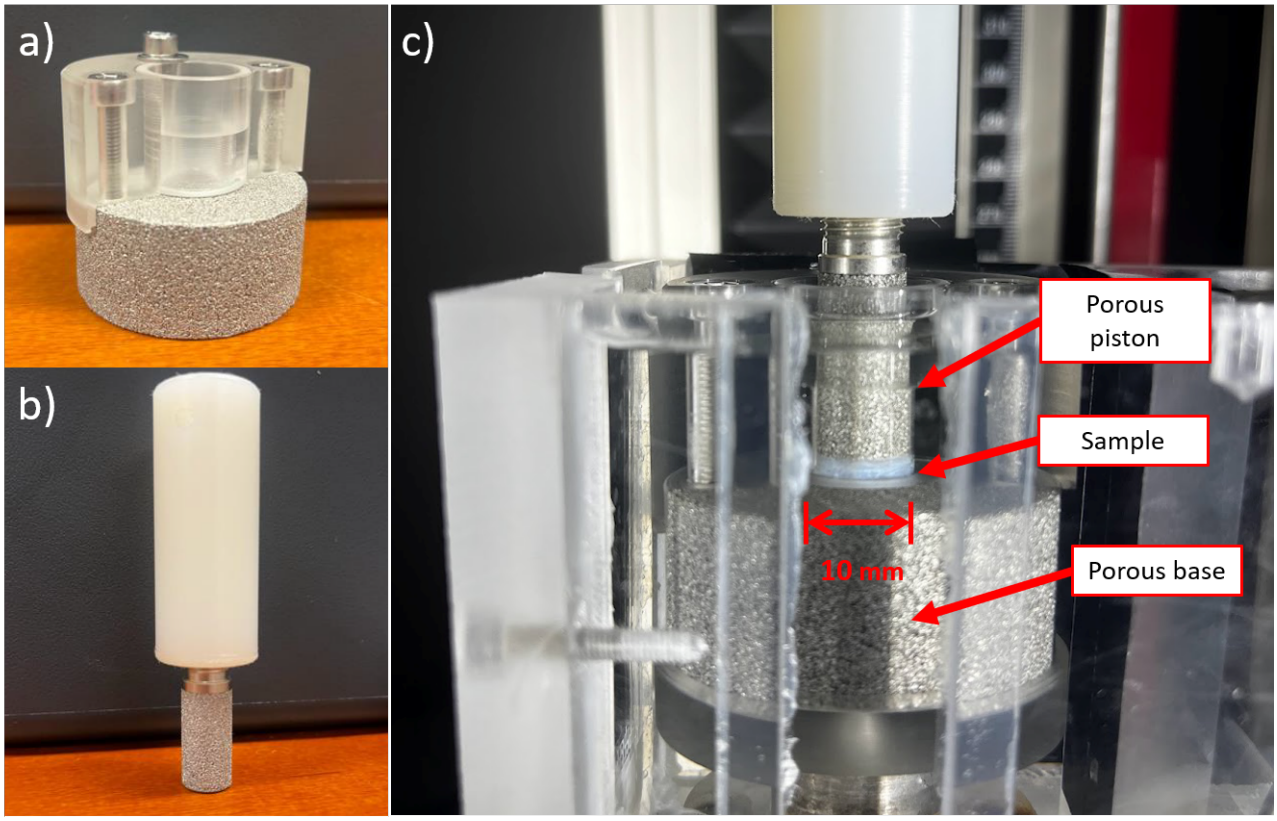

Figure 3.3: Confined compression device, showing a) porous base and lateral confinement chamber, b) porous piston and c) complete system submerged in saline solution during testing with a TMJ sample.

3.2.1.2 Test protocol

Preliminary tests on samples remaining from the work of Tappert (2020) were thawed and used for prior validation of confined compression system. During the creep tests, the main objective was to monitor the compression displacement of the samples, seeking to reach the equilibrium strain characterized by the stabilization of the height variation, and therefore obtain maximum information about the fluid flow within the material. It was observed that the application of a constant force of 4 N was sufficient to reach a sufficiently stabilized state over the period of 2 hours, which was considered adequate for carrying out the tests. This is also the period reported by Kuo et al. (2011b) as necessary to achieve a steady state in the compression of human discs submitted to creep.

Once the saline solution reached a temperature of 37°C in circulation, the samples were positioned inside the chamber as in Figure 3.3c. The piston was then slowly lowered, taking care to avoid bubbles formation and friction against the confinement chamber.

Once inside the chamber and close enough to the sample surface, a force of 4 N was then applied at 0.5 mm/s and maintained for a period of two hours. The theory requires an instantaneous application of force, which is difficult to be reproduced experimentally. This chosen velocity was the maximum that could be applied based on limitations of the experimental

setup. Faster approaches made it difficult for the Zwick machine control system to respond and regulate against inertial effects, particularly when the set force was reached. Nevertheless, when compared to the rest of the recorded data we assume that the imposed approach to the sample was close enough with the theoretical requirement. The displacement was recorded over the two hours and the piston was raised from the system at the end of the test, releasing the stress on the sample and allowing it to recover. Besides, force and displacement data are also collected during the loading phase and could also be used be used to feed a finite element model taking into account this phase using the forthcoming results as initial guess.

The same stiffness calibration procedure described in Appendix A was performed with the empty system. Since the components were not the same as for the spherical compression, this allowed the identification of the new system's stiffness ($k_m \approx 12.33$ N/mm), to be taken into account in machine's displacement during testing.

3.2.2 Parameter obtention through finite differences optimization

3.2.2.1 Compressive displacement analysis

The data treatment for the confined compression tests (see Section 1.2.1) was based on the biphasic model proposed by Selvadurai & Suvorov (2016) for soft biological tissues. This model, which assumes a hyperelastic solid phase, was selected for the project since it considers the large deformations of the material's ECM, introducing greater complexity through its nonlinear behavior. Nevertheless, it still allows the use of small-strain simplifications to recover the linear elastic case.

The theory proposes the simulation of a constant force applied over the upper surface of a cylindrical specimen during a creep test. The sample is radially confined, keeping then a constant cross section and allowing fluid exudation exclusively through its superior face. The material is assumed biphasic, with a liquid phase permeating and fully saturating the pores of a solid hyperelastic matrix. A one-dimensional column of height L is compressed by a constant stress σ_0 that acts instantaneously on its superior surface, being defined by the relationship $\sigma_0 = F/A$ between the applied force $\vec{F}$ to sample's cross section A. By assuming a Heaviside step function for the application of this compressive stress, it is possible to calculate the vertical displacement of the sample as a function of time. A symmetry condition is applied in the central part of the sample to match experimental boundary conditions and an example of uni-dimensional spacial division is shown in Figure 3.4.

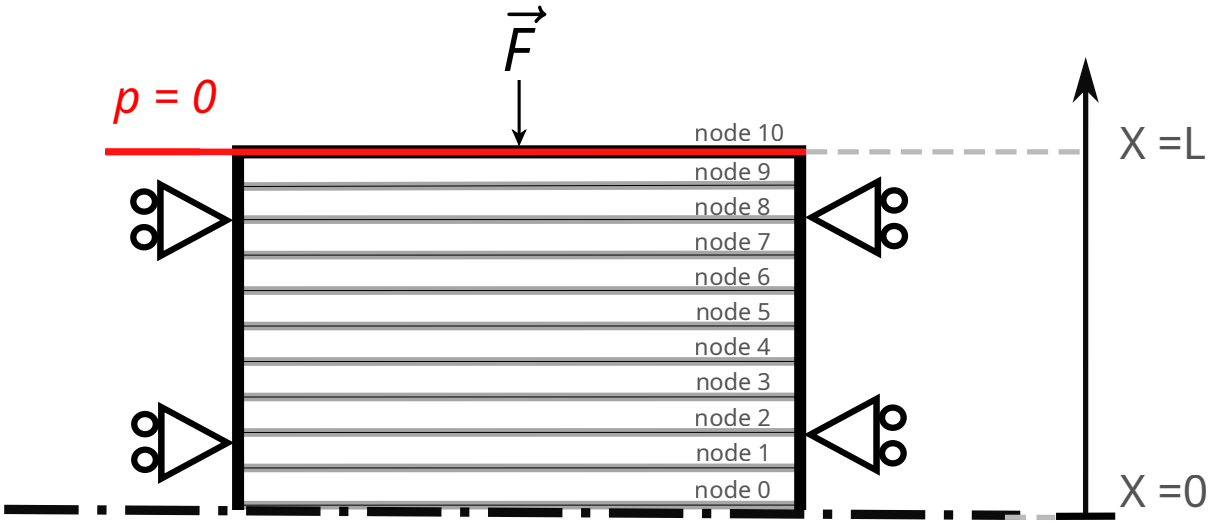

Figure 3.4: Uni-dimensional model proposed in Selvadurai & Suvorov (2016). Figure shows the example of a spacial division of the sample in 11 nodes, with a symmetry condition applied at the bottom of the sample (dashed line). Since it is a one-dimensional problem, the column can only be compressed vertically, through the action of the force vector $\vec{F}$. Zero pore pressure, shown in red, is applied at the top of the sample representing free fluid flow at the extremities of the sample.

The vertical displacement vector is $u = x - X$, where X is the independent initial coordinate system and x represents the coordinate system of the current position of an arbitrary point. The lateral and lower portions of the column have impermeable outlets with zero fluid velocity. The upper surface allows free flow, translated by a pore pressure equal to zero. The porous matrix in question is completely saturated with fluid and the flow within it is isotropic, described by Darcy's law (equation 1.12) with the adoption of constant hydraulic permeability. The displacement velocity of the solid phase ($\mathbf{v}_s$) is

$$\mathbf{v_s} = \frac{\partial u}{\partial t} \tag{3.1}$$

To define the hyperelastic solid phase, the reduced polynomial form was chosen as its strain energy density function

$$W = \sum_{i=1}^{N} C_{i0}(\bar{I}_1 - 3)^i + \sum_{i=1}^{N} \frac{1}{D_i}(J-1)^{2i} \tag{3.2}$$

$\bar{I}_1$ is the first invariant of the strain tensor $\bar{\mathbf{B}}$. C_{i0} and D_i are material constants. By choosing the second-order term of Equation 3.2, the strain energy density takes the form

$$W = C_{10}(\bar{I}_1 - 3) + C_{20}(\bar{I}_1 - 3)^2 + \frac{1}{D_1}(J-1)^2 + \frac{1}{D_2}(J-1)^4 \tag{3.3}$$

The left Cauchy-Green tensor $\bar{\mathbf{B}}$ is defined through the deformation gradient $\mathbf{F}$ (equation 1.6)

$$\bar{\mathbf{B}} = \bar{\mathbf{F}}\bar{\mathbf{F}}^T \tag{3.4}$$

where $\bar{\mathbf{F}} = J^{-1/3}\mathbf{F}$.

The Cauchy stress over the tissue's structure as a whole (σ) can be defined as a function of the effective stress acting on the hyperelastic porous matrix (σ_e) and the isotropic stress of

the fluid (p) (see equation 1.18). Through the development proposed in Selvadurai & Suvorov (2016), the equation 1.25 was obtained describing the axial effective stress σ_e acting over the solid phase.

By knowing the column's vertical displacement, it would then be possible to calculate the stress on the matrix through equation 1.25 and consequently the pore pressure through equation 1.18. It was demonstrated that the one-dimensional displacement may be defined by the following partial differential equation

$$\begin{aligned}\left(1+\frac{\partial u}{\partial X}\right)\frac{\partial u}{\partial t} = \frac{\hat{k}}{\eta}\frac{\partial^2 u}{\partial X^2}\Bigg\{&\frac{4}{3}\left(C_{10}+2C_{20}\left[\left(1+\frac{\partial u}{\partial X}\right)^{4/3}+2\left(1+\frac{\partial u}{\partial X}\right)^{-2/3}-3\right]\right)\times\\ &\times\left[\frac{1}{3}\left(1+\frac{\partial u}{\partial X}\right)^{-2/3}+\frac{5}{3}\left(1+\frac{\partial u}{\partial X}\right)^{-8/3}\right]+\\ &+\frac{32}{9}C_{20}\left[\left(1+\frac{\partial u}{\partial X}\right)^{1/3}-\left(1+\frac{\partial u}{\partial X}\right)^{-5/3}\right]^2+\\ &+\frac{2}{D_1}+\frac{12}{D_2}\left(\frac{\partial u}{\partial X}\right)^2\Bigg\}\end{aligned} \tag{3.5}$$

where $\hat{k}$ corresponds to the intrinsic permeability. The coefficients C_{10}, C_{20}, D_1, D_2 enable the adaptation of equation 3.3 to describe other material behavior laws. In both the work of Selvadurai & Suvorov (2016) and the present study, the second-order term related to volumetric deformation was neglected by setting $D_2 \to \infty$ for all cases. This allowed the elimination of one of the parameters to be optimized in the future, still enabling the definition of a compressible behavior for the material.

The neo-Hookean strain energy density function is obtained by defining $C_{20} = 0$. For small strains, the expression for $\partial u(L,t)/\partial X$ can be approximated by the first-order term of its Taylor series expansion. In this way, only its linear contribution term is maintained and the equation 3.5 simplifies to a linearized, linear elastic formulation. In this context, the resulting constants can be used to describe the linear elastic shear modulus (μ) and bulk modulus (κ)

$$\mu = 2C_{10} \qquad \text{and} \qquad \kappa = 2/D_1 \tag{3.6}$$

The displacement equation can be reduced in this case to

$$\frac{\partial u}{\partial t} = \frac{\hat{k}}{\eta}\left(\frac{8}{3}C_{10}+\frac{2}{D_1}\right)\frac{\partial^2 u}{\partial X^2} = \frac{\hat{k}}{\eta}\frac{E(1-\nu)}{(1+\nu)(1-2\nu)}\frac{\partial^2 u}{\partial X^2} \tag{3.7}$$

The linearized, neo-Hookean and reduced polynomial definitions will be also called LE, NH and RP respectively.

My first objective was then to develop a solution algorithm for equation 3.5. Selvadurai & Suvorov (2016) propose to use the explicit finite differences method for solving this problem. The derivatives were discretized by approximating them to their respective truncated Taylor series expansion terms:

$$\frac{\partial u}{\partial t}(X,t) = \frac{u(X,t+\Delta t)-u(X,t)}{\Delta t} = \frac{u_{i,j}-u_{i,j-1}}{\Delta t} \tag{3.8}$$

$$\frac{\partial u}{\partial X}(X,t) = \frac{u(X+\Delta X,t)-u(X,t)}{\Delta X} = \frac{u_{i+1,j}-u_{i,j}}{\Delta X} \tag{3.9}$$

$$\frac{\partial^2 u}{\partial X^2}(X,t) = \frac{u(X+\Delta X,t) - 2u(X,t) + u(X-\Delta X,t)}{(\Delta X)^2} = \frac{u_{i+1,j} - 2u_{i,j} + u_{i-1,j}}{(\Delta X)^2} \tag{3.10}$$

where $u_{i,j}$ indicates the vertical displacement of nodes for a discretized mesh over the length of the sample, for position i at an instant j. The spacial domain was divided into n parts of size ΔX, with $i \in [0, n]$ and the temporal domain divided into m parts of size Δt, where $j \in [0, m]$. By substituting equations 3.8, 3.9 and 3.10 into equation 3.5, the following relation is reached:

$$\begin{aligned}
u_{i,j} = u_{i,j-1} &+ \frac{\hat{k}\Delta t}{\eta \Delta X}\left(\frac{u_{i+1,j-1} - 2u_{i,j-1} + u_{i-1,j-1}}{\Delta X + u_{i+1,j-1} - u_{i,j-1}}\right) \\
&\times \left\{ \frac{4}{3}\left(C_{10} + 2C_{20}\left[\left(1 + \left(\frac{u_{i+1,j-1} - u_{i,j-1}}{\Delta X}\right)\right)^{4/3} \right.\right.\right. \\
&\left.\left.\left. + 2\left(1 + \left(\frac{u_{i+1,j-1} - u_{i,j-1}}{\Delta X}\right)\right)^{-2/3} - 3 \right] \right) \\
&\times \left[\frac{1}{3}\left(1 + \left(\frac{u_{i+1,j-1} - u_{i,j-1}}{\Delta X}\right)\right)^{-2/3} \right. \\
&\left. + \frac{5}{3}\left(1 + \left(\frac{u_{i+1,j-1} - u_{i,j-1}}{\Delta X}\right)\right)^{-8/3} \right] \\
&+ \frac{32}{9} C_{20}\left[\left(1 + \left(\frac{u_{i+1,j-1} - u_{i,j-1}}{\Delta X}\right)\right)^{1/3} \right. \\
&\left. - \left(1 + \left(\frac{u_{i+1,j-1} - u_{i,j-1}}{\Delta X}\right)\right)^{-5/3} \right]^2 \\
&+ \frac{2}{D_1} + \frac{12}{D_2}\left(\left(\frac{u_{i+1,j-1} - u_{i,j-1}}{\Delta X}\right)\right)^2 \Bigg\}
\end{aligned} \tag{3.11}$$

The initial condition of the problem must indicate zero displacement of all nodes in the beginning of the test

$$u_{i,0} = 0 \tag{3.12}$$

The lower boundary condition of fixed base represents zero displacement for $X = 0$

$$u_{0,j} = 0 \tag{3.13}$$

A Neumann boundary condition must be applied at the top of the sample, specifying the gradient of a field variable at the boundary, rather than its absolute value. In this case, $\partial u(L,t)/\partial X$ is to be obtained and will be called s_0 for simplicity. To define its value, the free fluid flow condition is applied at the upper boundary. This implies that pore pressure (p) is zero and has no contribution on the stress, meaning that $\sigma_e = \sigma_0$ for $X = L$ (see equation 1.18).

Under these conditons, the effective stress at the upper boundary, $\sigma_e(X = L, t)$, can be directly computed by simply dividing the applied loading force by the cross-sectional area of the structure, which are both constant. This stress is then substituted into equation 1.25 for $X = L$, and the real root of the resulting equation is the desired value of s_0.

Hence, by knowing s_0 and through $\partial u(L,t)/\partial X = s_0$, the first and second derivatives of displacement from equations 3.9 and 3.10 are

$$\frac{\partial u}{\partial X}(L,t) = s_0 = \frac{u_{n,j} - u_{n-1,j}}{\Delta X} \tag{3.14}$$

$$\frac{\partial^2 u}{\partial X^2}(L,t) = \frac{2s_0\Delta X - 2u(L,t) + 2u(L-\Delta X,t)}{(\Delta X)^2} = \frac{2s_0\Delta X - 2u_{n,j-1} + 2u_{n-1,j-1}}{(\Delta X)^2} \tag{3.15}$$

Equations 3.14 and 3.15 may then be substituted into equation 3.5 and the upper boundary condition may be calculated for each instant of time through the expression

$$\begin{aligned}
u_{n,j} = u_{n,j-1} &+ \frac{\hat{k}\Delta t}{\eta(1+s_0)}\left(\frac{2s_0\Delta X - 2u_{n,j-1} + 2u_{n-1,j-1}}{(\Delta X)^2}\right) \\
&\times \left\{\frac{4}{3}\left(C_{10} + 2C_{20}\left[\left(1+\left(\frac{u_{n,j-1}-u_{n-1,j-1}}{\Delta X}\right)\right)^{4/3}\right.\right.\right. \\
&\left.\left.\left. + 2\left(1+\left(\frac{u_{n,j-1}-u_{n-1,j-1}}{\Delta X}\right)\right)^{-2/3} - 3\right]\right) \\
&\times \left[\frac{1}{3}\left(1+\left(\frac{u_{n,j-1}-u_{n-1,j-1}}{\Delta X}\right)\right)^{-2/3}\right. \\
&\left. + \frac{5}{3}\left(1+\left(\frac{u_{n,j-1}-u_{n-1,j-1}}{\Delta X}\right)\right)^{-8/3}\right] \\
&+ \frac{32}{9}C_{20}\left[\left(1+\left(\frac{u_{n,j-1}-u_{n-1,j-1}}{\Delta X}\right)\right)^{1/3}\right. \\
&\left. - \left(1+\left(\frac{u_{n,j-1}-u_{n-1,j-1}}{\Delta X}\right)\right)^{-5/3}\right]^2 \\
&+ \frac{2}{D_1} + \frac{12}{D_2}\left(\left(\frac{u_{n,j-1}-u_{n-1,j-1}}{\Delta X}\right)\right)^2\Bigg\}
\end{aligned} \tag{3.16}$$

An algorithm was implemented in Python and integrated our team's python library bio2mslib to solve the problem, with the objective of identifying $u_{i,j}$ for all values of i and j. Knowing the equation 3.11, it is possible to establish a value for $u_{i,j}$ based on displacement for the same node in a previous time increment $u_{i,j-1}$ and of its adjacent nodes $u_{i+1,j-1}$ and $u_{i-1,j-1}$. The initial condition 3.14 and the two boundary conditions 3.15 and 3.16 determine the displacements at the extremities of the mesh in which $i = 0$, $i = n$ and $j = 0$.

By means of a loop going through the different time instants and positions, it was possible to apply the values of k, C_{10}, C_{20} and D_1 that were exemplified Selvadurai & Suvorov (2016). The same results for displacement of upper surface and fluid pressure at lower surface from Selvadurai & Suvorov (2016) shown in Figure 1.5 were obtained.

3.2.2.2 Optimization algorithm

After validating the code with the example in Selvadurai & Suvorov (2016), it was possible to calculate the displacement, stress and pore pressure given known initial material parameters. To adapt the algorithm for the identification of new parameters, it was necessary to implement an optimization based on the experimental results.

Experimentally, force application is not instantaneous. The testing machine naturally fluctuates around the target value, mainly in the beginning of the test due to its regulation against

inertia of the charging phase. To compensate that, the experimental curve was truncated by eliminating all preceding displacement values in which the applied force was lower than 99.9% of the creep force, as shown in Figure 3.5. To facilitate this identification, a noise elimination process using the moving average was implemented through the Python NumPy library.

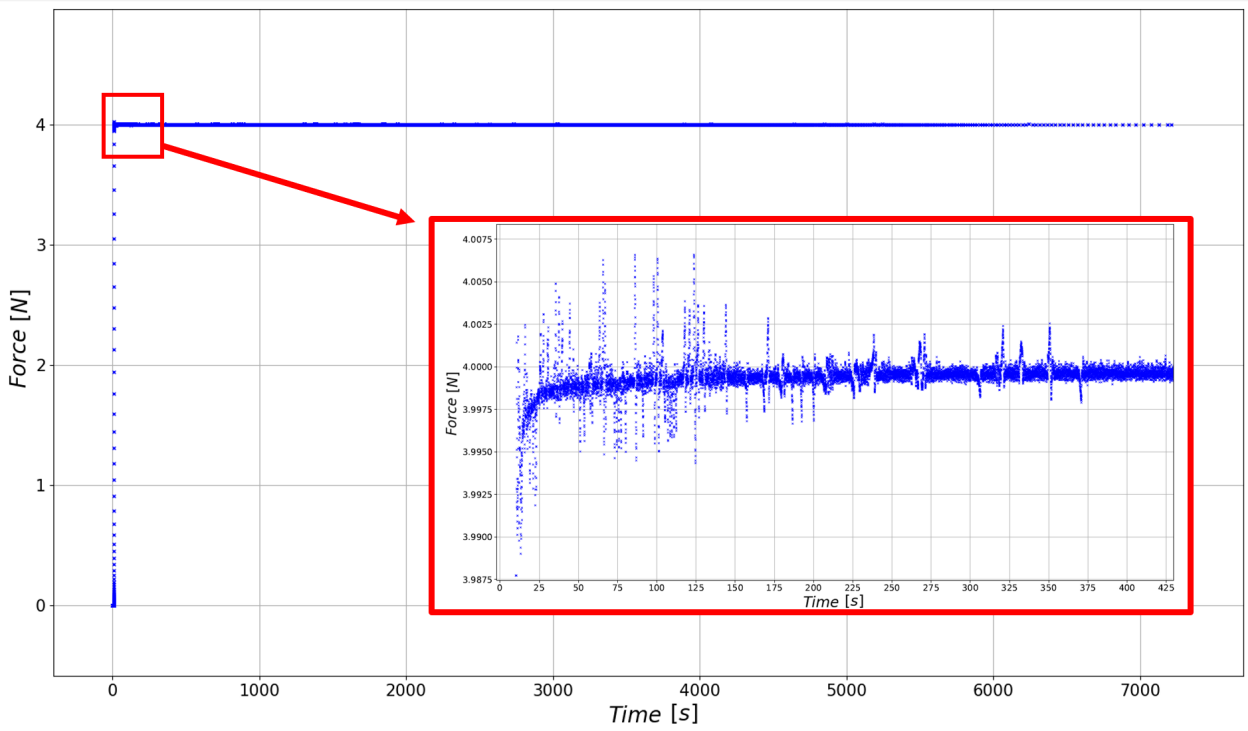

Figure 3.5: Confined compression results for sample 230524-Head1-Left. The force was recorded over time, and the transition to steady force creep load is shown in the zoom in the beginning of the curve.

To define the parameters, the COBYLA method (see section 2.6.1) was used through the Scipy Python library. Since this time the force is considered constant, the method compares the experimental curve to the model's displacement and reduces the least squares error for the displacement :

$$\mathrm{RMSE} = \sqrt{\frac{1}{n}\sum_{i=1}^{n}\left(u_i^{\mathrm{exp}} - u_i^{\mathrm{sim}}\right)^2} \tag{3.17}$$

where u_i^{exp} corresponds to the experimental creep displacement of the piston and u_i^{sim} to the simulated upper node surface displacement. In order to minimize the RMSE, the program iteratively adjusts the simulation input parameters $\hat{k}$, C_{10}, C_{20}, and D_1. Constraints were applied to ensure that these parameters remain within a range of physically coherent values.

The optimization constraints were defined to allow the limitation of the Poisson's coefficient in the LE optimizations, so that the algorithm could search for coefficients to be used in other FE simulation contexts in the future, if necessary to limit them. Thus, through the relationship between coefficients shown in the equation 3.6 and the definition of the Poisson's coefficient with respect to the bulk and shear modulus, the equation 3.18 was established to guarantee a consistent value of nu.

$$C_{10} \leq \frac{6(1-2\nu_{min})}{4D_1(1+\nu_{min})} \tag{3.18}$$

In the case of the simulations performed in this section, $\nu_{min} = 0$. A set of initial parameters based on the parameters of Model 2 (from table 2.6) was used as starting values for the LE results. Once obtained, the LE parameters were fed as input values into the NH and RP optimization processes.

3.2.3 Results and discussion

The results for the confined compression tests for eight TMJ discs were obtained and the data processing procedure described above was applied. Figure 3.6 shows an example of a raw machine displacement result, followed by the portion of the curve that was used for data processing.

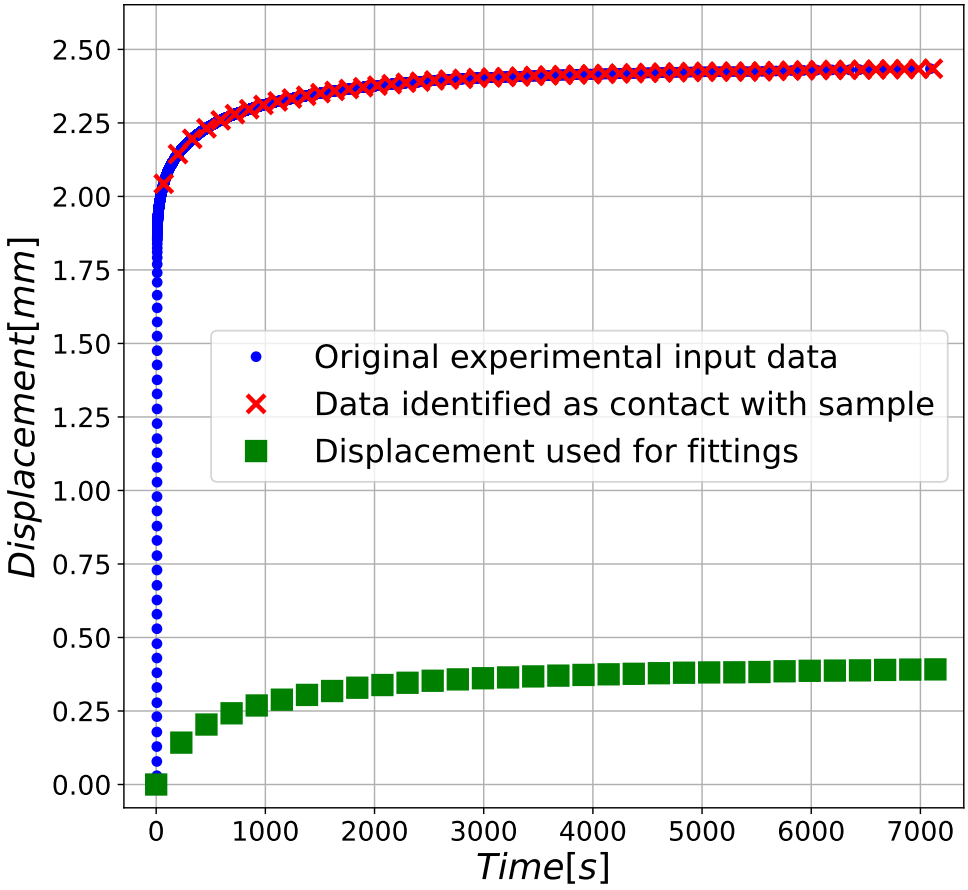

Figure 3.6: Experimental displacement for confined compression of a TMJ sample 230524-Head1-Left, showing the identification of the portion of the data to be used in fitting.

The displacement of the original curve (blue dots) shows a high variation at the beginning of the test, approaching the desired Heaviside function displacement. The piston was positioned close to the sample prior to testing, and the high initial acceleration of the curve indicates the phase in which contact had not yet been established. The experimental curve was truncated according to the contact definition described criterion and is shown in green (squares).

It is worth noting that the results shown in the graph in Figure 3.6 represents raw data without noise reduction. The experimental curves present the creep aspect expected according to another similar study in the literature (Kuo et al., 2010). The progressive evolution of the displacement due to the creep phenomenon and the tendency of the sample to reach a stabilized plateau can be observed towards the end of the test. Figure 3.7 shows a sample being compressed in different instants.

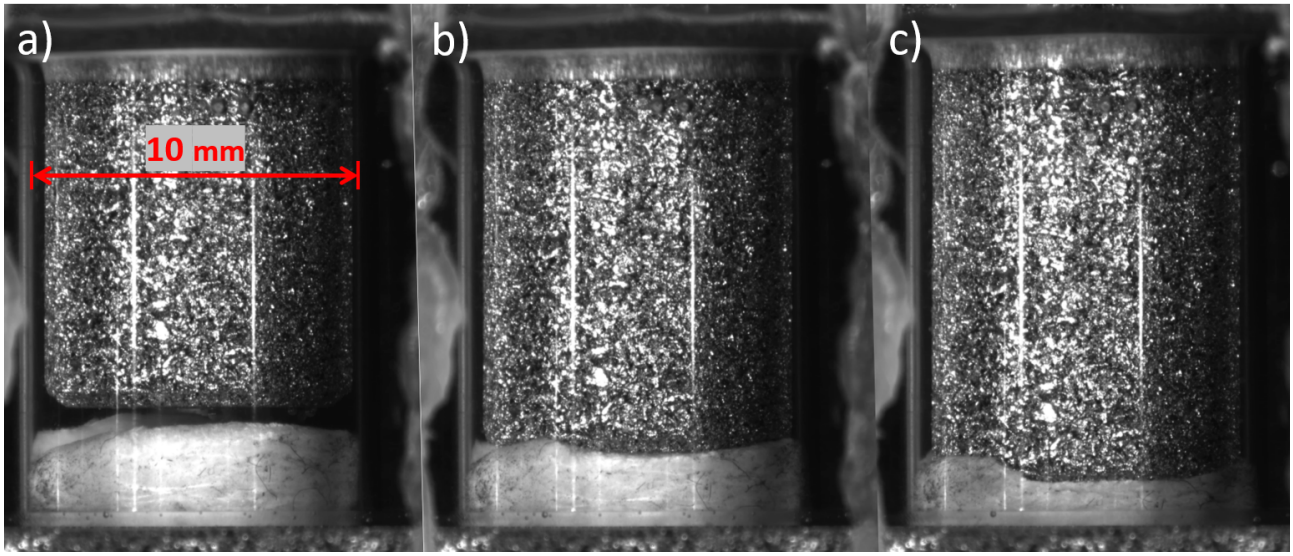

Figure 3.7: Confined compression a) before the beginning of the test, b) immediatly in contact establishment and c) after 2h of creep test. Sample 230524-Head1-Left.

Figure 3.7 represents the instant before contact (a) (corresponding to the beginning of the blue curve composed of dots in Figure 3.6), the approximate instant of contact establishment (b) and the end of the test (c) (respectively the beginning and end of the red curve (crosses) in Figure 3.6). Immediately after contact, it is possible to observe the lateral expansion of the sample, which ensures a certain tightness and establishes the lateral confinement condition.

Figure 3.7 shows some of the experimental difficulties inherent to this type of test. The sample had an approximately cylindrical geometry, but imperfections were visible due to deformations after cutting. The upper and lower surfaces of the disc naturally present a slight concavity. Even so, during the compression process, the sample soon assumes a flatter surface, adjusting to the shape of the piston and the base. Unlike other studies that remove the upper and lower surfaces of the disc (Kuo et al., 2010; Wu et al., 2017; Tverje & Nyashin, 2010), the present work purposely kept the sample surfaces intact. This allowed us to explore its behavior in conditions closer to physiological ones, not measuring the permeability of just the central layer of the material, but over its whole inferior-superior length.

Obtaining a cylindrical chamber machined from acrylic with good transparency is not simple. Acrylic tends to melt depending on the machining conditions and obtaining transparency requires the turning conditions be well parameterized. The clearance between the piston and the chamber, however, allows the sample to penetrate this gap and slightly deviate from the ideal experimental conditions. The presence of this gap is inevitable and the presented design is the result of an iterative process of clearance variation to eliminate friction between the two parts. Avoiding this friction does not depend only on the machining results, but also on the degree of alignment between all the components of the system illustrated in Figures 2.4 and 3.3.

According to Archimedes' principle, as the piston penetrates the fluid, the volume of displaced fluid increases and consequently the buoyant force also increases, affecting the machine's force measurement. Simultaneously, once a portion of the piston is submerged, the fluid infiltrates its pores, reducing this displaced water volume and consequently the buoyant force. Considering the worst case scenario, with a solid piston of 10 mm diameter and height, the maximum force measured would be around 7 mN, which was disregarded given the 4 N applied in the test. These effects cannot be neglected in the case of tests involving lesser forces in other contexts.

After performing the tests, the results processing algorithm was applied to the samples. A

spatial division identical to that illustrated in Figure 3.4 was considered. The optimization result for a sample with an initial height identified as approximately 1.4 mm is shown in Figure 3.8.

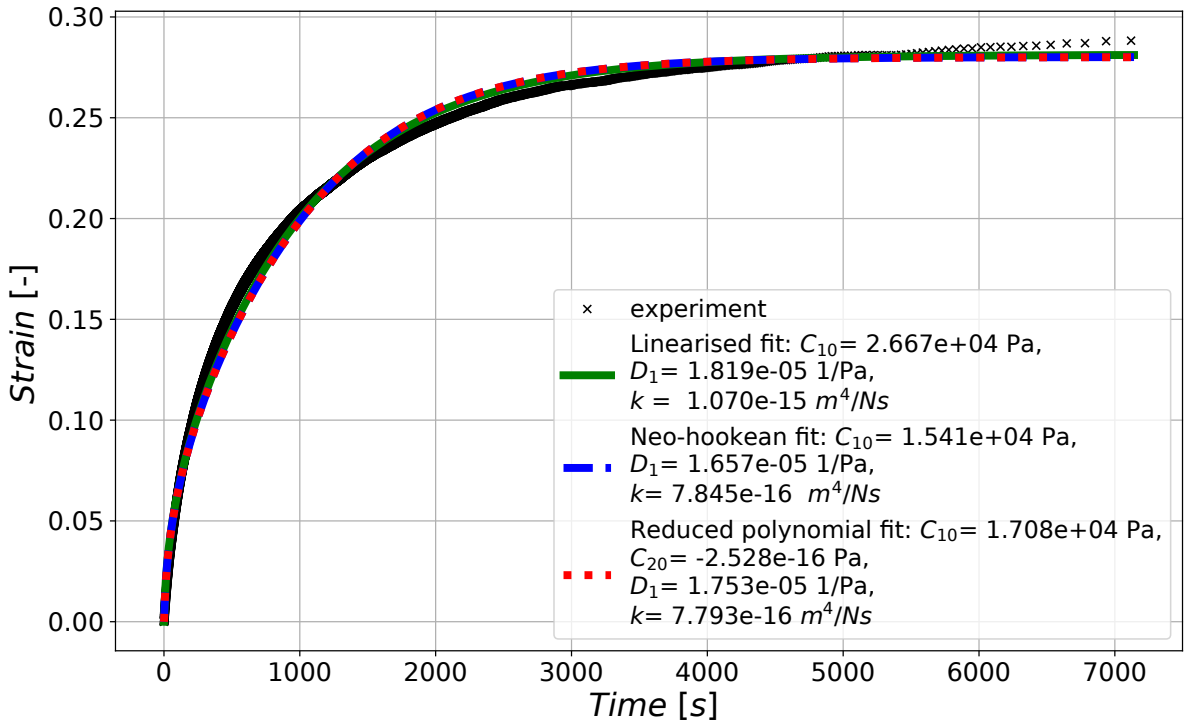

Figure 3.8: Experimental fitting of confined compression results for sample 230524-Head1-Left, with strains calculated based on the displacements of sample's superior surfaces. The parameters obtained for the three model definitions are provided. Strain here was calculated based on initial configuration L/L_0.

Figure 3.8 shows the fitting performed for the application of the three different solid phase definitions, for the experimental result of Figure 3.6. The results were close to the experimental curve (RMSE in the order of 1×10^{-11} for all of them) and were able to numerically reproduce the creep effect, reaching a stabilized strain around 28%.

Even though the three curves were able to reproduce the experimental one, the permeability and numerical values of the material parameters are different. To understand one of the causes of this phenomenon, we can refer to the results presented in the original work of Selvadurai & Suvorov (2016), shown in Figure 1.5, for a simulation where similar material parameters were used ($C_{10} = 115384$ Pa, $D_1 = 4 \times 10^{-6}$ 1/Pa, $k = 3 \times 10^{-11} m^4/Ns$ and $C_{20} = 0$ Pa for NH and LE or $C_{20} = 300000$ Pa for RP). Despite having numerically similar values, the result they presented illustrates three distinct displacement profiles (see Figure 1.5). The characterization of a material behavior is not given exclusively by the numerical values of the parameters, but also by how they interact in the constitutive equations. In other words, the displacement response to compression depends on the set of numerical values associated to a definition of displacement, that depends on the strain energy density function. As a consequence of this interdependence, it is expected that the application of an optimization process seeking to reproduce the same experimental curve with different associations of parameters requires their values to be distinct, compensating for their different patterns of interaction in the system energy.

In this case illustrated in Figure 3.8 the solid phase definition parameters remained in the same order of magnitude. For permeability, the observed values were $k = 1.07 \times 10^{-15} m^4/Ns$ for LE, while NH and RP definitions had closer results of $k = 7.845 \times 10^{-16} m^4/Ns$ and $k = 7.793 \times 10^{-16} m^4/Ns$, respectively. These values were consistent with what was observed in

confined compression on cylindrical microtomed human samples, where $k = 3.74 \times 10^{-15} m^4/Ns$ (Kuo et al., 2010) and on cylindrical microtomed porcine samples where $k = 8.8 \times 10^{-16} m^4/Ns$ (Wu et al., 2017). The exact force values applied in these studies from literature were not published and the experimental conditions differ in the preparation of the specimens, since the samples in the cited studies were cut with a microtome to obtain more plane surfaces.

Let us consider the configuration and spatial division of Figure 3.4, where node number 10 corresponds to the upper surface (which will have the same displacement as the piston) and node number 0 to the portion on the axis of symmetry (with zero displacement). Figure 3.9 shows the displacement (u) calculated over the test time for each of the nodes and all model definitions.

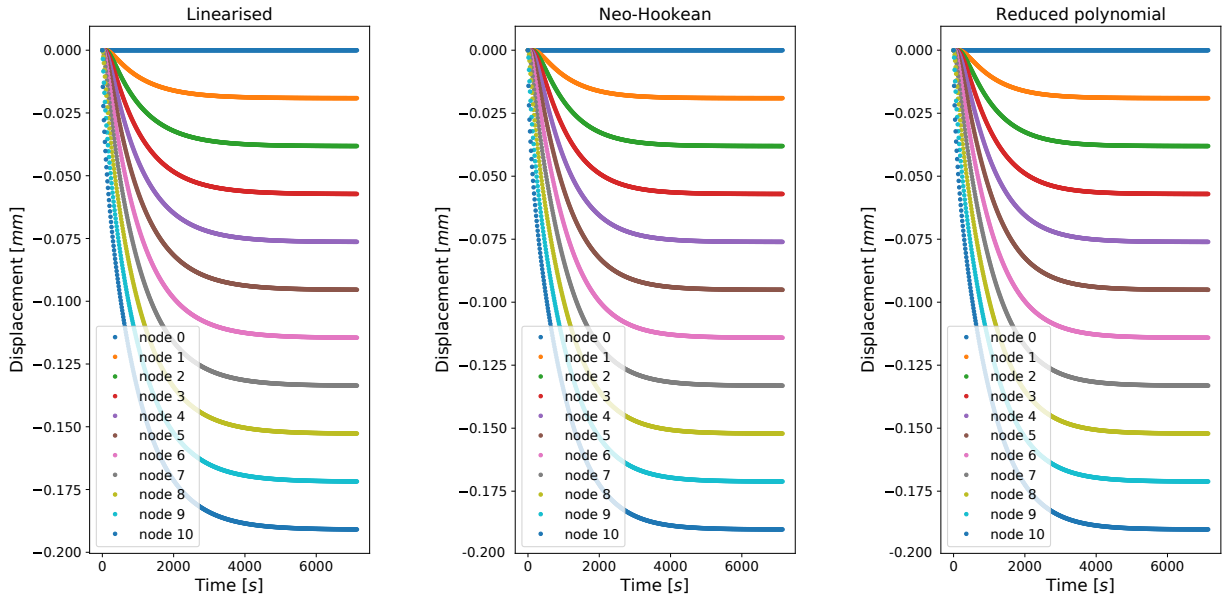

Figure 3.9: Simulated displacement for each of the nodes over the length of the test, for different model definitions for sample 230524-Head1-Left. The measured displacement corresponds to the solution of the partial differential equation governing the column displacement, calculated for the nodes of the symmetric one-dimensional mesh defined to represent the uniaxial compression of the TMJ disc specimen.

The variation of solid phase definitions of the material did not result in significant differences between the results. This is to be expected, given what was observed in Figure 3.8, where all simulated displacements were able to adjust in a similar way to the experimental one.

Initially, the symmetrical column under compression, has a height of around 0.7 mm (sample originally with a thickness of 1.4 mm). When partitioned as in Figure 3.4, the model presents elements contained between two adjacent nodes with a height of 0.07 mm. For instance, the results show that node number 10 moved the entire distance traveled by node 9 plus an increment, in this case measured as approximately 0.019 mm. The same relative displacement of 0.019 mm was observed for all other nodes. Thanks to this, it can be stated that once stabilization was reached, the adjacent nodes remained equidistant. This implies that, although this simulation considers constant permeability, future models in which strain affects the permeability would still have a homogeneous permeability tensor throughout the structure at each instant.

The inertial effects were disregarded in the model, which is consistent with what was imposed experimentally. Due to the low strain rate in a quasi-static loading, the compression of the column propagated uniformly. In the current context, both experimentally and numerically, the accelerated compression is disregarded for occurring in an infinitesimal time span, since the

application of the load is considered as a form of a Heaviside function.

This linearly distributed displacement field between the nodes is not observed in the case of effective stress. Once the displacement was calculated, the effective stress could be estimated using the equation 1.25. The result is illustrated in figure 3.10 for the LE model.

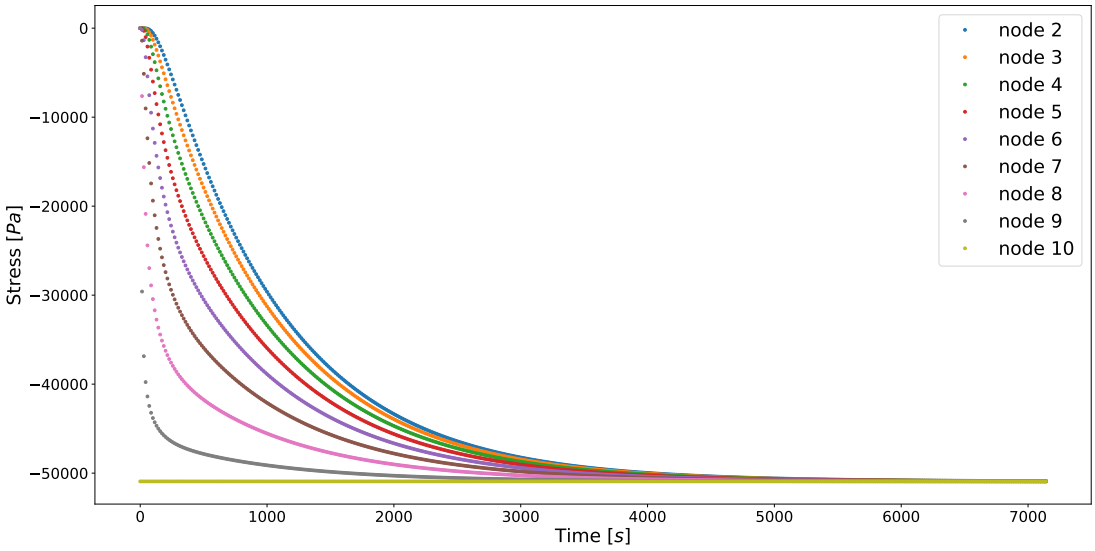

Figure 3.10: Effective stress evolution over the nodes of a LE solution. Results are based on the calculated displacement, that allowed to calculate the stress acting on the solid phase of the material for the experimental results of Sample 230524-Head1-Left.

The displacements were similar for all three definitions, as were the stress and pore pressure behaviors. Therefore, it is sufficient to present only one representative curve in Figure 3.10, which corresponds to the LE simulation.

At the beginning of the test, the stress is concentrated exclusively on the upper surface of the column and remains constant throughout the whole duration of the test for node 10. The assumed stress is approximately -51 kPa (negative to represent compression), calculated from the 4 N force applied to the circular area with a diameter of 10 mm. Immediately at the beginning of the test, the other inferior nodes have not yet had the stress transferred to their solid phase, and that's why they all begin at zero stress. As time progresses, the force begins to have an increasing effect on the ECM of the adjacent nodes, until at the end of the test it is estimated that all the stress applied to the top of the column is distributed uniformly over the whole structure's solid phase, represented by the value of -51 kPa for all nodes.

As previously mentioned, the fluid is a major actor in tissue's resistance to the compressive loads. Assuming this postulate, Figure 3.10, showing that solid phase solicitation increases with time, indicates the expulsion of fluid from inside the pores of the material, which will have increasingly less impact on the support of the column. Using the equation 1.18, the fluid pressure was also calculated.

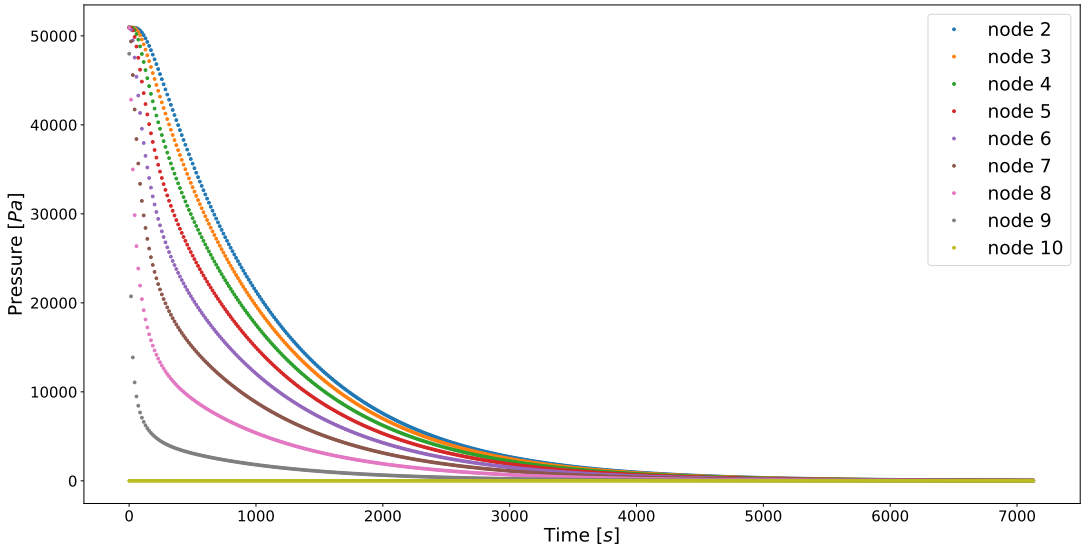

Figure 3.11: Pore pressure evolution over the nodes of a LE solution, calculated once the effective stress was known. Sample 230524-Head1-Left.

Figure 3.11 indicates a zero pressure for node 10 on the upper surface, which is an imposed boundary condition (see Figure 3.4). The compressive stress is immediately distributed to the fluid at the other nodes, turning into pore pressure and decaying as the fluid flows out. The pressure decays faster the closer the node is to the surface, indicating a non-uniform fluid distribution during the test. According to the assumed symmetry, the same logic applies to the lower surface of the sample.

For the results assuming the linear elastic approach for small strains, it is possible to define the shear modulus, bulk modulus and Poisson's ratio from the coefficients obtained by the optimization. Table 3.1 shows the results.

Disc	$k \times 10^{-15}$ $[m^4/Ns]$	C_{10} [kPa]	D_1 [1/kPa]	μ [kPa]	κ [kPa]	ν
230111-Head1-Left	1.86	21.72	0.033	43.44	60.12	0.209
230111-Head1-Right	2.11	21.81	0.0214	43.62	93.31	0.298
230524-Head1-Left	1.07	26.67	0.0182	53.33	110.00	0.291
230524-Head1-Right	9.26	20.54	0.0624	41.08	32.07	0.051
240311-Head1-Left	5.43	9.61	0.100	19.23	19.92	0.135
240311-Head1-Right	1.17	25.01	0.0453	50.02	44.19	0.089
240311-Head2-Left	2.21	24.56	0.0228	49.12	87.65	0.264
240311-Head2-Right	1.99	25.61	0.0447	51.23	44.70	0.085
Mean $\pm$ std	1.49 ± 0.63	21.94 ± 5.43	0.044 ± 0.027	43.88 ± 10.85	61.50 ± 31.37	0.178 ± 0.094

Table 3.1: Material parameters for linearized approach, obtained through confined compression optimization.

The complete results for each of the samples with other constitutive definitions are shown in Appendix E, in the table E.1. The mean values for each of them, associated to the standard deviation are presented in table 3.2.

Model	k $[m^4/Ns]$	C_{10} [kPa]	D_1 [1/kPa]	C_{20} [kPa]
LE	$(1.49 \pm 0.63) \times 10^{-15}$	21.94 ± 5.43	0.044 ± 0.0274	–
NH	$(1.8 \pm 0.47) \times 10^{-16}$	11.96 ± 4.39	0.034 ± 0.0240	–
RP	$(1.14 \pm 0.48) \times 10^{-15}$	11.14 ± 5.28	0.026 ± 0.0137	$(-2.56 \pm 3.11) \times 10^{-19}$

Table 3.2: Material parameters by model, showing mean results ± standard deviation (n=8).

The RP definition presented a negative and negligibly small value of C_{20} compared to C_{10}. The parameters were limited to positive numerical values, and the reported value C_{20} was a numerical approximation of the algorithm, and it can be considered that its value converged to zero. This effect was observed for all optimization simulations, indicating that the additional RP term does not necessarily represent a better convergence of the fitting compared to NH.

Even so, considering $C_{20} \approx 0$ kPa, a distinction is observed in the other parameters of NH and RP due to the lack of uniqueness of solution for this multi-parameter optimization problem. This difficulty is inherent to this type of analysis and becomes more pronounced as more optimization variables are added to the equations. Only two sets of data (force and displacement) are used to obtain, in this case, four parameters. This is one of the limitations of the biphasic characterization by this type of approach.

Nevertheless, the main interest of the project is to obtain a method to predict the behavior of the material in different contexts. If the found solution satisfies the experimental observations with good precision, it can be considered valid for practical purposes. The focus is to find a set of parameters that guarantees reproducibility.

The characterization, however, can be improved by including other types of tests. Through direct permeation tests, for example, it is possible to isolate the permeability parameter from the solid phase definitions, contributing to a more robust and independent identification of the other parameters involved.

3.3 Direct assessment of permeability

3.3.1 Development of a custom bench for direct permeation tests

The same samples used in the confined compression tests were subsequently tested in direct permeation. Direct permeation experiments (see Section 1.2.2) measure hydraulic permeability by imposing a fluid flow through the material with it being induced by external factors, in contrast to the confined compression method, in which the variation of the pore volume drives the fluid.

In this manner, it is possible to measure permeability through a different approach by imposing a theoretically constant strain to the tissue. It's not necessarily a measurement performed on undeformed tissue, since a clamping strain is applied on the sample to ensure tightness and the flow itself deforms the material (Ateshian, 2017). Even so, a stabilized flow regime, when reached, allows the identification of the degree of compression at which the measurement is performed and enables exploring the relationships between permeability and imposed strain (equations 1.14 and 1.15).

In order to conduct such tests to the disc samples, this thesis was supported by Marine Bekrar's master project (Bekrar, 2024). The project was carried out with the team involved in this current research and focused on the development of a device for measuring the permeability of soft biological tissues in collaboration with the Laboratory LMGC from Montpellier, France and the ANR project HyCareMat.

The purpose of the device was to allow the imposition of a unidirectional fluid flow through the sample, based on the principle shown in Figure 1.6. By measuring the fluid volumetric flow and the pressure difference between inlet and outlet, it would be possible to apply the equation 1.26 to calculate the permeability. The design of the chamber in which the sample is positioned is shown in Figure 3.12a. The device was machined in transparent acrylic and is shown in Figure 3.12b.

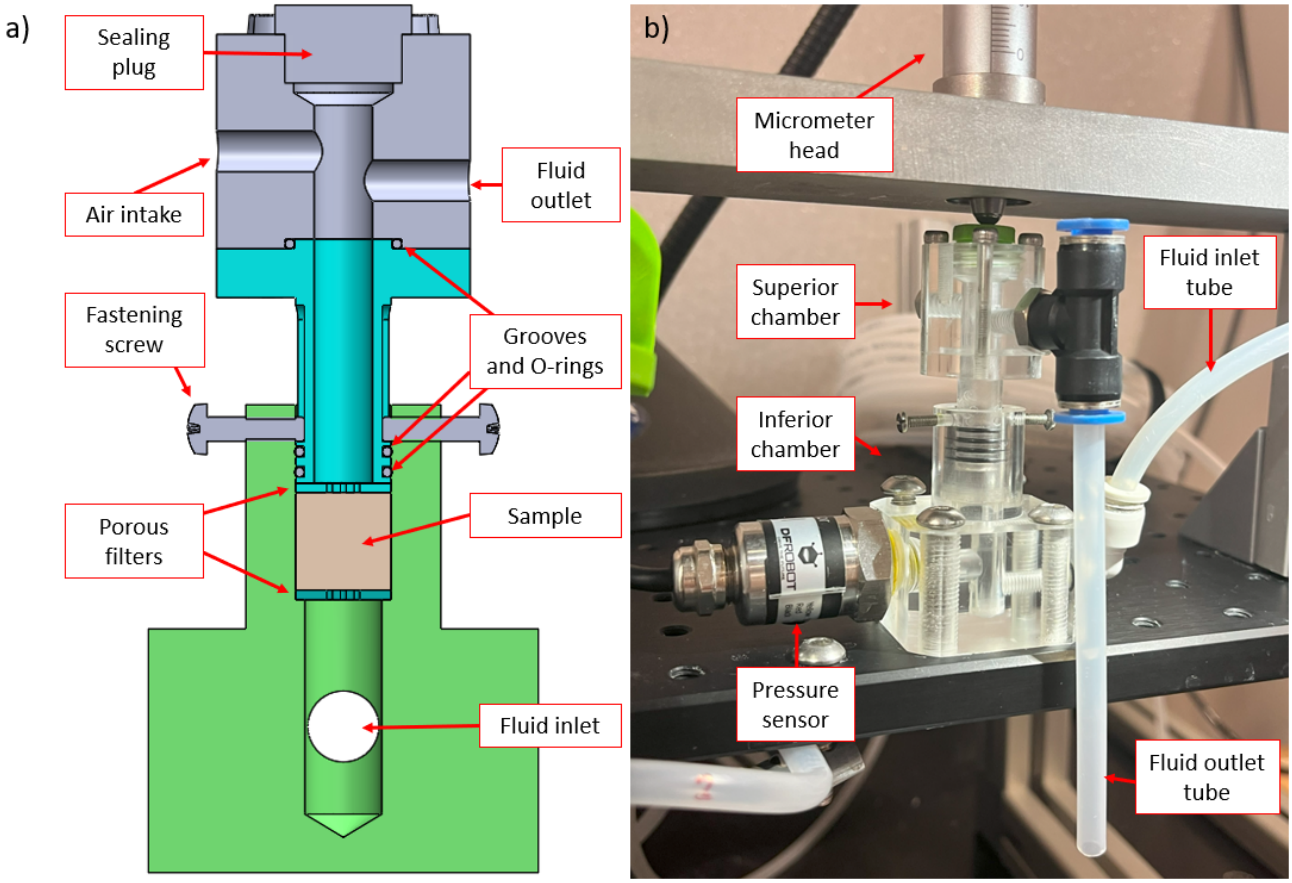

Figure 3.12: a) Design of the direct permeation device and b) manufactured prototype.

The sample is placed between two porous filters (Figure 3.12a) and a pressurized fluid is introduced into the lower section of the chamber. The fluid flows through the material and exits via the upper part of the device, which is open to atmospheric pressure.

Figure 3.12b indicates the pressure sensor positioned directly in contact with the fluid inlet zone (DFRobot Gravity Water Pressure Sensor SKU SEN0257). The sensor was calibrated so that its measure represents the difference between the atmospheric pressure and fluid pressure in the inlet zone. The entire device was placed inside a thermoregulated chamber that keeps the temperature of the system at 37 °C (Figure 3.13a).

The sample is positioned between two stainless steel pipe filters that were adapted to fit the device. The filters compressed the material in the desired degree of displacement since the upper portion of the chamber (in blue in Figure 3.12a) could slide, with its displacement controlled by a micrometer head (shown in Figures 3.12b and 3.13b). This allows the system to compress the sample in multiple controlled displacement degrees, with the lower chamber portion being fixed in place.

Initially, the fluid was propelled by means of a hospital syringe pump, which controlled the flow. However, this type of pump only allows volumetric flow control, and the imposed pressure cannot be controlled. The main difficulty was to achieve a stable flow rate, which requires both the flow and the pressure to stabilize and proved difficult to achieve in practice with the syringe

pump. The system was produced with the intention of being used initially for studying TMJ discs, but in the future would prove to be useful for other projects (Bekrar, 2024). It would be beneficial to adapt it to make it more versatile, with a more precise pressure control.

I adapted the system to operate using the compressed air available in the building's infrastructure, which can reach up to 700 kPa. Two pressure regulators, shown in Figure 3.13b, were connected in series. The first one operates between 5 kPa and 850 kPa, while the second between 5 kPa and 200 kPa and enables a finer adjustment of its output pressure values. The compressed air is introduced into the inlet tube which is previously filled with saline solution. The air pressure is transmitted to the fluid and measured by the pressure sensor, with a measurement range going from 0 to 1600 kPa. Since the sensor is located immediately before contact with the specimen, its measurement corresponds to the pressure of fluid that penetrates the sample.

Once the pressurized fluid passes through the specimen, it exits through the outlet tube and falls into the container positioned on top of the scale, also shown in 3.13b. Both pressure and mass values measured by the scale are recorded throughout the test via the device's control system, which was custom built with a Raspberry Pi.

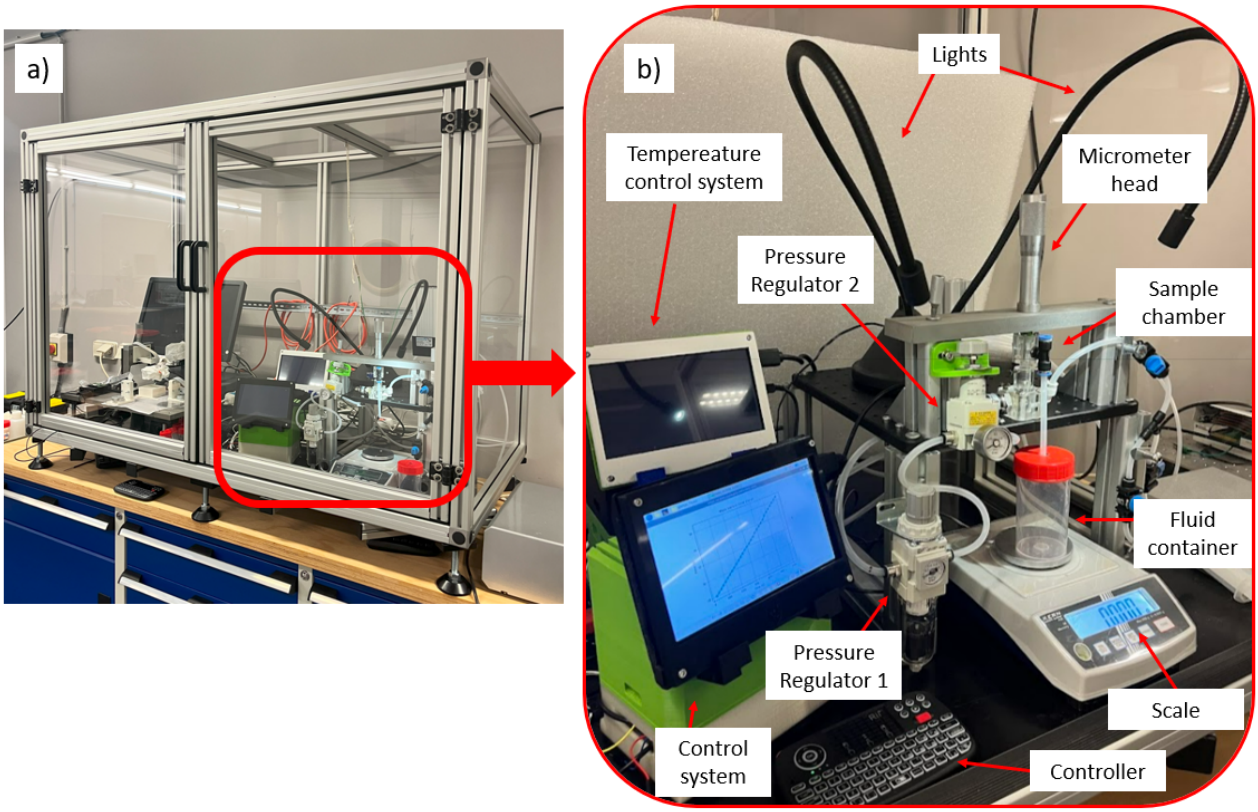

Figure 3.13: a) Thermoregulated chamber in which the device was placed. b) Final direct permeation device.

3.3.2 Device validation

The first samples tested in the device were potato cylinders, as this is an accessible material whose permeability has been previously characterized in the literature (Datta, 2006). However, due to the low lateral expansion of the potato when subjected to compression by the system, it was not possible to guarantee lateral tightness inside the chamber and the water passed through the system without passing exclusively through the samples inner structure. In fact, side leakage is one of the main problems which are inherent to this type of test. This highlights the limitation

of the system to materials capable of laterally expanding, either through osmotically imposed swelling or by the application of compressive strains, as described in Ateshian (2017).

3.3.2.1 Sponge samples

The system was designed to allow different degrees of compression on the samples through the use of the micrometer head. According to the theory described by the equations 1.14 and 1.15, it would then be possible to observe the influence of the imposed deformation on the decrease in permeability.

In order to verify whether the system was capable of enabling the visualization of this phenomenon, permeation tests were conducted on commercial kitchen sponge samples. Although their permeability was not previously known, the sponges, which are porous and permeable, could be subjected to high degrees of deformation and could be easily tested in the device.

A 27.3 mm height cylindrical sample of 10mm diameter was pre-compressed to 10mm to fit inside the direct permeation chamber. This pre-compression was applied since the sponges were too permeable when free of stress, and the fluid flow period was too short to allow a good measure by the setup. A total of 9 tests were performed, compressing the sample by 1 mm in each test. The pressure was set at 5 kPa for all tests. Each measurement was performed over a period of 10 minutes from the stabilization of the flow, when the fluid volume curves reached an apparently linear aspect, starting around two minutes from the beginning of the flow. The measured flow rates are visible in the Figure 3.14.

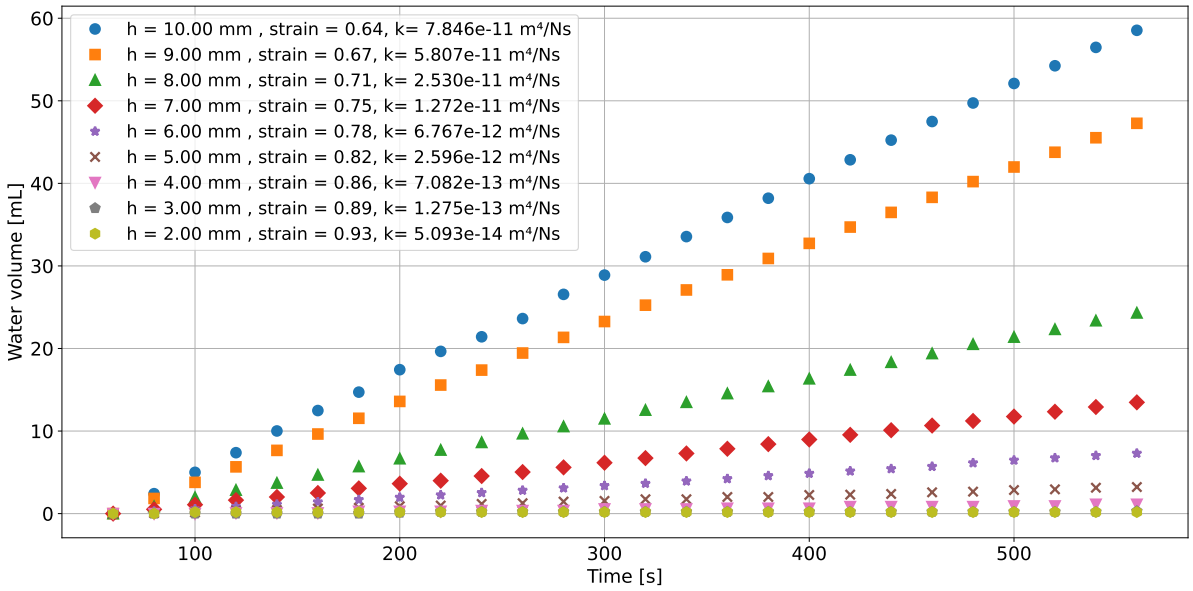

Figure 3.14: Direct permeation results on sponge sample for different degrees of compression.

As the height of the sample was reduced by the device, the greater the difficulty for the fluid to flow through it and the lower the measured permeability. Figure 3.15 shows the permeabilities that were measured for each of the cases.

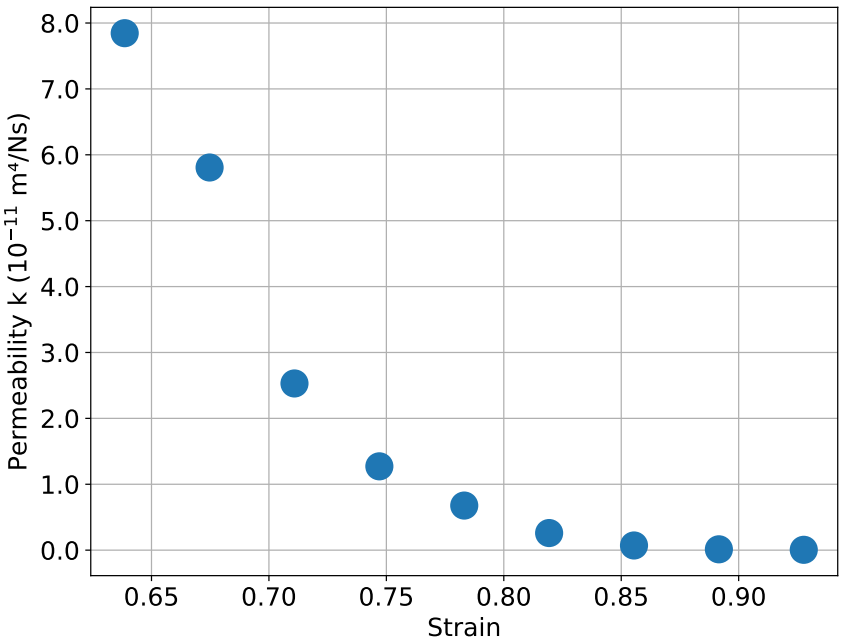

Figure 3.15: Measured values of permeability for different imposed strains on a sponge sample.

The tendency for permeability to decrease is clear as the sample is compressed. As the strain reaches higher values, the smaller the variation is between different compression ratios. The device was able to impose different degrees of compression and perform permeability measurements consistent with expectations, even if the exact numerical values to be expected were not known for this material.

3.3.2.2 Temporomandibular disc samples

The direct permeation test with the TMJ disc samples was conducted the day after the confined compression tests for each of the samples. During all the test campaigns, several experimental conditions were tested in order to obtain direct permeation measurements. The pressures applied varied throughout the possible range of values that the device allowed (from 5kPa to 700kPa), in tests with varying durations, ranging from minutes to tests lasting up to 30 hours.

The experimental difficulty of preventing fluid flow around the sample was observed, since some samples, over time, tended to present an oval aspect. In this cases, the fluid flow ignored the tissue's presence and quickly filled up the output container. This required meticulous preparation of the positioning of the specimens before the tests, which was achievable given proper preparation.

Once the samples were well positioned, it was observed that it was very difficult to make the fluid permeate through them. Even though the samples had recovered their initial appearance and height overnight, no flow was observed through their surfaces most of the times.

One possible explanation is the damage to the solid phase structure due to prior tests, which prevented fluid flow. Another possibility was the deformation imposed on the material due to the pressurized fluid, where high pressure could deform the material matrix and block its pores, preventing its flow.

To date, only one of the tests performed has allowed the obtaining of permeability values that were coherent, and the observed flow is shown in Figure 3.16.

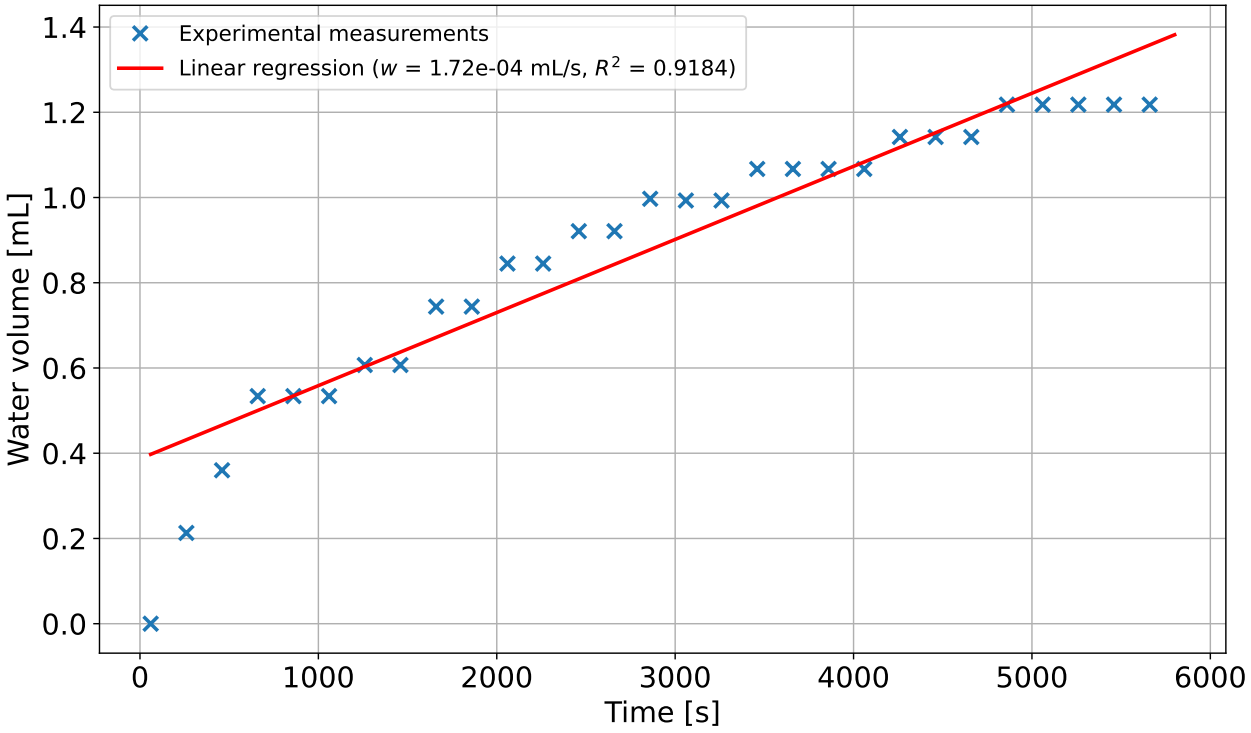

Figure 3.16: Fluid flow through one TMJ sample with 100 kPa applied. Sample 230524-Head1-Left.

In the test illustrated in Figure 3.16, an estimated flow of 1.72×10^{-4} mL/s was obtained through the linear regression illustrated in the figure. A pressure of 100 kPa was applied for a period of one hour where a permeability value of $k = 1.446 \times 10^{-15} m^4/Ns$ was obtained.

Although the result is close to the expected permeability's order of magnitude, this has not yet been repeatable with other samples. The use of the direct permeation device for these samples is still being explored to define a protocol that produces repeatable results.

3.3.2.3 Wharton's Jelly samples

In collaboration with other projects related to regenerative medicine of the team, samples of Hydrogel produced from Wharton's Jelly previously submitted to a tannic acid treatment were available for testing through the ANR HyCareMat project. These are materials obtained from human umbilical cords with biphasic characteristics, whose poromechanical behavior has only been tested in one other study in the literature currently Gervaso et al. (2007).

In order to obtain initial permeability values, a total of five hydrogel samples had been previously tested in the confined compression device. The estimated mean permeability value was $(3.64 \pm 0.59) \times 10^{-11} m^4/Ns$, by applying the data processing described in section 3.2, with a linear elastic approach.

A well-preserved sample with measured permeability of $k = 4.09 \times 10^{-11} m^4/Ns$ was selected to be subjected to a direct permeation test in the week following confined compression. An average pressure of 13 kPa was applied, which seemed sufficient to establish a stabilized flow, low enough so that its variation could be observed with a capture rate of mass measured every 20 s. The measurement was performed over a period of 10 minutes after flow stabilization, leading to $k = 2.96 \times 10^{-11} m^4/Ns$.

Despite the differences between the values obtained by both methods, it is worth noting that they are of the same order of magnitude. The observed proximity was encouraging, considering

the distinction in the experimental conditions applied to each of the tests, which were able to remain consistent with each other.

The results shown here concerning the Wharton's jelly samples are part of a collaborative article related to facial nerve regeneration, which will be submitted soon.

3.4 Microstructure observation

As discussed from the beginning of this thesis, the microstructure of biological tissues plays an essential role in their mechanical behavior. This section will explore some aspects of the TMJ disc's microstructure and relate it to the observed mechanical behavior.

Studies exploring disc permeability through confined compression (Wu et al., 2017; Kuo et al., 2010) and direct permeation (Tverje & Nyashin, 2010) sought to obtain samples with geometry as close to ideal as possible, in which the upper and lower surfaces of the disc were cut. The influence of the outer layer of the structure on the permeability measurement was then excluded, being limited to the analysis of the central layer of the structure in the superior-inferior direction. Studies analyzing the poromechanical structure of the disc do not include the inhomogeneity of the structure throughout its thickness, focusing instead on variations between the anteroposterior and mediolateral directions.

Works that explore imaging techniques in the disc analyse the orientations of the collagen network in the structure, which is essential for describing the anisotropy of the tissue under tension. However, variations in the material throughout its thickness have been less discussed in papers focusing on its mechanical aspect. In Juran et al. (2015), differences in the disc's structure between the upper and lower surfaces are presented, illustrated in Figure 1.13c. They claim, through SEM observations, that the inferior portion of the disc is supposedly composed of a zone of more uniform fiber distribution than the upper zones (see Figure 1.13c).

In the following sections, I will describe some of the techniques I applied to the samples harvested during this work, aiming to search for possible visual clues that can help us gain insights into the mechanics of the disc and enrich the current literature through imaging techniques.

3.4.1 Optical coherence tomography

To observe the structure of the disc throughout its thickness, a porcine TMJ disc of this work was observed in an OCT device (its principle was presented in Section 1.3.4.6) in collaboration with Professor Jean-Marc Allain from the Laboratoire de Mécanique des Solides of the Ecole Polytechnique de Paris. The samples were still hydrated, and an untested disc sample was passed through the device shown in Figure 3.17.

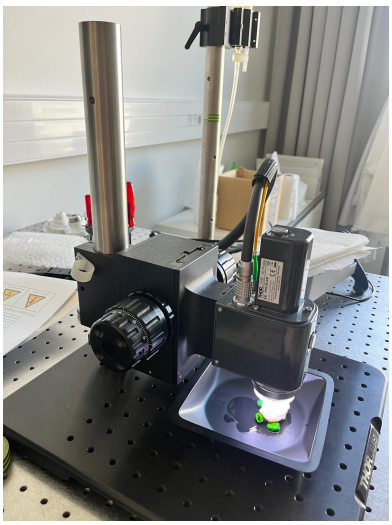

Figure 3.17: OCT device used on disc.

The upper and lower superficial zones of the discs were imaged, and an example of result is shown in Figure 3.18.

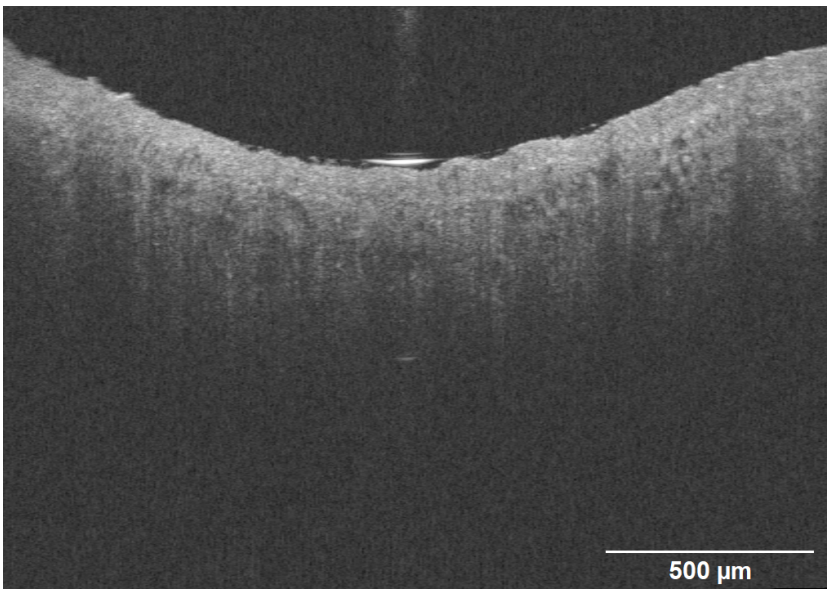

Figure 3.18: OCT image of the superior surface from central zone of sample 240311-Head2-Left.

Figure 3.18 shows the curved surface of the disc in the sagittal plane. The white highlight in the center of the figure is an artifact caused by reflection over internal layers. A lighter zone can be observed close to the disc's surface, where the grayscale indicates light incidence, which may suggest structural differences or attenuation of light penetration. Although the structure is not homogeneous, it is difficult to draw conclusions from these OCT images of the discs. Due to its operating principle, a progressive attenuation of the signal happens as it penetrates the structure, limiting the depth of analysis and leading to inconclusive experimental findings. The thin external layer reported by Mărcăuteanu et al. (2010) and shown covering the disc's surface in white in Figure 1.21b was not so evident in the images we obtained here. This may be linked to the different sample conditions (the discs were imaged still hydrated here), the nature of the OCT devices used or also the different type of sample, since in Mărcăuteanu et al. (2010) they worked with dry human discs. Other imaging techniques were then applied to the disc to explore it further.

3.4.2 Scanning electron microscopy

I also performed SEM imaging of the discs (the principle of which is explained in Section 1.3.4.6). To do so, it was necessary to cut the samples as shown in Figure 3.1.

The tensile specimens, in blue and green in Figure 3.1, have their collagen network oriented toward its largest dimension (see the orientation of the disc's fiber network in Figure 1.13b). Due to dimensional variability between samples and the practical difficulty of obtaining quality specimens, it was not possible to obtain specimens from the anterior and posterior zones for all discs (in blue in Figure 3.1).

These samples were firstly submitted to tensile tests, which will be discussed later, and then prepared for SEM visualization. After being tested, the discs were frozen at -80°C and then subjected to a freeze-drying process, consisting of removing water through sublimation in a lyophilizer, as shown in Figure 3.19.

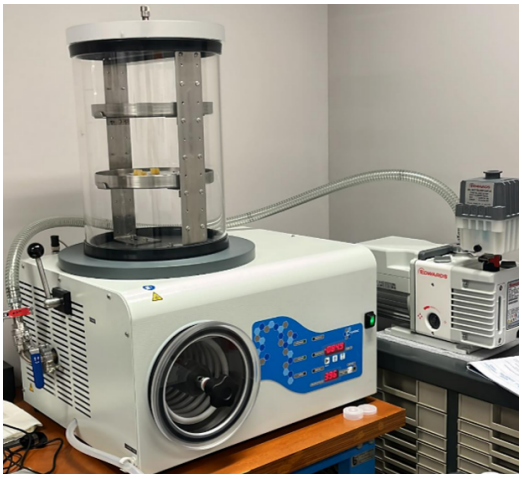

Figure 3.19: Lyophilizer used for freeze drying the samples.

The samples measured approximately 10x5x2 mm. Once frozen, they were left under vacuum for 48 hours at -80°C in the lyophilizer, being placed over a grid-like support so that the water could also escape from the bottom. Since they were dry and rigid after this process, it was easy to cut them with a scalpel to create a flat surface to better visualize them under the SEM. Figure 3.20 shows two disc positioning configurations that were adopted.

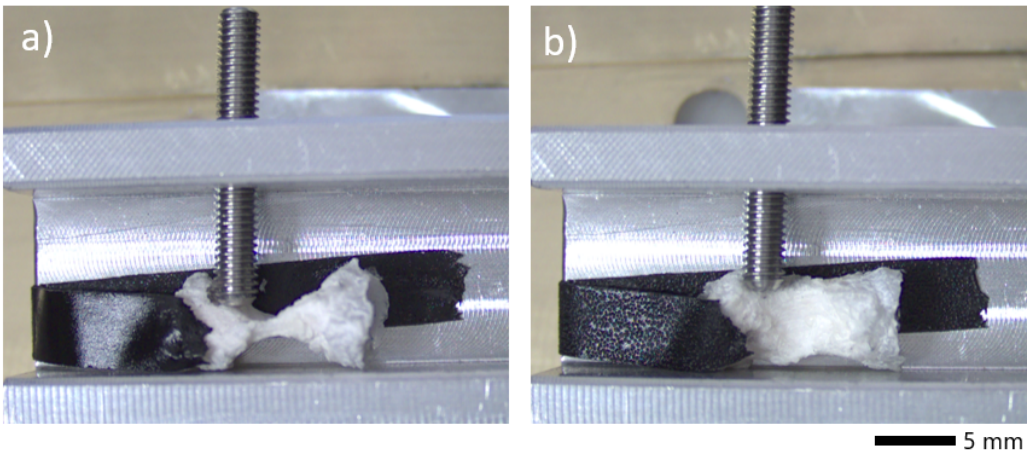

Figure 3.20: Top view of the positioning of the freeze-dried discs for SEM imaging, with conductive carbon adhesive tape (in black) and a fixation screw. Positioning for viewing a) sagittal and b) transverse planes (with the upper surface of the disc facing upwards).

For positioning in the SEM, conductive carbon adhesive tape was used to facilitate electron conduction during image acquisition. A fixation screw was also positioned, touching the sample lightly to hold it in place.

All SEM imaged samples from literature described in the section 1.3.4.6, were coated with a thin layer of gold or gold-palladium alloy to facilitate electron transmission to the sample. In this present study, the microscope that was used allows for low-vacuum imaging. The absence of air particles in the microscope chamber facilitates electron transmission, and it was not necessary to metallize the specimens to obtain good quality images. Figure 3.21 shows the result of a sagittal plane acquisition, with a sample positioned as in Figure 3.20a.

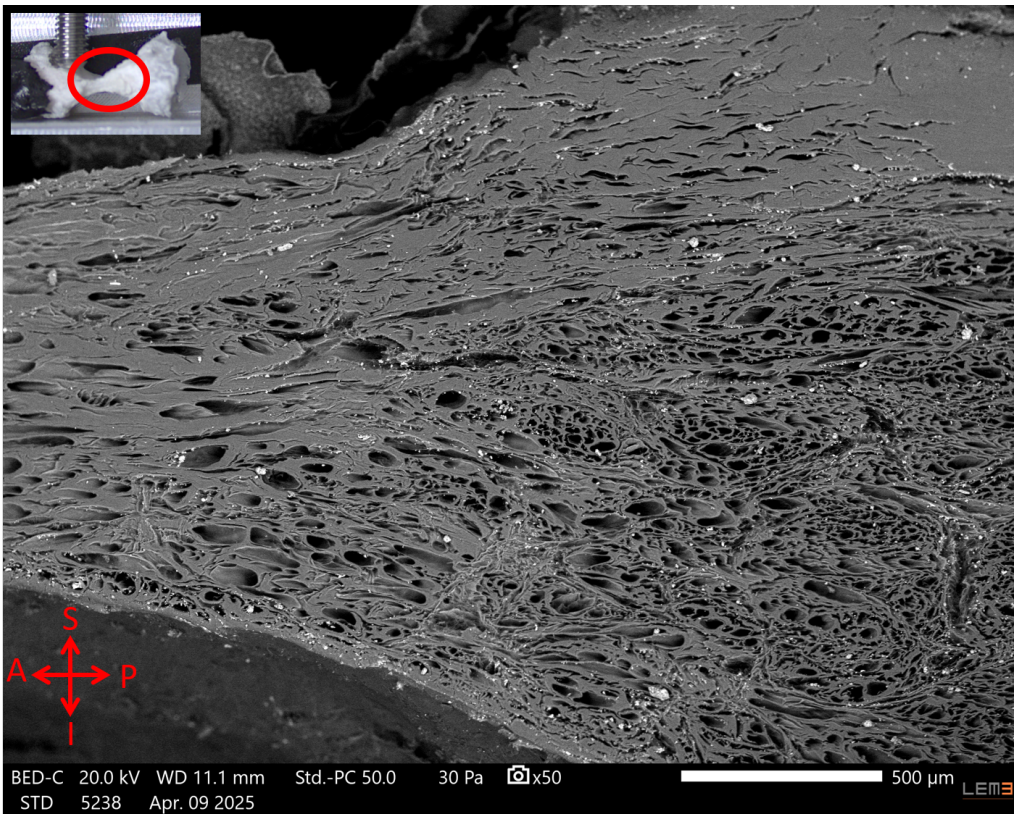

Figure 3.21: SEM image of sagittal view of freeze-dryed disc sample 230524-Head1-Right.

The pores in the disc's collagen structure are visible, distributed unevenly throughout the sample. This indicates the potential permeability of the material also in the mediolateral direction, which has never been explored by confined compression or direct permeation methods. Harvesting cylindrical samples from the discs, which would allow a good approximation of the ideal theoretical conditions of confined compression and direct permeation analyses, becomes progressively more difficult to perform as the samples are smaller. In fact, the only study that presented a model capable of estimating disc permeability values in the mediolateral direction, perpendicular to the pores shown in the cross-section in Figure 3.21, was the work by Li et al. (2021), which performed tensile tests assuming the same permeability for the coronal and sagittal planes (see table 1.1).

An interesting observation in Figure 3.21 is also the existence of an outer layer with a more uniform structure covering the exterior part of the disc, similar to what was observed by Mărcăuteanu et al. (2010) in Figure 1.21.

Figure 3.22 illustrates this layer in another sample also in the sagittal plane.

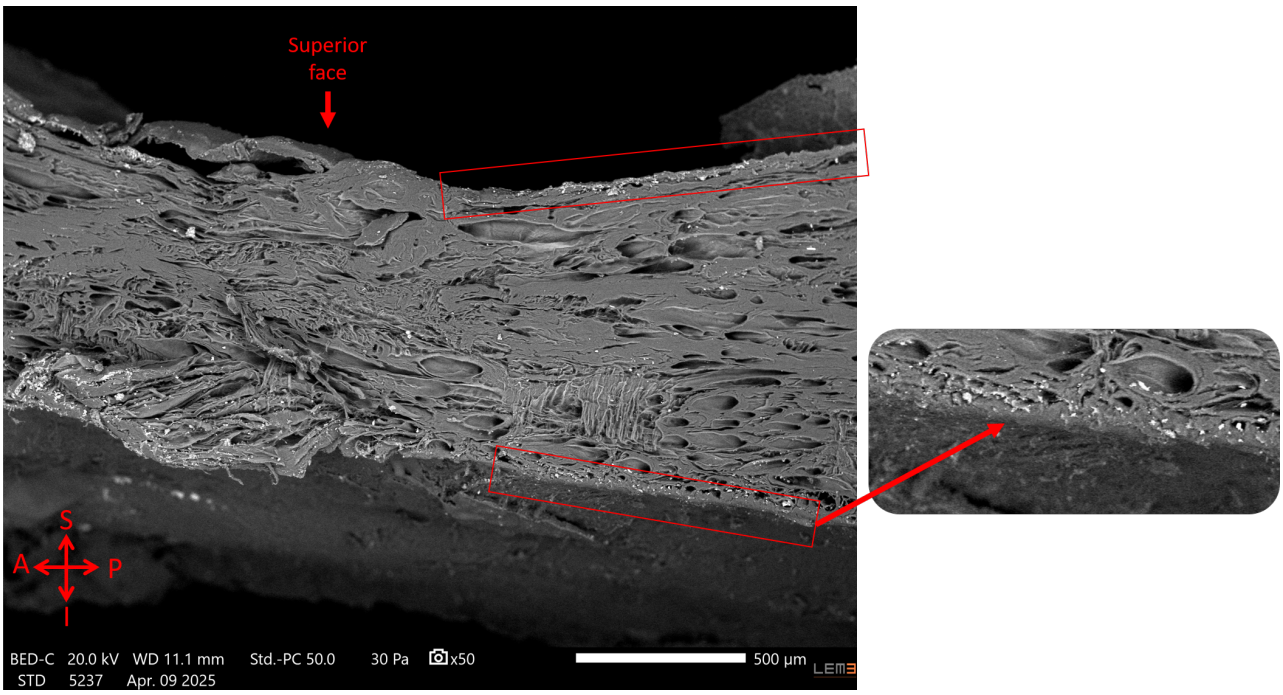

Figure 3.22: SEM image of sagittal view of freeze-dryed disc sample 240311-Head2-Right. The highlighted zones illustrate the exterior layer of different structure from the rest of the sample, that covers the superior and inferior surfaces of the disc.

This denser-looking layer of fibers covers the entire superior and inferior surfaces of the discs, and may correspond to what was observed in the OCT of human discs in Figure 3.17 (Mărcăuteanu et al., 2010). Indeed, it appears to be at the edge of the superior disc surface in Figure 1.13c from Juran et al. (2015). However, contrary to what was stated in Juran et al. (2015), the cross-sectional portions of the disc in the sagittal plane do not present major structural differences between their superior and inferior portions. The uniform-looking zone, attributed exclusively to the lower surface of the disc in Juran et al. (2015), was actually covering both the upper and lower parts of the discs that were imaged here.

Figure 3.23 was created by sectioning the sample in the frontal plane, also allowing visualization of this outer layer.

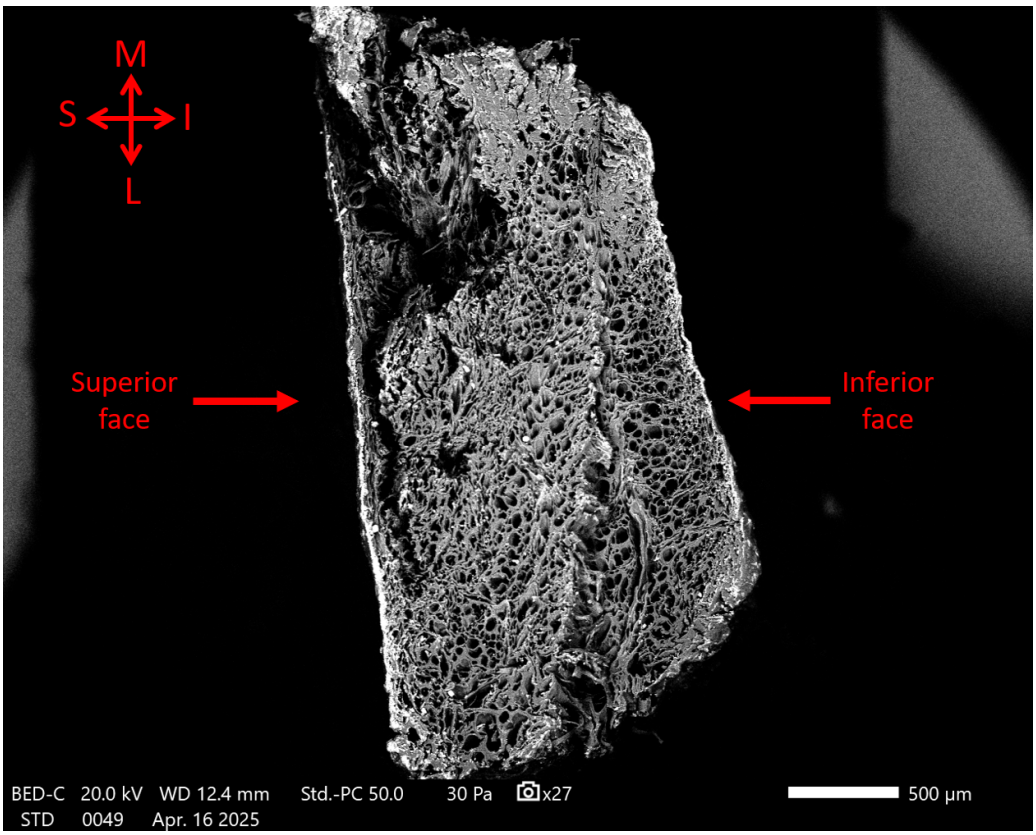

Figure 3.23: SEM image of frontal view of freeze-dryed disc sample 240311-Head2-Right.

Figure 3.23 allows visualization of the pores in the anteroposterior direction of the discs, which is the same direction in which the fibers are oriented. The outer layer covering the upper and lower surfaces is still visible. This layer is shown in a top view in Figure 3.24.

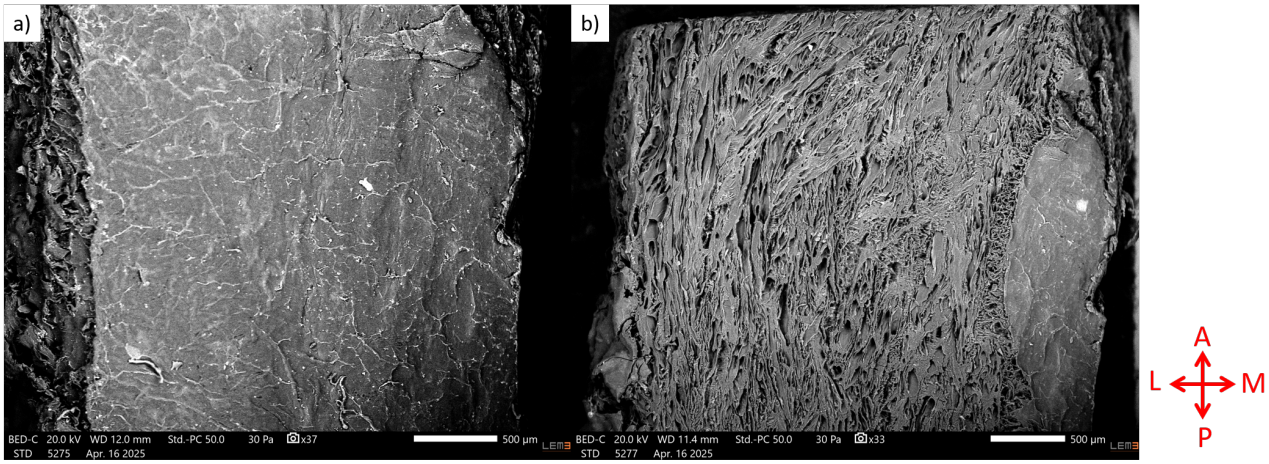

Figure 3.24: SEM image of superior view of freeze-dryed disc sample 240311-Head2-Right. a) Intact superior surface, b) disc after the removal of the superior surface.

Figure 3.24a illustrates this surface covering the upper part of the disc. Its appearance is denser, and pores are not as evident as in the other views. A scalpel was used to carefully remove this top layer, and Figure 3.24b reveals the structure under it after its removal. The change in porosity in both situations is evident.

The direction normal to Figure 3.24 is the one in which direct permeation and confined compression studies measure the disc's permeability. The apparently denser external layer observed

in the figures should not be seen as a direct indication of the disc's impermeability. The study of the material's permeability over its thickness in different layers has not yet been reported in literature. This layer, however, highlights the potential inhomogeneity of the structure in terms of porosity, which can potentially impact the material's mechanics and has not yet been adressed in mechanical models. This may also be related to the difficulties observed in direct permeation tests conducted in section 3.3.2.2. The imposition of flow throughout the entire thickness may have been hampered by the observed microstructure, and preparing thinner samples with techniques such as microtome cutting may be one way to increase the reliability of results from this type of test.

The existence of this outer surface has already been mentioned, as shown in Figure 1.21 (OCT). However, it is a fact that poromechanical characterization studies of TMJ discs fail to consider this aspect, either in sample preparation (cutting them with microtomes) or in the boundary conditions applied in numerical models.

Once removed, the outer layer of the disc revealed the previously covered fiber network (Figure 3.24b), which presents a privileged orientation in the anteroposterior direction (vertical in the image). This fiber orientation also plays a role in the mechanical response of the disc, and will be discussed in the following section.

3.4.3 Magnetic resonance imaging

Immediately after harvesting the pig head samples, MRI data were collected from the discs (described in section 2.1.1 and shown in Figure 2.2, where the fresh discs MRI was discussed and presented). The images allowed a good observation of the disc's volume, although due to resolution issues, details of the material's fiber network were not visible.

To visualize the microstructure, other MRI scans of the samples were also performed in collaboration with Dr. Sebastien Leclerc from the LEMTA laboratory in Nancy, after the testing of the samples. The used device was an Avance III 600 Wide Bore (Bruker, Germany), equipped with a 14.1 T vertical superconducting magnet, shown in Figure 3.25b.

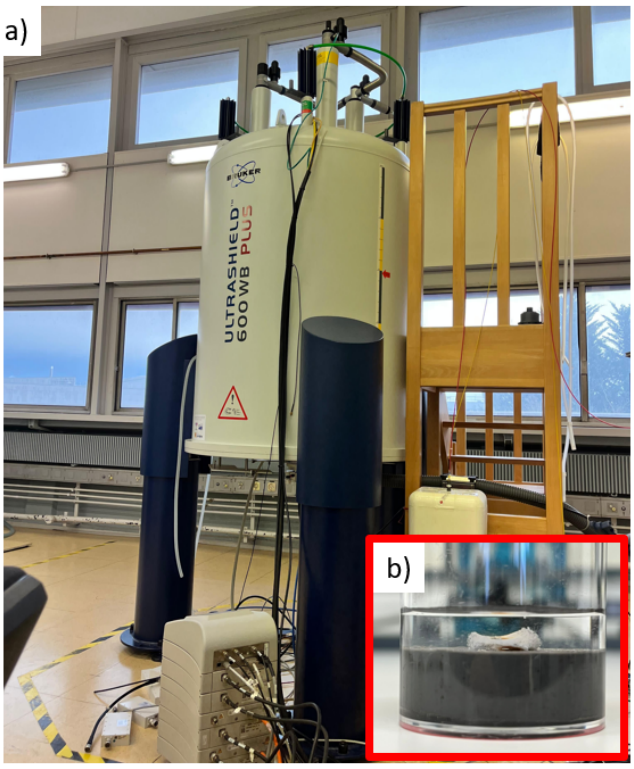

Figure 3.25: a) Avance III 600 Wide Bore (Bruker, Germany) MRI device used for visualizing discs. b) Disc sample inside of tube used for introduction into the MRI machine.

This device captured an image of one intact disc sample, as well as images of the previously tested cylindrical samples approximately one and a half weeks after being submitted to confined compression and direct permeation. Figure 3.25b shows an example of a cut TMJ sample positioning. The discs were not frozen after testing, but kept refrigerated and hydrated at 4°C until the day of image acquisition. They were placed inside a tube and immersed in saline solution to maintain hydration also during image capture. Figure 3.26 shows a middle layer of a whole disc captured in MRI.

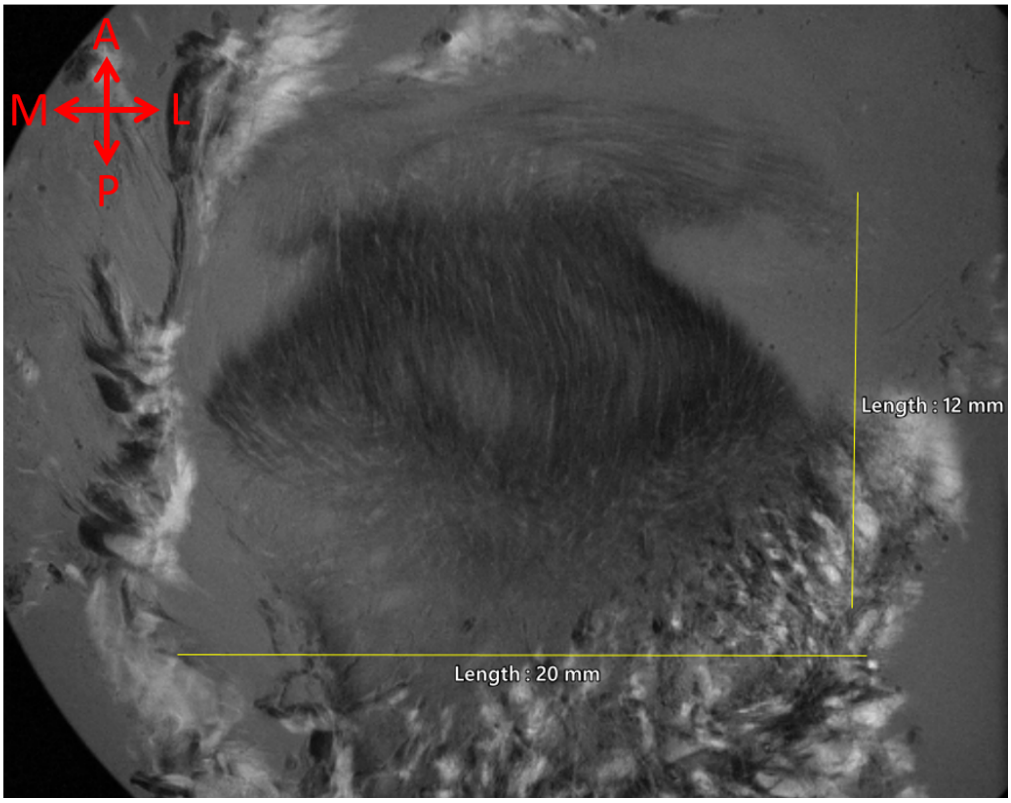

Figure 3.26: MRI image of middle layer of a whole porcine TMJ disc (sample 230524-Head1-Right). Acquisition parameters: Spin Echo (MSME) : FOV 3cm, slice 0.5mm, 512*512 pixels, TE 8.8ms, TR 2000ms, 15 slices, 16 averages.

The anteroposterior orientation of the fibers in the central area of the disc can be observed. This is the direction of the pterygoid muscle's line of action, which tensions the structure, and is also the direction along which the disc translates during its functioning. The peripheral fibers of the disc appears to surround this central structure, taking on a ring shape, as expected from Figure 1.13b. Considering the role of the fibers in tensile strength, this ring allows the disc to maintain its shape, hindering its lateral expansion when compressed.

This same sample was also subjected to DTI (introduced in the section 1.3.4.6), where we attempted to measure the diffusivity of water molecules within the structure, as shown in Figure 3.27.

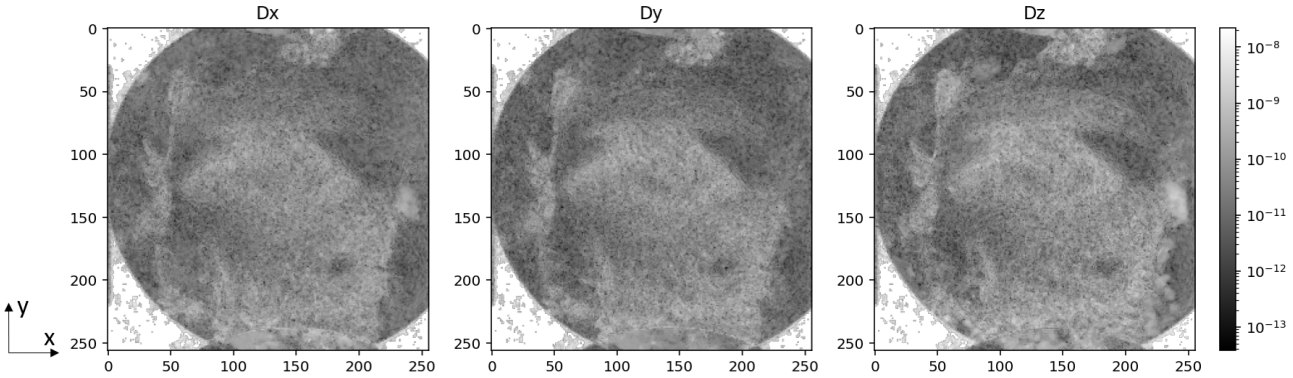

Figure 3.27: Diffusion Tensor Image of middle layer of a whole porcine TMJ disc (sample 230524-Head1-Right). The images show the diffisivity in the X, Y and Z directions, with a logarithmic scale on the left on m^2/s. Image specifications: FOV 3 cm, slice 1 mm, 256×256 pixels, TE 20.5 ms, TR 2000 ms, 4 averages, delta 5 ms, DELTA 8.8 ms, B values from 25 to 800.

The overall average diffusivity value obtained was 1.5×10^{-9} m^2/s. For comparison, the diffusivity of free water, without its molecules being impeded from moving, is 2.3×10^{-9} m^2/s, which still is close to that observed in the images. Still, this difference indicates that the choice of parameters for performing the DTI allowed to access effects related to diffusion. A slight variation in diffusivity is observed in different directions, indicating the anisotropy of the structure to the movement of water molecules. The scale in the figure is in logarithmic form to facilitate this visualization.

The images were captured over a period of one and a half days, during which varying degrees of molecular displacement were captured on MRI and fitted to create Figure 3.27, obtained in collaboration with the LEMTA laboratory in Nancy. Observing diffusivity in this material necessarily requires that the molecular displacement be sufficient for the influence of the ECM surrounding the fluid to be observed (Le Bihan et al., 2001). To improve the reliability of the results, it is necessary to explore other image capture parameters so that other fluid displacements can be observed. This will allow verification of the values presented here, which are an initial exploration in one of the TMJ samples.

The diffusivity tensor relates to the ease of diffusion of molecules in a medium caused by the thermal energy they carry. When interacting with the tissue microstructure, it allows to relate material's anisotropy to diffusion (Le Bihan et al., 2001). At the same time, permeability is related to the ease of flow in a medium (Vidotto et al., 2021), also being affected by the microstructure. These are two related concepts, and the use of DTI to obtain the permeability tensor is a possible approach, which requires models (Vidotto et al., 2021) that were not explored in the present work.

3.4.4 Inner stress release

The deformation on specimens immediately after being cut was filmed. The day after the spherical compression tests, the discs were cut with the 10 mm diameter punch to be prepared for confined compression testing.

Graphite powder was spread on the specimen surface to generate a high contrast speckle pattern, enabling accurate tracking of surface displacements during image correlation. Graphite was selected because it is chemically inert and does not interfere with the electrical properties of the sample, hence minimally affecting the surrounding fluid environment. This proved to be a good solution, as the particles adhere to the collagen. Immediately after being cut, both remaining surrounding tissues and the cylindrical specimens were placed inside of a petri dish,

as Figure 3.2 shows. A thin layer of water had been also spread inside of the dish, to avoid tissue dehydration during the filming period, still making sure that the graphite powder over the samples was not washed away.

The discs were filmed during a period of one hour, which was deemed sufficient to ensure visualization of the main deformation that occurred due to the release of the inner stresses, as stated in Tappert (2020) and Tappert et al. (2022), where the relaxation of TMJ discs tended to happen in a short period of time after cutting.

Figure 3.28 shows the state of one disc at three different instants.

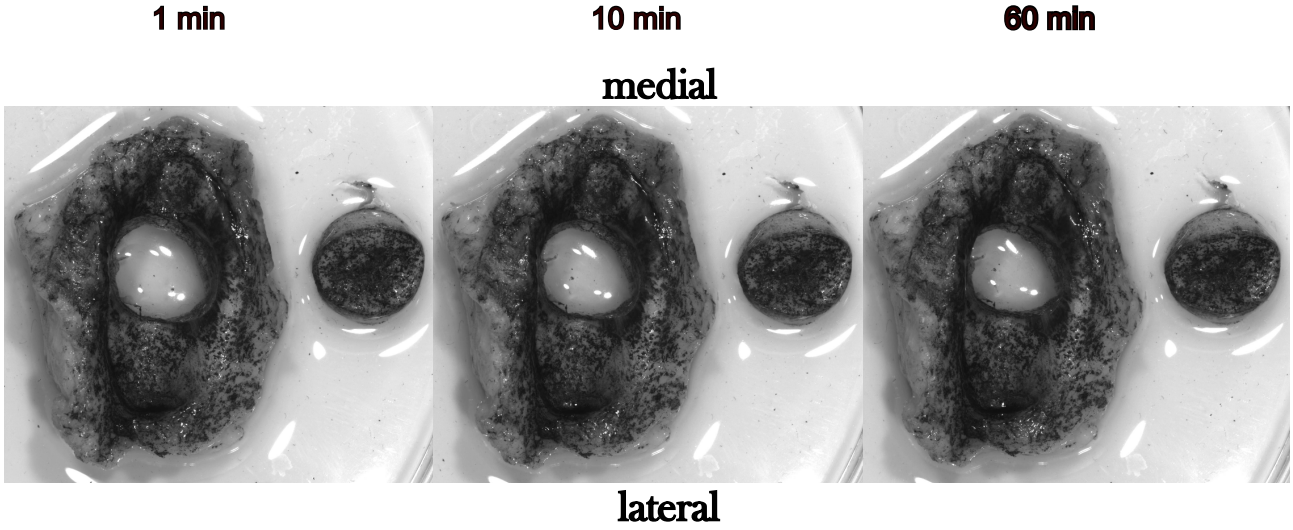

Figure 3.28: Cut disc filmed during a period of one hour. Sample 240311-Head2-Left.

Figure 3.28 shows both the disc and the cylindrical specimen that was cut. While the cylindrical specimen appeared to elongate in the mediolateral direction, the drilled hole in the middle of the sample tended to contract and shrink over time. The time between cutting and positioning the samples in front of the camera was estimated to be around 1 minute, and the deformations immediately after cutting could not be directly visualized.

To observe the internal strains, a backwards strain calculation method developed by Dusfour (2018) was applied, assuming that the strain measured from the displacement throughout the video corresponds to the one to which the structure was subjected before being cut. The videos were processed in collaboration with Gilles Dusfour, from CHU Montpellier. Based on the available images, a mesh was generated, following the displacement of the surface of the discs and allowing the superposition of results shown in Figure 3.29.

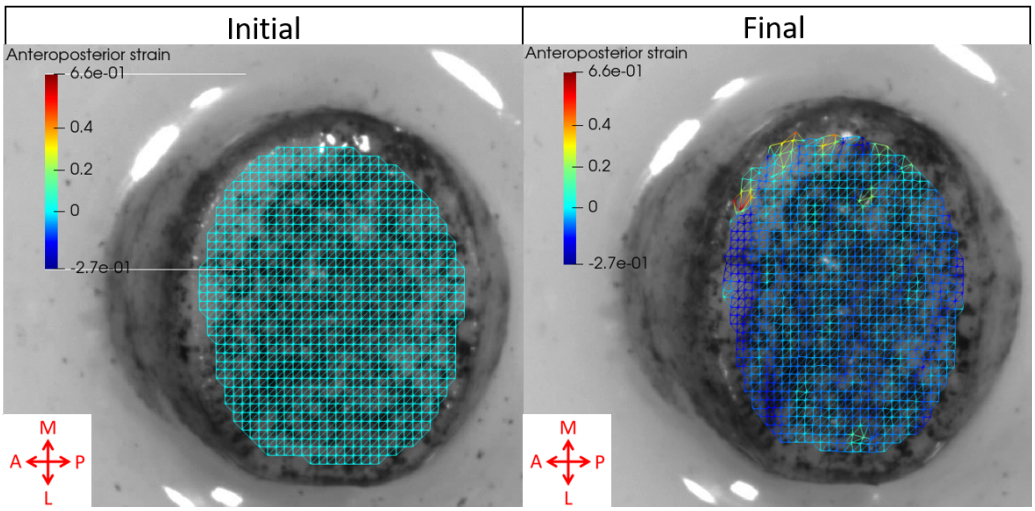

Figure 3.29: Anteroposterior strain measured by DIC method showing initial and final configuration of disc sample 240311-Head2-Right.

Figure 3.29 shows the developed mesh based on the sample speckle pattern and the measured strain by the end of the video. In this case, the scale indicates the deformation in the anteroposterior direction (horizontal in the figure). Despite some specific values of higher strains, the general behavior of the disc presented values on the order of up to -27%. The tendency for deviation towards negative values indicates contraction of the structure in that direction. Figure 3.30 shows the same disc, this time highlighting the deformation in the mediolateral direction.

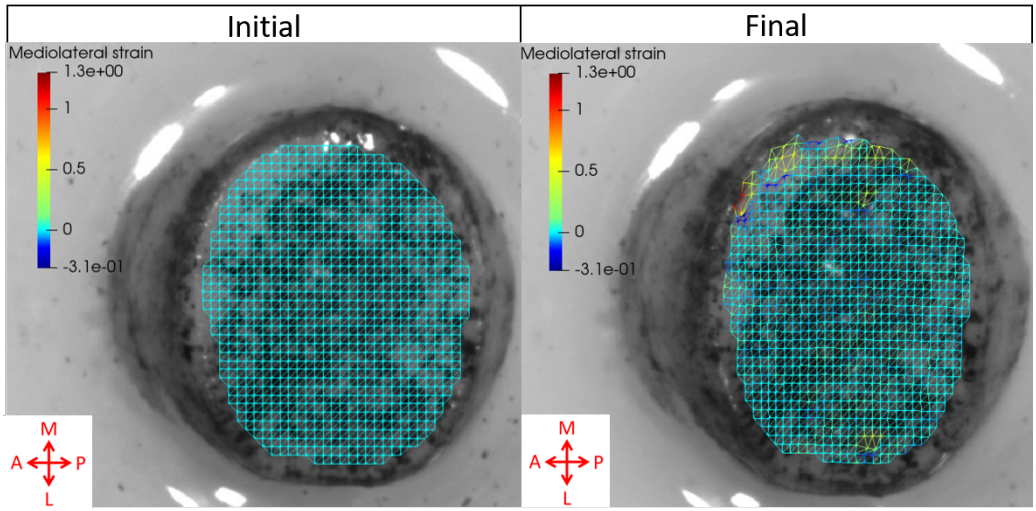

Figure 3.30: Mediolateral strain measured by DIC method showing initial and final configuration of disc sample 240311-Head2-Right.

Despite being cut with a perfectly cylindrical punch, the samples exhibited mediolateral elongation even in their initial state in the figures. As mentioned, there was a delay between cutting and positioning the discs (no more than a minute), which was sufficient for the discs to initially deform. Figure 3.30 shows a lower degree of strain in the mediolateral direction than Figure 3.29, indicating that the anteroposterior contraction was lower during the period of filming.

Ideally, by cutting the sample directly under the camera, it would be possible to record this immediate initial deformation and extend the analysis to the period not observed in this study. This would require a setup that allowed recording during the cutting process, which was

performed using a vertical press due to the high resistance of the disc. This condition, in the current setup, made it impossible to perform the cutting in this manner.

The strain was measured based on what was observable from the surface of the samples. Deformations outside the filming plane could not be captured, since only one camera was used. Image correlation requires good contrast of the speckles so that their displacements can be accurately detected. This was possible on the upper surface of the discs, which remained outside the fluid and the graphite particles adhered well to the surface. A lateral view of the thin cut cylinders would add another dimension to the analysis; however, experimentally this would be a significant challenge, since in the current setup the discs were partially submerged in fluid at the bottom of a petri dish, and obtaining an undistorted lateral view would be difficult and tricky for data extraction. The following section will present the MRI analysis of the same samples, allowing the analysis and measurement of the dimensions of the discs along its thickness.

3.4.5 MRI of cut specimens

After the whole test campaign, the cut circular specimens were once again imaged in MRI. Six of the tested discs were passed through the device in Figure 3.25 and the resulting images for one of the samples are shown in Figure 3.31.

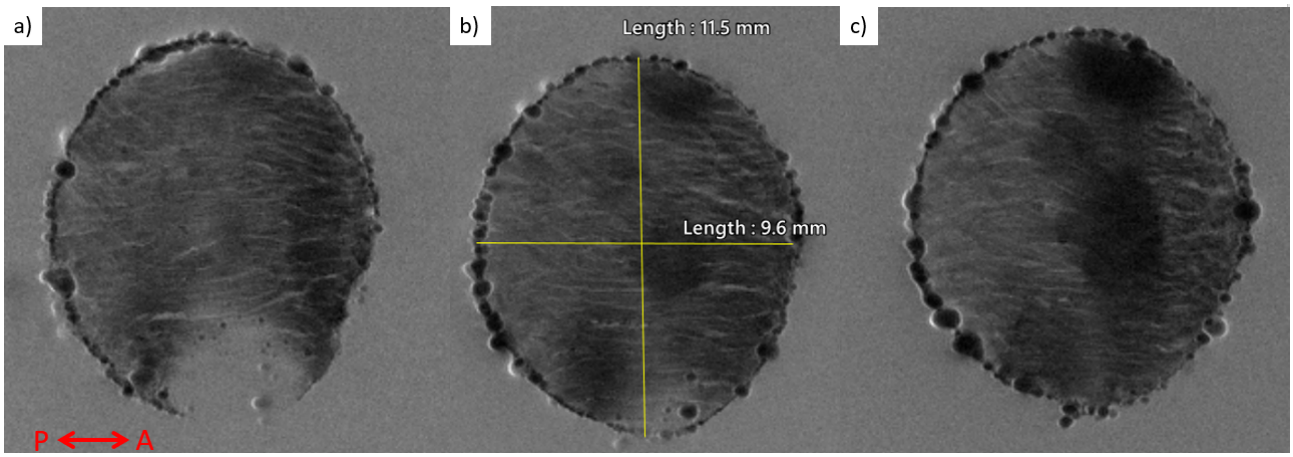

Figure 3.31: MRI of three different slices of the same disc (sample 240311-Head2-Right), with a 0.5 mm distance between slices. The orientation of the fiber network in the anteroposterior axis is visible, as is the deformation of the sample in relation to its original 10 mm circular geometry. Acquisition parameters: Spin Echo (MSME) – FOV 3 cm, slice thickness 0.5 mm, matrix 512 × 512 pixels, TE 8.8 ms, TR 2000 ms, 10 slices, 8 averages.

The distance between the slices in Figure 3.31 is 0.5 mm. Throughout its entire thickness, it is possible to observe the tendency for the material structure to orient itself in a preferred direction, identified as the anteroposterior direction.

The sample was originally cut with a 10 mm diameter circular tool. When measuring the final dimensions, an 1.5 mm expansion was observed in the mediolateral direction in the sample in Figure 3.31 and a shrinkage in the anteroposterior direction of the discs, which measured 9.6 mm. Upon cutting, the pre-stressed biological tissue in the disc was released and deformed, indicating the presence of internal stresses acting anisotropically on the material.

The same effect was observed systematically for all discs and MRI results are shown in Appendix F in Figure F.1. Table 3.3 shows the length variation along each axis.

Sample	Anteroposterior length change [%]	Mediolateral length change [%]
230524-Head1-Left	-10	5
230524-Head1-Right	-7	8
240311-Head1-Left	-5	6
240311-Head1-Right	-8	11
240311-Head2-Left	-7	12
240311-Head2-Right	-4	15
Mean±STD	-6.8±2.1	9.5±3.8

Table 3.3: Length changes in anteroposterior and mediolateral directions for different samples.

Table 3.3 was prepared from measurements obtained as shown in Figure 3.31. For this, it was assumed that the central layer of the discs was aligned with the image acquisition plane, and the discs were fixed to the support (Figure 3.25b) in order to meet this condition. However, small tilts of the discs may have influenced the measurements, since the alignment with the anatomical planes cannot be perfect.

It is interesting to observe the orientation of the fiber network in the material relative to the direction of deformation. Some hypotheses can be developed about what occurred. The absence of the structure surrounding the center of the disc may have caused the release of the pre-tensioned fiber network in the mediolateral direction to be released and expand, showing the initial elongation in that direction after cutting.

Associated with this, it can also be said that the material's fiber network does not exhibit isotropic resistance and it could not expand in the anteroposterior direction when the disc was cut. As the main contributor to the tensile response, the fibers oriented in the anteroposterior direction prevented expansion along this axis and, because they were pre-tensioned, they contracted.

The discs indicated the presence of internal stresses in their structure and non-uniform deformation, with greater resistance in the direction of the fiber network. While one direction shows a general tendency to expand, another tends to contract, making it interesting to evaluate the variation in volume of the discs. Having captured MRI information both before and after deformation, I conducted an analysis of disc volume change for the cut circular samples.

3.4.6 MRI volume analysis

The observed deformation motivated the analysis of volume variation. The software 3D Slicer was used to reconstruct the imaged geometries in 3D, allowing to measure their volume.

MRI scans of intact discs when fresh were performed on the 7T MRI device (Figure 2.3) as shown in Figure 2.2 in section 2.1.1. To estimate their geometry before being cut, a circular zone of 10 mm in diameter was measured and segmented along the disc's thickness. This procedure meant to digitally simulate the cutting process, since theoretically, the circular punch produces samples with cylindrical geometry. Segmentation of the images containing the cut discs was also performed, and the process is illustrated in Figure 3.32.

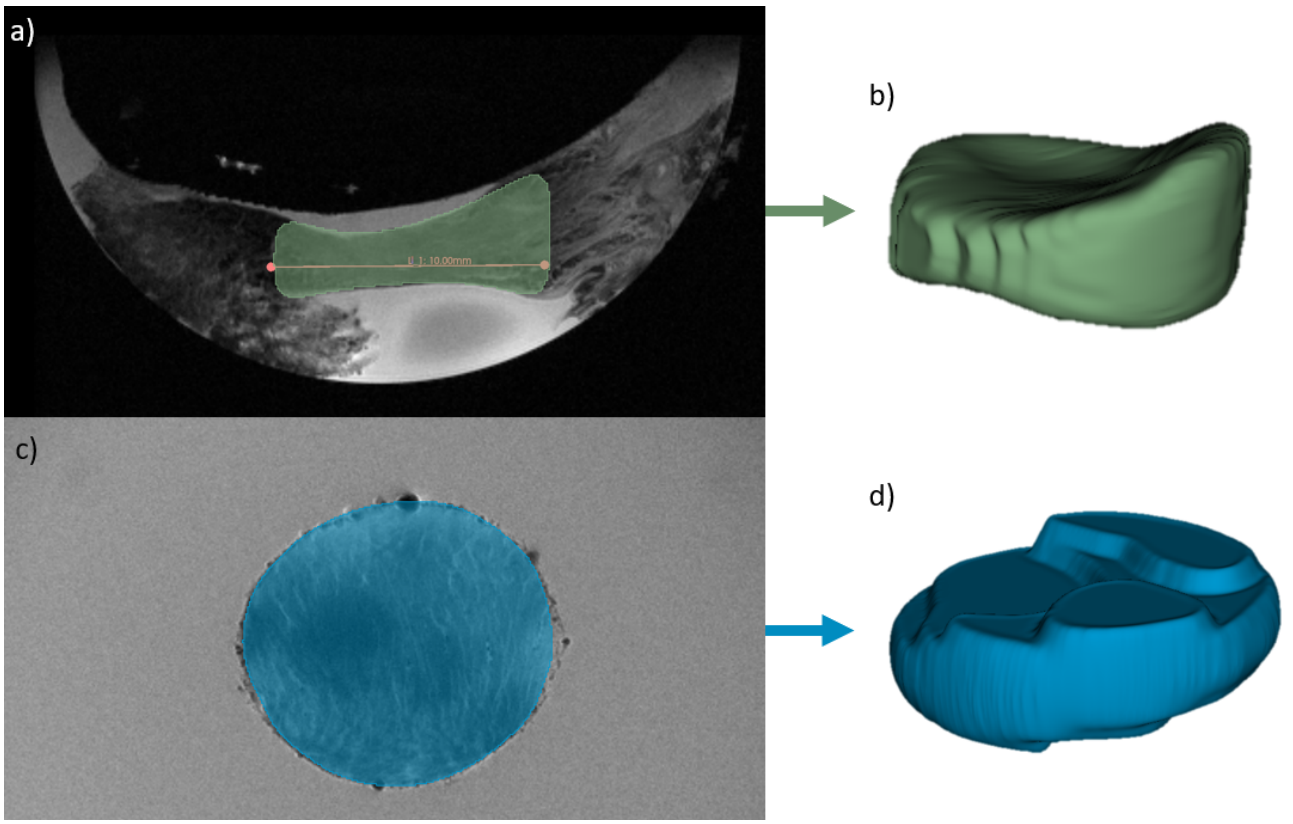

Figure 3.32: Segmentation workflow for sample 240311-Head1-Left. a) Full intact disc MRI with selected voxels for the segmentation. The red line indicates the 10 mm diameter b) Digitally selected 10 mm diameter undeformed disc, simulating the cut specimen from figure (a). c) Cut disc MRI, with selected voxels for segmentation. d) 3D structure obtained from the segmentation of figure (c).

The MRI of the intact discs was performed so that it contained approximately 70 slices along the central thickness of the discs. This provided good resolution for geometry acquisition, although it was offset by the challenge of reproducing a numerical punch exactly identical to the experimental one. The intact discs had to be introduced in the tube shown in Figure 2.2c and were submitted to slight compression in order to be accommodated within the device, which hindered a more accurate reproduction of the circular cut. Nevertheless, this procedure ensured sufficient image quality and structural detail to allow reliable numerical modeling of the discs.

When performing the MRI of the cut cylindrical specimens, some resolution along the thickness had to be sacrificed in order to achieve better visualization of the fiber network. Consequently, only five slices were acquired across the height of the deformed discs, resulting in a less refined segmentation resolution throughout the sample thickness.

These difficulties contribute to the uncertainty of the measurements, which are interpretations of the images but provide an idea of the direction in which the volumes varied. One might expect that by removing the physiological environment surrounding the center of the disc, they would swell and increase in volume. However, this did not happen and the discs had, on average, a $(18.26 \pm 14.82)\%$ decrease in volume between fresh and cut sample MRIs.

Considering an ideally cylindrical geometry and based on the measured volumes, Figure 3.33 shows how much height would have been lost from the samples before and after cutting and testing when converting all the volume variation into height change.

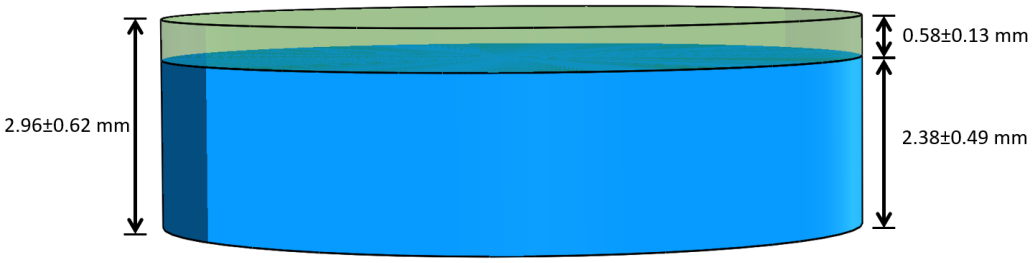

Figure 3.33: Ideal cylinder height for undeformed state of the disc (green) and deformed state (blue). The measured values correspond to the mean dimensions estimated from the segmentation of all MRI data, associated to the standard deviation for all six discs that were imaged.

It is important to emphasize that the change in height was not the only deformation observed. The discs also deformed in other directions, as shown in Figure 3.31, and this change was represented in Figure 3.33 exclusively as a change in height to help visualize the magnitude of the variations.

MRI scans were not performed immediately after cutting the samples since the harvesting, testing, pre and post-test images were performed in different cities. The final cut specimen images were captured after all the test campaigns were completed, allowing the effect on the structure to be visualized. Multiple factors may explain the decreased height of these discs. The compression applied to the samples during the confined compression tests may have damaged the collagen structure of the discs, leading to plastic deformation even though 4N of compression remains represents a low charge compared to the physiological daily loads.

Furthermore, temporomandibular discs have a low concentration of GAGs compared to other tissues more widely studied in the literature, such as hyaline cartilage, which has four to five times more GAGs than the TMJ disc (Detamore et al., 2005) (see Section 1.3.2). GAGs are hydrophilic and attract fluid to the interior of the tissue, thus being one of the factors responsible for the structure's fluid refilling after compression. Since this is a sample removed from its original physiological environment and devoid of the surrounding tissue structures, it is possible that the fluid did not return normally to the interior of the discs. Furthermore, the fluid movements involved in the tests may have removed the physiological fluid originally contained in the pores, eliminating potential free charges that also contributed to the material's basic osmotic balance. At the same time, one might expect that structural recovery would occur more easily in cut samples, since the cut opens a new flow route that would facilitate fluid entry. This decrease in volume may therefore be related to the contraction observed in its anteroposterior direction rather than a change in height.

The pre and post tests MRIs were performed using devices with different resolutions. The only sample tested both intact and cut in the MRI device shown in Figure 3.25 was 230524-Head1-Right, which exhibited a volume variation of only -2.33%. Although the tendency remained to decrease in volume.

Despite recovering some of their height after the testing campaign, the discs may not have returned to their initial thickness. Confined compression subjected the specimens to greater degrees of deformation for a longer period than other tests conducted in this word, keeping the material subjected to compression in the time reported by Kuo et al. (2010) as necessary to reach the steady-state in human discs. Nevertheless, the question arises as to whether potential damage to the material's collagen structure hampered direct permeation testing. An important conclusion emerges from this, indicating the caution that must be taken when performing confined compression tests if the discs are intended to be used for posterior testing.

The deformations observed in the structure were anisotropic, and all tests performed up to now consisted primarily of compressions of the discs in the superior-inferior direction. To

explore aspects of this observed anisotropy, I conducted tensile tests in other directions of the material.

3.5 Tensile response analysis

3.5.1 Experimental tests

The tensile specimens were developed by cutting the discs that had been tested in spherical compression, following the scheme shown in Figure 3.1. Due to the small dimensions of the discs, only two samples from the anterior portion and two from the posterior portion could be cut with enough quality to be used in tests. In total, 18 experimental results were explored in this section.

Tensile tests were performed on porcine TMJ discs by Beatty et al. (2001) (Figure 1.20), and other studies addressed the behavior of human discs (Wright et al., 2016) and sheep discs Labus et al. (2021).

The experimental setup shown in Figure 2.4 was used for the tensile tests, with the same physiological conditions of temperature and fluid osmolarity (described in Section 2.1). The disc samples were fabricated with an average geometry of approximately 10.2 mm in length and a cross-section at their central part of 5 x 2 mm. For fixation, the discs had their ends glued with cyanoacrylate to two metal rods.

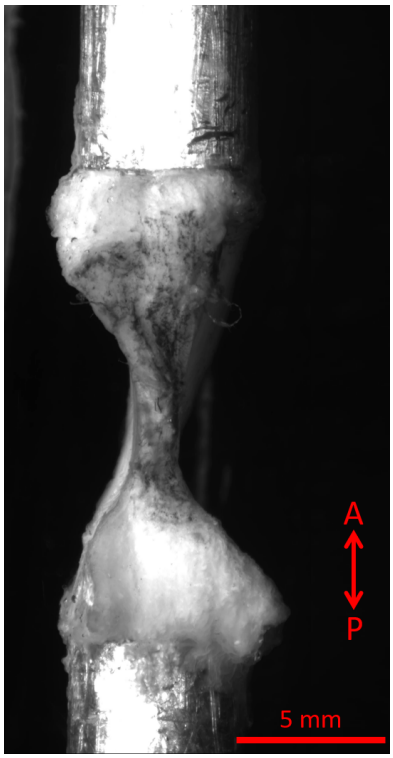

Figure 3.34: TMJ disc tensile specimen. Sample 240311-Head2-Right.

This fixation method allowed an uniform loading distribution along the fiber network at the end of the samples. This also prevents the compression of the clamps from affecting the porosity and natural fluid flow within the structure when grasping the sample. The disadvantage is that the adhesion condition depends on the strength of the applied glue and not on the applied clamping strain.

The loading protocol was based on what was applied in Wright et al. (2016) in human discs, taking advantage of the similarity in the geometry of the samples in this work. The following

protocol was applied :

- Pre-charge phase of 0.05 N at a strain rate of 1% strain /s.
- Nine displacement-controlled preconditioning cycles, with a 2% strain at a strain rate of 0.2%/s.
- After preconditioning, the initial position was reached again.
- A pre-charge of 0.05 N was reapplied.
- The following strain increments were then applied:
  - 5%, for 15 min
  - 10%, for 15 min
  - 15%, for 15 min
  - 20%, for 20 min

Strain increments were applied under displacement control and maintained constant to allow the observation of relaxation phenomena. The displacement plateaux were attained by imposing a strain rate of 1 %/s.

The application of this protocol allows the observation of stress relaxation effects, as shown in Figure 1.9b.

3.5.2 Tensile results data treatment method

The tensile results were processed using a fitting algorithm developed by the team, previously used for the hyperelastic characterization of other biological tissues (Baldit et al., 2022).

In this case, Lagrangian stress and strain measurements were used to process the results, calculated according to the equation 3.19

$$\sigma = \frac{F}{A_0} \qquad \text{and} \qquad E = \frac{1}{2}(\lambda^2 - 1) \tag{3.19}$$

where A_0 represents the cross-section and F the measured force. The Green-Lagrange strain E depends on the applied stretch, defined as $\lambda = L/L_0$, where L_0 is the initial length of the sample and L is the length after deformation.

To observe the magnitude of the stresses involved, the experimental curves were characterized using a bilinear approach, where the initial and final slopes were plotted as in Figure 1.9a. The stiffness moduli (E_{toe} and E_{linear}) at these two instants were calculated for the samples.

Next, a hyperelastic approach was adopted, where the stress and strain curves were fitted to Ogden's constitutive law (equation 2.14). Due to the lack of data on the sample's volumetric behavior, the spherical portion of the constitutive law was disregarded, and the material was considered incompressible. This simplification was adopted because it was assumed that the discs' tensile behavior depends on the fiber network's stress, and that the deviatoric portion of the equation 2.14 would be sufficient to represent their tensile characteristics through shear modulus.

3.5.3 Results

An example result is shown in Figure 3.35.

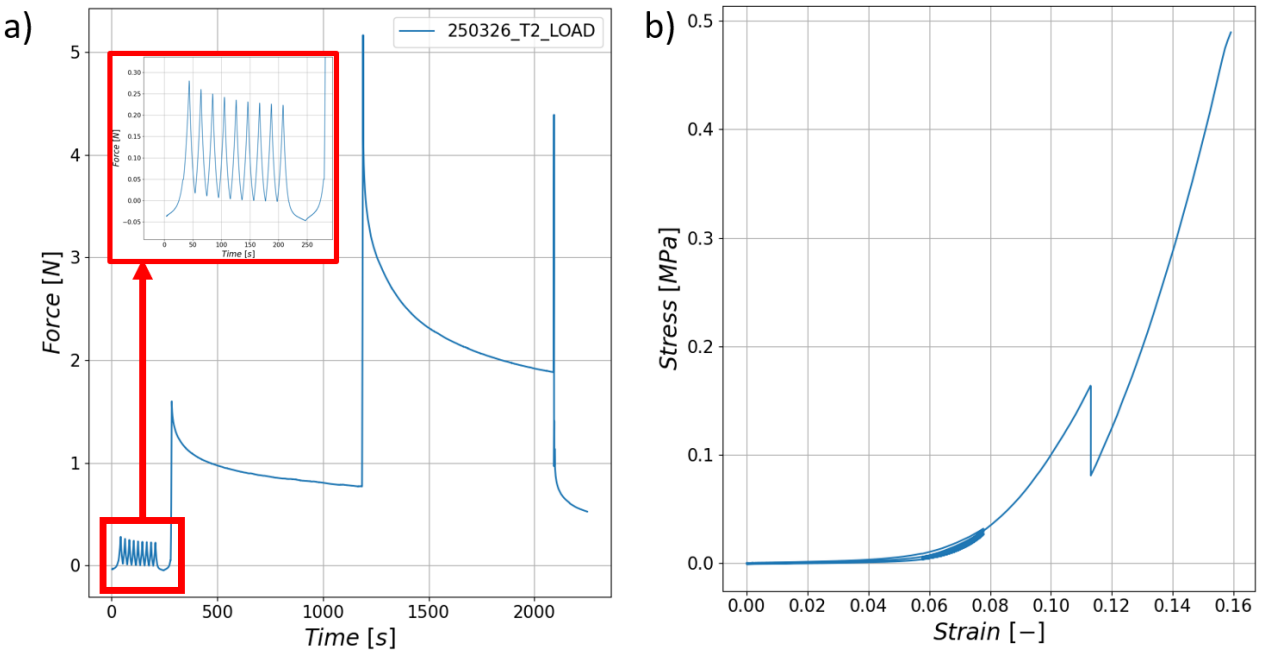

Figure 3.35: Experimental tensile results for sample 240311-Head2-Right. a) Measured force over time showing pre-conditionning cycle (in the zoom), two relaxation phases and sample detachment in the loading phase of the third relaxation step, around 2000 s. b) Stress-strain behavior derived from experimental result in figure (a).

Figure 3.35a shows the evolution of force over time. It is possible to observe the preconditioning phase (in the zoomed part of Figure 3.35a) and the moments of sudden force increases when the displacements were applied. Even if the sample tension is kept constant, for example, between 500 and 1000 seconds of the test, the force decay reveals the presence of viscous phenomena. This is translated by a vertical decay in Figure 3.35b, where the stress decreases at constant strain.

When the third displacement increment was applied (around 2000 seconds into the test), there was a sudden drop in force values, related to the sample's detatchment from the support. The test results from the debonding instants were disregarded, and the stress-strain data from only the first two displacement increments were considered. This was a disadvantage of the adopted fixation method, as higher tensile stresses could not be applied and rupture of the tensile specimens was not reached. Nevertheless, the observation of the stresses at the beginning of loading was considered sufficient to represent the structure's initial resistance.

Bilinear characterization was initially applied and is shown in Figure 3.36.

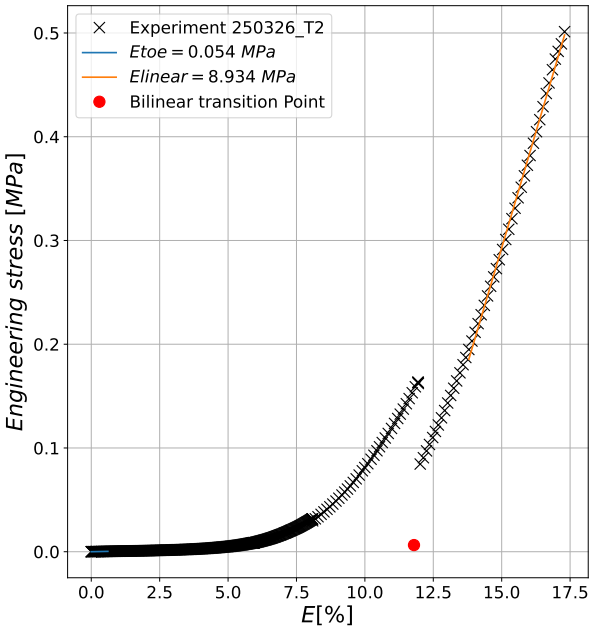

Figure 3.36: Bilinear fit of stress-strain cuve for sample 240311-Head2-right.

The figure shows the slope of the curves representing a Young's modulus E_{toe} for the toe region, representing the immediate behavior of the material under tension, and a modulus E_{linear}, representing the behavior at the end of the test, where the structure increased its stiffness. This increase in stiffness may be related to the progressive alignment of the fiber network, which becomes more stressed as the test progresses and increases its contribution to the strength of the sample structure.

The hyperelastic fitting is shown in Figure 3.37.

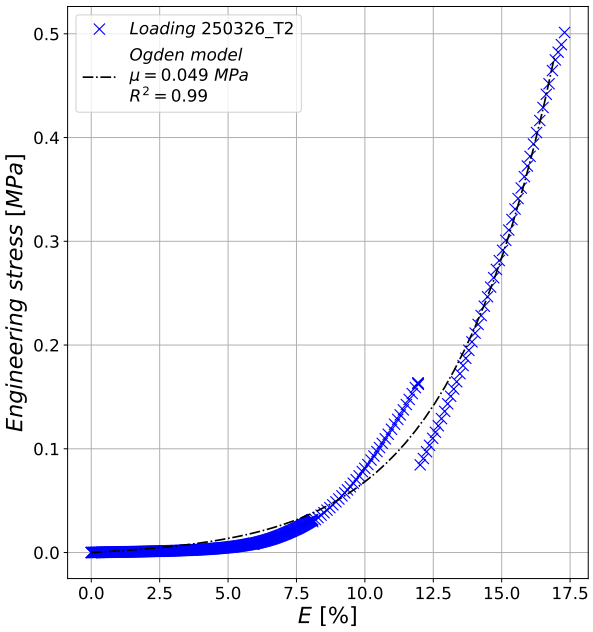

Figure 3.37: Hyperelastic fit of stress-strain curve for sample 240311-Head2-right.

The example shown in Figure 3.37 is representative of the fittings performed, which had an average correlation coefficient of $R^2 = 0.95$. The discontinuity caused by the relaxation effect was disregarded, and the fitting can well approximate the material behavior during the loading phases. A summary of the results for all experiments is shown in Table 3.4.

		Bilinear fit		Hyperelastic Ogden
Region	n	E_{toe} [kPa]	E_{linear} [kPa]	μ [kPa]
Medial	7	138.85 ± 185.55	10631.68 ± 6587.81	77.57 ± 106.83
Lateral	8	185.70 ± 166.69	13585.25 ± 9558.73	83.96 ± 105.52
Anterior	2	21.18 ± 5.11	11789.60 ± 10097.08	7.73 ± 6.07
Posterior	2	88.63 ± 61.56	29369.96 ± 4066.03	14.88 ± 5.52
Mean	19	150.68 ± 162.32	14684.64 ± 9031.23	70.73 ± 96.81

Table 3.4: Mechanical properties of the disc using bilinear and hyperelastic models.

Due to sample preparation issues, only seven quality samples could be produced from the medial portion, and, as mentioned above, the disc dimensions allowed only two anterior and two posterior samples to be used.

Regarding the bilinear fit, the increase in stiffness is clear when transitioning from the toe zone to the final zone. The posterior zone had the highest final stiffness, while the medial zone had the lowest stiffness. In the literature, the most similar metric to the one adopted here was the Instantaneous Modulus measurement in Wright et al. (2016), which corresponds to E_{linear} here. The values they found are of the same order of magnitude as those in the present study, where greater stiffness was observed for discs in the posterior position (around 9.3 MPa) and in the central anterior-posterior region (10 MPa), which was not tested in tension in the present study. Using the bilinear fit method, the least stiff zone was the medial, which also had values among the lowest (6.15 MPa) in Wright et al. (2016), which was only less stiff than the central mediolateral portion (not tested in this study).

The hyperelastic fitting was used to estimate shear modulus, which has not yet been measured in the context of tensile testing for porcine TMJ discs in the literature. The results for the hyperelastic fitting showed great variability, evidenced by the observed standard deviations. The medial and lateral portions presented the highest shear stiffness, while also having the lowest final tensile stiffness using the bilinear approach. The small number of samples for the anterior and posterior portions calls into question the comparison of the other results with these zones, and the large standard deviations indicate high variability in the results.

In general, the total average value obtained for the tensile shear modulus is $\mu = (70.73 \pm 96.8)$ kPa. In contrast, the same measurement obtained in the context of spherical compression was $\mu = (2.21 \pm 1.69)$ kPa for the medial portion and $\mu = (2.11 \pm 0.90)$ kPa for the lateral portion (see table 2.8). The same set of samples was tested, and this variability can be attributed to multiple factors, such as the distinct stress states imposed in the different tests, as well as the directional sensitivity of the tissue linked to its anisotropy, given that tension was performed in the anteroposterior and mediolateral directions, while compression occurred in the inferior-superior direction.

Ideally, conducting more tests would further enrich the results obtained here, which showed great variability in the tensile response. Furthermore, the central zones were not tested in tension, as this region of the disc had been reserved for other tests. Conducting another test campaign with samples dedicated exclusively to tensile testing would allow for a more in-depth exploration of regional property variations, with the production of larger specimens and also exploring the behavior of the disc in the direction perpendicular to the fiber network in the mediolateral direction of the central part of the discs, for instance.

Considering hyperelastic behavior for the solid phase, the observed viscous effects are related to fluid exudation from the structure. Therefore, the curves obtained after stabilization in stress relaxation proportionally reflect a greater contribution of the fiber network to the

sample's mechanical behavior. Conversely, assuming that the solid phase also exhibits intrinsically viscous behavior, viscosity is no longer related exclusively to fluid motion. This is a valid approach and a natural evolution for future models, given reports of a greater contribution from the solid phase than the fluid in the context of tension.

For now, the current model does not explore the relaxation effect and is limited to the loading phases. The monophasic characterization performed here does not take into account the biphasic aspects of the disc and the experimental data can be explored in future studies, serving as a first set of parameters to be based on. Nevertheless, tissue anisotropy was observed, explaining possible stiffness variations measured using different approaches in the literature, as discussed in the introductory section 1.4.

3.6 Conclusion

Observation of the SEM images highlighted the inhomogeneity of the disc's structure, which presents a denser outer layer covering its superior and inferior surfaces. This layer, although reported in a study using OCT images in the literature, could be visualized more clearly in the freeze-dried samples, raising the importance of considering the potential multilayer aspects of discs in future studies, which is still overlooked in the current literature.

Anisotropic deformation when releasing the disc's internal stresses after cutting indicated greater resistance of the material to expansion in the anteroposterior direction (in the direction of the fiber network), corroborating the idea that fibers play a major role in the material's tensile strength, given the fiber network orientation evidenced by MRI images. The cylindrical samples tended to decrease in volume, indicating permanent changes in the structure after removal from their physiological environment and testing.

Tensile tests indicated different magnitudes of shear modulus for different regions of the material, hinting for structural inhomogeneity and also anisotropy. The anterior and posterior samples presented a shear modulus μ of 7.73 ± 6.07 kPa and 14.88 ± 5.52 kPa, while medial and lateral regions had μ equal to 77.57 ± 106.83 kPa and 83.96 ± 105.52 kPa respectively, which differed when compared with the shear modulus obtained through compression in the superior-inferior direction of the material by spherical or confined compression.

This chapter initially presented the results for confined compression and direct permeation tests, using experiments performed on custom-made devices. Unlike spherical compression, which compressed only the most superficial part of the discs, confined compression stressed the entire structure of the samples in the superior-inferior direction. The method allowed estimating average shear modulus values of $\mu = 43.88 \pm 10.85$ kPa and bulk modulus $\kappa = 61.50 \pm 32.13$ kPa, assuming linearized behavior for the solid phase, and $\mu = 22.98 \pm 9.04$ kPa and $\kappa = 74.56 \pm 38.26$ kPa for the compressible neo-Hookean approach, representing an order of magnitude increase over the results found in Chapter 2. Extending the definition to a second order reduced polynomial strain energy definition presented no advantages in the current optimization framework. The permeability values for confined compression were on the order of $10^{-15} m^4/Ns$, demonstrating equivalence with what was measured through spherical compression in Chapter 2.

To date, direct permeation has yielded only one result, also on the order of $10^{-15} m^4/Ns$, which could not be reproduced for the other samples. Future tests on previously unexplored samples will be performed for more in-depth analysis.

General conclusion and perspectives

The temporomandibular disc plays an essential role in the functioning of the TMJ. Understanding the diffusion phenomena within it is relevant not only to explain tissue mechanics but also to understand how pathological changes can compromise its nutrition. Therefore, the characterizations performed here sought to identify models capable of describing the behavior of the solid phase, using the shear modulus (μ) and the bulk modulus (κ), associated with a permeability (k) representative of fluid dynamics. The interest in the biphasic approach is widely supported by the literature, given the nature of the disc. However, a researcher attempting to reproduce its behavior, whether numerically or experimentally, is confronted with a wide range of material definitions. This inconsistency is concerning, especially considering the persistent challenges in developing effective and lasting solutions for TMJ disorders.

This study characterized porcine temporomandibular discs, considered the closest to humans in terms of composition and physiological stimuli. Eight discs were collected and subjected to an extensive experimental campaign, seeking to extract maximum information from each specimen. MRI images were taken while the discs were still fresh, providing data on their initial volume. The discs were then evaluated in non-destructive spherical compression tests, replicating the Tappert (2020) protocol and expanding the team's database. Subsequently, a cylindrical cut was made at their center, and progressive deformation was observed, evidencing internal stresses and structural anisotropy. These approximately cylindrical specimens were then tested in confined compression and direct permeation, and were again evaluated by MRI, where variations in volume and final shape were observed, dependent on the orientation of the collagen fibers. Concurrently, rectangular samples were subjected to tensile tests, revealing the anisotropic nature of the material. They were then freeze-dried and analyzed using a scanning electron microscope (SEM), where heterogeneous aspects of the structure, little explored in the literature, were observed.

Chapter 2 presented spherical compression, in which cyclic tests were conducted with spheres of different radii. Increasing the radius resulted in greater forces, as expected, due to the compression of wider portions of the material. The viscoelastic response was evidenced by the variation in loading frequency and inter and intracyclic hysteresis. The results corroborated the applicability of the biphasic theory to tissue behavior. Higher compression speeds generated higher reaction forces, associated with the fluid flow and its drag resistance. The lateral, central, and medial regions of the TMJ discs were compared, but showed no significant differences in stiffness when submitted to spherical compression.

The same chapter presented the evolution of the monophasic hyperelastic characterization method by spherical compression, initiated in Tappert (2020). Currently in the publication process (de Oliveira Cafiero et al., in preparation), the method has great application potential due to the scarcity of approaches that adapt the Hertz model to characterize thin layers of hyperelastic tissues submitted to spherical compression when detached from the bottom surface. Applied to the TMJ disc results, it provided parameters indicative of stiffness, yet without incorporating the poromechanical framework.

The finite element analysis of spherical compression showed that the models available in the literature do not adequately reproduce the mechanics experimentally observed here. The optimization performed on the material definition for the FE models was effective in adjusting force and displacement from the simulations based on experimental data. Permeability values were found to be on the order of $10^{-15} m^4/Ns$ and shear and bulk modulus values on the order of kPa.

While Chapter 2 characterized the disc's most superficial zone by compressing it partially, the confined compression described in Chapter 3 loaded the entire structure in creep tests. The applied model provided results an order of magnitude higher than the values obtained with spherical compression. Although these are the same specimens, the difference may be related to both the particularities of each model and the distinct regions that were stressed.

Confined compression attributed a Poisson's ratio of $\nu = 0.178 \pm 0.094$ to the solid phase, in contrast to the incompressibility usually assumed for water-rich biological tissues. The consideration of fluid flow in the model eliminates this often adopted simplification, demonstrating macroscopically compressible behavior, even in materials composed of intrinsically incompressible phases. The shear modulus was also estimated in tension, using monophasic characterization, showing high variability between the medial, lateral, anterior, and posterior regions. The image correlation process showed progressive deformations induced by the cutting of the samples, with contraction along the fibers direction and perpendicular stretching, resulting in a reduction in volume during the tests, measured through MRI data analysis. SEM analyses revealed structural heterogeneity, with a thin outer layer denser than the inner regions, still overlooked in biomechanical studies of the disc.

The applied models have limitations, such as the assumption of constant, isotropic, and homogeneous permeability. The tensile tests were treated as monophasic, considering the hyperelastic solid phase. The parameters obtained in this work can serve as an initial guess in further developments.

The multilayered appearance observed under the microscope raises questions about the material definitions adopted. Variation of permeability in the outer region may affect fluid flow. This can be modeled by different properties in a surface layer of elements under spherical compression FE simulations. Furthermore, the contact with the sphere was assumed to be permeable, and flow conditions dependent on contact pressure (non-trivial in Abaqus) and local property variations are prospects for future work.

Putting aside the non negligible effect of stress release, permeability differences across the disc thickness could be determined by direct permeation tests on thinner layers obtained by microtomy, as in Tverje & Nyashin (2010), which studied the middle layer of the disc. The large structural thickness of the disc used here may have been one of the causes of the difficulty in conducting the direct permeation tests, which resulted in only one experimental measurement, while other disc samples were not able to be permeated. A possible future perspective is to perform permeation on microtomed samples from different points along the thickness of the discs, which would allow mapping the permeability variation in that direction. This multilayered disc could then be simulated in a spherical compression FE simulation, assigning layers of elements with distinct properties throughout its thickness. Thus, the optimization process performed in Chapter 2 could be applied to an axisymmetric multilayer simulation where only the solid phase definition parameters would be unknown and a non homogeneous definition of the disc could be proposed.

Furthermore, the spherical compression experiments were not yet explored in the FE simulation optimization in terms of loading frequency influence. Due to the viscoelastic nature of the discs, variations in the forces involved with different frequencies have been observed, but simulations of this type have not yet been performed and only low loading velocities were treated here. This is possibly related to the limitations of the software used (Abaqus), particularly when dealing with poromechanics, suggesting the need to explore alternative tools in future studies. The open-source software FEBio, for instance, allows for biphasic simulations including constitutive laws that consider permeability dependent on the imposed strain. Assigning a more complex law to permeability is interesting, being closer to reality. This, however, adds at least one more optimization variable that relates strain to permeability. This challenge can be mitigated by acquiring experimental permeability data at different compression levels

of the TMJ discs, as it has been done with the sponge. This would require modifications of the permeation device which are not discarded for now and open for discussion. The BIO2MS TMJ database has been enriched with 8 more discs with various experimental results. The discs were also subjected to spherical compression under stress relaxation (constant imposed displacement of spheres), which has not yet been addressed, and these results were not included in the thesis. Since this is the same test campaign as the discs here, it would be interesting to verify the estimated parameters through optimization for the stress relaxation context. Besides, the tensile tests were treated only through monophasic characterization, and the exploration of their poromechanical aspects was not studied due to time constraints. In future biphasic numerical simulations of tensile behavior, it would be relevant to include the intrinsic viscosity to the solid phase in this case, given the greater contribution of the collagen network to tensile stress. With more disc samples, it will also be possible to further explore the anisotropy of the discs through other testing campaigns, with discs that can be dedicated exclusively to the production of specimens with different orientations of the fiber network within them.

On the other hand, diffusion MRI could be a valuable tool for analyzing solute diffusivity in discs, which has also been little explored in the literature, and only a preliminary result was presented in this thesis. Compressing a sample at different degrees of strain while simultaneously performing a field capture would be particularly interesting. Actually, it allows observing the influence of pore volume variation on diffusivity within the material, which is relevant for studies aimed at analyzing disc compression and its effect on cellular nutrition. Confined compression in MRI and the design of a device that allows this to be achieved are currently being discussed by the team through the ANR project HyCareMat.

Currently, the BIO2MS team has a 3D-scanned FE model of a porcine disc, in which the obtained biphasic parameters can be applied to more realistic geometries than the axisymmetric model. So the axisymmetric tests conducted here can be validated in the future with a more realistic disc geometry. In parallel, an Abaqus model integrating the bone structure of the TMJ, mandible, and skull, with kinematics corresponding to the same healthy patient, is also available (de Oliveira Cafiero, 2021), and the incorporation of poromechanical definitions is a planned step in its development. The definition of a complete TMJ model, with the integration of biphasic disc components obtained through an extensive testing campaign, presents a great opening for future studies, analyzing pathological contexts and their possible solutions.

This work gave me the opportunity to participate in two international conferences during the period of the thesis (de Oliveira Cafiero et al., 2024a, 2025c) and one French conference (de Oliveira Cafiero et al., 2025a). During my PhD, I worked on three published articles (de Oliveira Cafiero et al., 2024b, 2025b; Schall et al., 2025) and contributed to two additional articles that will be submitted soon (de Oliveira Cafiero et al., in preparation; Krawiec et al., in preparation).

Appendix A

Spherical compression system stiffness compensation

This appendix complements the experimental protocol of the spherical compression tests described in section 2.1.2. Before the experimental data treatment of the sperical compression tests, a system stiffness compensation procedure was performed in order to isolate the behavior of the tested tissue from the rest of the system. To achieve this, it was necessary to measure the stiffness of the load cell, the used tools for each of the spheres, the 3D printed support and the micrometric positioning stage. A force of 1 N was applied at 0.05 mm/s to the system without the presence of the disc, where force-displacement curves were recorded. This compression protocol was applied to each of the compression spheres, which were positioned in the medial, central and lateral regions of the condyle support, based on the position measurements previously performed when the disc was still glued to the system.

The slope of the force-displacement curves corresponding to the machine stiffness were obtained, with an overall average value of $k_m \approx 12.33$ N/mm. Following the technique proposed in Kalidindi et al. (1997), the displacements measured during the tests were corrected based on this stiffness, according to

$$d_s = d_t - \frac{F}{k_m} \tag{A.1}$$

where d_s is the corrected sample displacement, d_t is the total displacement measured by the machine and F is the corresponding measured force at each instant of the test. This procedure allowed isolating sample displacement from the surrounding system's deformation and the values of d_s were the ones used in subsequent data treatment.

Appendix B

Spherical compression monophasic characterization complementary results

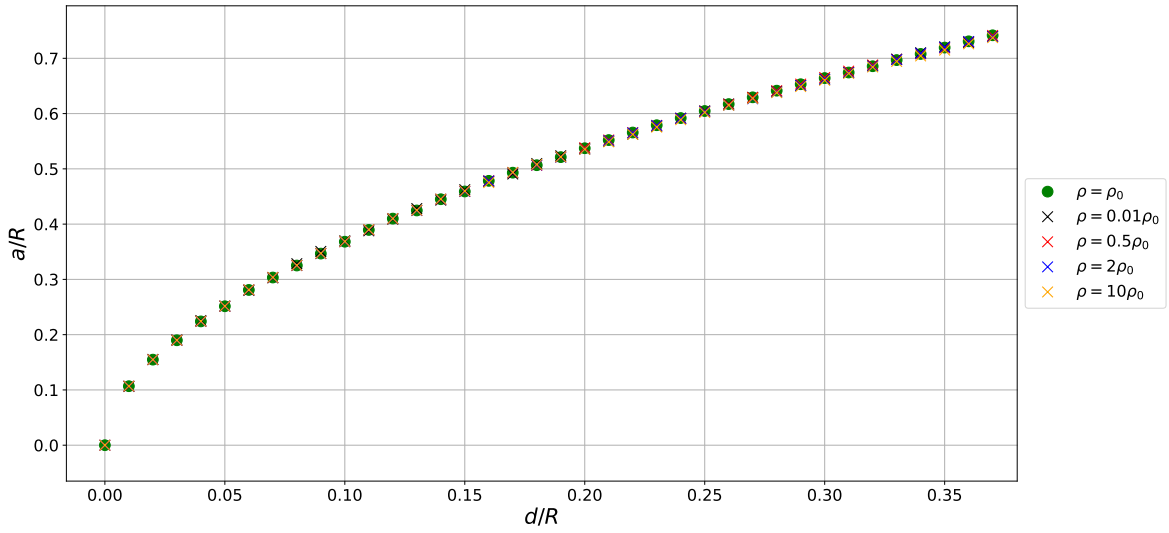

Figure B.1: Influence of density variation on contact radius evolution for simulations of $h = 0.5$, $L = 25R$, $\nu = 0.499$

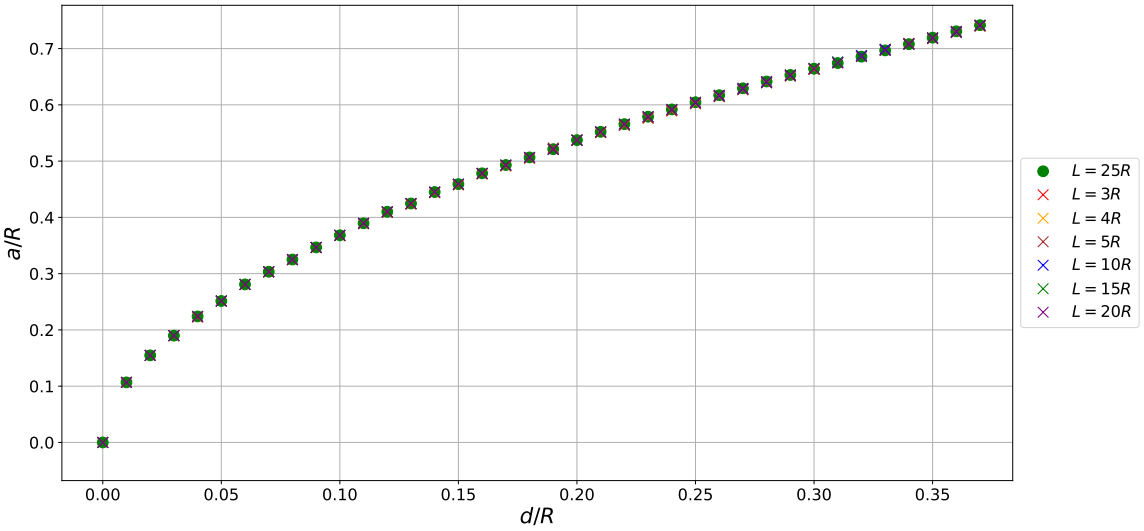

Figure B.2: Influence of sample length variation on contact radius evolution for simulations of $h = 0.5$, $\rho = \rho_0$, $\nu = 0.499$

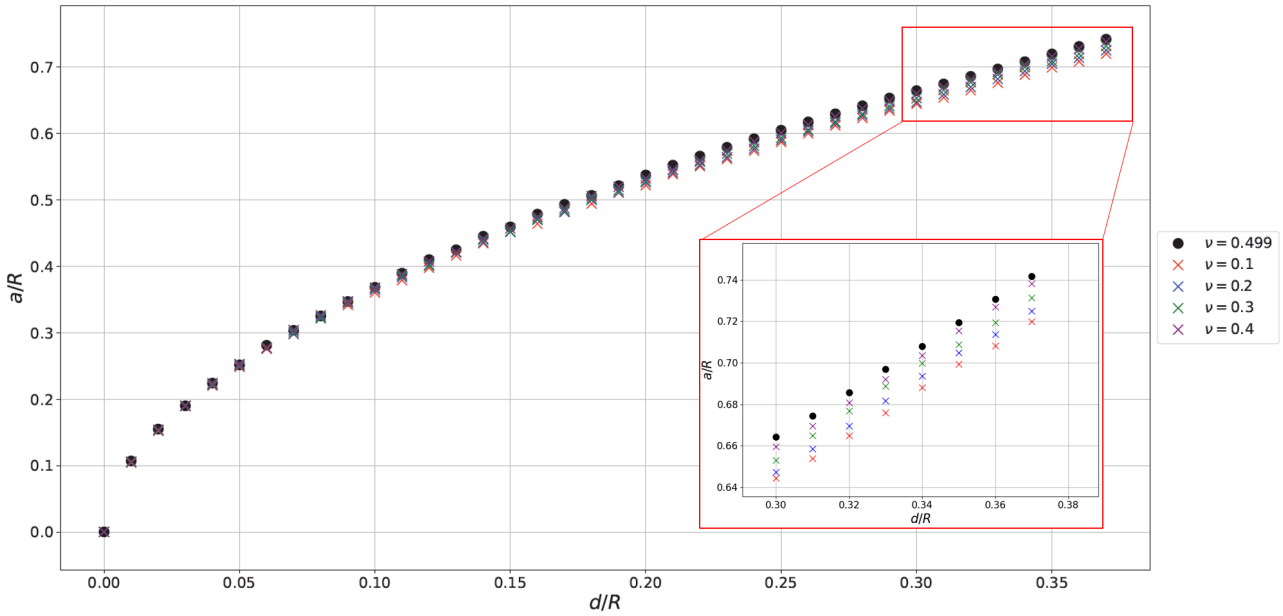

Figure B.3: Influence of Poisson's ratio variation on contact radius evolution $h = 0.5$, $\rho = \rho_0$, $L = 25R$.

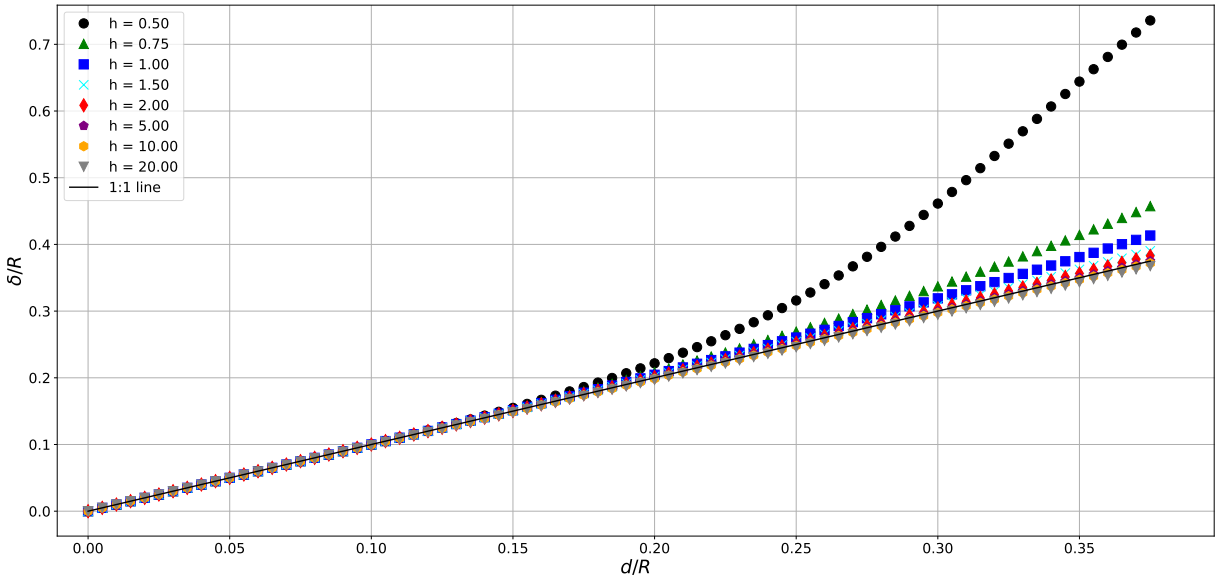

Figure B.4: Relationship between d/R and δ/R for measurements of δ/R at distance $R_\delta = 5R$ from the symmetry axis.

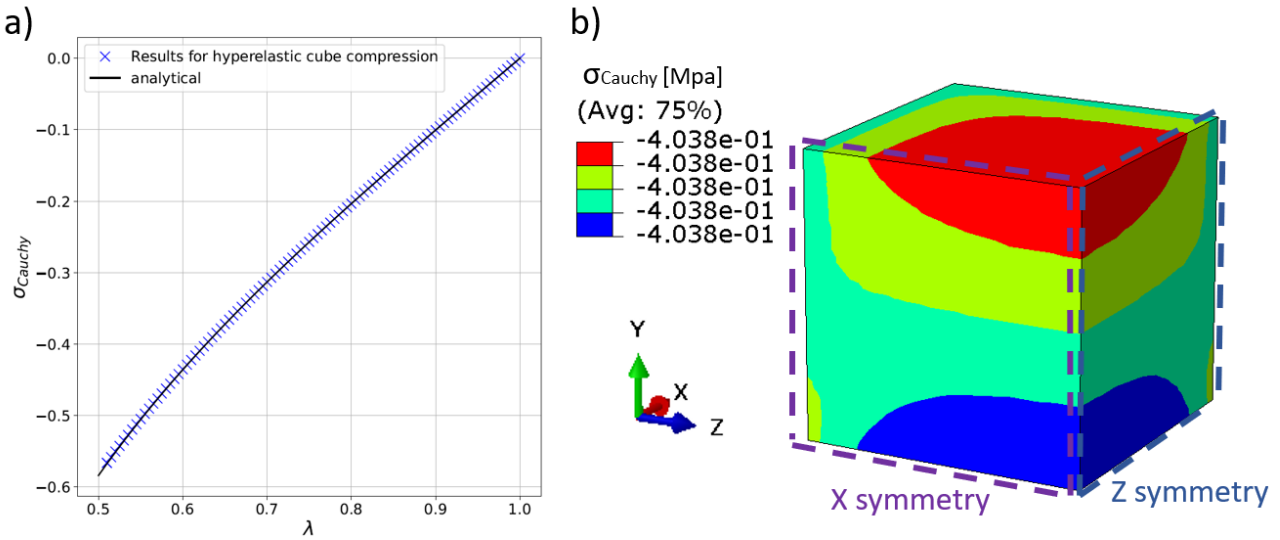

Figure B.5: a) Comparison of analytical stress vs stretch to the uni-axial cube compression. b) Finite elements results 1/4th of 3D neo-Hookean cube in uniaxial compression with 37.5% imposed strain .

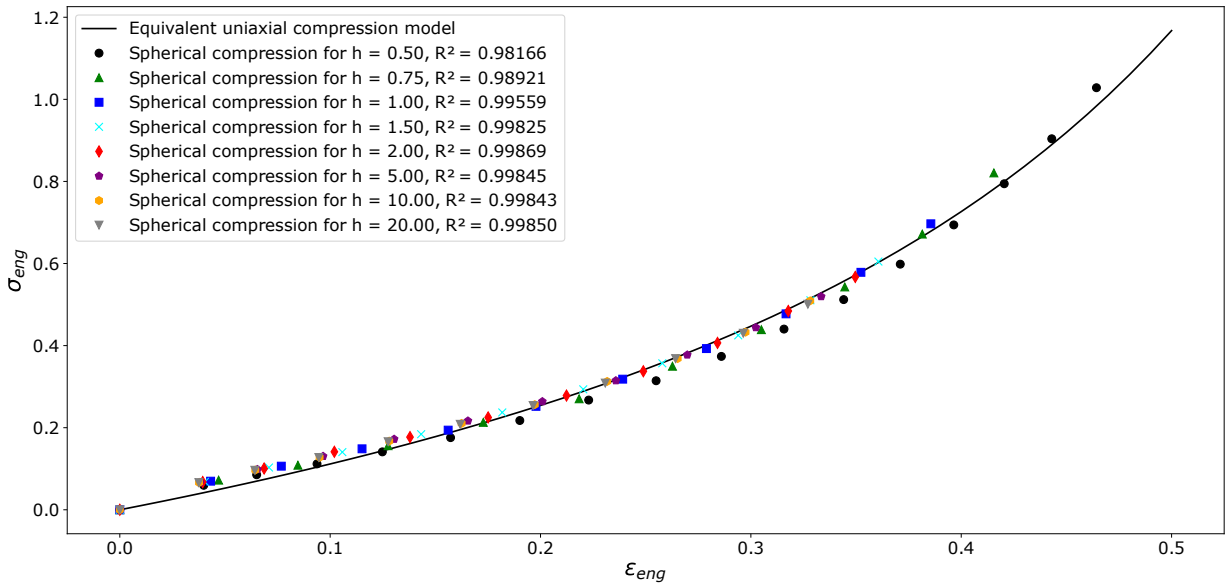

Figure B.6: Engineering effective stress (σ_{eng}) vs strain (ε_{eng}) for spherical compression simulations in comparison to the neo-Hookean uniaxial compression model.

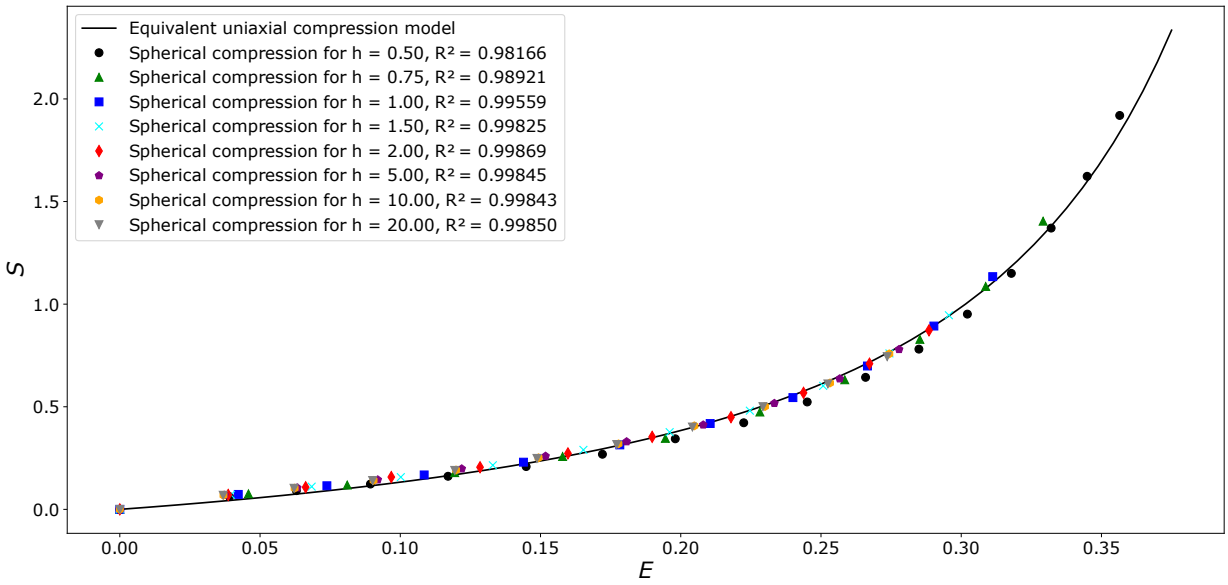

Figure B.7: Lagrangian effective stress (S) vs strain (E) for spherical compression simulations compared to a neo-Hookean uniaxial compression model.

Appendix C

Spherical compression biphasic simulation fluid velocity for blocked superficial flow

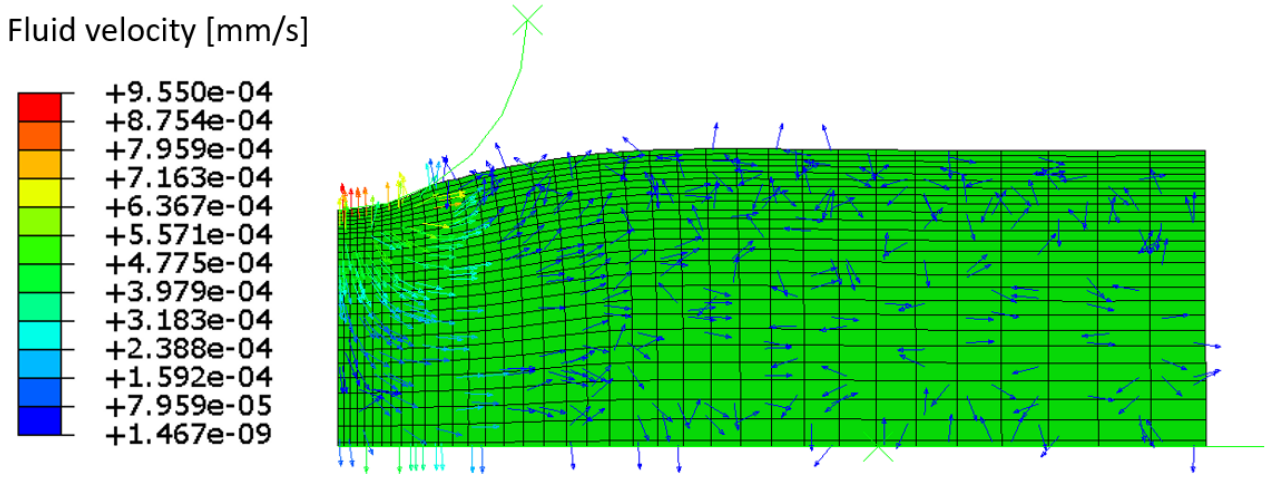

Figure C.1: Fluid flow velocity field for biphasic axisymmetric compression referring to section 2.5 with Model 2 parameters from table 2.6, analogous to Figure 2.22 but with the application of the impermeable boundary condition referring to Figure 2.23.

Appendix D

Spherical compression biphasic optimization results details

Permeability k [$\times 10^{-15}$ m^4/Ns]			
	Disc Zone		
Radius	Medial	Central	Lateral
0.875	1.11 ± 0.15	1.30 ± 1.11	1.11 ± 0.52
1.75	1.24 ± 0.20	1.03 ± 0.52	1.14 ± 0.29
3	0.94 ± 0.51	1.02 ± 0.42	1.02 ± 0.47

Table D.1: Permeability Data by radius and disc zone.

Shear modulus μ [kPa]			
	Disc Zone		
Radius	Medial	Central	Lateral
0.875	4.41 ± 2.40	4.62 ± 3.29	2.84 ± 1.32
1.75	1.39 ± 0.51	1.38 ± 0.74	1.65 ± 0.62
3	1.46 ± 0.82	1.86 ± 0.88	1.47 ± 0.72

Table D.2: Shear modulus by radius and disc zone.

Bulk modulus κ [kPa]			
	Disc Zone		
Radius	Medial	Central	Lateral
0.875	5.07 ± 3.33	4.57 ± 3.02	2.54 ± 1.23
1.75	1.50 ± 0.68	1.51 ± 0.81	1.81 ± 0.76
3	1.83 ± 1.11	2.86 ± 2.51	1.84 ± 0.97

Table D.3: Bulk modulus by radius and disc zone.

Appendix E

Confined compression results details

Table E.1: Confined compression parameter results for multiple behavior laws

Disc	Model	k $[m^4/Ns]$	μ [kPa]	ν	κ [kPa]	C_{10} [Pa]	D_1 [1/Pa]	C_{20} [Pa]
230111-Head1-Left	LE	1.86×10^{-15}	43.44	0.209	60.12	21.72	0.033	
	NH	1.11×10^{-15}	16.34		76.51	8.17	0.026	
	RP	1.18×10^{-15}				3.68	0.020	-9.07×10^{-19}
230111-Head1-Right	LE	2.11×10^{-15}	43.62	0.298	93.31	21.81	0.021	
	NH	1.49×10^{-15}	16.28		117.23	8.14	0.017	
	RP	1.42×10^{-15}				15.67	0.024	-7.34×10^{-20}
230524-Head1-Left	LE	1.07×10^{-15}	53.33	0.291	110.00	26.67	0.018	
	NH	7.85×10^{-16}	30.82		120.70	15.41	0.017	
	RP	7.79×10^{-16}				17.08	0.018	-2.53×10^{-19}
230524-Head1-Right	LE	9.26×10^{-15}	41.08	0.051	32.07	20.54	0.062	
	NH	3.89×10^{-15}	9.29		50.11	4.65	0.040	
	RP	4.12×10^{-16}				3.43	0.033	-1.36×10^{-19}
240311-Head1-Left	LE	5.43×10^{-16}	19.23	0.135	19.92	9.61	0.100	
	NH	1.70×10^{-15}	30.54		131.06	15.27	0.015	
	RP	1.61×10^{-15}				14.95	0.017	1.54×10^{-19}
240311-Head1-Right	LE	1.17×10^{-15}	50.02	0.089	44.19	25.01	0.045	
	NH	6.18×10^{-16}	26.54		39.24	13.27	0.051	
	RP	6.12×10^{-16}				13.97	0.057	-3.39×10^{-20}
240311-Head2-Left	LE	2.21×10^{-15}	49.12	0.264	87.65	24.56	0.023	
	NH	1.52×10^{-15}	27.86		94.43	13.93	0.021	
	RP	1.55×10^{-15}				10.17	0.018	-1.93×10^{-19}
240311-Head2-Right	LE	1.99×10^{-15}	51.23	0.085	44.70	25.61	0.045	
	NH	1.03×10^{-15}	33.76		23.67	16.88	0.084	
	RP	1.55×10^{-15}				10.17	0.018	-1.93×10^{-19}
Mean	LE	$(1.49 \pm 0.63) \times 10^{-15}$	43.88 ± 10.85	0.178 ± 0.100	61.50 ± 32.13	21.94 ± 5.43	0.044 ± 0.027	
	NH	$(1.08 \pm 0.47) \times 10^{-15}$	23.93 ± 8.79		81.62 ± 40.67	11.96 ± 4.39	0.034 ± 0.024	
	RP	$(1.14 \pm 0.48) \times 10^{-15}$				11.14 ± 5.28	0.026 ± 0.014	$(-2.56 \pm 3.11) \times 10^{-19}$

Appendix F

MRI images of cut samples

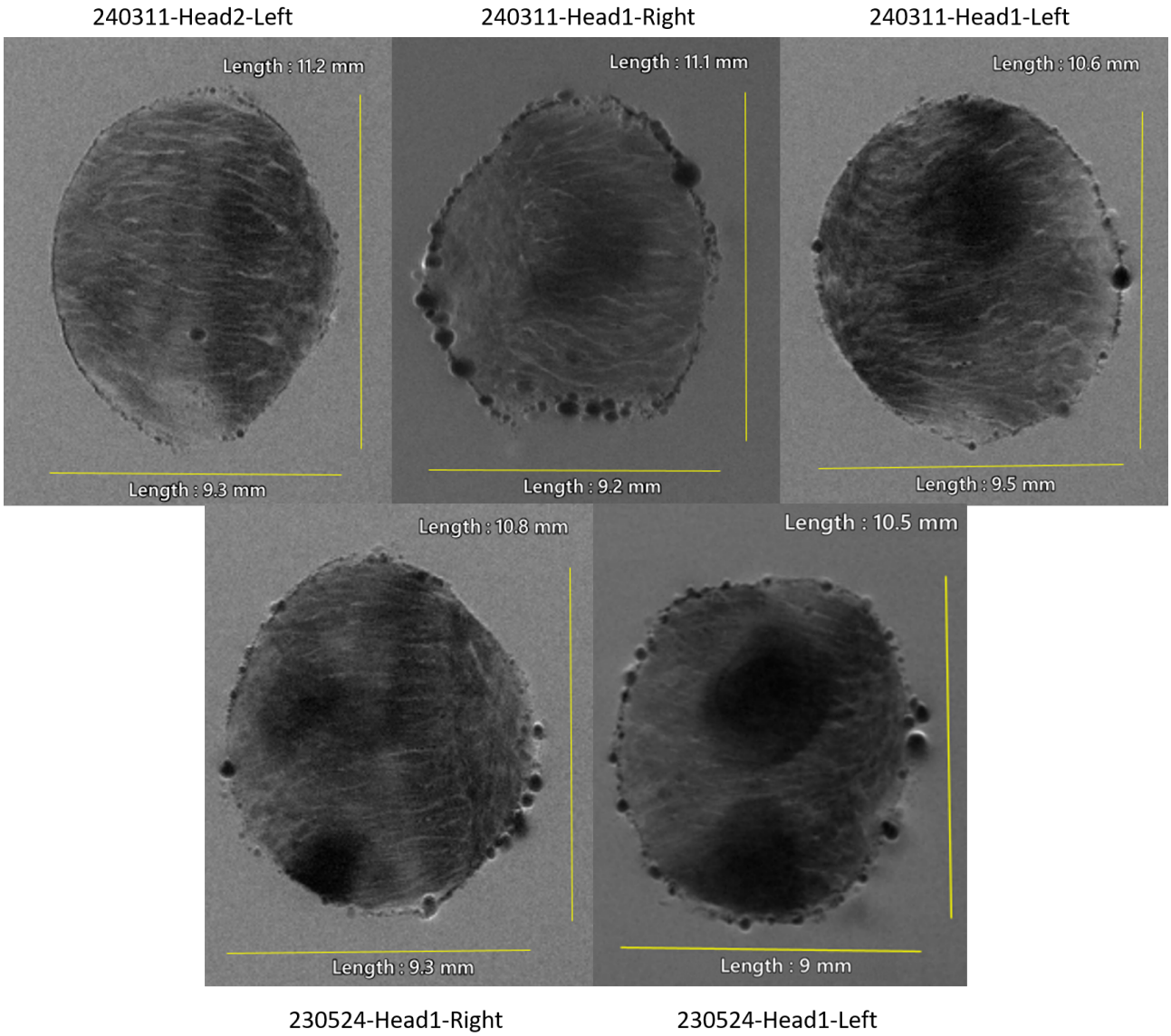

Figure F.1: MRI of disc samples (names on images) on the central slice. The deformation pattern was the same in relation to the orientation of the fiber network for all discs. Acquisition parameters: Spin Echo (MSME) – FOV 3 cm, slice thickness 0.5 mm, matrix 512 × 512 pixels, TE 8.8 ms, TR 2000 ms, 10 slices, 8 averages.

Bibliography

Accadbled, F., Ambard, D., de Gauzy, J. S., & Swider, P. (2008). A measurement technique to evaluate the macroscopic permeability of the vertebral end-plate. Medical Engineering & Physics, 30(1), 116–122.

Acri, T. M., Shin, K., Seol, D., Laird, N. Z., Song, I., Geary, S. M., Chakka, J. L., Martin, J. A., & Salem, A. K. (2019). Tissue Engineering for the Temporomandibular Joint. Advanced Healthcare Materials, 8(2), 1801236.

Aernouts, J., Aerts, J. R., & Dirckx, J. J. (2012). Mechanical properties of human tympanic membrane in the quasi-static regime from in situ point indentation measurements. Hearing Research, 290(1-2), 45–54.

Almarza, A., Bean, A., Baggett, L., & Athanasiou, K. (2006). Biochemical analysis of the porcine temporomandibular joint disc. British Journal of Oral and Maxillofacial Surgery, 44(2), 124–128.

Almarza, A. J. & Athanasiou, K. A. (2004). Design Characteristics for the Tissue Engineering of Cartilaginous Tissues. Annals of Biomedical Engineering, 32(1), 2–17.

Alomar, X., Medrano, J., Cabratosa, J., Clavero, J., Lorente, M., Serra, I., Monill, J., & Salvador, A. (2007). Anatomy of the Temporomandibular Joint. Seminars in Ultrasound, CT and MRI, 28(3), 170–183.

Aoun, M., Mesnard, M., Monède-Hocquard, L., & Ramos, A. (2014). Stress Analysis of Temporomandibular Joint Disc During Maintained Clenching Using a Viscohyperelastic Finite Element Model. Journal of Oral and Maxillofacial Surgery, 72(6), 1070–1077.

Argoubi, M. & Shirazi-Adl, A. (1996). Poroelastic creep response analysis of a lumbar motion segment in compression. Journal of Biomechanics, 29(10), 1331–1339.

Ateshian, G. A. (2017). Mixture Theory for Modeling Biological Tissues: Illustrations from Articular Cartilage. In G. A. Holzapfel & R. W. Ogden (Eds.), Biomechanics: Trends in Modeling and Simulation, volume 20 (pp. 1–51). Cham: Springer International Publishing.

Ateshian, G. A., Warden, W. H., Kim, J. J., Grelsamer, R. P., & Mow, V. C. (1997). BIPHASIC MATERIAL PROPERTIES ARTICULAR CARTILAGE COMPRESSION EXPERIMENTS. 30(11/12), 1157–1164.

Baldit, A., Dubus, M., Sergheraert, J., Kerdjoudj, H., Mauprivez, C., & Rahouadj, R. (2022). Biomechanical tensile behavior of human Wharton's jelly. Journal of the Mechanical Behavior of Biomedical Materials, 126, 104981.

Barrientos, E., Pelayo, F., Tanaka, E., Lamela-Rey, M. J., & Fernández-Canteli, A. (2016). Dynamic and stress relaxation properties of the whole porcine temporomandibular joint disc under compression. Journal of the Mechanical Behavior of Biomedical Materials, 57, 109–115.

Baykal, D., Underwood, R., Mansmann, K., Marcolongo, M., & Kurtz, S. (2013). Evaluation of friction properties of hydrogels based on a biphasic cartilage model. Journal of the Mechanical Behavior of Biomedical Materials, 28, 263–273.

Beatty, M. W., Bruno, M. J., Iwasaki, L. R., & Nickel, J. C. (2001). Strain rate dependent orthotropic properties of pristine and impulsively loaded porcine temporomandibular joint disk. Journal of Biomedical Materials Research, 57(1), 25–34.

Beek, M., Aarnts, M., Koolstra, J., Feilzer, A., & Van Eijden, T. (2001). Dynamic Properties of the Human Temporomandibular Joint Disc. Journal of Dental Research, 80(3), 876–880.

Beek, M., Koolstra, J., & van Eijden, T. (2003). Human temporomandibular joint disc cartilage as a poroelastic material. Clinical Biomechanics, 18(1), 69–76.

Bekrar, M. (2024). Design of a device for measuring the permeability of soft biological tissues (Master's Thesis). Université de Lorraine / École nationale d'ingénieurs de Metz.

Benavides, E., Bilgen, M., Al-Hafez, B., Alrefae, T., Wang, Y., & Spencer, P. (2009). High-resolution magnetic resonance imaging and diffusion tensor imaging of the porcine temporomandibular joint disc. Dentomaxillofacial Radiology, 38(3), 148–155.

Benjamin, M. & Evans, E. J. (1990). Research Review Fibrocartilage. J. Anat., 171, 1–15.

Bermejo, A., González, O., & González, J. (1993). The pig as an animal model for experimentation on the temporomandibular articular complex. Oral Surgery, Oral Medicine, Oral Pathology, 75(1), 18–23.

Biot, M. A. (1941). General Theory of Three-Dimensional Consolidation. Journal of Applied Physics, 12(2), 155–164.

Budday, S., Nay, R., de Rooij, R., Steinmann, P., Wyrobek, T., Ovaert, T. C., & Kuhl, E. (2015). Mechanical properties of gray and white matter brain tissue by indentation. Journal of the Mechanical Behavior of Biomedical Materials, 46, 318–330.

Calvo-Gallego, J. L., Commisso, M. S., Domínguez, J., Tanaka, E., & Martínez-Reina, J. (2017). Effect of freezing storage time on the elastic and viscous properties of the porcine TMJ disc. Journal of the Mechanical Behavior of Biomedical Materials, 71, 314–319.

Carman, P. (1937). Fluid flow through granular beds. Chemical Engineering Research and Design, 75, S32–S48.

Cederlund, A. A. & Aspden, R. M. (2022). Walking on water: Revisiting the role of water in articular cartilage biomechanics in relation to tissue engineering and regenerative medicine. Journal of The Royal Society Interface, 19(193), 20220364.

Chagnon, G., Rebouah, M., & Favier, D. (2015). Hyperelastic Energy Densities for Soft Biological Tissues: A Review. Journal of Elasticity, 120(2), 129–160.

Chen, X., Wang, Y., Mao, Y., Zhou, Z., Zheng, J., Zhen, J., Qiu, Y., Zhang, S., Qin, H., & Yang, C. (2018). Biomechanical evaluation of Chinese customized three-dimensionally printed total temporomandibular joint prostheses: A finite element analysis. Journal of Cranio-Maxillofacial Surgery, 46(9), 1561–1568.

Chow, M.-J. & Zhang, Y. (2011). Changes in the Mechanical and Biochemical Properties of Aortic Tissue due to Cold Storage. Journal of Surgical Research, 171(2), 434–442.

Cisewski, S., Zhang, L., Kuo, J., Wright, G., Wu, Y., Kern, M., & Yao, H. (2015). The effects of oxygen level and glucose concentration on the metabolism of porcine TMJ disc cells. Osteoarthritis and Cartilage, 23(10), 1790–1796.

Commisso, M. S., Martínez-Reina, J., Mayo, J., Domínguez, J., & Tanaka, E. (2014). Effect of non-uniform thickness of samples in stress relaxation tests under unconfined compression of samples of articular discs. Journal of Biomechanics, 47(6), 1526–1530.

Cowin, S. C. & Doty, S. B., Eds. (2007). Tissue Mechanics. SpringerLink Bücher. New York, NY: Springer Science+Business Media, LLC.

Creuillot, V., Dreistadt, C., Kaliński, K. J., & Lipinski, P. (2016). Mechatronic Design Towards Investigation of the Temporo-Mandibular Joint Behaviour. In J. Awrejcewicz, K. J. Kaliński, R. Szewczyk, & M. Kaliczyńska (Eds.), Mechatronics: Ideas, Challenges, Solutions and Applications, volume 414 (pp. 15–32). Cham: Springer International Publishing.

Cutcliffe, H. C. & DeFrate, L. E. (2020). Comparison of Cartilage Mechanical Properties Measured During Creep and Recovery. Scientific Reports, 10(1), 1547.

Dai, A., Wang, S., Zhou, L., Wei, H., Wang, Z., & He, W. (2019). In vivo mechanical characterization of human facial skin combining curved surface imaging and indentation techniques. Skin Research and Technology, 25(2), 142–149.

Danso, E., Julkunen, P., & Korhonen, R. (2018). Poisson's ratio of bovine meniscus determined combining unconfined and confined compression. Journal of Biomechanics, 77, 233–237.

Datta, A. (2006). Hydraulic Permeability of Food Tissues. International Journal of Food Properties, 9(4), 767–780.

de Boer, R. & Ehlers, W. (1990). The development of the concept of effective stresses. Acta Mechanica, 83(1-2), 77–92.

de Oliveira Cafiero, C. (2021). Development of a finite element musculoskeletal model of the maxillofacial area for studies of the temporomandibular joint during biting (Master thesis). Université de Lorraine / École nationale d'ingénieurs de Metz.

de Oliveira Cafiero, C., Baldit, A., & Bonnet, A.-S. (2024a). A first poro-mechanical characterization of temporomandibular joint disc tissue undergoing spherical compression. Oral communication at the 49ème Congrès de la Societé de Biomécanique (October 29-31, 2024), Compiègne, France.

de Oliveira Cafiero, C., Baldit, A., & Bonnet, A.-S. (2025a). Contribution to the understanding of the temporomandibular joint disc behaviour. Oral communication at the 26ème Congrès Français de Mécanique (August 25-29, 2025), Metz, France.

de Oliveira Cafiero, C., Baldit, A., & Bonnet, A.-S. (2025b). A first poro-mechanical characterization of temporomandibular joint disc tissue undergoing spherical compression. Multidisciplinary Biomechanics Journal, 49th congress of the of the Société de Biomécanique.

de Oliveira Cafiero, C., Baldit, A., & Bonnet, A.-S. (2025c). First results on poro-mechanical characterization of temporomandibular joint disc through multiple testing. Oral communication at the 12th European Solid Mechanics Conference (July 7-11, 2025), Lyon, France.

de Oliveira Cafiero, C., Baldit, A., Landier, J., & Rimbert, F. (2024b). Combining experiments, theory, and computer simulation: Application of dynamics analysis of unbalanced wheels rolling without sliding on horizontal paths. Computer Applications in Engineering Education, 32(2), e22692.

de Oliveira Cafiero, C., Tappert, L. K., Baldit, A., Lipinski, P., & Bonnet, A. S. (Manuscript in preparation). Numerical characterization of quasi incompressible soft biological materials' thin layer behavior through macro spherical compression.

Detamore, M. S. & Athanasiou, K. A. (2003). Motivation, Characterization, and Strategy for Tissue Engineering the Temporomandibular Joint Disc. Tissue Engineering, 9(6), 1065–1087.

Detamore, M. S., Orfanos, J. G., Almarza, A. J., French, M. M., Wong, M. E., & Athanasiou, K. A. (2005). Quantitative analysis and comparative regional investigation of the extracellular matrix of the porcine temporomandibular joint disc. Matrix Biology, 24(1), 45–57.

DiSilvestro, M. R., Zhu, Q., Wong, M., Jurvelin, J. S., & Suh, J.-K. F. (2001). Biphasic Poroviscoelastic Simulation of the Unconfined Compression of Articular Cartilage: I—Simultaneous Prediction of Reaction Force and Lateral Displacement. Journal of Biomechanical Engineering, 123(2), 191–197.

Drake, R. L., Wayne Vogl, A., & Mitchell, A. W. M. (2010). Gray's Anatomy for Students. Philadelphia: Elsevier, Churchill Livingstone, 2. ed edition.

Druzinsky, R. E. (1993). The Time Allometry of Mammalian Chewing Movements: Chewing Frequency Scales with Body Mass in Mammals. Journal of Theoretical Biology, 160(4), 427–440.

Du, Y., Stewart, P., Hill, N. A., Yin, H., Penta, R., Köry, J., Luo, X., & Ogden, R. (2023). Nonlinear indentation of second-order hyperelastic materials. Journal of the Mechanics and Physics of Solids, 171, 105139.

Dusfour, G. (2018). Contribution à l'étude de la croissance du disque intervertébral et de cartilage de synt PhD thesis, Université Montpellier.

Edmonds, H. M. & Glowacka, H. (2020). The ontogeny of maximum bite force in humans. Journal of Anatomy, 237(3), 529–542.

Eriksson, L. & Westesson, P.-L. (1992). Temporomandibular joint diskectomy. Oral Surgery, Oral Medicine, Oral Pathology, 74(3), 259–272.

Fazaeli, S., Ghazanfari, S., Everts, V., Smit, T., & Koolstra, J. (2016). The contribution of collagen fibers to the mechanical compressive properties of the temporomandibular joint disc. Osteoarthritis and Cartilage, 24(7), 1292–1301.

Fazaeli, S., Ghazanfari, S., Mirahmadi, F., Everts, V., Smit, T. H., & Koolstra, J. H. (2019). The dynamic mechanical viscoelastic properties of the temporomandibular joint disc: The role of collagen and elastin fibers from a perspective of polymer dynamics. Journal of the Mechanical Behavior of Biomedical Materials, 100, 103406.

Franchi, M., De Pasquale, V., Martini, D., Quaranta, M., Macciocca, M., Dionisi, A., & Ottani, V. (2010). Contribution of Glycosaminoglycans to the Microstructural Integrity of Fibrillar and Fiber Crimps in Tendons and Ligaments. The Scientific World JOURNAL, 10, 1932–1940.

Fung, Y.-C. (1993). Biomechanics : Mechanical Properties of Living Tissues. New York, NY: Springer New York, 2 edition.

Geerligs, M., van Breemen, L., Peters, G., Ackermans, P., Baaijens, F., & Oomens, C. (2011). In vitro indentation to determine the mechanical properties of epidermis. Journal of Biomechanics, 44(6), 1176–1181.

Gervaso, F., Boschetti, F., & Pennati, G. (2014). Evaluation of the Wharton's jelly poroelastic parameters through compressive tests on placental and foetal ends of human umbilical cords. Journal of the Mechanical Behavior of Biomedical Materials, 35, 51–58.

Gervaso, F., Pennati, G., & Boschetti, F. (2007). Effect of geometrical imperfections in confined compression tests on parameter evaluation of hydrated soft tissues. Journal of Biomechanics, 40(13), 3041–3044.

González-Sánchez, B., García Monterey, P., Ramírez-Durán, M. d. V., Garrido-Ardila, E. M., Rodríguez-Mansilla, J., & Jiménez-Palomares, M. (2023). Temporomandibular Joint Dysfunctions: A Systematic Review of Treatment Approaches. Journal of Clinical Medicine, 12(12), 4156.

Griffin, M., Premakumar, Y., Seifalian, A., Butler, P. E., & Szarko, M. (2016). Biomechanical Characterization of Human Soft Tissues Using Indentation and Tensile Testing. Journal of Visualized Experiments, (118), 54872.

Guo, Z., Hao, M., Jiang, L., Li, D., Chen, Y., & Dong, L. (2020a). A modified Hertz model for finite spherical indentation inspired by numerical simulations. European Journal of Mechanics - A/Solids, 83, 104042.

Guo, Z., Lyu, Q., Jiang, L., Chen, Y., Dong, L., & Zhang, H. (2020b). Contact Model for Incompressible Neo-Hookean Materials Under Finite Spherical Indentation. Journal of Applied Mechanics, 87(5), 051003.

Gutman, S., Kim, D., Tarafder, S., Velez, S., Jeong, J., & Lee, C. H. (2018). Regionally variant collagen alignment correlates with viscoelastic properties of the disc of the human temporomandibular joint. Archives of Oral Biology, 86, 1–6.

Haslach, H. W., Leahy, L. N., Riley, P., Gullapalli, R., Xu, S., & Hsieh, A. H. (2014). Solid–extracellular fluid interaction and damage in the mechanical response of rat brain tissue under confined compression. Journal of the Mechanical Behavior of Biomedical Materials, 29, 138–150.

Heneghan, P. & Riches, P. E. (2008). Determination of the strain-dependent hydraulic permeability of the compressed bovine nucleus pulposus. Journal of Biomechanics, 41(4), 903–906.

Henry, C. H. & Wolford, L. M. (1993). Treatment outcomes for temporomandibular joint reconstruction after Proplast-Teflon implant failure. Journal of Oral and Maxillofacial Surgery, 51(4), 352–358.

Herbert, E. G., Pharr, G. M., Oliver, W. C., Lucas, B. N., & Hay, J. L. (2001). On the measurement of stress–strain curves by spherical indentation. Thin Solid Films, 398, 331–335.

Herring, S. W., Decker, J. D., Liu, Z., & Ma, T. (2002). Temporomandibular joint in miniature pigs: Anatomy, cell replication, and relation to loading. The Anatomical Record, 266(3), 152–166.

Hertz, H. (1882). Ueber die Berührung fester elastischer Körper. Journal für reine und angewandte Mathematik, 1882(92), 156–171.

Hirose, M., Tanaka, E., Tanaka, M., Fujita, R., Kuroda, Y., Yamano, E., Van Eijden, T. M. G. J., & Tanne, K. (2006). Three-dimensional finite-element model of the human temporomandibular joint disc during prolonged clenching. European Journal of Oral Sciences, 114(5), 441–448.

Holmes, M. & Mow, V. (1990). The nonlinear characteristics of soft gels and hydrated connective tissues in ultrafiltration. Journal of Biomechanics, 23(11), 1145–1156.

Holmes, M. H. (1985). A THEORETICAL ANALYSIS FOR DETERMINING THE NONLINEAR HYDRAULIC PERMEABILITY OF A SOFT TISSUE FROM A PERMEATION EXPERIMENT. Bulletin of Mathematical Biology, 47, 669–683.

Huang, D., Hee, M. R., & Fujimoto, J. G. (1991). Optical Coherence Tomography. Science, 254, 1178–1181.

Iivarinen, J. T., Korhonen, R. K., Julkunen, P., & Jurvelin, J. S. (2011). Experimental and computational analysis of soft tissue stiffness in forearm using a manual indentation device. Medical Engineering & Physics, 33(10), 1245–1253.

Jachowicz, J., McMullen, R., & Prettypaul, D. (2007). Indentometric analysis of in vivo skin and comparison with artificial skin models. Skin Research and Technology, 13(3), 299–309.

Jiang, N., Zhang, J., Li, Z., & Zhu, S. S. (2023). SCAFFOLD-BASED TISSUE ENGINEERING STRATEGIES FOR TEMPOROMANDIBULAR JOINT DISC REGENERATION AND REPLACEMENT. European Cells and Materials, 45, 131–142.

Johnson, N., Roberts, M., Doi, S., & Batstone, M. (2017). Total temporomandibular joint replacement prostheses: A systematic review and bias-adjusted meta-analysis. International Journal of Oral and Maxillofacial Surgery, 46(1), 86–92.

Juran, C. M., Dolwick, M. F., & McFetridge, P. S. (2015). Mechanobiological Assessment of TMJ Disc Surfaces: Nanoindentation and Transmission Electron Microscopy. Journal of Oral and Maxillofacial Research, 6(4).

Kaburagi, Y. & Hishiyama, Y. (2016). Scanning Electron Microscopy. In A. Yoshida (Ed.), Materials Science and Engineering of Carbon (pp. 71–93). Elsevier.

Kalidindi, S. R., Abusafieh, A., & El-Danaf, E. (1997). Accurate characterization of machine compliance for simple compression testing. Experimental Mechanics, 37(2), 210–215.

Kalpakci, K., Willard, V., Wong, M., & Athanasiou, K. (2011). An Interspecies Comparison of the Temporomandibular Joint Disc. Journal of Dental Research, 90(2), 193–198.

Kalyanam, S., Toohey, K. S., & Insana, M. F. (2021). Modeling biphasic hydrogels under spherical indentation: Application to soft tissues. Mechanics of Materials, 161, 103987.

Kang, H., Bao, G.-j., & Qi, S.-n. (2006). Biomechanical responses of human temporomandibular joint disc under tension and compression. International Journal of Oral and Maxillofacial Surgery, 35(9), 817–821.

Kanungo, B. P. & Gibson, L. J. (2009). Density–property relationships in mineralized collagen–glycosaminoglycan scaffolds. Acta Biomaterialia, 5(4), 1006–1018.

Kazemi, M. & Li, L. (2014). A viscoelastic poromechanical model of the knee joint in large compression. Medical Engineering & Physics, 36(8), 998–1006.

Kim, K.-W., Wong, M. E., Helfrick, J. F., Thomas, J. B., & Athanasiou, K. A. (2003). Biomechanical Tissue Characterization of the Superior Joint Space of the Porcine Temporomandibular Joint. Annals of Biomedical Engineering, 31(8), 924–930.

Kleinhans, K. L. & Jackson, A. R. (2018). Hydraulic permeability of meniscus fibrocartilage measured via direct permeation: Effects of tissue anisotropy, water volume content, and compressive strain. Journal of Biomechanics, 72, 215–221.

Koolstra, J. H. & Tanaka, E. (2009). Tensile stress patterns predicted in the articular disc of the human temporomandibular joint. Journal of Anatomy, 215(4), 411–416.

Kopp, M., Wiesmueller, M., Buchbender, M., Kesting, M., Nagel, A. M., May, M. S., Uder, M., Roemer, F. W., & Heiss, R. (2024). MRI of Temporomandibular Joint Disorders: A Comparative Study of 0.55 T and 1.5 T MRI. Investigative Radiology, 59(3), 223–229.

Krawiec, E., Lemaire, F., Lavrand, A., Adam, L., Boulagnon, C., Baldit, A., de Oliveira Cafiero, C., Da Rocha, A., Cavinato, C., de Isla, N., Dubernard, X., Boulmedais, F., Mauprivez, C., Kerdjoudj, H., & Brenet, E. (Manuscript in preparation). Optimizing the Properties of a Cell-Free Hydrogel System Based on Wharton's Jelly Extracellular Matrix for Facial Nerve Regeneration.

Kumar, A. & Lopez-Pamies, O. (2016). On the two-potential constitutive modeling of rubber viscoelastic materials. Comptes Rendus. Mécanique, 344(2), 102–112.

Kuo, J., Shi, C., Cisewski, S., Zhang, L., Kern, M., & Yao, H. (2011a). Regional cell density distribution and oxygen consumption rates in porcine TMJ discs: An explant study. Osteoarthritis and Cartilage, 19(7), 911–918.

Kuo, J., Wright, G., Bach, D., Slate, E., & Yao, H. (2011b). Effect of Mechanical Loading on Electrical Conductivity in Porcine TMJ Discs. Journal of Dental Research, 90(10), 1216–1220.

Kuo, J., Zhang, L., Bacro, T., & Yao, H. (2010). The region-dependent biphasic viscoelastic properties of human temporomandibular joint discs under confined compression. Journal of Biomechanics, 43(7), 1316–1321.

Labus, K. M., Kuiper, J. P., Rawlinson, J., & Puttlitz, C. M. (2021). Mechanical characterization and viscoelastic model of the ovine temporomandibular joint Disc in indentation, uniaxial tension, and biaxial tension. Journal of the Mechanical Behavior of Biomedical Materials, 116, 104300.

Lai, W. M., Mow, V. C., & Roth, V. (1981). Effects of Nonlinear Strain-Dependent Permeability and Rate of Compression on the Stress Behavior of Articular Cartilage. Journal of Biomechanical Engineering, 103(2), 61–66.

Le Bihan, D., Mangin, J., Poupon, C., Clark, C. A., Pappata, S., Molko, N., & Chabriat, H. (2001). Diffusion tensor imaging: Concepts and applications. Journal of Magnetic Resonance Imaging, 13(4), 534–546.

Lee, H., Campbell, W. D., Canning, M. E., Theis, K. M., Ennis, H. Y., Jackson, R. L., Wright, J. C., & Hanson, R. R. (2016). Correlation between signalment and the biphasic hyperelastic mechanical properties of equine articular cartilage. Biotribology, 7, 31–37.

Li, W., Trbojevic, S., & Almarza, A. J. (2021). Comparison of the Trueness of Fits of the Biphasic Transverse Isotropic and Kelvin Models to the Tensile Behavior of Temporomandibular Joint Disc. Journal of Biomechanical Engineering, 143(6), 064501.

Li, Y., Li, W., Wang, L., Wang, X., Gao, S., Liao, Y., Ji, Y., Lin, L., Liu, Y., & Chen, J. (2024). Detecting anteriorly displaced temporomandibular joint discs using super-resolution magnetic resonance imaging: A multi-center study. Frontiers in Physiology, 14, 1272814.

Lin, D. C., Shreiber, D. I., Dimitriadis, E. K., & Horkay, F. (2009). Spherical indentation of soft matter beyond the Hertzian regime: Numerical and experimental validation of hyperelastic models. Biomechanics and Modeling in Mechanobiology, 8(5), 345–358.

List, T. & Jensen, R. H. (2017). Temporomandibular disorders: Old ideas and new concepts. Cephalalgia, 37(7), 692–704.

Lumpkins, S. B. & McFetridge, P. S. (2009). Regional variations in the viscoelastic compressive properties of the temporomandibular joint disc and implications toward tissue engineering. Journal of Biomedical Materials Research Part A, 90A(3), 784–791.

MacManus, D. B., Gilchrist, M. D., & Murphy, J. G. (2017). An empirical measure of nonlinear strain for soft tissue indentation. Royal Society Open Science, 4(11), 170894.

Mak, A., Lai, W., & Mow, V. (1987). Biphasic indentation of articular cartilage—I. Theoretical analysis. Journal of Biomechanics, 20(7), 703–714.

Matuska, A. M., Muller, S., Dolwick, M., & McFetridge, P. S. (2016). Biomechanical and biochemical outcomes of porcine temporomandibular joint disc deformation. Archives of Oral Biology, 64, 72–79.

McCreery, K. P., Luetkemeyer, C. M., Calve, S., & Neu, C. P. (2023). Hyperelastic characterization reveals proteoglycans drive the nanoscale strain-stiffening response in hyaline cartilage. Journal of Biomechanics, 146, 111397.

Merson, J., Parvez, N., & Picu, R. (2023). Probing soft fibrous materials by indentation. Acta Biomaterialia, 163, 25–34.

Mesarovic, S. D. & Fleck, N. A. (1999). Spherical indentation of elastic–plastic solids. Proceedings of the Royal Society of London. Series A: Mathematical, Physical and Engineering Sciences, 455(1987), 2707–2728.

Miller, K. (2005). Method of testing very soft biological tissues in compression. Journal of Biomechanics, 38(1), 153–158.

Minarelli, A. M. (1997). The Structure of the Human Temporomandibular Joint Disc: A Scanning Electron Microscopy Study. J OROFACIAL PAIN 1, 11, 95–100.

Moghaddam, A. O., Wei, J., Kim, J., Dunn, A. C., & Wagoner Johnson, A. J. (2020). An indentation-based approach to determine the elastic constants of soft anisotropic tissues. Journal of the Mechanical Behavior of Biomedical Materials, 103, 103539.

Mooney, M. (1940). A Theory of Large Elastic Deformation. Journal of Applied Physics, 11(9), 582–592.

Morejon, A., Norberg, C. D., De Rosa, M., Best, T. M., Jackson, A. R., & Travascio, F. (2021). Compressive Properties and Hydraulic Permeability of Human Meniscus: Relationships With Tissue Structure and Composition. Frontiers in Bioengineering and Biotechnology, 8, 622552.

Mori, H., Horiuchi, S., Nishimura, S., Nikawa, H., Murayama, T., Ueda, K., Ogawa, D., Kuroda, S., Kawano, F., Naito, H., Tanaka, M., Koolstra, J. H., & Tanaka, E. (2010). Three-dimensional finite element analysis of cartilaginous tissues in human temporomandibular joint during prolonged clenching. Archives of Oral Biology, 55(11), 879–886.

Mow, V., Gibbs, M., Lai, W., Zhu, W., & Athanasiou, K. (1989). Biphasic indentation of articular cartilage—II. A numerical algorithm and an experimental study. Journal of Biomechanics, 22(8-9), 853–861.

Mow, V. C., Holmes, M. H., & Michael Lai, W. (1984). Fluid transport and mechanical properties of articular cartilage: A review. Journal of Biomechanics, 17(5), 377–394.

Mow, V. C., Kuei, S. C., Lai, W. M., & Armstrong, C. G. (1980). Biphasic Creep and Stress Relaxation of Articular Cartilage in Compression: Theory and Experiments. Journal of Biomechanical Engineering, 102(1), 73–84.

Mărcăuteanu, C., Demjan, E., Sinescu, C., Negrutiu, M., Motoc, A., Lighezan, R., Vasile, L., Hughes, M., Bradu, A., Dobre, G., & Podoleanu, A. G. (2010). Preliminary optical coherence tomography investigation of the temporo-mandibular joint disc. In J. A. Izatt, J. G. Fujimoto, & V. V. Tuchin (Eds.), SPIE Proceedings, volume 7554 (pp. 75542G). San Francisco, California: SPIE.

Nachman, M. & Franklin, S. (2016). Artificial Skin Model simulating dry and moist in vivo human skin friction and deformation behaviour. Tribology International, 97, 431–439.

Navindaran, K., Kang, J. S., & Moon, K. (2023). Techniques for characterizing mechanical properties of soft tissues. Journal of the Mechanical Behavior of Biomedical Materials, 138, 105575.

Nickel, J., Iwasaki, L., Gonzalez, Y., Gallo, L., & Yao, H. (2018). Mechanobehavior and Ontogenesis of the Temporomandibular Joint. Journal of Dental Research, 97(11), 1185–1192.

Oatis, C. A. (2009). Kinesiology: The Mechanics and Pathomechanics of Human Movement. Baltimore: Lippincott Williams & Wilkins, 2nd ed edition.

Oddes, Z. & Solav, D. (2023). Identifiability of soft tissue constitutive parameters from in-vivo macro-indentation. Journal of the Mechanical Behavior of Biomedical Materials, 140, 105708.

Ortún-Terrazas, J., Cegoñino, J., & Pérez del Palomar, A. (2021). Biomechanical impact of the porous-fibrous tissue behaviour in the temporomandibular joint movements. An in silico approach. Journal of the Mechanical Behavior of Biomedical Materials, 120, 104542.

Ortún-Terrazas, J., Cegoñino, J., & Pérez del Palomar, A. (2020). Computational characterization of the porous-fibrous behavior of the soft tissues in the temporomandibular joint. Journal of Biomedical Materials Research Part B: Applied Biomaterials, 108(5), 2204–2217.

Poole, J. J. A. & Mostaço-Guidolin, L. B. (2021). Optical Microscopy and the Extracellular Matrix Structure: A Review. Cells, 10(7), 1760.

Proctor, C. S., Schmidt, M. B., Whipple, R. R., Kelly, M. A., & Mow, V. C. (1989). Material properties of the normal medial bovine meniscus. Journal of Orthopaedic Research, 7(6), 771–782.

Psomadakis, C. E., Marghoob, N., Bleicher, B., & Markowitz, O. (2021). Optical coherence tomography. Clinics in Dermatology, 39(4), 624–634.

Puso, M. A. & Weiss, J. A. (1998). Finite Element Implementation of Anisotropic Quasi-Linear Viscoelasticity Using a Discrete Spectrum Approximation. Journal of Biomechanical Engineering, 120(1), 62–70.

Rashid, B., Destrade, M., & Gilchrist, M. D. (2012). Determination of friction coefficient in unconfined compression of brain tissue. Journal of the Mechanical Behavior of Biomedical Materials, 14, 163–171.

Rivlin, R. & Saunders, D. (1950). Large elastic deformations of isotropic materials VII. Experiments on the deformation of rubber. Philosophical Transactions of the Royal Society of London. Series A, Mathematical and Physical Sciences, 243(865), 251–288.

Rodrigues, Y., Mathew, M., Mercuri, L., da Silva, J., Henriques, B., & Souza, J. (2018). Biomechanical simulation of temporomandibular joint replacement (TMJR) devices: A scoping review of the finite element method. International Journal of Oral and Maxillofacial Surgery, 47(8), 1032–1042.

Sagl, B., Schmid-Schwap, M., Piehslinger, E., Kundi, M., & Stavness, I. (2019). A Dynamic Jaw Model With a Finite-Element Temporomandibular Joint. Frontiers in Physiology, 10, 1156.

Savoldelli, C., Bouchard, P.-O., Manière-Ezvan, A., Bettega, G., & Tillier, Y. (2012). Comparison of stress distribution in the temporomandibular joint during jaw closing before and after symphyseal distraction: A finite element study. International Journal of Oral and Maxillofacial Surgery, 41(12), 1474–1482.

Schall, E., de Oliveira Cafiero, C., Sapin- de Brosses, E., Losser, M. R., Bonnet, A. S., & Baldit, A. (2025). Handling complexity of soft biological tissues mechanics through practice and open science resources: Application to the spherical compression of a muscle. International Journal of Mechanical Engineering Education, (pp. 03064190251379355).

Schmolke, C. & Hugger, A. (1999). The human temporomandibular joint region in different positions of the mandible. Annals of Anatomy - Anatomischer Anzeiger, 181(1), 61–64.

Scholze, M., Safavi, S., Li, K. C., Ondruschka, B., Werner, M., Zwirner, J., & Hammer, N. (2020). Standardized tensile testing of soft tissue using a 3D printed clamping system. HardwareX, 8, e00159.

Scholze, M., Singh, A., Lozano, P. F., Ondruschka, B., Ramezani, M., Werner, M., & Hammer, N. (2018). Utilization of 3D printing technology to facilitate and standardize soft tissue testing. Scientific Reports, 8(1), 11340.

Seifzadeh, A., Wang, J., Oguamanam, D. C. D., & Papini, M. (2011). A Nonlinear Biphasic Fiber-Reinforced Porohyperviscoelastic Model of Articular Cartilage Incorporating Fiber Reorientation and Dispersion. Journal of Biomechanical Engineering, 133(8), 081004.

Selvadurai, A. & Suvorov, A. (2016). Coupled hydro-mechanical effects in a poro-hyperelastic material. Journal of the Mechanics and Physics of Solids, 91, 311–333.

Sharabi, M. (2022). Structural Mechanisms in Soft Fibrous Tissues: A Review. Frontiers in Materials, 8, 793647.

Shi, C., Wright, G., Ex-Lubeskie, C., Bradshaw, A., & Yao, H. (2013). Relationship between anisotropic diffusion properties and tissue morphology in porcine TMJ disc. Osteoarthritis and Cartilage, 21(4), 625–633.

Shi, L. & Myers, K. (2023). A Finite Porous-Viscoelastic Model Capturing Mechanical Behavior of Human Cervix Under Multi-Step Spherical Indentation. SSRN Electronic Journal.

Shu, J., Teng, H., Shao, B., Zheng, T., Liu, Y., & Liu, Z. (2020). Biomechanical responses of temporomandibular joints during the lateral protrusions: A 3D finite element study. Computer Methods and Programs in Biomedicine, 195, 105671.

Singh, A. K., Khanal, N., & Chaulagain, R. (2022). Advances in Tissue Engineering of the Temporomandibular Joint Disc: An Overview of Current Status and Future Directions. International Journal of Dentistry, 2022, 1–8.

Solis-Cordova, J., Edwards, J. H., Fermor, H. L., Riches, P., Brockett, C. L., & Herbert, A. (2023). Characterisation of native and decellularised porcine tendon under tension and compression: A closer look at glycosaminoglycan contribution to tendon mechanics. Journal of the Mechanical Behavior of Biomedical Materials, 139, 105671.

Stehling, C., Vieth, V., Bachmann, R., Nassenstein, I., Kugel, H., Kooijman, H., Heindel, W., & Fischbach, R. (2007). High-Resolution Magnetic Resonance Imaging of the Temporomandibular Joint: Image Quality at 1.5 and 3.0 Tesla in Volunteers. Investigative Radiology, 42(6), 428–434.

Storåkers, B. (1986). On material representation and constitutive branching in finite compressible elasticity. Journal of the Mechanics and Physics of Solids, 34(2), 125–145.

Tanaka, E., del Pozo, R., Tanaka, M., Aoyama, J., Hanaoka, K., Nakajima, A., Inuzuka, S., & Tanne, K. (2003a). Strain-rate effect on the biomechanical response of bovine temporomandibular joint disk under compression. Journal of Biomedical Materials Research, 67A(3), 761–765.

Tanaka, E., Kikuzaki, M., Hanaoka, K., Tanaka, M., Sasaki, A., Kawai, N., Ishino, Y., Takeuchi, M., & Tanne, K. (2003b). Dynamic compressive properties of porcine temporomandibular joint disc. European Journal of Oral Sciences, 111(5), 434–439.

Tanaka, E., Tanaka, M., Watanabe, M., Del Pozo, R., & Tanne, K. (2001). Influences of occlusal and skeletal discrepancies on biomechanical environment in the TMJ during maximum clenching: An analytic approach with the finite element method. Journal of Oral Rehabilitation, 28(9), 888–894.

Tanne, K., Tanaka, E., & Sakuda, M. (1991). The Elastic Modulus of the Temporomandibular Joint Disc from Adult Dogs. Journal of Dental Research, 70(12), 1545–1548.

Tappert, L., Dusfour, G., Baldit, A., Le Floc'H, S., & Lipinski, P. (2022). Experimental study of eigenstrains in temporomandibular joint discs using digital image analysis. Journal of the Mechanical Behavior of Biomedical Materials, 134, 105395.

Tappert, L. K. (2020). Experimental and Numerical Analysis of the Temporomandibular Joint Disc Behaviour. PhD thesis, Université de Lorraine.

Tappert, L. K., Baldit, A., Guillaume, C., Velard, F., & Lipinski, P. (2020). Identification of macro-heterogenous mechanical behaviour of temporomandibular joint disc. Computer Methods in Biomechanics and Biomedical Engineering, 23(sup1), S291–S293.

Tappert, Lk., Baldit, A., Rahouadj, R., & Lipinski, P. (2017). Local elastic properties characterization of the temporo-mandibular joint disc through macro-indentation. Computer Methods in Biomechanics and Biomedical Engineering, 20(sup1), S201–S202.

Throckmorton, G. & Dechow, P. (1994). In vitro strain measurements in the condylar process of the human mandible. 39(10), 853–867.

Throckmorton, G. S. & Throckmorton, L. S. (1985). Quantitative calculations of temporomandibular joint reaction forces—I. The importance of the magnitude of the jaw muscle forces. Journal of Biomechanics, 18(6), 445–452.

Tong, P. & Fung, Y.-C. (1976). The stress-strain relationship for the skin. Journal of Biomechanics, 9(10), 649–657.

Trindade, D., Cordeiro, R., José, H. C., Ângelo, D. F., Alves, N., & Moura, C. (2021). Biological Treatments for Temporomandibular Joint Disc Disorders: Strategies in Tissue Engineering. Biomolecules, 11(7), 933.

Tverje, V. M. & Nyashin, Y. I. (2010). КОЭФФИЦИЕНТ ГИДРАВЛИЧЕСКОЙ ПРОНИЦАЕМОСТИ ДИСКА ВИСОЧНО-НИЖНЕЧЕЛЮСТНОГО СУСТАВА: ЭКСПЕРИМЕНТАЛЬНОЕ ОПРЕДЕЛЕНИЕ. Российский журнал биомеханики, 14(2), 28–36.

Vapniarsky, N., Huwe, L. W., Arzi, B., Houghton, M. K., Wong, M. E., Wilson, J. W., Hatcher, D. C., Hu, J. C., & Athanasiou, K. A. (2018). Tissue engineering toward temporomandibular joint disc regeneration. Science Translational Medicine, 10(446), eaaq1802.

Vidotto, M., Pederzani, M., Castellano, A., Pieri, V., Falini, A., Dini, D., & De Momi, E. (2021). Integrating Diffusion Tensor Imaging and Neurite Orientation Dispersion and Density Imaging to Improve the Predictive Capabilities of CED Models. Annals of Biomedical Engineering, 49(2), 689–702.

Vignesh, U., Mehrotra, D., Bhave, S., Katrolia, R., & Sharma, S. (2020). Finite element analysis of patient-specific TMJ implants to replace bilateral joints with simultaneous correction of facial deformity. Journal of Oral Biology and Craniofacial Research, 10(4), 674–679.

Wang, M., Liu, S., Xu, Z., Qu, K., Li, M., Chen, X., Xue, Q., Genin, G. M., Lu, T. J., & Xu, F. (2020). Characterizing poroelasticity of biological tissues by spherical indentation: An improved theory for large relaxation. Journal of the Mechanics and Physics of Solids, 138, 103920.

Wei, Z., Yu, X., Xu, X., & Chen, X. (2014). Experiment and hydro-mechanical coupling simulation study on the human periodontal ligament. Computer Methods and Programs in Biomedicine, 113(3), 749–756.

Weiss, J. A. & Maakestad, B. J. (2006). Permeability of human medial collateral ligament in compression transverse to the collagen fiber direction. Journal of Biomechanics, 39(2), 276–283.

Whitaker, S. (1986). Flow in porous media I: A theoretical derivation of Darcy's law. Transport in Porous Media, 1(1), 3–25.

Whyte, A., Boeddinghaus, R., Bartley, A., & Vijeyaendra, R. (2021). Imaging of the temporomandibular joint. Clinical Radiology, 76(1), 76.e21–76.e35.

Willard, V., Zhang, L., & Athanasiou, K. (2011). Tissue Engineering of the Temporomandibular Joint. In Comprehensive Biomaterials (pp. 221–235). Elsevier.

Woo, S.-Y., Akeson, W., & Jemmott, G. (1976). Measurements of nonhomogeneous, directional mechanical properties of articular cartilage in tension. Journal of Biomechanics, 9(12), 785–791.

Wriggers, P. (2008). Nonlinear Finite Element Methods. Berlin, Heidelberg: Springer Berlin / Heidelberg.

Wright, G. J., Coombs, M. C., Hepfer, R. G., Damon, B. J., Bacro, T. H., Lecholop, M. K., Slate, E. H., & Yao, H. (2016). Tensile biomechanical properties of human temporomandibular joint disc: Effects of direction, region and sex. Journal of Biomechanics, 49(16), 3762–3769.

Wright, G. J., Kuo, J., Shi, C., Bacro, T. R. H., Slate, E. H., & Yao, H. (2013). Effect of Mechanical Strain on Solute Diffusion in Human TMJ Discs: An Electrical Conductivity Study. Annals of Biomedical Engineering, 41(11), 2349–2357.

Wu, C.-E., Lin, K.-H., & Juang, J.-Y. (2016). Hertzian load–displacement relation holds for spherical indentation on soft elastic solids undergoing large deformations. Tribology International, 97, 71–76.

Wu, L.-C., Chiang, C.-J., Liu, Z.-H., Tsuang, Y.-H., Sun, J.-S., & Huang, Y.-Y. (2014). Fabrication and properties of acellular porcine anulus fibrosus for tissue engineering in spine surgery. Journal of Orthopaedic Surgery and Research, 9(1), 118.

Wu, Y., Cisewski, S., Coombs, M., Brown, M., Wei, F., She, X., Kern, M., Gonzalez, Y., Gallo, L., Colombo, V., Iwasaki, L., Nickel, J., & Yao, H. (2019). Effect of Sustained Joint Loading on TMJ Disc Nutrient Environment. Journal of Dental Research, 98(8), 888–895.

Wu, Y., Cisewski, S. E., Wei, F., She, X., Gonzales, T. S., Iwasaki, L. R., Nickel, J. C., & Yao, H. (2017). Fluid pressurization and tractional forces during TMJ disc loading: A biphasic finite element analysis. Orthodontics & Craniofacial Research, 20(S1), 151–156.

Wu, Y., Kuo, J., Wright, G. J., Cisewski, S. E., Wei, F., Kern, M. J., & Yao, H. (2015). Viscoelastic shear properties of porcine temporomandibular joint disc. Orthodontics & Craniofacial Research, 18, 156–163.

Xu, X., Li, Z., Cai, L., Calve, S., & Neu, C. P. (2016). Mapping the Nonreciprocal Micromechanics of Individual Cells and the Surrounding Matrix Within Living Tissues. Scientific Reports, 6(1), 24272.

Yambe, S., Yoshimoto, Y., Ikeda, K., Maki, K., Takimoto, A., Tokuyama, A., Higuchi, S., Yu, X., Uchibe, K., Miura, S., Watanabe, H., Sakuma, T., Yamamoto, T., Tanimoto, K., Kondoh, G., Kasahara, M., Mizoguchi, T., Docheva, D., Adachi, T., & Shukunami, C. (2024). Sclerostin modulates mineralization degree and stiffness profile in the fibrocartilaginous enthesis for mechanical tissue integrity. Frontiers in Cell and Developmental Biology, 12, 1360041.

Yang, W., Sherman, V. R., Gludovatz, B., Schaible, E., Stewart, P., Ritchie, R. O., & Meyers, M. A. (2015). On the tear resistance of skin. Nature Communications, 6(1), 6649.

Yu, J., Manouchehri, N., Yamamoto, S., Kwon, B. K., & Oxland, T. R. (2020). Mechanical properties of spinal cord grey matter and white matter in confined compression. Journal of the Mechanical Behavior of Biomedical Materials, 112, 104044.

Yuya, P. A., Amborn, E. K., Beatty, M. W., & Turner, J. A. (2010). Evaluating Anisotropic Properties in the Porcine Temporomandibular Joint Disc Using Nanoindentation. Annals of Biomedical Engineering, 38(7), 2428–2437.

Zhang, M.-G., Cao, Y.-P., Li, G.-Y., & Feng, X.-Q. (2014). Spherical indentation method for determining the constitutive parameters of hyperelastic soft materials. Biomechanics and Modeling in Mechanobiology, 13(1), 1–11.

Zieliński, G., Pająk-Zielińska, B., & Ginszt, M. (2024). A Meta-Analysis of the Global Prevalence of Temporomandibular Disorders. Journal of Clinical Medicine, 13(5), 1365.

Zimmerman, B. K., Maas, S. A., Weiss, J. A., & Ateshian, G. A. (2022). A Finite Element Algorithm for Large Deformation Biphasic Frictional Contact Between Porous-Permeable Hydrated Soft Tissues. Journal of Biomechanical Engineering, 144(2), 021008.

Zimmerman, B. K., Nims, R. J., Chen, A., Hung, C. T., & Ateshian, G. A. (2021). Direct Osmotic Pressure Measurements in Articular Cartilage Demonstrate Nonideal and Concentration-Dependent Phenomena. Journal of Biomechanical Engineering, 143(4), 041007.

Characterization of the poromechanical coupling in soft biological tissues: application to the temporomandibular joint disc.

Abstract: The characterization of soft biological tissues aims to predict their mechanical behavior in order to guide studies of substitutes for these materials, as well as numerical analyses aimed at understanding pathologies and developing prostheses. For this characterization, it is important to consider the complexity of these tissues, which are subjected to large deformations, are anisotropic, viscoelastic, and heterogeneous. Cartilaginous tissues, for example, are porous and rich in fluid, with internal dynamics directly linked to the observed mechanics. Therefore, the use of poromechanical models to describe their behavior is particularly relevant. The temporomandibular joint connects the mandible to the skull, and the high incidence of associated dysfunctions motivates the study of the mechanics of its components. The temporomandibular disc is a fibrocartilage essential for the proper functioning of this joint. It acts as a stress-distributing mechanism, in addition to guiding mandibular movements. This work focuses on the application of poromechanical concepts to the characterization of the temporomandibular disc. There are many gaps in current knowledge about the mechanics of this tissue, and existing studies, although numerous, do not allow for clear conclusions, given the diversity of approaches used. The study was conducted experimentally on porcine temporomandibular discs, initially tested using non-destructive spherical compression tests. A procedure was proposed to allow for the identification of material parameters using these tests on thin biological tissues considering monophasic hyperelastic model. Then, finite element simulations were performed to determine, through optimization, the values of the poromechanical parameters that most accurately reproduce the experimental tests. Besides, the discs were sectioned to prepare samples, which were tested under confined compression and direct perfusion. The values of the poromechanical parameters obtained confirmed the one coming from the spherical compression tests. Finally, tensile tests were performed revealing the anisotropy of the disc. Meanwhile, the immediate deformation of the samples after cutting was analyzed using video correlation, allowing visualization of the internal stresses' effects within the material, its anisotropy, and the role of its microstructure.
Keywords: poromechanical coupling; soft biological tissues; temporomandibular joint disc; experimentation; simulation.

Caractérisation des couplages poromécaniques dans les tissus biologiques mous : application au disque de l'articulation temporomandibulaire.

Résumé : La caractérisation des tissus biologiques mous vise à prédire leur comportement mécanique afin de guider des études portant sur le développement de substituts, ainsi que de nourrir les analyses numériques visant à comprendre les pathologies et à développer des prothèses. Pour cette caractérisation, il est important de prendre en compte la complexité de ces tissus, soumis à des grandes déformations, étant anisotropes, visqueux et non homogènes. Les tissus cartilagineux par exemple, sont poreux et riches en fluides et leur dynamique interne est directement liée à la mécanique observée. La prise en compte des lois de type poromécanique pour décrire leur comportement s'avère donc particulièrement intéressante. L'articulation temporomandibulaire relie la mandibule au crâne, et la forte incidence des dysfonctions qui lui sont associées motive l'étude de la mécanique de ses composants. Le disque temporomandibulaire est un fibrocartilage essentiel au bon fonctionnement de l'articulation. Il agit comme un mécanisme de répartition des contraintes, en plus de guider les mouvements mandibulaires. Ce travail porte sur l'application de concepts poromécaniques à la caractérisation du disque de l'articulation temporo-mandibulaire. Il existe de nombreuses lacunes dans les connaissances actuelles sur la mécanique de ce tissu et les études existantes, bien que nombreuses, ne permettent pas d'établir de conclusions claires, étant donné la diversité des approches utilisées. L'étude a été menée expérimentalement sur des disques temporomandibulaires de porc, testés initialement lors d'essais non destructifs de compression sphérique. Une méthodologie a été porposée pour permettre l'identification de paramètres initiaux par ces essais sur tissus biologiques minces considérés comme hyperélastiques monophasiques. Puis, des simulations par éléments finis ont été réalisées pour déterminer, par optimisation, les valeurs des paramètres poromécaniques permettant de reproduire le plus fidèlement possible les essais expérimentaux. Les disques ont ensuite été sectionnés pour préparer des échantillons, qui ont été testés sur des dispositifs conçus sur mesure en compression confinée et perfusion directe. Les valeurs des paramètres poromécaniques extraits par ces essais ont confirmé celles fournies par les essais de compression sphérique. Finalement, des essais de traction ont été réalisés et ont permis de mettre en évidence la réponse mécanique anisotrope du disque. Lors de la découpe des échantillons, la déformation immédiate observée a été évaluée par corrélation d'images, ce qui a permis de visualiser l'effets des contraintes internes du matériau, son anisotropie et le rôle de sa microstructure.
Mots clés : couplage poromécanique; tissus biologiques mous; disque de l'articulation temporomandibulaire; expérimentation; simulation.